UNIVERSITY OF OKLAHOMA

GRADUATE COLLEGE

GEOMECHANICAL MODELING OF RESERVOIR USING FINITE ELEMENT METHOD

A DISSERTATION

SUBMITTED TO THE GRADUATE FACULTY

in partial fulfillment of the requirements for the

Degree of

DOCTOR OF PHILOSOPHY

By

SHAHLA FEIZI MASOULEH
Norman, Oklahoma
2020

GEOMECHANICAL MODELING OF RESERVOIR USING FINITE ELEMENT METHOD

A DISSERTATION APPROVED FOR THE
MEWBOURNE SCHOOL OF PETROLEUM AND GEOLOGICAL ENGINEERING

BY THE COMMITTEE CONSISTING OF

Dr. Ahmad Ghassemi, Chair

Dr. Matthew J. Pranter

Dr. Jean-Claude Roegiers

Dr. Deepak Devegowda

Dr. Mashhad Fahes

To HIM

To my father, mother, brother and sister who supported me through years of my Ph.D. study.

Acknowledgements

I would like to express my sincere gratitude to my advisor, Dr. Ahmad Ghassemi, for his constant guidance, inspiration and encouragement throughout my Ph.D. study. Dr. Ghassemi enlightened my horizons of geomechanics and enhanced my interest in reservoir rock mechanics, through providing me the opportunity to know, work with, learn from, and conference with a group of excellent experts in this field around the world. Without his support and supervising, the completion of this dissertation would not be possible.

I would like to thank Dr. Mashhad Fahs, Dr. Deepak Devegowda, Dr. Matthew Pranter and Dr. Jean-Claude Roegiers for serving in my thesis committee. I benefited a lot from their pertinent comments and suggestions.

I also would like to thank Theresa Marks for her support and inspiration during the preparation of this dissertation. I greatly appreciate the help and encouragement from my former and present colleagues Dr. Dharmendra Kumar, Qian Gao, Amir Kamali, Behzad Hemami, Varahanaresh Sesetty, Lianbo Hu, Kai Huang, Jian Huang, Reza Safari, Vahid Serajian and Yawei Li who made my PhD study a great experience.

Table of Contents

List of Tables

List of Figures

Abstract

Importance of refracturing horizontal wells in low permeability reservoirs is well recognized in oil and gas industry. As a result of production from a propped open fracture, the stress changes in the reservoir. However, the stress change is anisotropic. This change in stresses near the producing horizontal well will act as a sink for infill well fractures and they tend to propagate towards the primary well, resulting in communications between producing and infill wells or so-called “frac-hits”. Previous studies have shown the effect of stress reorientation on refracturing of vertical and horizontal wells. By figuring out the extent and timing of stress reorientation, potential increase in well production after refracturing can be evaluated.

Coupled processes between matrix deformation and fluid flow are very important for predicting reservoir behavior and pore pressure evolution. Hydrocarbon production causes significant changes in pore pressure and stress in the reservoir. In this work, a coupled flow and geomechanics model was developed to capture changes of stress in magnitude and orientation during reservoir depletion. The simulator is based on finite element method. The developed model is used to predict refracturing performance and help with planning infill wells. As reservoirs usually contain more than one phase, it’s important to consider all the phases in geomechanical calculations.

Although sequentially coupled multiphase flow and geomechanics simulators have been developed and applied to describe multiphase flow in deformable porous media, they have limitations in modelling fractures and heterogeneous reservoir.

Saturation weighted average pore pressure is commonly used in geomechanical calculations of two-phase flow; However, “equivalent pore pressure” is used in this work since capillary

pressure is not negligible in the cases considered and using average pressure may lead to numerical errors.

To our knowledge, fully coupling of multiphase flow and geomechanics to study refrac jobs has not been studied before and previous studies have limitations on time step size and mesh type, uses average pore pressure instead of equivalent pore pressure, and ignores capillary pressure in the case studies.

The developed model was applied to analyze a waterflooding problem in homogeneous domain. Time dependent field variables such as pressure distribution, saturation profile, displacements and reservoir stresses were computed as water was injected and produced from the reservoir.

The present model is used to simulate the case of production from a fracture in a 3D reservoir. A comparative analysis of stresses, pore pressure, cumulative production and rotation of principal stresses between single-phase and two-phase analysis is performed to investigate the impact of including multiphase flow in the design of fracturing operations.

The results show that the diffusion front travels farther into reservoir in case of single-phase flow due to the impact of relative permeability in multiphase flow. This causes the isotropic point to be at a greater distance from the well in single flow model and can have an impact on the design of refrac jobs.

The new numerical poroelastic solution provides more realistic estimates for the time-dependent stress and pore pressure distribution around fractures thus allowing the production engineer to more accurately design refrac jobs and avoid frac hits.

1. Introduction

1.1 Literature Review

Geological materials such as soils and rocks are usually two-phase materials consisting of a solid skeleton and voids filled with fluid. Such materials are usually called poroelastic materials. Many fields of engineering are interested in the behavior of poroelastic materials including geomechanics, geotechnical engineering, biomechanics, petroleum engineering, earthquake engineering and environmental engineering. Influence of pore pressure on matrix deformation of fluid saturated porous materials was first studied by Terzaghi in 1923 who introduced the notion of effective stress for consolidation of soils under a constant load without lateral movement. In his one-dimensional isothermal consolidation theory, the deformation was due to rearrangement of soil particles whereas compressibility of solid grains and pore fluid were disregarded. This uncoupled approach doesn't consider the contribution of rock deformation to the pressure because geomechanical equilibrium is not coupled with mass conservation equation. Terzaghi theory was later extended to more general three-dimensional systems by Biot (1941) who developed the mathematical framework for the poroelasticity theory. Biot theory rigorously couples the mechanical and pore fluid processes by accounting for the compressibility of fluid and solid particles predicting phenomena such as Mandel-Cryer effect (Mandel, 1953) which could not be predicted by the uncoupled Terzaghi theory. However, some constants in Biot theory are hard to interpret. Rice and Cleary (1976) linked the new poroelastic parameters introduced by Biot to more familiar constants that are well understood in rock and soil mechanics. A set of five independent material constants must be supplied to provide a full description of an isotropic poroelastic material. An

example set includes drained shear modulus, bulk modulus, grain compressibility, permeability and porosity (Detournay and Cheng 1993). Biot formulation of poroelasticity was generalized to include the influence of temperature (McTigue 1986, Kurashige 1989). It included the general formulation of conductive heat transfer mechanism and considered compressibility and expansion of solid and fluid phases, setting the framework of thermo-poroelasticity. The Theory was later expanded to chemically active environments (Heidug and Wong 1996) based on irreversible thermodynamics.

Various analytical and numerical methods have been developed for the solution of boundary value problems in poroelasticity. Due to complexity of the coupled set of partial differential equations, an analytical solution for a fully coupled problem is not possible without making simplifying assumptions such as homogeneity, specialized load and boundary conditions, etc. (Neaupane and Yamabe,1999). Nevertheless, analytical solutions are invaluable in providing benchmarks for verifying accuracy of numerical schemes (Nguyen, 1995).

The advent of greater computational capabilities has been accompanied by the development of different numerical schemes including the finite element method, the indirect boundary element method, the direct coupled and uncoupled boundary element method, and displacement discontinuity method. The continuous Galerkin finite element method is one of the most popular methods and is widely used in engineering applications (Nguyen, 1995).

1.2 Research Motivation

Sometimes, simplifying the physics of a problem results in unreliability of the results. Neglecting the coupled nature of fluid flow in porous media could result in significant prediction errors. In the past, the primary focus of poroelasticity has been on single phase flow.

But since multiphase systems are more common in petroleum engineering applications, focus is shifting towards modeling coupled flow and geomechanics phenomena comprising two or more immiscible fluids in deformable rock.

Conventional reservoir simulations don't consider volumetric changes due to effective stress changes and external load application. They assume that volume changes only result from porosity changes which is related to pore pressure only through pore compressibility (Lee 2008).

Today, the high-speed computers allow engineers to solve large systems of equations simultaneously involving poroelasticity or thermo-poroelasticity.

1.3 Research objectives

The main objective of this work is to develop techniques to solve Biot fully coupled equations in an efficient way and study the behavior of one and two-phase fluid flow through deformable reservoirs. For this purpose, finite element codes have been developed for axisymmetric and three-dimensional cases. The codes are capable to solve single and multiphase flow in porous rock and their performance and validity will be studied and demonstrated through examples. In brief, the objectives can be stated as follows:

- Necessary mathematical formulations for describing one-phase and two-phase fluid flow and reservoir deformations are proposed. The equations consider the effects of capillarity, saturation and change of relative permeability.
- A three-dimensional code is developed for the Biot theory of poroelasticity based of formulations derived in the previous step using finite element method. It can handle different boundary conditions and irregular reservoir geometries and heterogeneities.
- the code is validated using analytical solutions of published results

- The model in applied in petroleum engineering applications to get a better understanding of the behavior of porous media

In the first part of the thesis, axisymmetric finite element code is developed based on linear stress-strain relation and single phase Biot's theory. Later the code is expanded to three-dimensional case and then upgraded to multiphase systems to be able to solve more complex problems in reservoirs with more than one phase and nonzero capillary pressure. Validation of the model is conducted by comparing the numerical results with available analytical solutions, experiments and published numerical results.

1.4 Dissertation outline

In chapter 2, differential equations that govern the thermo-poroelasticity in axisymmetric conditions are reviewed.

In chapter 3, numerical procedures to solve finite element equations are briefly explained. In the time integration scheme used in this analysis, fully implicit method is adopted to reduce the oscillations of the numerical solution and obtain more accurate solutions. It should be noted that throughout this dissertation, the sign convention is positive for tension unless specified otherwise. The developed model is verified against known analytical solutions such as Mandel's problem, borehole stability, thermal consolidation and well production.

In chapter 4, the 3D fully coupled model using finite element method is utilized to analyze the poroelastic behavior of producing vertical and horizontal wells including single or multiple fractures. The concepts of stress reorientation/reversal due to reservoir depletion and "frac-hits" in horizontal well refracturing are discussed using numerical examples. Case studies include heterogenous and homogeneous reservoirs.

In Chapter 5 the 3D fully coupled model is generalized to the multiphase flow describing the governing equations and the implementation into a finite element model. Several verification cases are presented and later the model is applied to study an enhanced oil recovery problem and production from a fracture in a two-phase reservoir.

In chapter 6, the results of this study are discussed, and conclusions are made. Also, future work in this area is suggested.

2. Axisymmetric thermo-poroelasticity

2.1 Introduction

In this chapter the governing equations for fluid saturated porous media for the axisymmetric problems are developed. The basic assumption in an axisymmetric model is that geometry, loading, boundary conditions and material properties do not vary in θ-direction and the circumferential displacement component is equal to zero, $u_\theta = 0$. Figure 2-1a shows an axisymmetric element in cylindrical coordinate system. All nonzero stress components are shown in this figure. The problem can be simply treated as a two-dimensional model in *rz* plane as depicted in Figure 2-1c. The sign convention used here is tension positive for the solid phase, and inflow positive for the fluid.

2.2 Constitutive equation

To formulate the constitutive equations for time evolution of stress and pore volume fraction, free energy density of wetted mineral matrix needs to be differentiated in respect to time. The change in Helmholtz free energy density represents three processes: elastic deformation, inflow or outflow of fluid mass and entropy change per unit volume (Zhou and Ghassemi 2009, Heidug and Wong 1996). Through this approach, the general incremental constitutive equations for axisymmetric thermo-poroelasticity in cylindrical coordinates can be written as (McTigue 1986, Ghassemi and Zhang 2006):

$$\dot{\sigma}_{rr} = 2G\dot{\epsilon}_{rr} + \frac{2G\nu}{1-2\nu}\dot{\varepsilon} - \alpha\dot{p} - \beta\dot{T} \tag{2.1}$$

$$\dot{\sigma}_{\theta\theta} = 2G\dot{\epsilon}_{\theta\theta} + \frac{2G\nu}{1-2\nu}\dot{\varepsilon} - \alpha\dot{p} - \beta\dot{T} \tag{2.2}$$

$$\dot{\sigma}_{zz} = 2G\dot{\epsilon}_{zz} + \frac{2G\nu}{1-2\nu}\dot{\varepsilon} - \alpha\dot{p} - \beta\dot{T} \tag{2.3}$$

$$\dot{\sigma}_{rz} = 2G\dot{\epsilon}_{rz} \tag{2.4}$$

$$\tau_{r\theta} = 0; \tau_{\theta z} = 0; \tag{2.5}$$

$$\dot{\zeta} = \alpha\dot{\epsilon} + \frac{1}{M}\dot{p} - \gamma_2\dot{T} \tag{2.6}$$

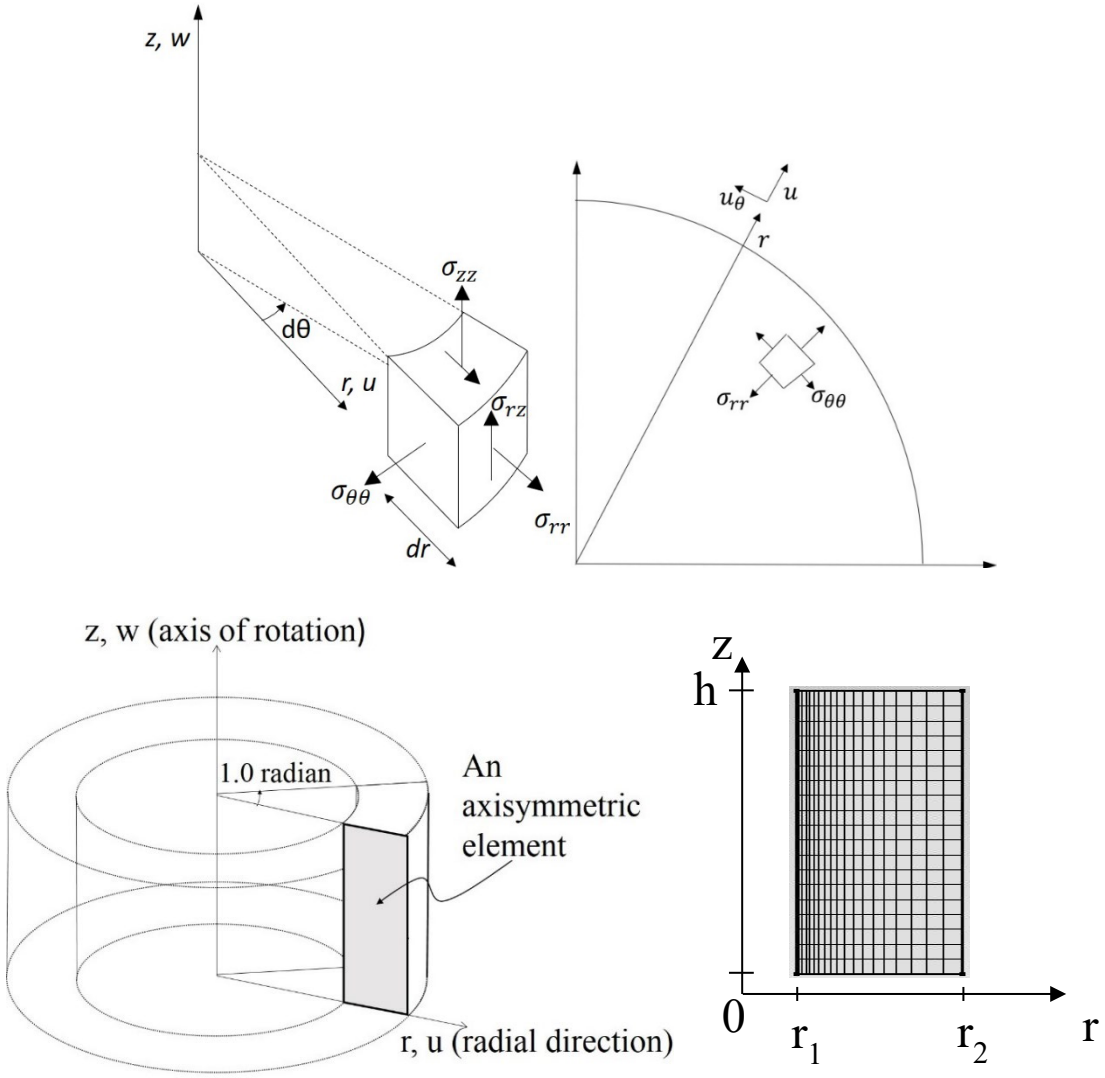

Figure 2-1. (a) The stresses applied to an element in axisymmetric conditions (b) Stress and displacement components in horizontal plane. Due to axisymmetric conditions, $u_\theta = 0$ and (c) an example case of a hollow cylinder for which an axisymmetric model in rz plane is used (d) 2D representation of the problem with axisymmetric mesh in rz plane.

where σ_{rr}, $\sigma_{\theta\theta}$, σ_{zz} and σ_{rz} are radial, tangential, vertical and shear stresses respectively and ε_{rr}, $\varepsilon_{\theta\theta}$, ε_{zz} and ε_{rz} are the corresponding strains. p, T, G and ν denote pore pressure, temperature, shear modulus of porous media and Poisson's ratio, respectively. α is Biot's

coefficient and $\dot{\zeta}$ is the variation of fluid volume per unit initial volume of porous material due to diffusive mass transport. M is the Biot modulus. The notations in Eqs. (2.1) through (2.6) are defined as follows:

$$\beta = K\alpha_m \tag{2.7}$$

$$\varepsilon = \varepsilon_{rr} + \varepsilon_{\theta\theta} + \varepsilon_{zz} \tag{2.8}$$

$$\frac{1}{M} = \frac{(\alpha - \phi)}{K_s} + \frac{\phi}{K_f} \tag{2.9}$$

$$\gamma_2 = \alpha\alpha_m + (\alpha_f - \alpha_m)\phi \tag{2.10}$$

where ϕ, K , K_s and K_f are porosity and bulk moduli of porous material, solid matrix and pore fluid, respectively. α_m and α_f denote the volumetric thermal expansion coefficients of solid matrix and fluid, respectively.

Note that shear stresses $\sigma_{r\theta}$, $\sigma_{\theta z}$ and their corresponding strains $\varepsilon_{r\theta}$ and $\varepsilon_{\theta z}$ are equal to zero due to the presence of axial symmetry with respect to both geometry and loading.

Effective stress is defined as a combination of applied stress and pore pressure which produces the same effect irrespective of the individual magnitudes of applied stress or pore pressure. It was given by Nur and Byerlee (1971) as:

$$\sigma_{ij} = \acute{\sigma}_{ij} - \alpha\delta_{ij}p \tag{2.11}$$

This definition of effective stress signifies a modification and generalization of Terzaghi's effective stress law. The Biot coefficient, α , is related to the bulk moduli of the saturated rock, K, and the grains in the rock, K_s, with the following equation (Biot and Willis, 1957; Nur and Byerlee, 1971)

$$\alpha = 1 - \frac{K}{K_s} \tag{2.12}$$

2.3 Strain-displacement relationship

Under assumptions of infinitesimal displacements, strain-displacement relations are given by:

$$\varepsilon_{zz} = \frac{\partial w}{\partial z} \tag{2.13}$$

$$\varepsilon_{rr} = \frac{\partial u}{\partial r} \tag{2.14}$$

$$\varepsilon_{\theta\theta} = \frac{u}{r} \tag{2.15}$$

$$\varepsilon_{rz} = \frac{1}{2}\left(\frac{\partial w}{\partial r} + \frac{\partial u}{\partial z}\right) \tag{2.16}$$

where *u* and *w* are displacements in radial and vertical directions (Figure 2-1).

2.4 Transport equations

Flow in porous media is governed by Darcy's law which states that the fluid volume flux, $\mathbf{J^f}$, is related to the pressure difference between two points in the rock:

$$\mathbf{J^f} = -\frac{\mathbf{k}}{\mu}(\nabla p - \rho_f \mathbf{g}) \tag{2.17}$$

where ρ_f is fluid density, $\boldsymbol{k}$ is the intrinsic permeability tensor of the rock, μ is the viscosity of the pore fluid and $\boldsymbol{g}$ is the vector of gravity acceleration.

In porous media, heat transport can be incorporated as a combination of conduction and convection processes. In heat transport calculation, for nearly impermeable rocks like shales, the velocity of pore fluid is expected to be small and consequently it will be permissible to ignore the convective component of heat transfer (Delany, 19..;Ghassemi and Diek, 2003) as coefficient of thermal diffusivity is several orders of magnitude greater than hydraulic diffusivity. So, the conductive transport will be dominant.

Fourier's law states that the heat flux, J^q, is directly proportional to temperature gradient in the medium:

$$\boldsymbol{J^q = -k^T \nabla T} \tag{2.17}$$

where k^T is the thermal conductivity of the porous media.

2.5 Balance of momentum

Balance of momentum for axisymmetric conditions can be written in terms of total stress as:

$$\frac{\partial \sigma_{rr}}{\partial r} + \frac{\partial \sigma_{rz}}{\partial z} + \frac{1}{r}(\sigma_{rr} - \sigma_{\theta\theta}) = 0 \tag{2.18}$$

$$\frac{\partial \sigma_{rz}}{\partial r} + \frac{\partial \sigma_{zz}}{\partial z} + \frac{1}{r}\sigma_{rz} + \rho g = 0 \tag{2.19}$$

where ρ is the rock density. Inertia terms have been neglected.

2.6 Continuity equations

In many applications, mechanical contributions to energy balance may be neglected when compared to thermal contributions. In such cases, the net rate of inflow of energy into an element of the material will be just balanced by increase in the internal energy of the pore water and the soil skeleton. So, the energy balance equation can be written as:

$$\rho c \frac{\partial T}{\partial t} + \nabla . J^q = q^{th} \tag{2.20}$$

where ρ and c are the total mass density and specific heat for the bulk porous material respectively and q^{th} is the volumetric rate of heat generation. The product ρc can be expressed as:

$$\rho c = (1 - \varphi)\rho_s c_s + \varphi \rho_f c_f \tag{2.21}$$

ρ_s is the grain density while c_f and c_s are the specific heat of pore fluid and solid grains respectively. It should be noted that mechanical contributions to energy balance equation are ignored in this work.

The fluid mass balance relation (continuity equation) is expressed in the form:

$$\dot{\zeta} + \nabla . \boldsymbol{J^f} = q^f \tag{2.22}$$

where q^f is the rate of injected fluid volume per unit volume of the porous solid (represents sources/sinks).

2.7 Field equations

Using equations of fluid transport Eq. (2.17), fluid mass balance Eq. (2.22) and constitutive Eq. (2.6) we get:

$$\alpha\dot{\varepsilon}_{ii} + \frac{1}{M}\dot{p} - \gamma_2\dot{T} - \frac{\kappa}{r}\frac{\partial}{\partial r}\left(r\frac{\partial p}{\partial r}\right) - \kappa\frac{\partial}{\partial z}\left(\frac{\partial p}{\partial z} - \rho g\right) = q^f \tag{2.23}$$

In the above equation $\kappa = \frac{k}{\mu}$. The energy balance Eq. (2.20) and heat flow Eq. (2.17) can be combined into a single heat diffusivity equation as below:

$$\frac{\partial T}{\partial t} - \frac{c^T}{r}\frac{\partial}{\partial r}\left(r\frac{\partial T}{\partial r}\right) - c^T\frac{\partial}{\partial z}\left(\frac{\partial T}{\partial z}\right) = q^{th} \tag{2.24}$$

c^T denotes the thermal diffusivity of the rock and is given by:

$$c^T = \left(\frac{k^T}{\rho c}\right) \tag{2.25}$$

ρc can be evaluated from Eq. (2.21). It is observed that by neglecting the convective heat transport, the heat diffusion equation is uncoupled from pore pressure. Eqs. (2.18), (2.19), (2.23) and (2.24) constitute the set of governing equations for axisymmetric poro-thermo-elasticity.

2.8 Initial and boundary conditions

It is further necessary to define the initial and boundary conditions. The initial conditions specify the full fields of displacement, pore pressure and temperature at $t = t_0$:

$$u = u_0\,; w = w_0\,; p = p_0\,; T = T_0 \quad at \;\; t = t_0 \tag{2.26}$$

The boundary conditions can be of the first kind or Dirichlet boundary condition, Γ_i^1 or of the second type or Neumann boundary condition, Γ_i^2.

Boundary condition of the first kind, where displacement, pore water pressure and temperature are prescribed on the boundary are as follows:

$$u = \hat{u} \quad on \quad \Gamma_u^1 \tag{2.27}$$

$$w = \hat{w} \quad on \quad \Gamma_w^1 \tag{2.28}$$

$$p = \hat{p} \quad on \quad \Gamma_p^1 \tag{2.29}$$

$$T = \hat{T} \quad on \quad \Gamma_T^1 \tag{2.30}$$

Boundary condition of the second kind, where tractions or fluxes on the boundary are prescribed can be written in the form:

$$\sigma_{rr} n_r + \sigma_{rz} n_z = t_r \quad on \quad \Gamma_u^2 \tag{2.31}$$

$$\sigma_{rz} n_r + \sigma_{zz} n_z = t_z \quad on \quad \Gamma_u^2 \tag{2.32}$$

$$\left(-\kappa(\nabla p - \rho_w g)\right).n = q^w \quad on \quad \Gamma_p^2 \tag{2.33}$$

$$(-k^T \nabla T).n = q^T \quad on \quad \Gamma_T^2 \tag{2.34}$$

where n is the unit normal vector, t_r and t_z are the components of applied traction in *r* and *z* directions respectively, and $q^w$and $q^T$are the prescribed fluid and heat flux normal to the boundary. The solution of the above equations is given in the following chapter.

3. Finite element analysis

3.1 Introduction

Normally the problems arising from mathematical physics are described by partial differential equations defined in the domain of interest. These boundary value problems are usually approximately solved by numerical discretization techniques. The early work on numerical solution of boundary value problems can be traced to the use of finite difference schemes. Finite element method was introduced in late 1950s. The emergence of the finite element method stems from these early numerical methods and the challenges associated with trying to use finite difference methods on complex geometries or problems with non-homogeneous boundary conditions.

The derivation of finite element equations is mainly done in two ways: (1) variational method, (2) weighted residual method. In the variational method, a functional (or variational principle) is required such that by minimizing it, the stiffness matrix and related element equations are obtained. However, functionals are not always available in exact form. The weighted residual method is directly applied to any system of differential equations and is a good procedure when we cannot write a variational formulation. Depending on the choice of weighting function, there are different types of weighted residual methods. Some of the most common methods are Galerkin or Bubnov-Galerkin (standard finite element method), least square Galerkin, point collocation (finite difference method), subdomain collocation (finite volume method) and Petrov-Galerkin method (Diersch 2013).

In this work, the finite element equations are developed from Galerkin method of weighted residuals. An axisymmetric finite element formulation for thermo-poro-elastic analysis has been developed. Detailed derivations of finite element equations are given in Appendix A.

8-node hexahedral elements are adopted for space discretization. Although the proposed model is derived for the axisymmetric case, it is very easy to derive a similar set of coupled equations for the full 3D case. For the sake of brevity, the corresponding equations are not repeated here. The proposed solution is verified against known analytical solutions. The verified cases include injection into a well in poroelastic medium with a constant rate, Mandel's problem, poroelastic cylinder subject to vertical loading, drilling a vertical well in poroelastic rock and thermally induced consolidation of a medium with an embedded cylindrical heat source.

3.2 Model Verification

To demonstrate and verify the performance of proposed thermo-poroelastic formulation, a series of axisymmetric benchmark analysis have been performed and the results are shown in the next session.

3.2.1 Constant rate injection into a wellbore in a poroelastic medium

In petroleum engineering, fluid is sometimes injected into a reservoir from a well to displace the oil and increase its production. Here, we consider the problem of water injection into a cylindrical borehole in an infinite poroelastic medium. This problem was analytically solved by Rajapakse (1993). Based on Biot's consolidation theory, a circular borehole embedded in an infinite poroelastic medium and subject to an axisymmetric load is considered. The analytical solution was derived using Laplace and Fourier transform technique for different borehole boundary conditions including constant borehole pressure and constant injection rate over a segment of the borehole. In this section, numerical results for the constant injection rate are compared with the analytical results obtained by the finite element method. The poroelastic medium is assumed to be isotropic and homogenous. The layout of the wellbore is shown in Figure 3-1. The boundary conditions set for this problem pertain to a wellbore

with impermeable casing which is perforated only along a segment of length 2b. Dimensionless time is defined as $\tau = \frac{2Gk(1-\nu)t}{a^2\mu(1-2\nu)}$ and dimensionless perforated length is defined as $\bar{b} = \frac{b}{a}$, where a is the wellbore radius, G and ν are the shear modulus and Poisson's ratio, k is the permeability, t is the time and μ is the dynamic viscosity of the fluid. Fluid is injected at the rate of q_0 along the length 2b. The resulting pore pressure at midplane of the wellbore (Z=0) is normalized by $\frac{\kappa p}{a q_0}$ ($\kappa = \frac{k}{\mu}$) and plotted against the normalized radial distance. Figure 3-2 shows the induced pore pressure along the radial direction for $z = 0.0$, $\tau = 10$ and**Error! Bookmark not defined.** $\bar{b}$ =1.0. A good match is observed between the numerical and analytical solutions. Different cases with different wellbore radii were modeled and it was observed that they yielded the same results if z, τ and $\bar{b}$ were kept constant

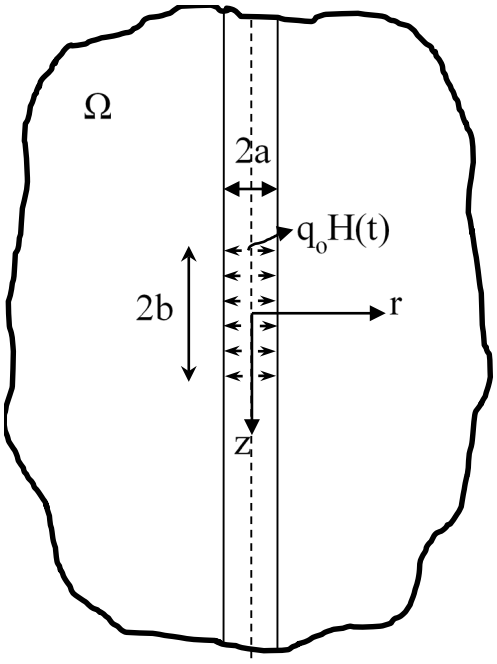

Figure 3-1. Wellbore layout for analytical solution of constant rate injection into the wellbore.

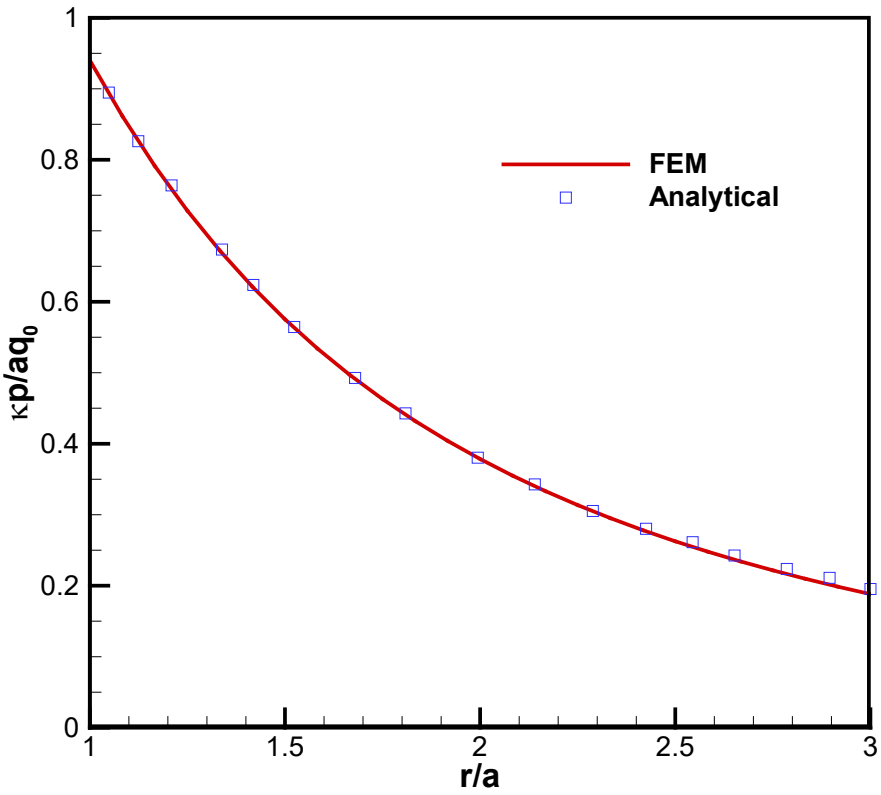

Figure 3-2. Pore pressure induced by injection at different radial distances ($z = 0.0, \tau = 10.0, \bar{b} = 1.0$)

3.2.2 Mandel's Problem

Classical Mandel's problem (Mandel 1953, Cheng and Detournay 1988) serves as a good benchmark to examine the validity of numerical solutions for poroelasticity. It also demonstrates the non-monotonic pore pressure response arising from coupled effect of pore pressure diffusion and solid deformation. The poroelastic response of an infinitely long sample ~~specimen~~ loaded under plane strain conditions is examined. The poroelastic sample ~~specimen~~ is sandwiched between two rigid impermeable frictionless plates and is in equilibrium with zero pore pressure. Compressive forces of magnitude 2F per unit length in y direction are applied at $t=0^+$ on the rigid plates (Figure 3-3). The sample dimensions are 2a × 2b in XZ-plane. Drainage is permitted on the lateral boundaries and they are traction free.

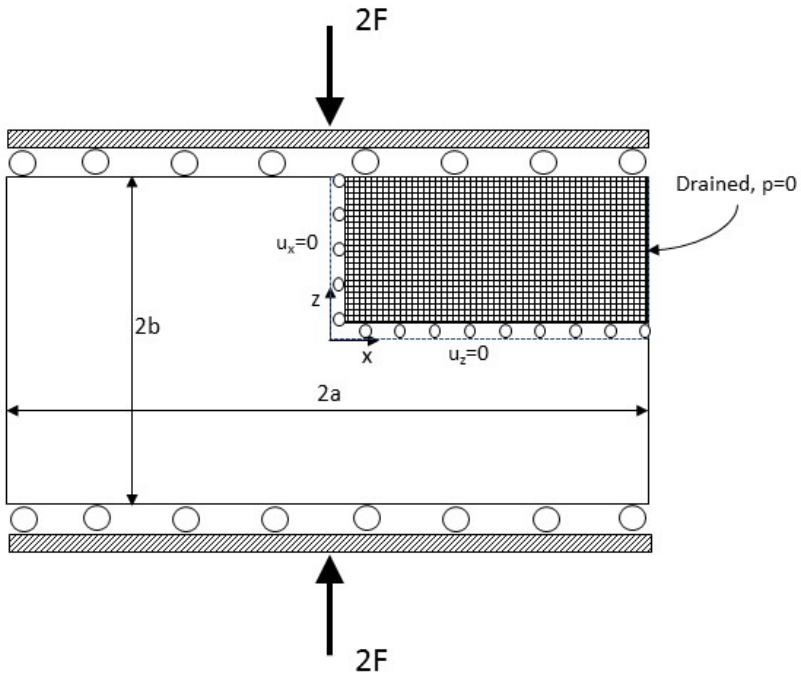

Figure 3-3. Mandel's problem, boundary conditions and simulation domain discretization.

When the load is applied instantaneously at t=0, an initial uniform pore pressure rise is observed since the instantaneous response to the loading is undrained. This uniform pressure drops quickly in the proximity of lateral boundaries as drainage evolves. A load transfer happens from outer weaker zones to the stiffer inner zones of the sample due to compatibility requirement causing the pore pressure to rise in the middle of the sample for some time before dissipating. The pore pressure rise above its initial undrained value is referred to as Mandel-Cryer effect (Cryer 1963, Mandel 1953). This non-monotonic behavior cannot be predicted by uncoupled theory of Terzaghi-Rendulic 3D consolidation. Finally, the pore pressure returns to zero as the fluid flows

out through the outer surface. The original problem was solved analytically by Mandel (1953) for the limiting case of incompressible fluid and solid particles and it was later generalized to compressible constituents by Cheng and Detournay (1988). The analytical solution for pore pressure and displacements is given below (Cheng and Detournay, 1988):

$$p = \frac{2FB(1+\nu_u)}{3a}\sum_{i=1}^{\infty}\frac{sin\alpha_i}{\alpha_i - sin\alpha_i cos\alpha_i}\left(cos\frac{\alpha_i x}{a} - cos\alpha_i\right)\exp(\frac{-{\alpha_i}^2 ct}{a^2}) \quad (3.88)$$

$$\begin{aligned} u_x = &\left[\frac{F\nu}{2Ga} - \frac{F\nu_u}{Ga}\sum_{i=1}^{\infty}\frac{sin\alpha_i}{\alpha_i - sin\alpha_i cos\alpha_i}\exp(\frac{-{\alpha_i}^2 ct}{a^2})\right]x \\ &+ \frac{F}{G}\sum_{i=1}^{\infty}\frac{cos\alpha_i}{\alpha_i - sin\alpha_i cos\alpha_i}sin\frac{\alpha_i x}{a}\exp(\frac{-{\alpha_i}^2 ct}{a^2}) \end{aligned} \quad (3.89)$$

$$u_y = \left[-\frac{F(1-\nu)}{2Ga} + \frac{F(1-\nu_u)}{Ga}\sum_{i=1}^{\infty}\frac{sin\alpha_i cos\alpha_i}{\alpha_i - sin\alpha_i cos\alpha_i}\exp(\frac{-{\alpha_i}^2 ct}{a^2})\right]y \quad (3.90)$$

where c is hydraulic diffusivity and B is Skempton coefficient. α_i should satisfy:

$$tan\alpha_i = \frac{1-\nu}{\nu_u - \nu}\alpha_i \quad (3.91)$$

A homogenous and isotropic 3D finite element model with dimensions a×b×L and properties given in Table 3-1 is built. The constituents are assumed incompressible. The model only considers one quarter of the domain due to problem symmetry. Proper boundary conditions are set in place to ensure the plane strain condition in y direction. The rigid plate is modeled by assuming that all the nodes on top of the model have equal unknown constant value. The simulation domain is discretized using 8-node isoparametric brick elements. The pore pressure distribution, horizontal and vertical displacements at five different times (Table 3-2) are shown in Figures 3-4 to 3-6 and compared with the analytical solution given above. In these figures, horizontal distance is normalized by a, u_x is normalized by a, u_y is normalized by b and normalized pore pressure is $\frac{ap}{F}$. In Figure 3-4, it can be observed that the pressure rises

above the initial uniform pressure (the Mandel-Cryer effect). Also, a good agreement between analytical and FEM results can be observed for the horizontal and vertical displacements.

Table 3-1. Poroelastic rock properties and parameters used in Mandel's problem.

Parameters	Values
Young's modulus, E	1×10^{2} MPa
Poisson's ratio, ν	0.2
Undrained Poisson's ratio, ν_u	0.5
Permeability, *k*	100 md
Fluid Viscosity, μ	1×10^{-3} Pa.s
Biot's coefficient, α	1.0
Applied force, F	1×10^{8} N/m
Sample width, 2a	200.0 m
Sample thickness, 2b	20.0 m
Sample length, L	1000.0 m

Table 3-2. Output time steps

t_i	t_1	t_2	t_3	t_4	t_5
Time (s)	1×10^{3}	1×10^{4}	1×10^{5}	1×10^{6}	2×10^{6}

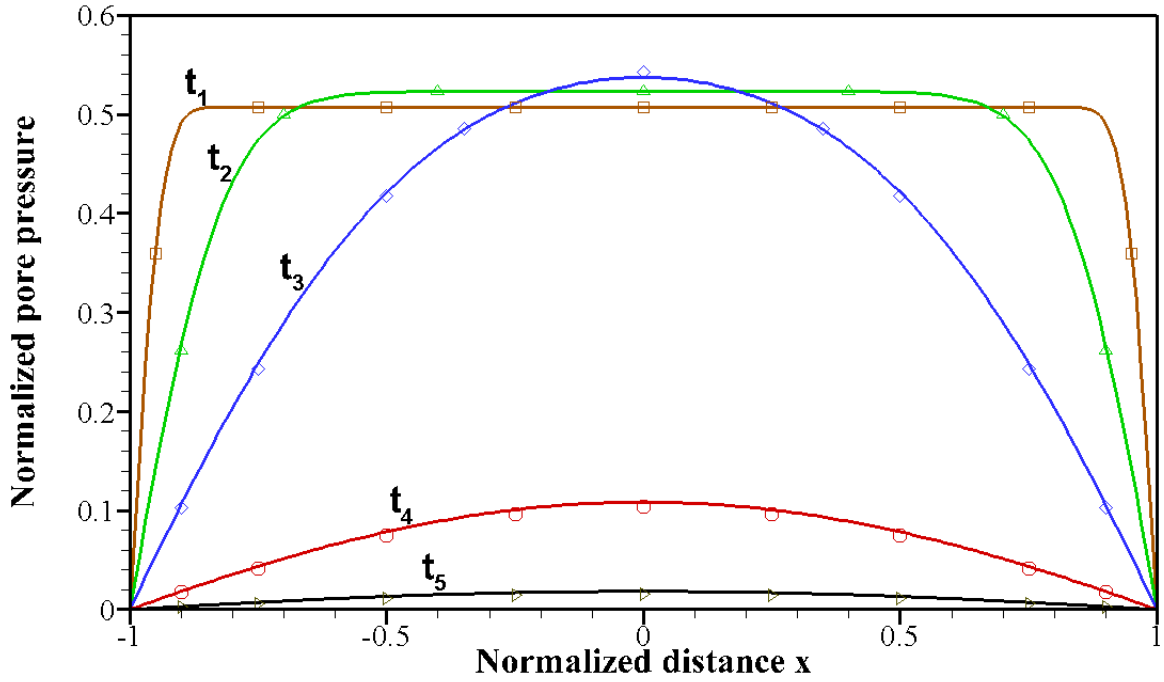

Figure 3-4. Pore pressure profile along horizontal direction at various times (symbols: analytical, lines: FEM)

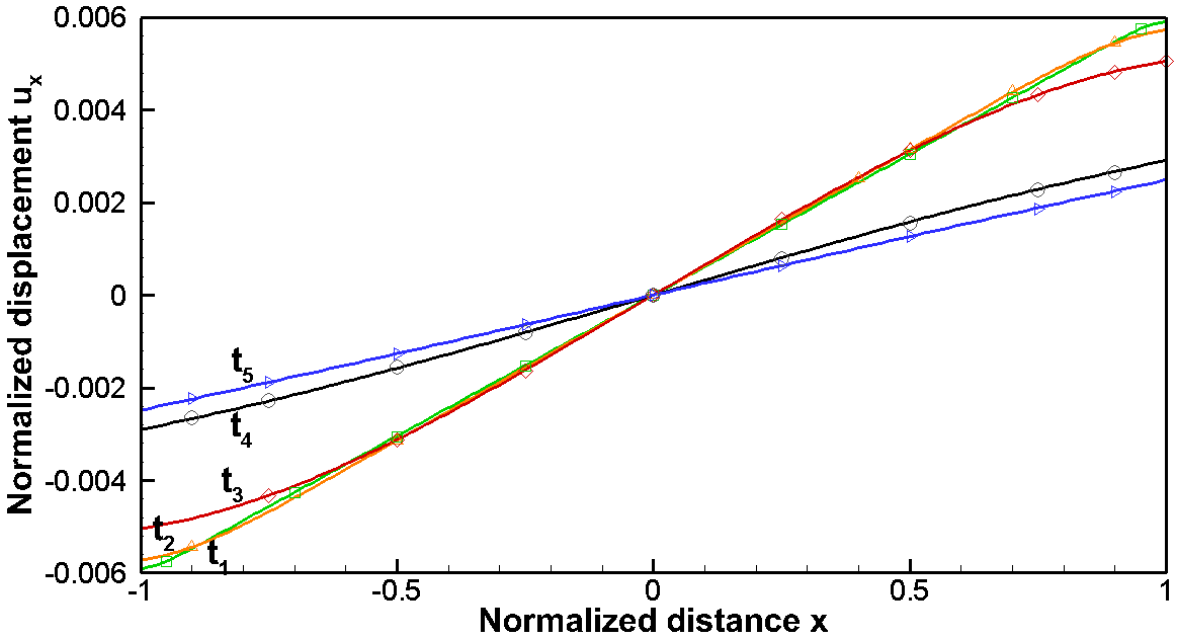

Figure 3-5. Horizontal displacement profile at different times (symbols: analytical, lines: FEM).

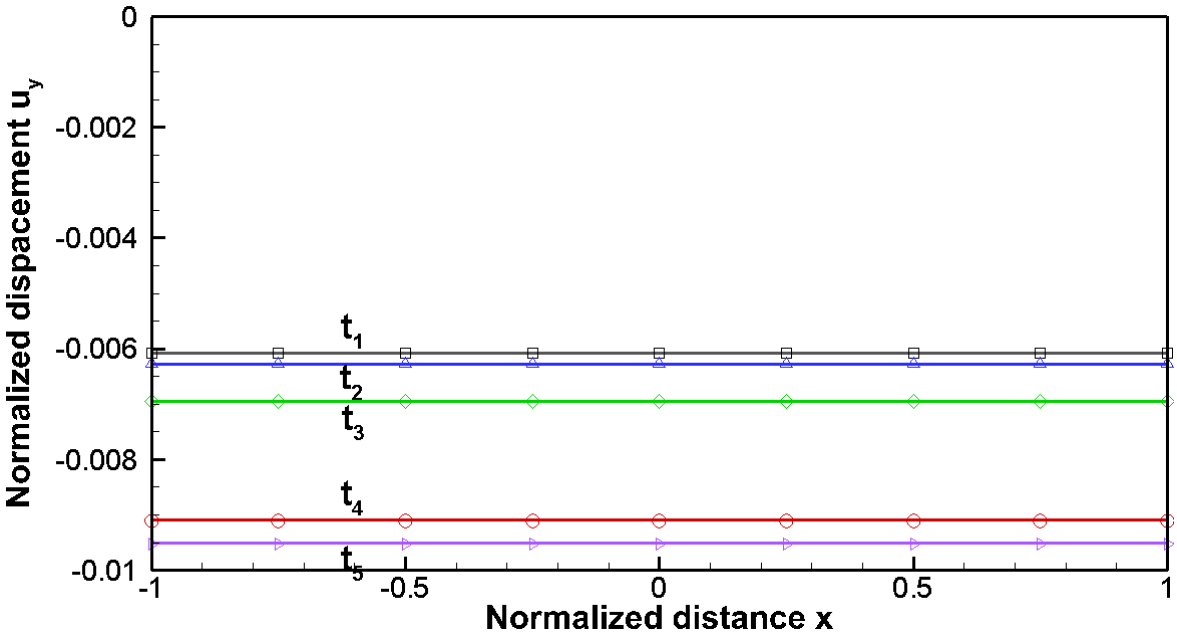

Figure 3-6. Vertical displacement profile of sample top at different times (symbols: analytical, lines: FEM).

3.2.3 A poroelastic cylinder subject to vertical loading

The problem of a poroelastic cylinder under vertical loading is studied in this example. Figure 3-7 shows a cylindrical sample with radius a and height $2h$. The sample undergoes constant displacement rate, u_0, on its upper and lower ends. So, at time t, the vertical displacement is $u(r, \pm h, t) = u_0 t$. Two rigid, permeable and frictionless plates on top and bottom of the sample are used to apply the displacement, so that the displacement will be uniform on upper and lower ends of the sample. The sample can only drain through the top and bottom plates and a membrane around the curved boundary prevents any flow to occur from side surface. Initial pore pressure is zero since the sample has been consolidated under confining pressure before applying the displacement. No confining pressure is applied to the sample. The sample properties are shown in Table 3-3.

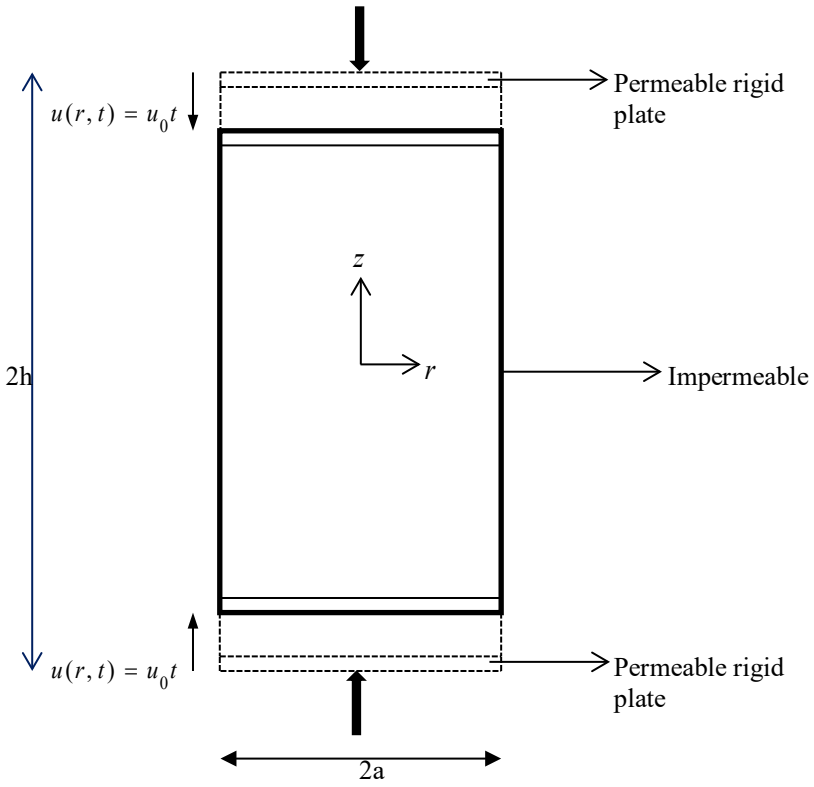

Figure 3-7. Cylinder under loading, a constant displacement rate applied to the two ends of cylinder.

Table 3-3. Physical properties of the rock sample

Parameter	**Value**
Fluid viscosity, μ_f (Pa.s)	1.0×10^{-3}
Shear modulus, G (GPa)	7.6
Intrinsic permeability, k (md)	0.1
Poisson's ratio, ν	0.2
Undrained Poisson's ratio, ν_u	0.4
Skempton coefficient, B	0.9

The radial displacement of the outer surface of the cylinder at its mid-plane ($z=0,\ r=a$) is normalized by $\frac{a^2 u_0}{c}$ where c is diffusion coefficient given by:

$$c = \frac{2kGB^2(1+\nu_u)^2(1-\nu)}{9\mu(\nu_u-\nu)(1-\nu_u)} \tag{3.92}$$

The dimensionless plot of radial displacement vs. time is shown in Figure 3-9. The results are depicted for cylinders with different height to radius ratios. The comparison with the analytical results presented by Kaewjuea et al. (2011) shows a good match. As we can see from this figure, the sample extends in radial direction over time. It is observed that for a constant sample radius, radial displacements increase as sample height decreases. The tangential stress at the surface of the cylinder mid-plane is normalized by $\frac{Gau_0}{c}$ and its time evolution is shown in Figure 3-10. Tangential stress magnitude increases over time until they reach a point when they maintain a nearly constant value afterwards. Except for the short cylinder with $\frac{h}{a} = 0.5$, the induced tangential stress is tensile. The tangential stress is very small compared to the axial stress and pore pressure. If the rate of displacement is small, the tensile tangential stress will not cause fractures in the rock. Figure 3-11 shows the time history of dimensionless axial stress at the curved surface of the sample at mid-plane. The axial stress increases with time following vertical displacements. For a fixed sample diameter, longer samples have smaller vertical strain compared to shorter ones since they all undergo identical vertical displacement rates. Pore pressure evolution over time is depicted in Figure 3-8. By applying displacement, pore pressure is increased and then stays constant as the steady state condition is reached. It takes less time for the shorter cylinder to reach the steady state since the flow has a shorter path to free draining boundary.

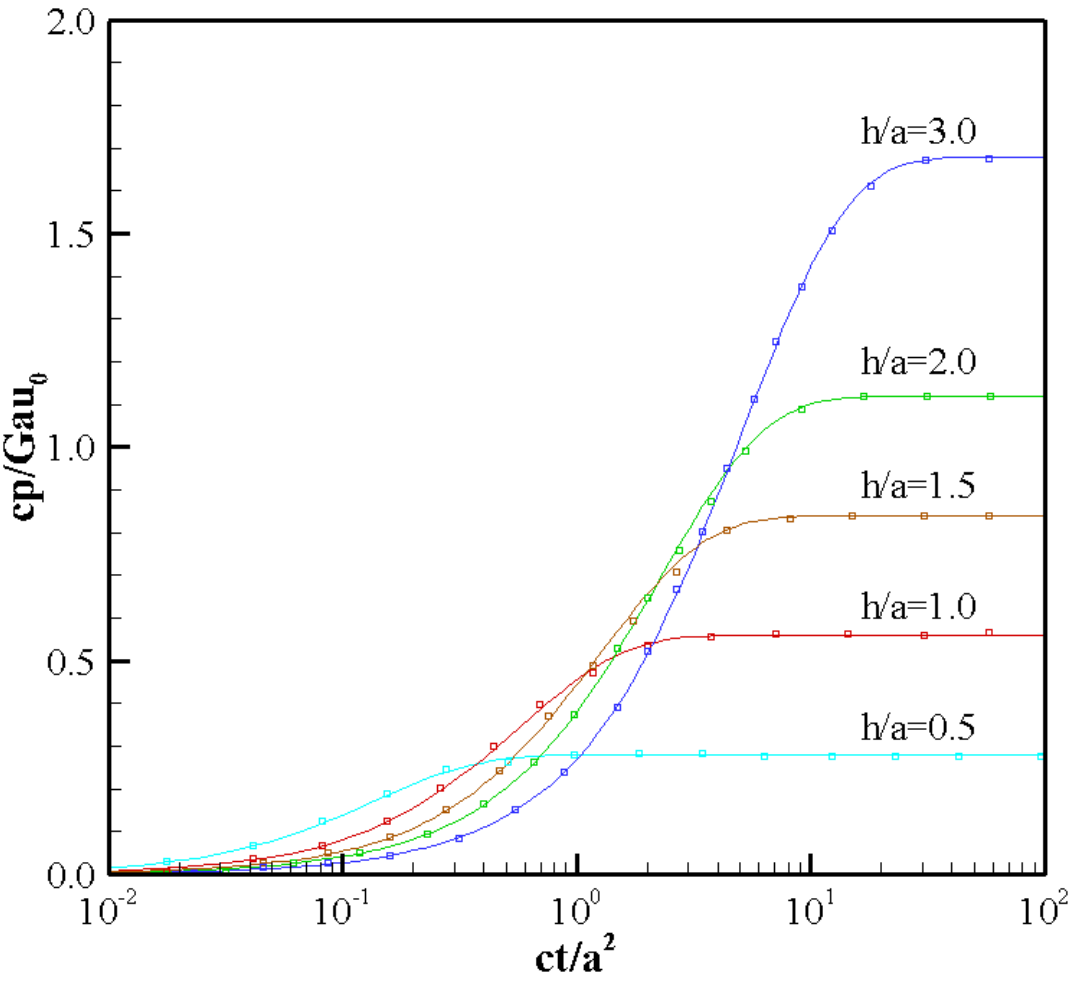

Figure 3-8. Evolution of pore pressure over time at the cylinder mid-plane curved boundary (symbols: Kaewjuea et al. (2011), lines: FEM). Results are shown for different height to radius ratio cases.

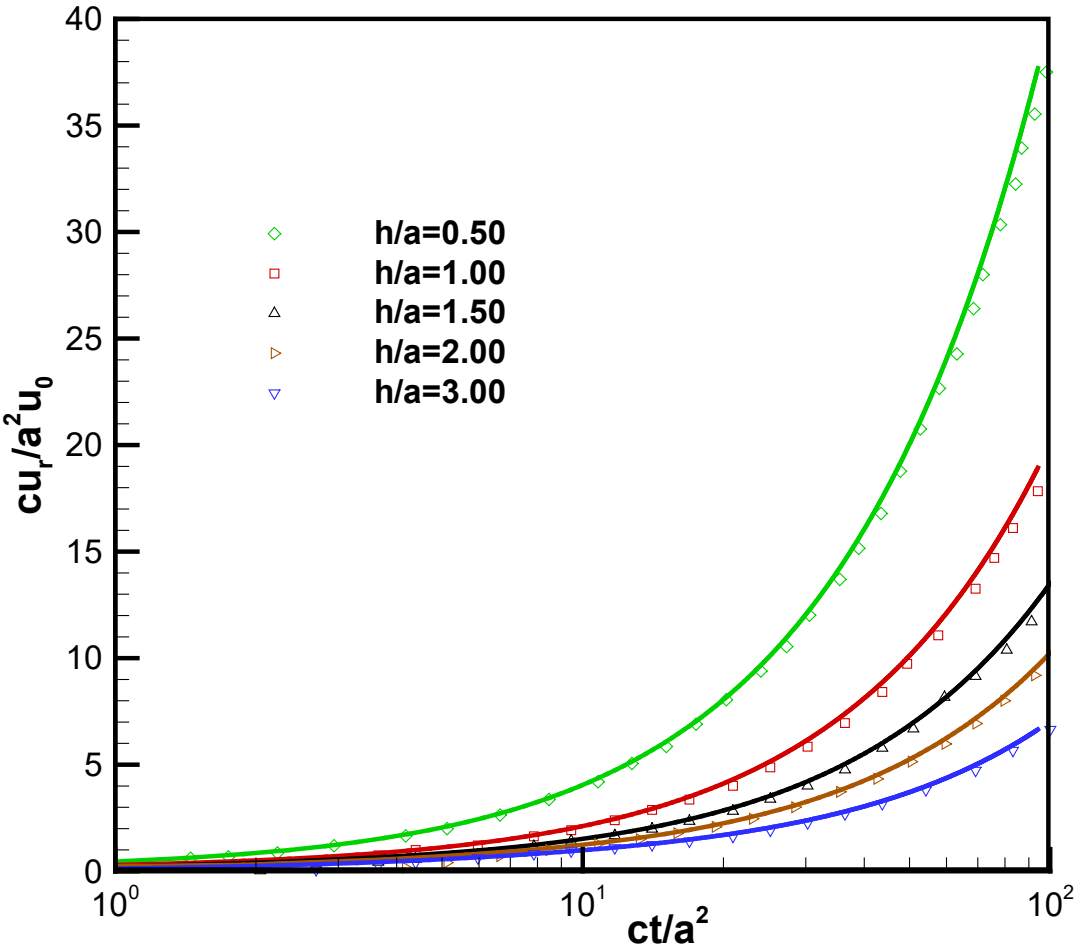

Figure 3-9. Change of radial displacement with time at the boundary of cylinder mid-plane (symbols: Kaewjuea et al. (2011), lines: FEM). Results are shown for different height to radius ratio cases.

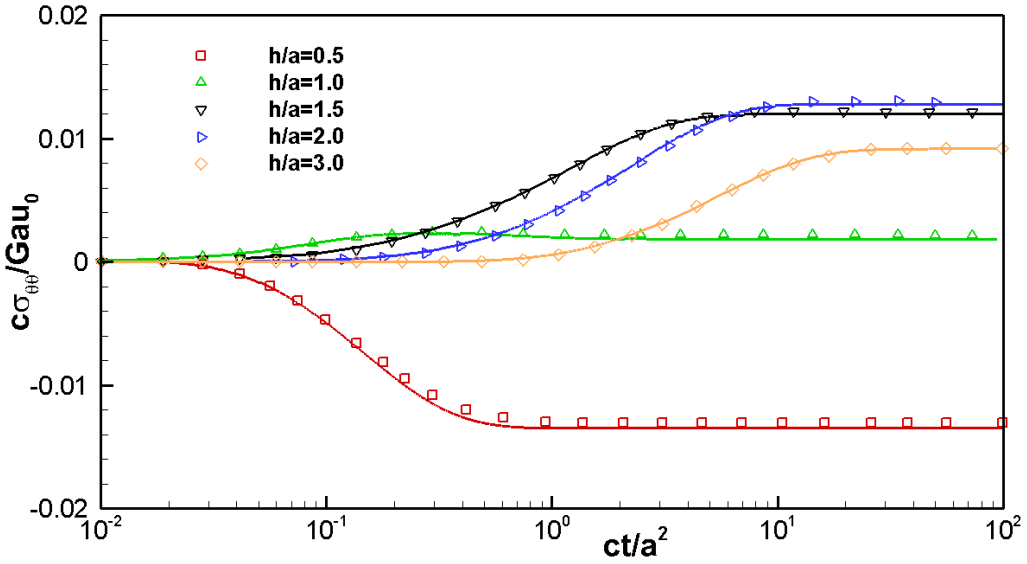

Figure 3-10. Change of tangential stress with time at the cylinder mid-plane curved boundary (symbols: Kaewjuea et al. (2011), lines: FEM). Results are shown for different height to radius ratio cases.

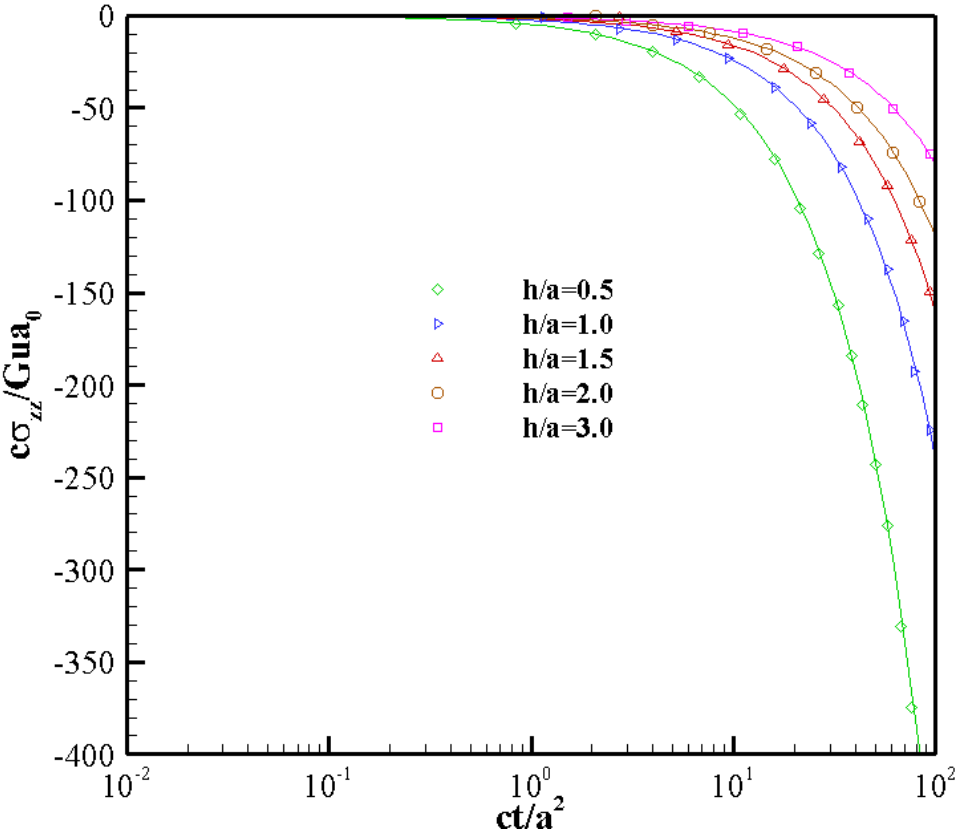

Figure 3-11. Change of axial stress with time at cylinder mid-plane curved boundary (symbols: Kaewjuea et al. (2011), lines: FEM). Results are shown for different height to radius ratio cases.

3.2.4 Drilling a vertical wellbore in a poroelastic formation with given far field stresses

Creating a circular hole and applying drilling fluid could result in wellbore instability or casing collapse. Therefore, it is very important to develop mathematical models to simulate drilling and production processes and predict rock deformation. When oil and gas are produced in harsher environments such as deepwater or high-pressure high-temperature reservoirs, the knowledge of wellbore stability becomes even more important.

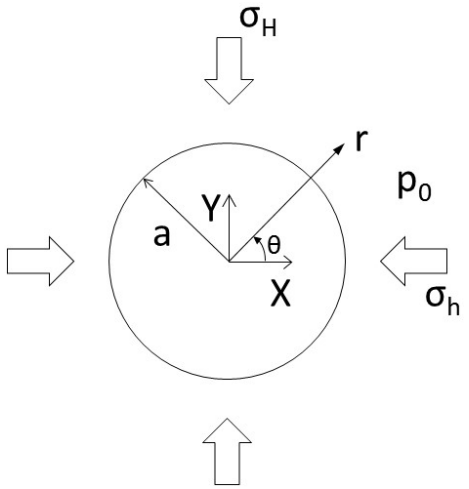

Figure 3-12. Schematic of wellbore drilling problem with in-situ stresses, σ_H and σ_h.

The concentration of stress around the wellbore can lead to compressive failure also known as breakouts. Excessive breakouts will result in collapse failure of the well. Fracturing of wellbore occurs when rock stress changes to tension leading to tensile fractures. The stress distribution around a circular hole in a homogenous isotropic elastic medium subjected to far field stresses in an infinite medium was first solved analytically by Kirsch (1898). The elastic solution fails to address the time dependent fluid flow effect resulting from drilling, which might significantly change the near wellbore pore pressure and stress concentration, making it only applicable to steady state cases. By incorporating the transient fluid diffusion

process, Carter and Booker (1984), presented an analytical solution for the displacements and stress changes around a deep and long circular tunnel, cut in a saturated rock material based on Biot's poroelasticity theory. However, the pore fluid and rock particles were assumed to be incompressible. Later, the solution for a vertical wellbore in a linear poroelastic medium in a non-hydrostatic stress field was obtained by Detournay and Cheng (1988) which accounted for the compressibility of the grains and fluid. Wellbore was considered permeable and mud pressure could penetrate the formation. In order to explain this problem, let's suppose a well drilled in an isotropic poroelastic saturated porous medium with far field stresses σ_H and σ_h and in-situ pore pressure p_0 as shown in Figure 3-12. The well length is assumed to be infinite, therefore a plane strain condition is assumed in the cross section of the well (zero strain along Z axis). It is also assumed that the well is drilled instantaneously, and it is aligned with vertical principal stress. Zero normal displacements and impermeable boundary condition are imposed at far field boundary. Drilling can be modelled as removing the stresses at the periphery of the wellbore at $t = 0^+$ and reducing the pore pressure from p_0 to zero or mud pressure. The induced stresses resulting from removing these stresses was analytically obtained (Detournay and Cheng 1988, Carter and Brooker 1984). In order to simplify the problem, the loading was decomposed into three different modes. Each of these were solved separately and then the principle of superposition was employed to obtain the full solution of pore pressure and stresses. The loading condition at wellbore wall for each of the loading modes can be identified as (zero mud pressure is assumed):

Mode 1 (isotropic stress loading):

$$\Delta\sigma_{rr} = P_0$$

$$\Delta\sigma_{r\theta} = 0$$

$$\Delta p = 0$$

Mode 2 (pore pressure loading):

$$\Delta\sigma_{rr} = 0$$

$$\Delta\sigma_{r\theta} = 0$$

$$\Delta p = -p_0$$

Mode 3 (deviatoric stress loading):

$$\Delta\sigma_{rr} = -S_0 cos\ 2\theta$$

$$\Delta\sigma_{r\theta} = S_0 sin\ 2\theta$$

$$\Delta p = 0$$

where:

$$P_0 = -\frac{1}{2}(\sigma_H + \sigma_h)$$

$$S_0 = -\frac{1}{2}(\sigma_H - \sigma_h)$$

Stress and pore pressure distribution from mode 1 and 2 are axisymmetric since the loading is independent of θ. No rotation is generated in these modes. Analytical solution to each of the subproblems mentioned above were given in the Laplace transform domain and then transformed to time domain. We will check the validity of the FEM code by comparing the analytical solution of each mode to the numerical results. The input data used for the simulations are given in Table 3-4. Isoparametric quadrilateral elements with 8 displacement nodes and 4 pressure nodes were used in the analysis. Only the results in the vicinity of the well are presented. Figure 3-13 shows the variation of radial displacement with radial distance for isotropic stress loading, mode 1. The solution is independent of time since there is

no volumetric strain in this mode. Pore pressure is not generated in this mode so the poroelastic solution is equivalent to elastic solution and can be found using Kirsch equations. The symmetrical loading in mode 1 causes the rock to move inward and reduce the size of the well. There is a good agreement between numerical and analytical results.

Table 3-4. Poroelastic properties used in modelling the response of wellbore

Parameter	**Value**
Fluid viscosity, μ_f (Pa.s)	1.0×10^{-3}
Shear modulus, G (MPa)	833
Intrinsic permeability, k (md)	500
Poisson's ratio, ν	0.2
Undrained Poisson's ratio, ν_u	0.4
Skempton coefficient, B	0.8

Figure 3-14 shows the variation of tangential stress with radius for mode 1. A good match between the results is observed. It can be observed from this figure that loading by mode 1 induces a time independent compressive tangential stress and the maximum stress is on wellbore wall.

Figure 3-15 shows pore pressure history for mode 2 at different locations. Dimensionless time is defined as $t_d = \frac{ct}{a^2}$. Initially formation pore pressure is p_0 and over time the pore pressure perturbation applied at the wellbore wall propagates into the formation and at very large time the pore pressure of the formation will approach zero. The results are in good agreement with analytical solution reported by Detournay and Cheng (1988).

Figure 3-16 shows the tangential stress profile for mode 2 for a range of dimensionless radial distances at a given dimensionless time. η is a poroelastic coefficient defined as $\eta =$

$\frac{3(v_u - v)}{2B(1-v)(1+v_u)}$. At every point in the reservoir except at the wellbore wall, the tangential stress is first compressive and over time it changes to tensile.

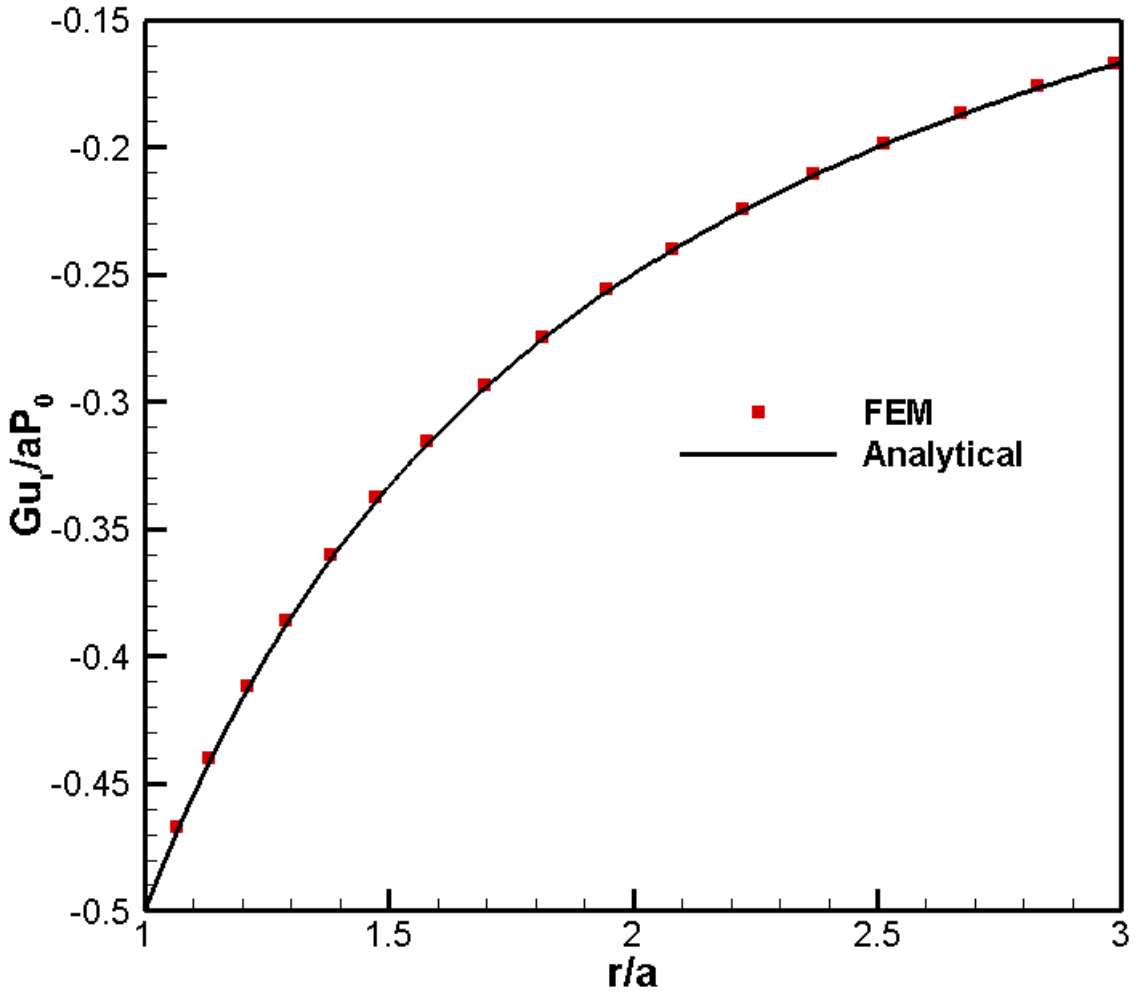

Figure 3-13. Analytical and numerical results comparison for radial deformation along the radial distance due to mode 1 loading

For mode 3 (deviatoric loading), the induced stress and pore pressure vary not only in radial direction but also in tangential direction. The maximum induced pore pressure is initially in the close vicinity of wellbore and over time it travels further away from the well and dissipates (Figure 3-17). The induced pore pressure is positive in the direction of maximum principal stress (as shown) and negative in the minimum principal stress direction. At the instant

of loading ($t \rightarrow 0^+$), total tangential stress from mode 3 at the wellbore wall is $\sigma_{\theta\theta} = 4S\frac{(1-\nu_u)}{(1-\nu)}cos\ 2\theta$. Shortly after, ($0^+ < t_d \leq 10^{-3}$), fluid drains out from the wellbore wall while the inner region stays undrained, which makes it a stiffer zone compared to the immediate vicinity of the wellbore, giving rise to stress concentration in the inner region. This is depicted in Figure 3-19 where the peak of tangential stress is inside the formation for $t_d \leq 10^{-3}$. Over time, the pore pressure in the formation dissipates and stiffness contrast will be decreased. After certain time, the peak will be at wellbore wall and it will increase until it reaches the drained solution, $\sigma_{\theta\theta} = 4S\ cos2\theta$ (Figure 3-19). Since the tangential stress in undrained case is smaller than the drained case at the wellbore wall ($\nu_u > \nu$), it can be concluded that considering the poroelastic effect results in a lower tangential stress value at wellbore wall (less compressive) compared to elastic analysis. Consequently, the breakdown pressure predicted by poroelastic analysis will be less than its elastic analysis prediction value (Jaeger *et al.*, 2009).

3.2.5 Thermally induced consolidation of a medium with an embedded cylindrical heat source

The classical theory of thermo-poroelasticity is an extension of Biot's theory which shows the effect of temperature changes on pore pressure and stresses. The main mechanisms can be summarized as below:

1) The effect of temperature change on pore fluid pressure

2) The effect of temperature change on volumetric rock deformation

3) The effect of pore pressure changes on deformations

The coupling between heat transfer, fluid flow and stress/deformation in fluid saturated porous medium has attracted considerable attention in many engineering fields. In petroleum

industry, enhanced oil recovery by steam or hot water injection, fluid injection/extraction for enhanced geothermal systems (Ghassemi et al. 2008), wellbore stability (Chen and Ewy, 2005) and coal beds exploitation for methane are examples of its application. Other engineering problems, in which heat and fluids play important roles, involve underground radioactive waste disposal (Fall et al. 2014) and containment transport analysis. Thermo-poroelastic effects can materialize in the host rock as heating/cooling is taking place. Thus, understanding and quantifying thermo-poro-elasticity is important for mathematical modeling and numerical simulation of engineering projects. Brownell et al. (1977) discussed rock-fluid interactions in geothermal systems, which involve momentum and energy transfer and the dependence of porosity and fluid flow and solid deformations. However, the effect of convection, pore fluid compressibility and its expansion due to temperature change was ignored. Thermoelastic consolidation was investigated by Aboustit et al. (1983) using a general variational formulation. However, the effect of matrix and fluid compressibility and coupling between pore pressure and temperature were disregarded. Numerical results were presented for a 1D thermoelastic consolidation.

The poroelastic solution for a cylindrical radiating heat source in an infinite porous and saturated medium was investigated analytically by Booker and Savvidou (1985). Their formulation neglected the effect of fluid and solid compressibility and convection. They used the Fourier and Laplace transform techniques to derive a solution for a point heat source neglecting the convective terms. Then they extended the point source solution to a cylindrical heat source introducing a heat density, q_v , which is the thermal energy release per unit time per unit volume. The cylindrical source is approximated by a series of heat point sources and

solution is derived using volume integration. Pore pressures, displacements, temperatures and stresses are calculated by this method. The details of analysis can be found in their paper. According to Booker and Savvidou (1985), if heat source energy release is q_v per unit time per unit volume and the source volume is V_s, the solutions for temperature and pore pressure at a point with coordinates (x_F, y_F, z_F) at time t are as follows:

$$T(x_F, y_F, z_F, t) = \iiint_{V_s} \frac{q_v}{4\pi k^T R} f\left(\frac{c^T t}{R^2}\right) dV \tag{3.93}$$

$$p(x_F, y_F, z_F, t) = \iiint_{V_s} \frac{X}{\left(1 - \frac{c}{c^T}\right)} \frac{q_v}{4\pi k^T R} \left[f\left(\frac{c^T t}{R^2}\right) - f\left(\frac{ct}{R^2}\right) \right] dV \tag{3.94}$$

where:

$$x = x_F - x_s \tag{3.95}$$

$$y = y_F - y_s \tag{3.96}$$

$$z = z_F - z_s \tag{3.97}$$

$$R^2 = (x_F - x_s)^2 + (y_F - y_s)^2 + (z_F - z_s)^2 \tag{3.98}$$

$$f\left(\frac{c^T t}{R^2}\right) = erfc\left(\frac{R}{2\sqrt{c^T t}}\right) \tag{3.99}$$

$$X = a_u(\lambda + 2G) - b' \tag{3.100}$$

In the above equations x_s, y_s and z_s denote the coordinates of a point within the heat source, k^T is thermal conductivity, λ and G are Lame constants, c^T is the thermal diffusivity as defined in Eq. (2.25) and c is hydraulic diffusivity. Fluid and solid grains are assumed to be incompressible ($\alpha = 1, B = 1\,; v_u = 0.5$); So, hydraulic diffusivity from Eq. (3.92) reduces to:

$$c = \frac{k(\lambda + 2G)}{\mu} \tag{3.101}$$

a_u and b' are defined as:

$$a_u = \alpha_m(1-\phi) + \alpha_f\phi \tag{3.202}$$

$$b' = (\lambda + \frac{2G}{3})a' \tag{3.303}$$

where α_m and α_f are the coefficients of volume thermal expansion of solid matrix and pore fluid respectively and ϕ is porosity. a' is the coefficient of volume thermal expansion of the solid matrix. Gravitational forces are neglected. Using Eqs. (3.93) and (3.94), analytical solutions for temperature and pore pressure were obtained for the case of a cylindrical heat source in a continuum and compared with the numerical results from finite element method. An axisymmetric finite element model was used for this purpose. The finite element mesh used for this problem is shown in Figure 3-20. The cylindrical heat source radius and height are 0.16 m and 0.32 m respectively. It is represented by four elements in the finite element mesh. Only a quarter of the cylinder and the surrounding rock is analyzed due to the symmetry. For boundaries r=0 and z=0, normal displacements are assumed to be zero and impermeable to fluid and heat flow due to symmetry. Far field boundaries have fixed pressure and temperature and zero displacements to simulate the infinity:

$$T(r_{max},t) = 0; p(r_{max},t) = 0; u_r(r_{max},t) = 0; u_z(r_{max},t) = 0$$
$$T(z_{max},t) = 0; p(z_{max},t) = 0; u_r(z_{max},t) = 0; u_z(z_{max},t) = 0$$

The initial conditions may be expressed in cylindrical coordinates as:

$$T(r,0) = 0; p(r,0) = 0; u_r(r,0) = 0$$

The heat output is q_v=1000 cal/(m^{3}day) and $\frac{\acute{a}}{a_u} = \frac{1}{4}$. The surrounding rock properties are shown in Table 3-5. To better compare numerical results with closed form results, the normalized system of plotting is adopted. The temperature is normalized against T_{max}:

$$T_{\max} = 1.45\frac{q_v r_0^{\,2}}{k^T} \tag{3.404}$$

where r_0 is the radius of heat source. The pore pressure is normalized against P_N given by:

$$P_N = T_{\max}\left\{\frac{E}{1-2\nu}\left[a_u\frac{1-\nu}{1+\nu}-\frac{a'}{3}\right]\right\} \tag{3.505}$$

Also normalized time is given by:

$$t_N = \frac{c^T t}{r_0^{\,2}} \tag{3.606}$$

Figure 3-21 shows the temperature variation with time at the mid-plane of the cylindrical heat source for three different distances from cylinder axis. It can be seen that the temperature of the medium around the cylinder increases with until it reaches a steady value. For the points closer to the heat source, the temperature rise begins earlier and over time reaches a higher value compared to the points farther from the heat source. This figure also indicates a good agreement between the numerical results and the analytical solution provided by Booker and Savvidou (1985). Figure 3-22 shows the pore pressure evolution with time at the mid-plane of the heat source (Z=0) for three different distances from cylinder axis. It is observed that initially at all three points the pore pressure increases owing to the pore fluid and solid grains expansion and reaches a peak value. Later, the pore pressure is decreased as pore pressure diffusion and consolidation takes place. Obviously, closer points to the source experience higher peak in pore pressure and the increase starts earlier. The agreement between the results is good, though not perfect. Lewis et al. (1986) observed the sensitivity of the results to the ratio between the heat source size and the length of the domain.

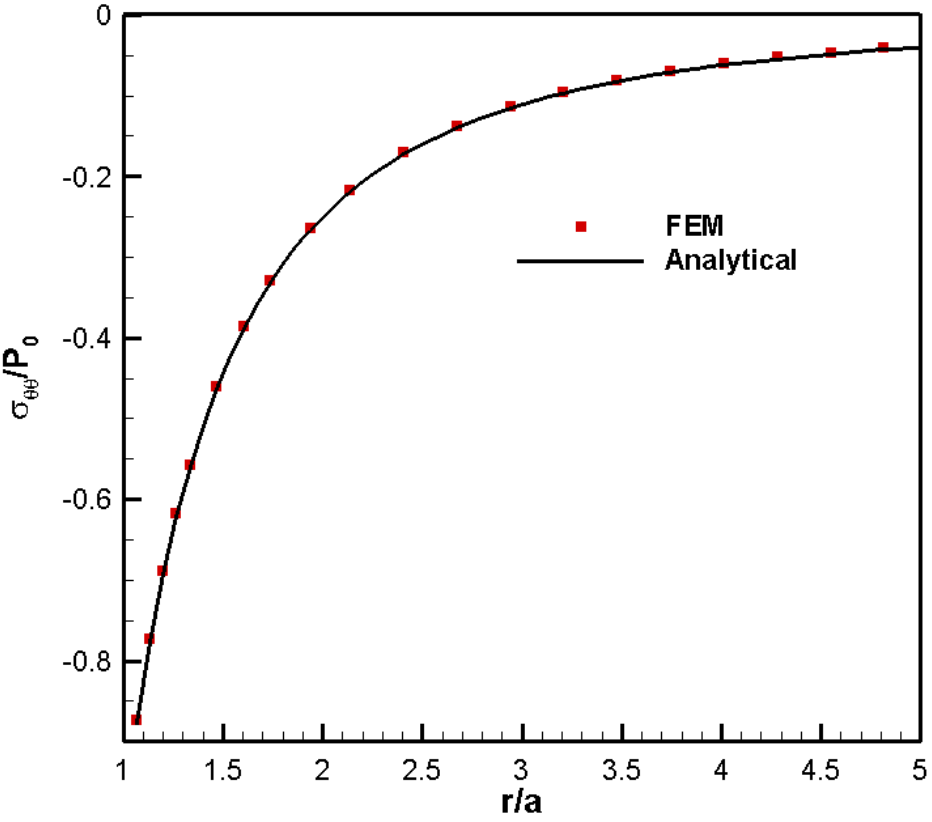

Figure 3-14. Induced total tangential stress along the radial distance due to mode 1 loading

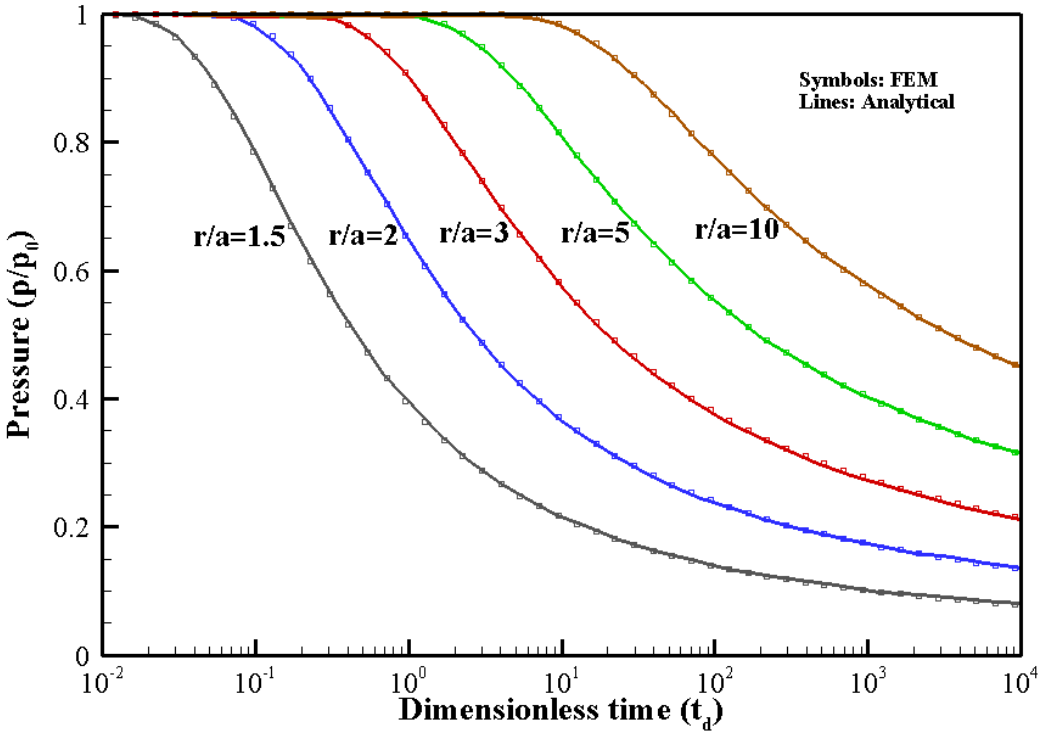

Figure 3-15. Analytical and numerical results comparison for pore pressure variation with time at different distances from the well due to mode 2 loading

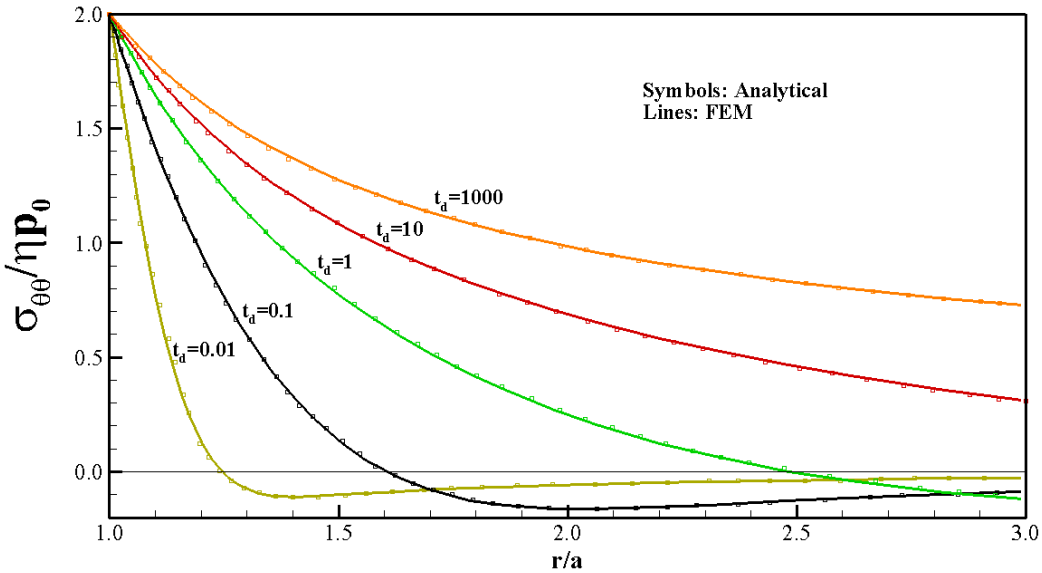

Figure 3-16. Temporal variation of total tangential stress with radius due to mode 2 loading

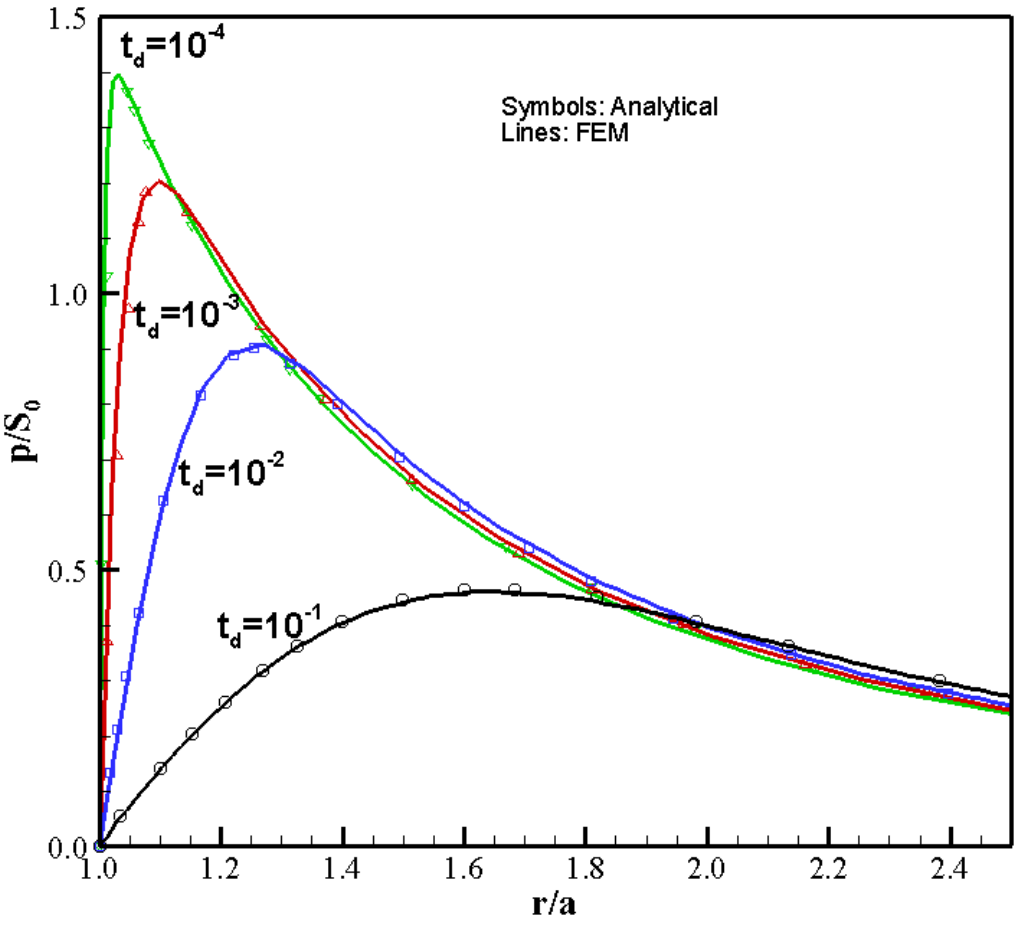

Figure 3-17. Analytical and numerical results comparison for induced pore pressure variation with time along X axis due to mode 3 loading (θ=0)

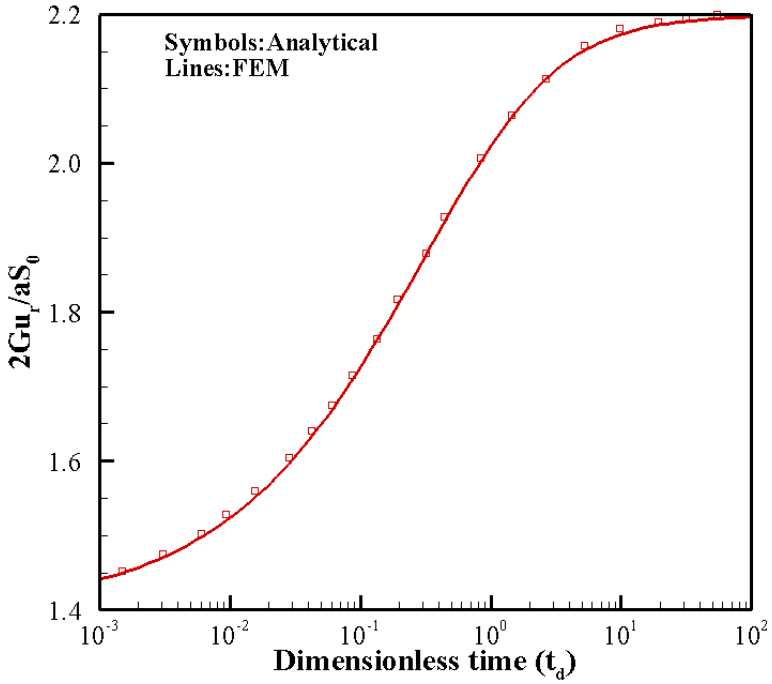

Figure 3-18. Radial displacement variation with time for a point on the borehole wall (r=a and θ=0) due to mode 3 loading

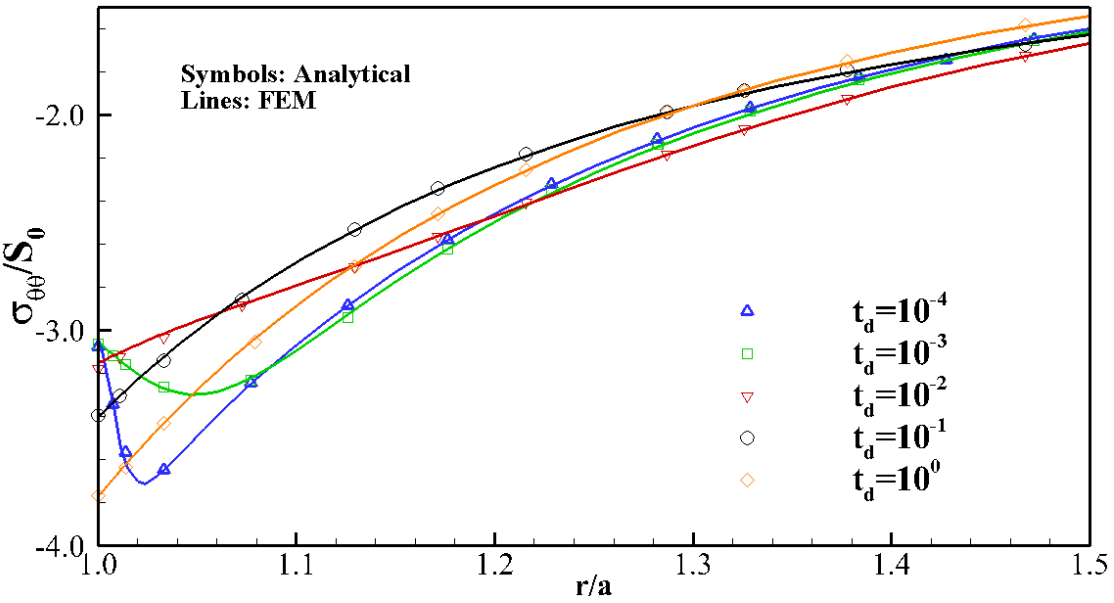

Figure 3-19. Temporal variation of total tangential stress with radius due to mode 3 loading for θ=0

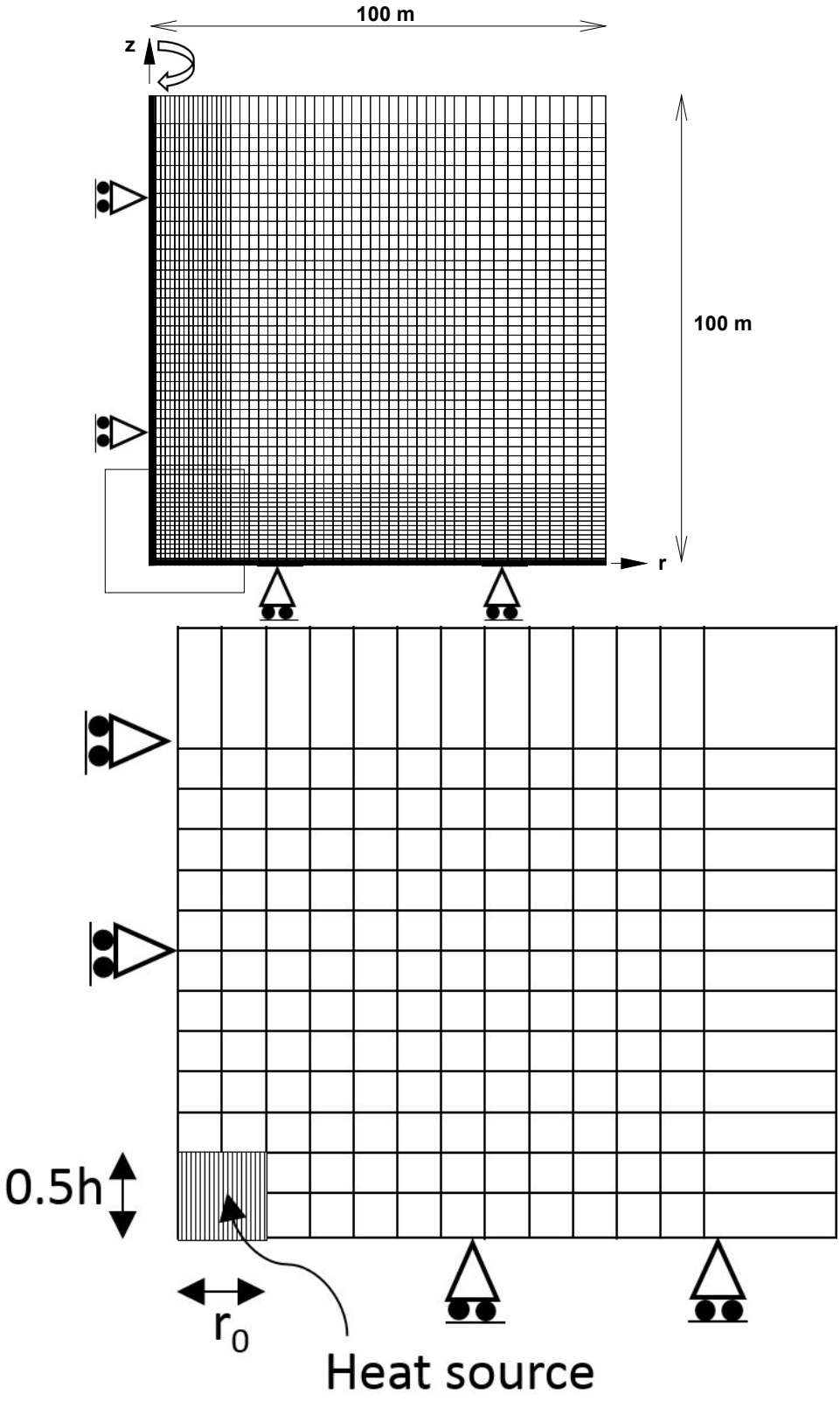

Figure 3-20. Finite element mesh for the axisymmetric heat source problem

Table 3-5. Properties of soil for thermal analysis

Parameter	**Value**
Radius of heat source, r_0	0.16 m
Height of the heat source, h	0.32 m
Thermal conductivity, k^T	1.02857 cal m^{-1} K^{-1} day^{-1}
Heat generation, q_v	1000 cal m^{-3} day^{-1}
Porosity, ϕ	0.5
Heat capacity, ρc	40 cal m^{-3} K^{-1}
Solid thermal expansion coefficient, α_m	0.9×10^{-6} K^{-1}
Pore fluid thermal expansion coefficient, α_f	0.63×10^{-5} K^{-1}
Permeability coefficient, k	$0.4 \times 10^{-5}\ m/day$
Young modulus, E	$6.0 \times 10^{7}\ Pa$
Poisson's ratio, ν	0.4
Biot coefficient, α	1
Fluid compressibility, c_f	0
Fluid density, ρ	1000 kg/m^3

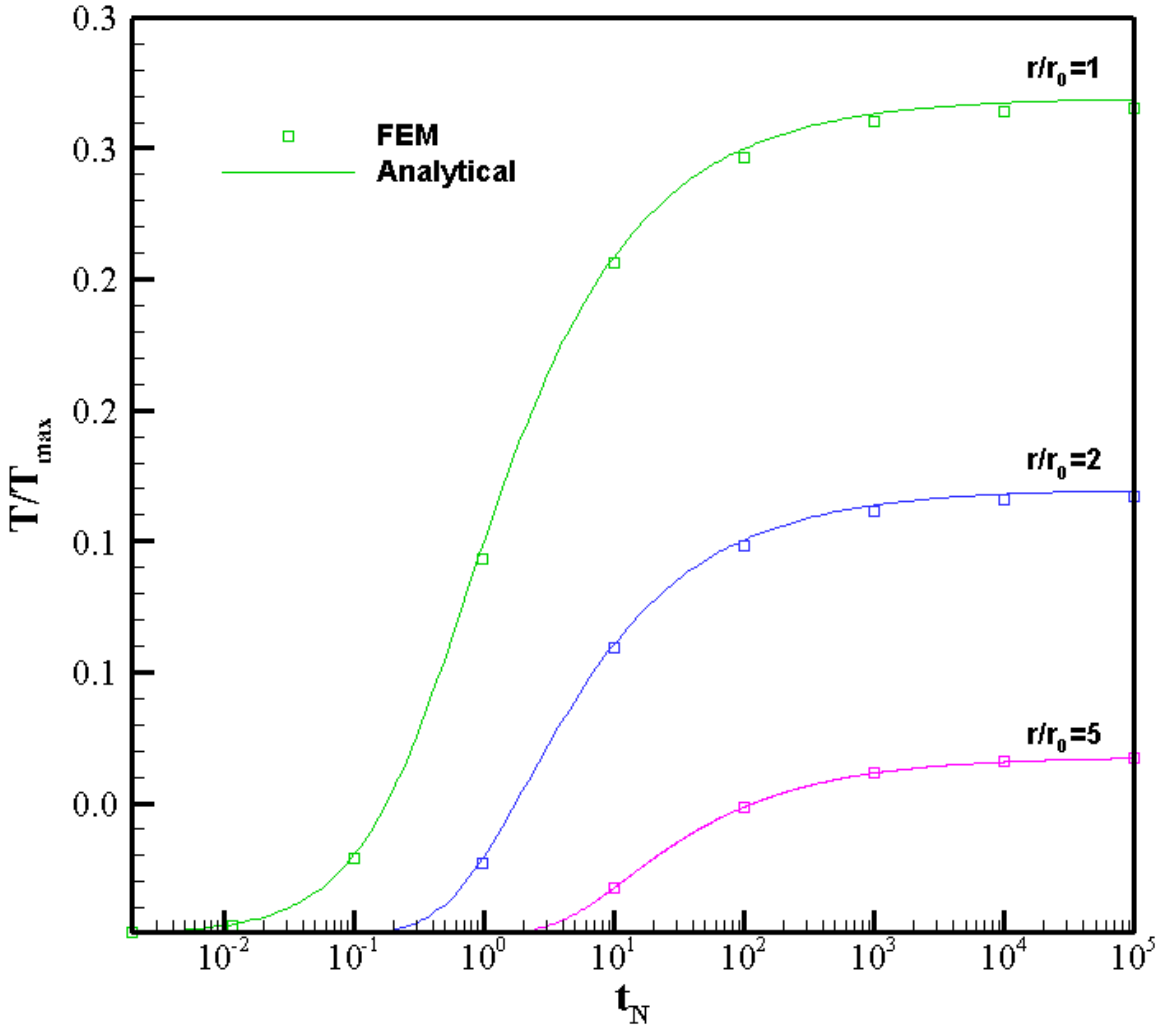

Figure 3-21. Variation of temperature with time for a cylindrical heat source

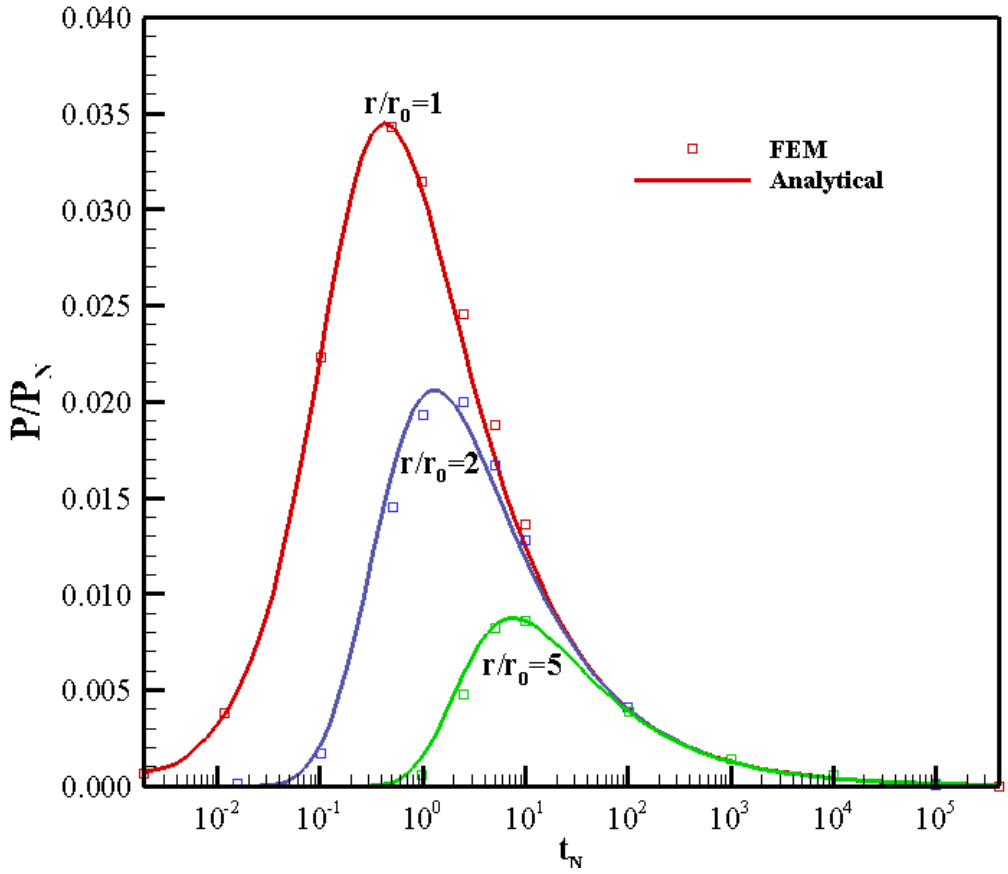

Figure 3-22. Comparison between analytical and numerical results for pore pressure

4. Impact of Poroelasticity on Refrac Operations

4.1 Introduction

Importance of refracturing of horizontal wells in the low permeability reservoirs is well recognized in oil and gas industry. Under certain reservoir conditions, the refracturing technique can restore or increase well productivity and may provide additional reserves by improving hydrocarbon recovery. Common practices include refracturing of the original production ("Parent") well or that of an infill ("Child") well drilled near the "Parent" well (e.g., Martinez et al., 2012; Agharazi and Kashikar, 2016; Miller et al. 2016; Morales et al., 2016). The production from the parent well fractures creates a "pressure sink" and reduced stress. If an infill well is drilled nearby this zone and is stimulated, its hydraulic fractures would have tendency to grow towards areas of lowest reservoir stresses or in other words towards depleted reservoir zones (e.g., Safari et al., 2016). This may involve communication between the parent and child wells, which is termed as a "frac-hit". It is realized that the "frac-hit" problem usually reduces productivity of the parent wells and in some cases may lead to complete damage of the parent well. Subsequently, the production potential of the child well is also decreased since it is now draining from the same reservoir area as the parent well. Re-pressurization of the parent well before infill well stimulation has been suggested as a technique for mitigation of "frac-hit" risks (e.g., Martinez et al., 2012; Miller et al., 2016).

In last three decades, several numerical and experimental studies have been presented to demonstrate and quantify the effects of fluid injection or reservoir depletion on the reservoir pore pressure and stress state (Perkins and Gonzalez, 1985; Warpinski and Branagan, 1989; Elbel and Mack, 1993; Palmer, 1993; Wright and Conant, 1995; Berchenko and Detorunay, 1997, Siebrits et al., 1998; Zhang, 2004). The concept of stress reorientation/reversal was

discussed by Perkins and Gonzalez (1985) in the context of the thermoelastic stress changes in injection well fracturing. They introduced the concept of the stress reorientation or reversal as shown in Figure 4-1. The production from an initial fracture causes a local redistribution of pore pressure in an expanding elliptical region around the wellbore and fracture surfaces. Due to the coupling between pore pressure and deformations in a poroelastic medium, pore pressure depletion results in the change of reservoir stress state in the vicinity of the production fractures. With increase of the production time, the horizontal stress component parallel to the initial fracture (i.e., σ_H in this case) reduces more than the horizontal stress component orthogonal to the production fractures (i.e., σ_h in this case), which results in an anisotropic variation of the in-situ stresses in the reservoir. This anisotropic variation of the horizontal stress will cause the modification of principal stresses both in the magnitude and orientation and may lead to complete stress reversal as shown in Figure 4-1, if the induced stress changes are large enough to overcome the effect of the initial horizontal in-situ stress contrast ($\sigma_H - \sigma_h$). Thermo-poroelastic coupling is also important in this context (Ghassemi and Zhang, 2006, Ghassemi et al., 2013). If the well is refractured after stress reversal has occurred, the new fracture will tend to propagate in the direction orthogonal to the initial preferred fracture propagation direction until the limit of this stress reversal region is reached. Beyond that zone, the new hydraulic fracture would tend to realign with the original in-situ maximum horizontal stress direction. This is because fractures tend to propagate in the direction of maximum compressional stress since they tend to open against the least principal stress.

As the stress reversal zone is a function of pore pressure depletion, its development is time dependent and varies with reservoir poroelastic properties and the background stress contrast. The problem of stress variation in the infill region has been treated in a number of studies. Roussel et al. (2013) and Safari et al. (2015) aspects of infill well fracturing in the case of closely spaced multiple horizontal wells using 3D models. Through extensive parametric analysis, Safari et al. [21] demonstrated that protecting parent wells from infill well fractures has a greater chance of success in a reservoir with low stress anisotropy, low hydrocarbon viscosity, low bottomhole production pressure, high reservoir pore pressure gradient, high reservoir permeability, and high Biot's constant. Most of these earlier simulations were carried out using two different models for the reservoir depletion analysis and the subsequent fracturing of the infill wells. Rezaei et al. (2017) presented a refracturing analysis using a two-dimensional (2D) poroelastic displacement discontinuity model built on the work of Zhang (2004), Ghassemi and Zhang (2006), and Chun (2013).

Kumar et al. (2018) presented primary and infill (or "parent" and "child") well fracturing simulations to address the "frac-hit" issue in horizontal well refracturing and its mitigation strategy. They used a fully coupled 3D poroelastic model "GeoFrac-3D" for the numerical simulations. The model was based on the 3D poroelastic displacement discontinuity (DD) method for the solid rock deformation and pore fluid diffusion in the rock matrix. The fluid flow inside the fractures was simulated using the Galerkin's finite element method (FEM). The fracture propagation was implemented in the framework of the linear elastic fracture mechanics approach (LEFM). with "GeoFrac-3D" model, they simulated multistage fracturing of the multiple horizontal wells considering both aspects of refracturing simulation (i.e., reservoir depletion analysis and subsequent fracturing of the infill well). However, the DD

model was limited to homogenous reservoir rock mass. To investigate the impact of reservoir heterogeneities on the depletion induced reservoir pore pressure and stress change, they used a coupled Galerkin's FEM model to simulate the same problem. The results from both models were compared and a good match was observed.

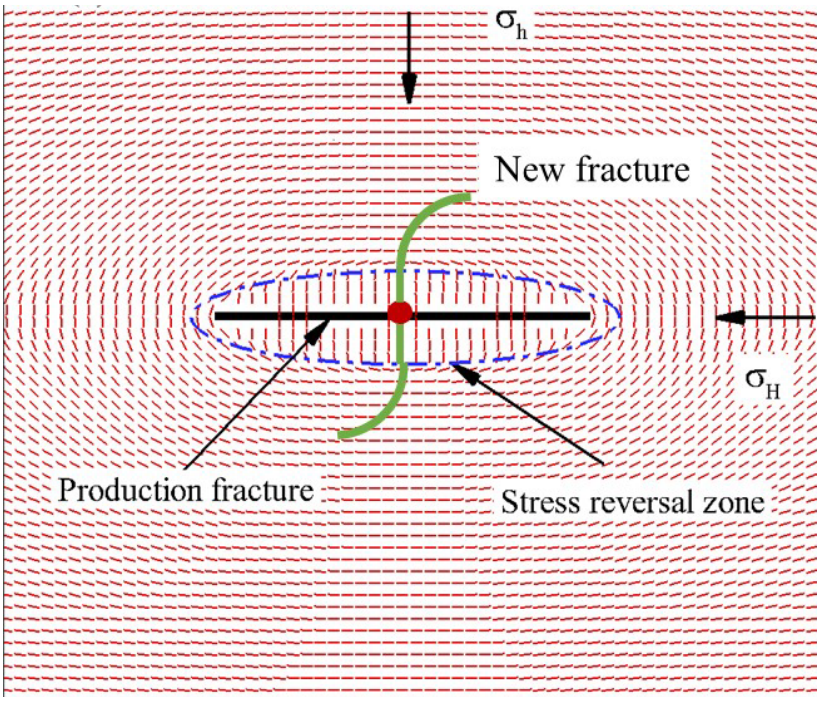

Figure 4-1. Schematic showing expanding elliptical reservoir pore pressure and stress reversal zone around a production fracture (solid black lines show the trajectories of the local maximum principal stress).

In this chapter, a fully coupled 3D poroelastic model is developed which can analyze reservoir depletion and predict frac-hit issues. The model is based on Galerkin's finite element method to simulate solid rock and fracture deformation and fluid diffusion in rock matrix. The model is then used to study the stress reorientation in several cases including a single vertical well, a single vertical fracture intersected by a horizontal well and one or two horizontal wells intersected with multiple hydraulic fractures. The results of 3D analysis have

been discussed and its applications in the design of hydraulic fractures in shale reservoirs have been presented.

4.2 Poroelastic coupling for 3D FEM

The theory for fluid saturated poroelastic media which is under mechanical and hydraulic loading is governed by the following equation:

$$\dot{\sigma}_{ij} = 2G\dot{\varepsilon}_{ij} + \frac{2G\nu}{1-2\nu}\dot{\varepsilon}_{kk}\delta_{ij} - \alpha\dot{p}\delta_{ij} \tag{4.1}$$

$$\dot{\zeta} = \alpha\dot{\varepsilon} + \frac{1}{M}\dot{p} \tag{4.2}$$

where σ_{ij} is the total stress and ε_{ij} is the corresponding strain. The relation between strain and displacement is given as:

$$\varepsilon_{ij} = \frac{1}{2}(u_{i,j} + u_{j,i}) \tag{4.3}$$

Balance of momentum is given as below:

$$\sigma_{ij,j} + \rho g_i = 0 \tag{4.4}$$

The poroelastic governing equations can be derived from Eqs. (4.1)-(4.4) considering Eqs. (2.16) and (2.22).

4.2.1 FEM discretization

By applying Green's theorem and Galerkin weighted residual method to the governing equations and integration in time using finite difference method, matrix equations for each element are obtained as below:

$$\begin{bmatrix} \mathbf{K} & -\mathbf{L} \\ \mathbf{L}^T & (\mathbf{K_{pp}} + \theta\Delta t\mathbf{H_{pp}}) \end{bmatrix} \begin{bmatrix} \Delta\mathbf{u} \\ \Delta\mathbf{p} \end{bmatrix} = \begin{bmatrix} \Delta\mathbf{F}_u \\ -\Delta t\mathbf{H_{pp}}\mathbf{p_0} \end{bmatrix} \tag{4.5}$$

where:

$$\boldsymbol{K} = \int_{\Omega} [\boldsymbol{B}^T][\boldsymbol{D}][\boldsymbol{B}]d\Omega \tag{4.6}$$

$$\boldsymbol{L} = \int_{\Omega} [\boldsymbol{B}^T][\boldsymbol{m}][\boldsymbol{N}_p]\alpha d\Omega \tag{4.7}$$

$$\boldsymbol{H_{pp}} = \int_{\Omega} [\nabla \boldsymbol{N}_p{}^T][\boldsymbol{k}]\,[\nabla \boldsymbol{N}_p] d\Omega \tag{4.8}$$

$$\boldsymbol{K_{pp}} = \int_{\Omega} \frac{1}{M}[\boldsymbol{N}_p^T][\boldsymbol{N}_p] d\Omega \tag{4.9}$$

$$\boldsymbol{F^u} = \int_{\Omega} [\boldsymbol{N^u}]^T \rho[\boldsymbol{g}] d\Omega + \int_{\Gamma_u^N} [\boldsymbol{N^u}]^T [\boldsymbol{t}] d\Gamma \tag{4.10}$$

θ is a coefficient characterizing temporal discretization. Smith and Griffith (2004) have shown that the system of equations in (4.5) is unconditionally stable only if $\theta \geq \frac{1}{2}$. Δt is the time step size and ΔF_u is the external loading vector. In the following numerical examples, we chose $\theta = 1$ which is the "fully implicit" method.

4.3 Case 1: production from a single vertical well

Figure 4-2 shows a single vertical well in a homogenous reservoir. The well is under production with bottomhole pressure of 20.7 MPa and initial reservoir pressure of 68.9 MPa. The in-situ stresses in X and Y direction are equal (isotropic stress state in XY plane) $\sigma_x = \sigma_y = 75.8\ MPa$. A high in-situ stress magnitude in Z direction is chosen, $\sigma_{zz} = 99.6\ MPa$ so that it always remains as maximum principal stress. The reservoir mechanical properties and fluid properties can be found in Table 4-1. The perforated zone of the well is 1 m long and is in the middle of the well's length. The model dimensions are 20 m×20 m×15 m. The wellbore radius and length are 10 cm and 10 m respectively. The domain was discretized into 44,941 nodes and 259,038 tetrahedral elements. A variable time stepping scheme was adopted with the initial time step of $\Delta t = 8.3 \times 10^3$ s and the following time steps increased by a factor of 1.1. After producing for 12 days, the pore pressure distribution in the reservoir is

shown in Figures 4-2 and 4-3 in 3D and 2D respectively. A circular pore pressure depletion zone is observed in XY plane. In Figure 4-4, the direction of maximum principal stress in XY plane and near the wellbore is depicted. It can be observed that at the near proximity of the well, trajectories are normal to the well and pressure contour lines. As we get farther from the well, the maximum stress direction shows a circular pattern, as seen in Figure 4-5, which is due to the high gradient of pore pressure in radial direction, making the radial direction the minimum principal stress and tangential stresses the maximum principal stress.

Table 4-1. Rock mechanical properties and in-situ stresses.

Parameter	Units	Value
Initial reservoir pressure, p_i	MPa (psi)	68.9 (10,000)
Bottomhole producing pressure, p_b	MPa (psi)	20.7 (3,000)
Reservoir rock intrinsic permeability, k	m^2 (nd)	3×10^{-19} (300)
Reservoir fluid viscosity, μ_f	Pa.s (cP)	2.5×10^{-4} (0.25)
Poisson's ratio, drained, v		0.2
Biot coefficient, α		0.7
Biot Modulus, M	GPa (psi)	5.86 (8.5×10^5)
Young Modulus, E	GPa (psi)	13.8 (2.0×10^6)

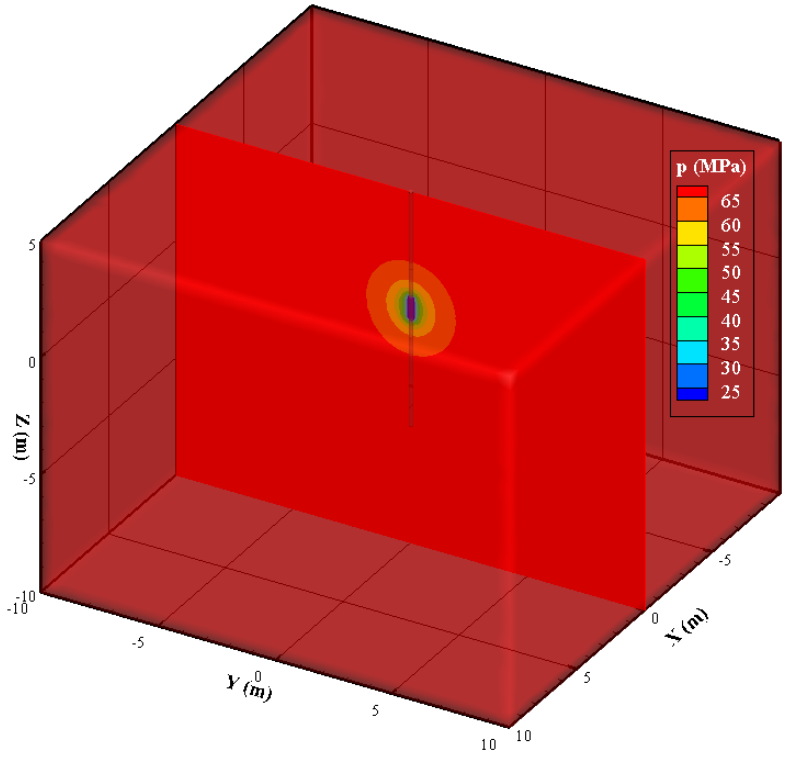

Figure 4-2. 3D view of a single vertical well under production along part of its length. The pore pressure contours after 12 days of production are shown.

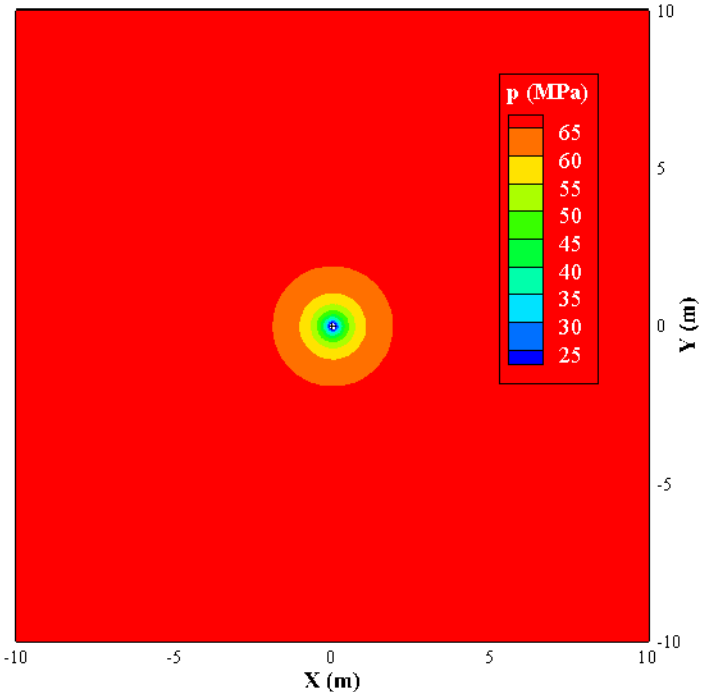

Figure 4-3. Horizontal section of the well at the middle of production zone showing the contours of pore pressure after 12 days of production.

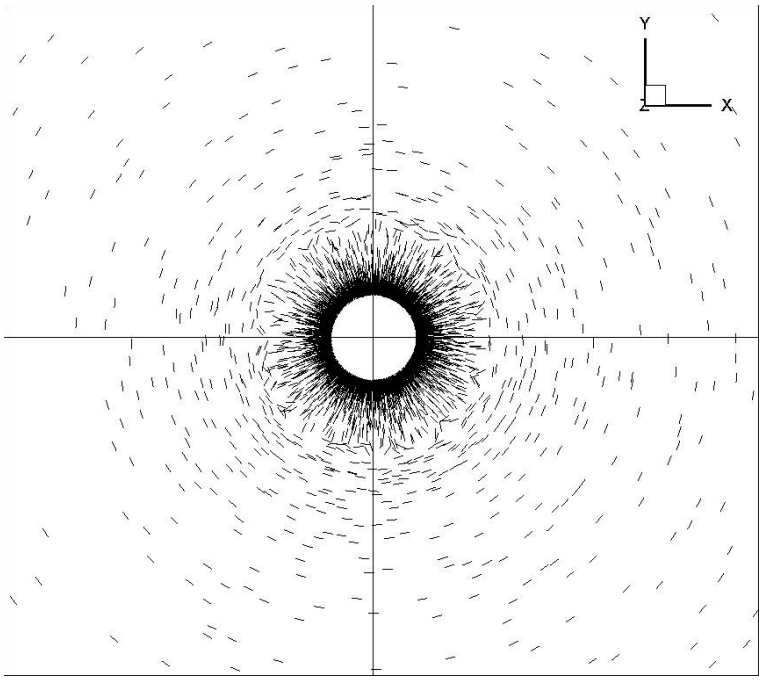

Figure 4-4. Near wellbore direction of maximum principal stress after 12 days of production from a single well. The section is made at the middle of production zone.

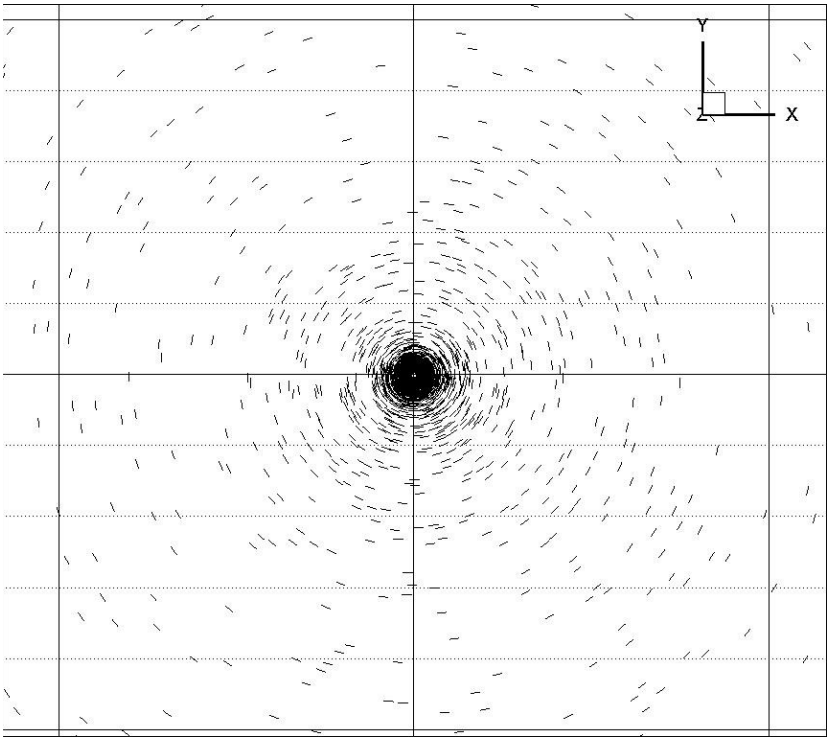

Figure 4-5. Far field direction of maximum principal stress after 12 days of production. The section is made at the middle of production zone

4.4 Case 2: Effects of production from one fracture

As an illustrative example, the case of production from a single vertical fracture which is produced by a horizontal well is considered. The fracture and the reservoir properties are given in Tables 4-1 and 4-2. The fracture is in the middle of a homogenous reservoir (reservoir size is assumed to be 200 m×200 m×200 m which is very large compared to the size of fracture) and is intersected by a horizontal well at the fracture center. The fracture and finite element mesh near the fracture are shown in Figure 4-6. The FE mesh consists of 88,800 nodes and 82,859 hexahedral elements. A variable time stepping scheme was adopted with the initial time step of $\Delta t=8.3\times10^3$ s and the following time steps increased by a factor of 1.1 Because of production, pore pressure will decrease in the form of elliptical regions around the fracture surface (Figure 4-7). The decrease in pore pressure will increase the effective stresses in the reservoir. This increase in effective stress will cause the matrix to contract which induces a tensile stress to the neighboring elements. Considering the pore pressure contours in Figure 4-7, the highest gradient of pore pressure reduction for every point is normal to the pore pressure contour line at that point. The pore pressure reduction in this direction causes a significant decrease of total stress along this direction which makes it the direction of the minimum principal stress. Therefore, the direction tangent to the pore pressure contour curve will be the maximum principal stress direction. It has been shown in Figure 4-7 that the maximum principal stresses are tangent to the pore pressure contour lines except for the proximity of fracture which will be discussed later. In Figure 4-9, the vector components represent induced total stresses in X and Y direction after 12 days of production. Negative or positive direction of vector components signify the decrease or increase of total stress for that component. It is observed that the magnitude of induced stress parallel to

production fracture is greater than the horizontal stress component orthogonal to the production fracture in the close vicinity of fracture. In other words, the horizontal stress component parallel to the production fracture (i.e., σ_H) decreases more than the horizontal stress component perpendicular to the fractures (i.e., σ_h). This is due to the fact that the length of the depleted zone (along fracture azimuth) is much longer than the width of depleted zone (normal to fracture). This anisotropic reduction in horizontal stresses can result in complete stress reorientation/reversal if the induced stress changes are large enough to overcome the effect of the initial horizontal stress contrast (i.e., $\sigma_H - \sigma_h$). This direction change can be observed in Figure 4-8. A zone of stress reversal has formed in the vicinity of the fracture. If a refracture treatment is being considered, it's important to note that it will propagate normal to original fracture until it reaches the limits of stress reversal zone where it will reorient parallel to the original in-situ maximum horizontal stress direction. The point on Y axis which is located on the limit of this zone is identified as isotropic point. After a refracture reaches the isotropic point, its direction gradually reverts parallel to the initial fracture. As the stress reversal zone is a function of pore pressure depletion, its development is time dependent and dependent on reservoir poroelastic properties and the in-situ stress contrast. The size of stress reversal zone is characterized by parameter L_f' past which the maximum principal stress turns back to its initial position.

The development of the stress reversal zone was first noted by Elbel and Mack (1993).

Using a finite difference, 2D model, they showed that producing from a fractured well changes the distribution of stress, and refracturing leads to propagation normal to the original fracture in its close proximity.

Siebrits et al. (1998) also reported the occurrence of stress reversal zone near a fracture. They attributed this stress reversal to the production induced displacements, suggesting that the displacement field close to the fracture and near the Y axis is towards the fracture but away from the well. This will cause expansion parallel to the fracture on the Y axis and reduces the total stress in x direction, making the Y direction the maximum principal stress direction. However, looking at our simulation results for one fracture (Figure 4-10), it is clearly shown that displacements are towards the well, not away from it. So, the explanation given by Siebrits et al. (1998) doesn't seem to be valid.

In reservoirs where the difference between the principal stresses is minimal, switching between directions of principal stresses frequently occurs (Elbel and Mack, 1993). To show this concept, two different models were constructed with identical fracture size and properties. The only difference between the two models was the magnitude of stress anisotropy. For case a, in-situ stresses are $\sigma_{xx} = 79.25\ MPa;\ \sigma_{yy} = 75.8\ MPa$; while for case b, $\sigma_{xx} = 84.25\ MPa$ and $\sigma_{yy} = 70.8\ MPa$. Other parameters of the reservoir and fracture are given in Tables 4-1 and 4-2. Figure 4-11 shows the direction of maximum principal stress directions after 12 days of production for both cases. It can be observed that the stress reversal zone didn't form in case (b) where the stress contrast is high. As the stresses become more isotropic, it's easier to alter the direction of principal stresses by producing from a fracture.

Table 4-2. In-situ stress and hydraulic fracture properties

Parameter	Units	Value
Fracture permeability, k_f	m^2 (D)	1.5×10^{-7} (1.5×10^{5})
Fracture half length, $0.5L_f$	m (ft)	1.5 (4.92)
Fracture height, h_f	m (ft)	1.0 (3.28)
Fracture aperture	m (ft)	0.05 (0.16)
Maximum horizontal compressive stress, σ_{xx}	MPa (psi)	79.25 (11,500)
Minimum horizontal compressive stress, σ_{yy}	MPa (psi)	75.8 (11,000)
Vertical in situ stress, σ_{zz}	MPa (psi)	89.6 (13,000)
Orientation of max. horizontal compressive stress		XX direction

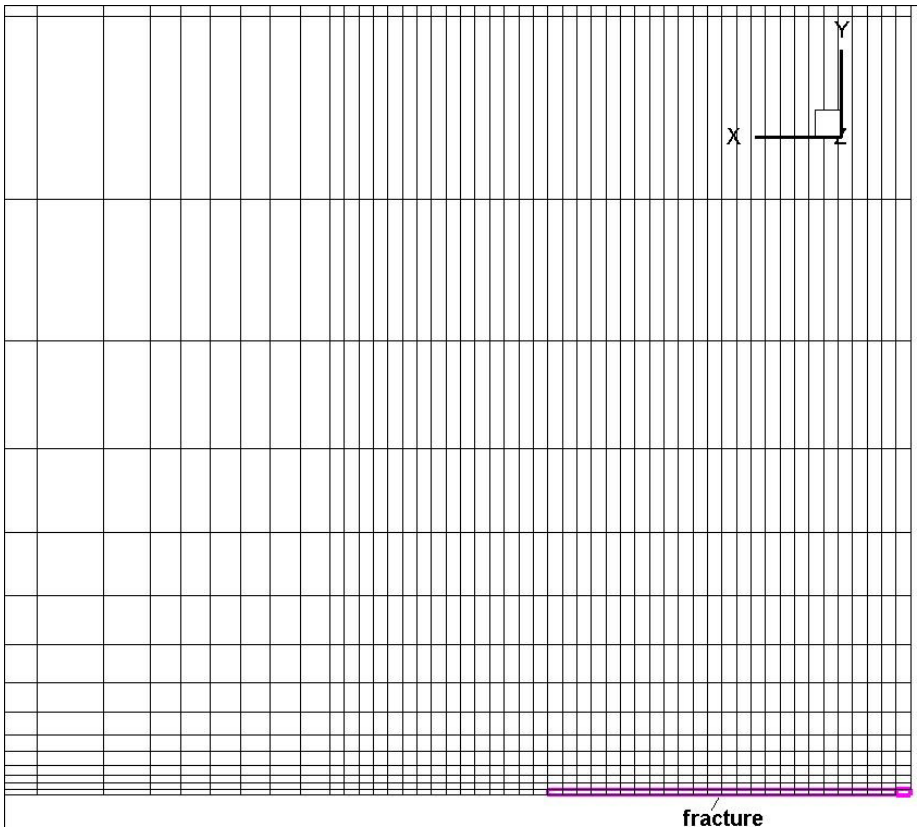

Figure 4-6. Illustration of a single vertical fracture and part of the finite element mesh in XY plane. Only one eighth of the region has been modeled due to symmetry relative to X, Y and Z axes

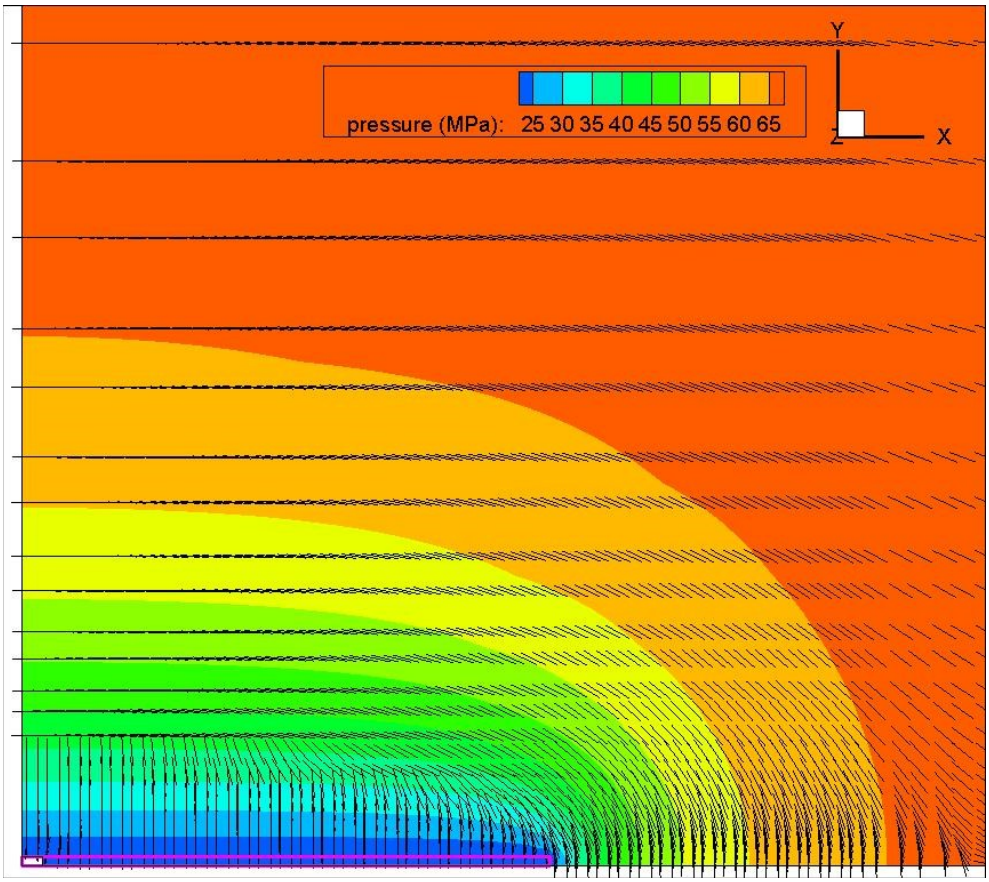

Figure 4-7. Plan view of depletion induced reservoir pore pressure around a fracture after 12 days of production. The maximum principal stress direction is also shown in this figure.

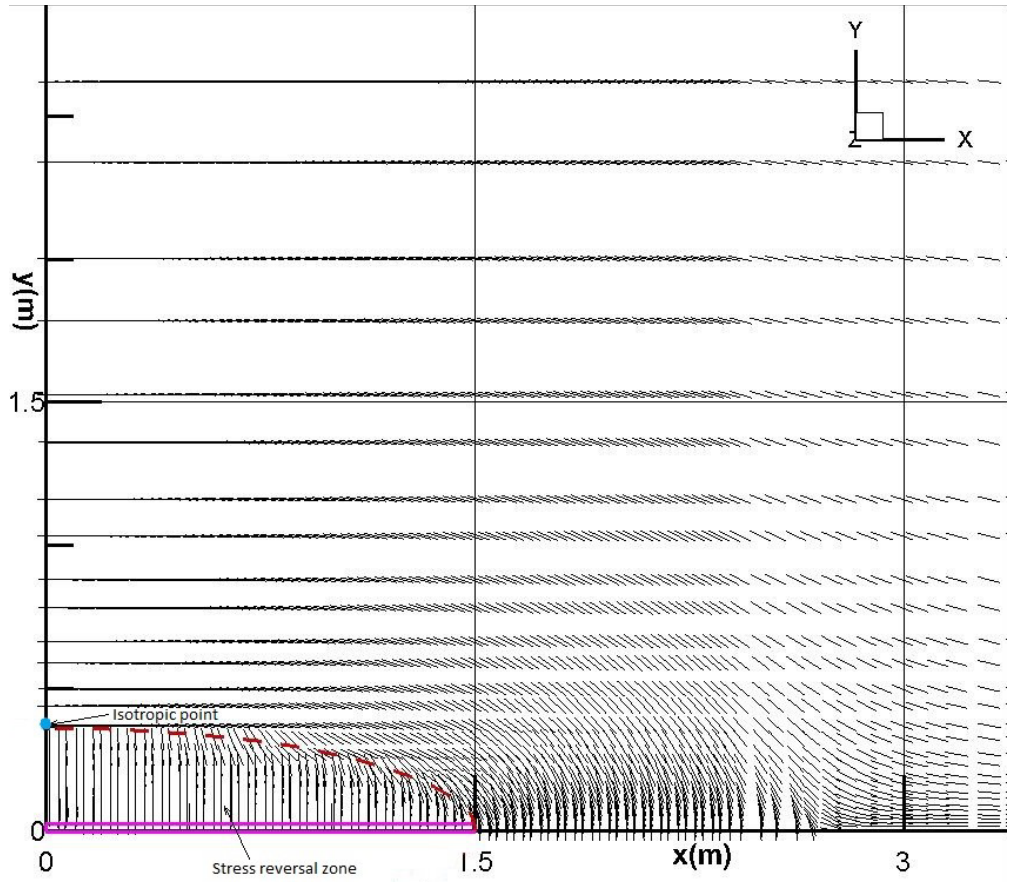

Figure 4-8. Stress reversal zone and direction of maximum principal stress after 12 days of production from a single fracture. Dashed red line shows the boundary of this zone.

4.5 Case 3: Production from two parallel horizontal wells with multiple fractures

Unconventional shale oil and gas reservoirs require horizontal well drilling with multiple transverse fractures to create a stimulated reservoir volume (SRV). Within the SRV, reservoir fluids flow from shale with nano-Darcy permeability to the created fracture network. Reducing the horizontal well spacing by drilling new horizontal wells and fracturing them can significantly increase the field recovery.

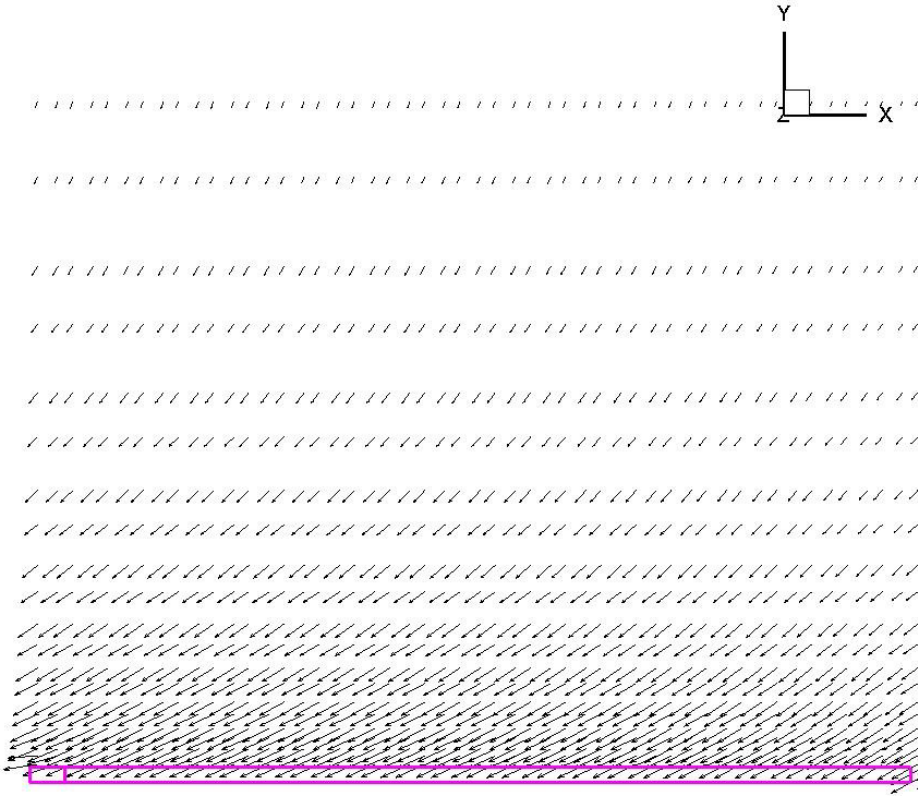

Figure 4-9. Induced stress components in X and Y direction shown as a vector plot after 12 days of production from a single fracture.

To better understand the effect of production on the direction of principal stresses, a hypothetical tight oil reservoir is considered. The reservoir is confined on top and bottom by very low permeability layers which have similar mechanical properties with the pay zone (Figure 4-13b). The fluid and mechanical properties and geometry of fractures are taken from Roussel et al. (2013). The stress regime in this reservoir is normal faulting regime where minimum horizontal stress is the least principal stress. It's well known that drilling horizontal wells in the direction of minimum principal stress is optimal to create transverse fractures as it will maximize the stimulated reservoir volume (SRV).

To develop this reservoir, two horizontal wells are drilled in the minimum horizontal stress direction (YY) and several fractures are created along the length of the horizontal well (Fig

ure 4-12). The fractures are perpendicular to the horizontal wells, opening against the least principal stress. An enhanced permeability region between the fractures was modeled as SRV and was assigned a higher permeability value compared to the host rock as shown in Table 4-3. The two horizontal wells are producing at constant bottom hole pressure of 20.7 MPa. In this problem the frictional losses due to flow along the horizontal wells are neglected and pressure drops along the horizontal well are small. The initial reservoir pressure is 68.9 MPa. The well completion method for fractured horizontal wells is cased/perforated completion. In this type of completion, wellbore flow is only contributed by fractures. There is no direct communication between reservoir and wellbore. A schematic diagram showing flow direction in this completion method is shown in Figure 4-14. The horizontal plane stress anisotropy in this example is small ($\sigma_H - \sigma_h = 500\ psi$). We have deliberately chosen a small stress contrast so that the reorientation of stresses could be observed. As previously illustrated, it is more difficult to change the direction of principal stress by production if the stress contrast is large. If the stress contrast is too large, the induced stresses from production are not adequate to change the principal stress directions. The reservoir permeability is isotropic but in situ stress is anisotropic as mentioned before. Inertial effects are neglected. The basic reservoir and wellbore properties used in this problem are shown in Table 4-3. The fluid phase is assumed to be isothermal, single phase and slightly compressible. The reservoir behaves according to the Biot's linear poroelastic theory.

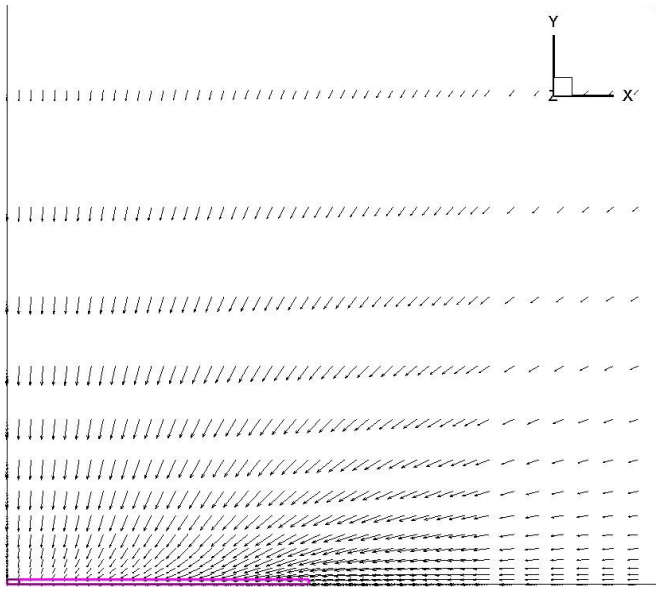

Figure 4-10. Displacement vectors close to the fracture after 12 days of production.

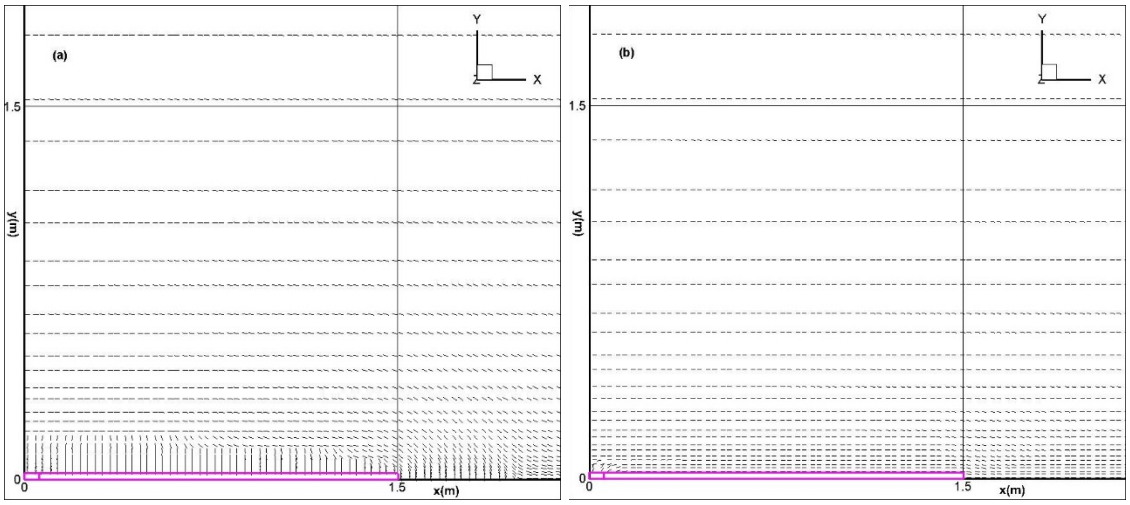

Figure 4-11. Direction of maximum principal stress in case of (a) low stress contrast (b) high stress contrast.

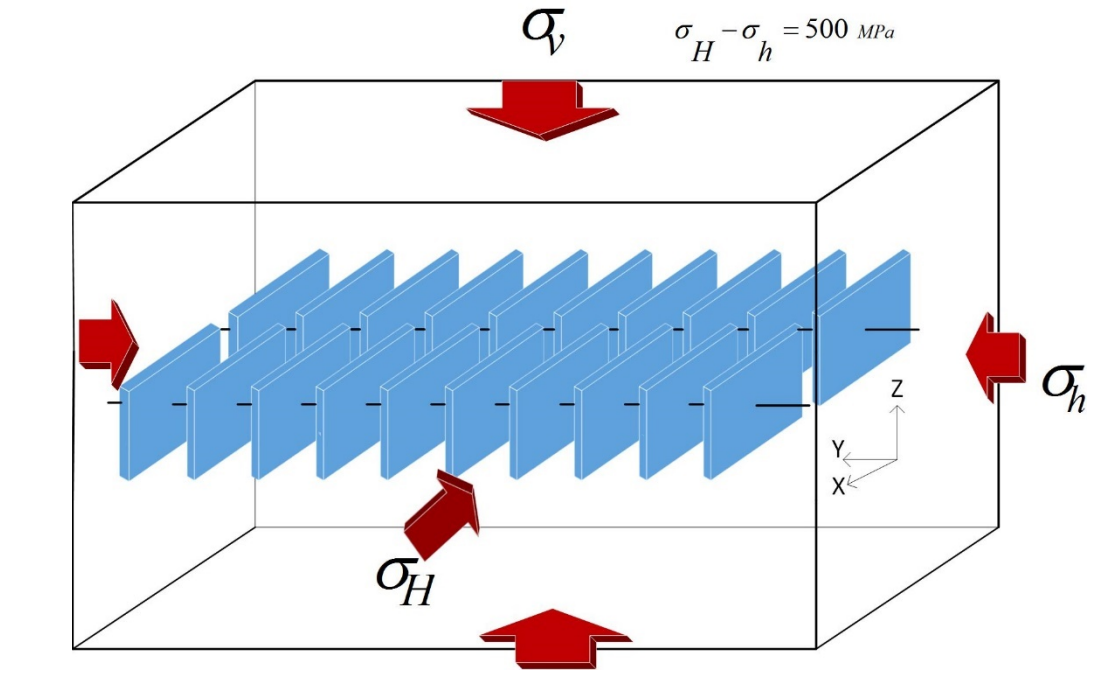

Figure 4-12. Illustration of horizontal wells intersected by multiple transverse vertical fracture.

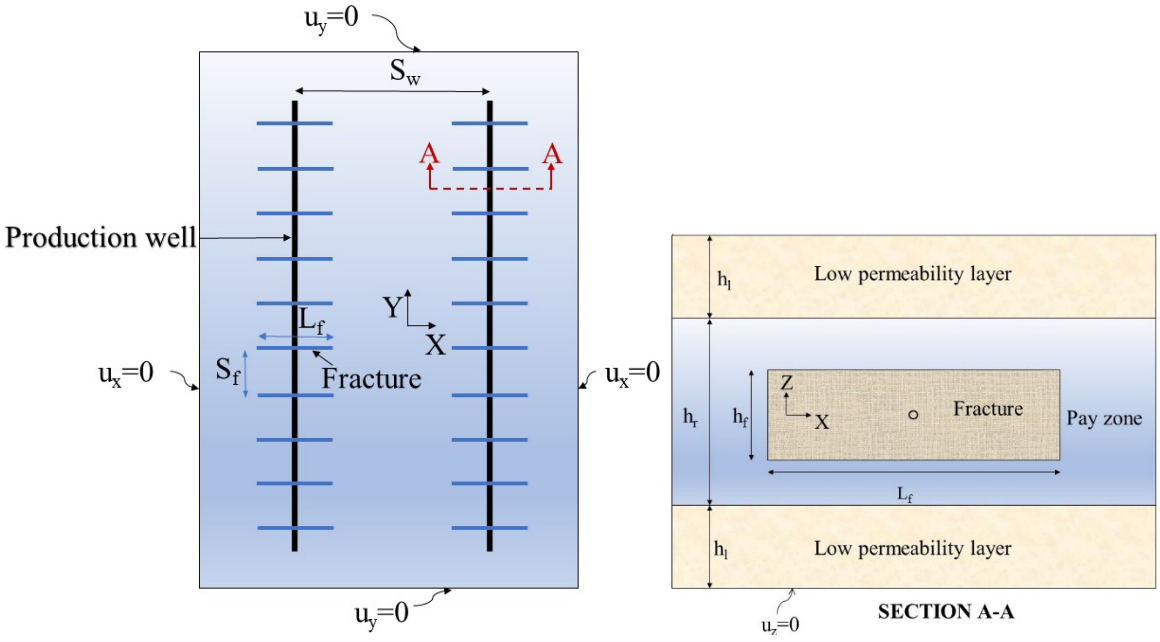

Figure 4-13. Layout of the reservoir with fractures. Top: the plan view; bottom: section AA from top figure. The displacement boundary conditions are also shown in both figures.

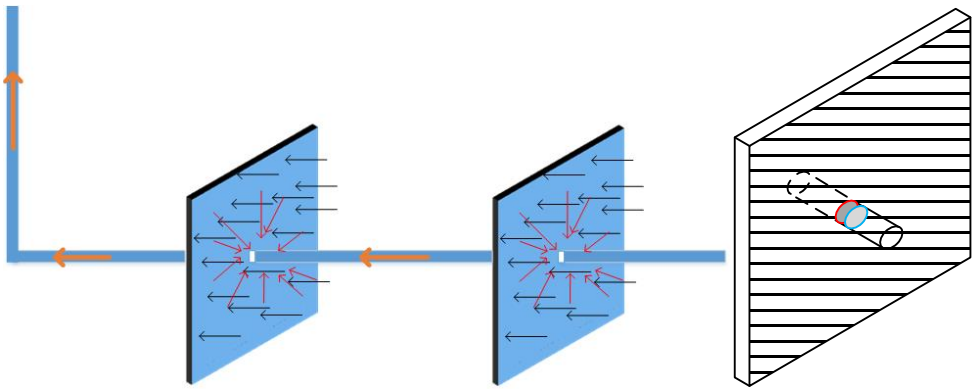

Figure 4-14. Close view of fractures and horizontal well. Right: intersection of well and fracture; The elements along the horizontal well which are located inside the fracture (portion of the well between two colored circles) are removed and nodes on lateral surface of this cylinder are specified to have constant pressure equal to bottom hole pressure. Left: schematic of flow direction from reservoir to the well

Table 4-3. Rock mechanical properties and in-situ stresses

Parameter	**Units**	**Value**
Initial reservoir pressure, p_{ini}	MPa (psi)	68.9 (10,000)
Bottomhole producing pressure, p_{bot}	MPa (psi)	20.7 (3,000)
Reservoir rock intrinsic permeability, k	m^2 (nd)	3×10^{-19} (300)
Reservoir fluid viscosity, μ	Pa.s (cp)	2.5×10^{-4} (0.25)
Intrinsic permeability of SRV zone, k_{SRV}	m^2 (μd)	1.5×10^{-18} (1.5)
Maximum horizontal compressive stress, $\boldsymbol{\sigma_{xx}}$	MPa (psi)	79.25 (11,500)
Minimum horizontal compressive stress, $\boldsymbol{\sigma_{yy}}$	MPa (psi)	75.8 (11,000)
Vertical in situ stress, $\boldsymbol{\sigma_{zz}}$	MPa (psi)	89.6 (13,000)
Orientation of max. horizontal compressive stress		XX direction
Poisson's ratio, drained, ν		0.2
Biot coefficient, α		0.7
Biot modulus, M	GPa (psi)	5.86 (8.5×10^5)
Young modulus, E	GPa (psi)	13.8 (2.0×10^6)
Fracture half length, $0.5L_f$	m (ft)	88 (289)
Fracture height, h_f	m (ft)	60 (197)
Fracture spacing, S_f	m (ft)	91 (299)
Fracture aperture	m (ft)	1 (3.28)
Fracture permeability, k_f	m^2 (md)	1.5×10^{-7} (1.5×10^8)
Total number of fractures		20
Pay zone thickness, h_r	m (ft)	121 (397)
Low permeability layer thickness, h_l	m (ft)	122 (400)
Horizontal well spacing, S_w	m (ft)	465 (1525)

4.5.1 Model description

A 3D model representing two horizontal wells with 10 hydraulic fractures in each well was set up. The model dimensions are 1600 m long, 1400 m wide and 366 m thick. 10 equi-

spaced hydraulic fractures are located along and perpendicular to each of two horizontal wells with a length of 914 m. The fractures dimensions are given in Table 4-3. The model consists of three layers as shown in Figure 4-13b. The middle layer is the pay zone and has a thickness of 121 m and is enclosed on the top and bottom with layers having very low permeability but similar mechanical properties with the pay zone. The fractures are idealized having fixed length, aperture and orientation. The fractures aperture was set to 1 m.

This problem is obviously symmetric under such geometry and loading conditions about X, Y and Z axes. So only one eighth of the reservoir has been modelled to speed up the simulation. The fractures were explicitly modeled with an unstructured fine grid so that the model was capable of capturing fracture flow and the large pressure gradients involved. Unstructured grid for fractures and porous media was generated with the open-source 3D FE mesh generator Gmsh (Geuzaine and Remacle, 2009) and is shown in Figure 4-15. 20-node second order hexahedrons were employed with 60 displacement degrees of freedom and 8 pressure degrees of freedom as illustrated in Figure 4-16. The smallest element size is 1.0 m and the largest element size is 21.9 m. Fractures are modeled by thin and high permeability elements. In total, 268,784 brick elements and 280,924 nodes were used in the finite element mesh.an initial time step of Δt=28,140 was used in the simulation and increased by a factor of 1.1 in subsequent steps.

4.5.2 Boundary Condition

The model outer boundaries have zero flow rate boundary condition. The displacement boundary condition is also specified as depicted in Figure 4-13.

Recall that the boundary conditions for a wellbore are specified as constant pressure or constant rate. In the present work, constant well pressure is employed for the portion of the well

inside fracture. Typically, the horizontal wells have small diameter and modelling them could result in excessive computation time. Therefore, only cavity formed at the intersection of the well and the fractures is modelled, and pore pressure is applied to outer boundary of the cavity to represent a well with constant bottomhole pressure (Figure 4-14). Flow transport along the horizontal well between the fractures is not studied here and only the production in the portion of the well intersecting each fracture is considered. The specified pore pressure in the well is smaller than the initial reservoir pressure which leads to flow from fractures into the horizontal well.

4.5.3 Solution

To compute pore pressures and stresses at a given time step, the induced pore pressures and displacements determined from Eq. (4.5) are added to the known values at previous time step. Stresses can be determined from the displacements using Eq. (4.1). Time marching starts at time zero in which we already know the pore pressure and displacements, given as initial conditions. Figure 4-17 shows the pore pressure distribution and maximum compressive stress directions at t=0, 6 months, 9 months and 7.5 years from the start of production. The maximum principal stress directions are also shown in this figure. Initially, the maximum principal stress is in X direction which is the way the problem was defined. Production induces a pore pressure reduction in the region around the fracture. Since the pore pressure contours are in the form of concentric ellipses, at every point on the ellipse, the largest decrease of pore pressure is in the direction normal to the contour line. This large decrease is equivalent to large decrease of total stress in this direction which renders the direction that is tangent to the pressure contour ellipse at that point, the maximum principal stress direction. In this way, the direction of maximum principal stress becomes ortho-radial around

each fracture. However, in very close vicinity of each fracture, stress reversal zone forms, and the maximum principal stress is normal to the fracture as was already observed in the case of a single well and a single fracture.

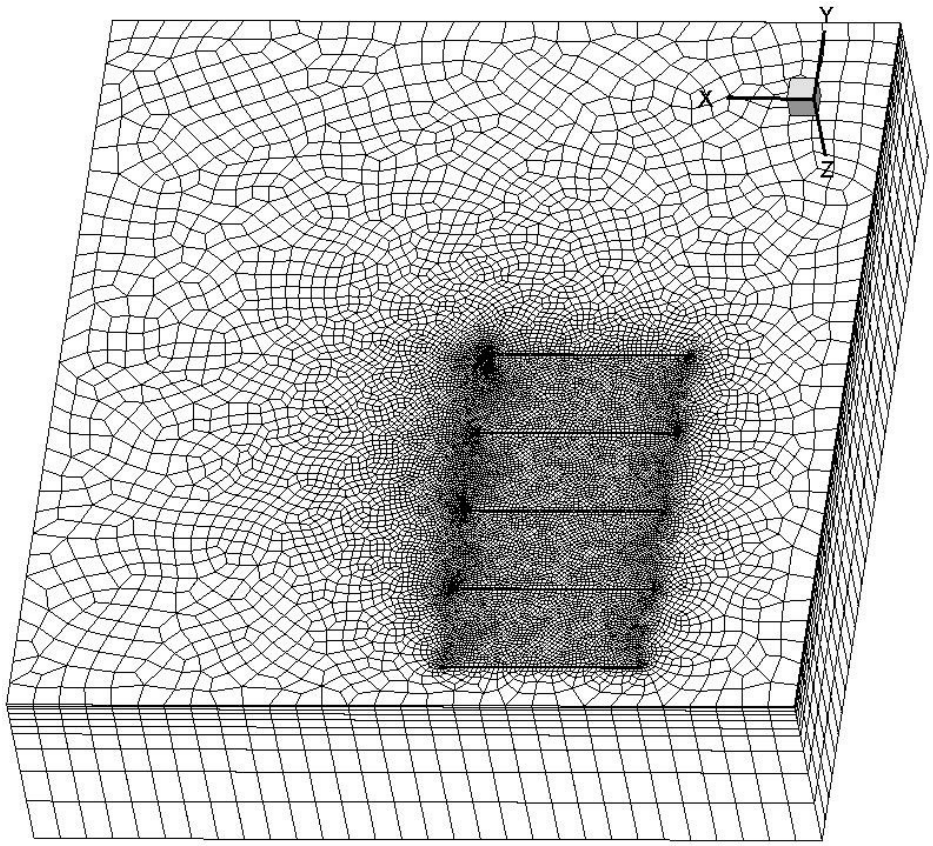

Figure 4-15. The numerical mesh for 3D fracture model. Only one eighth of the region is modelled due to symmetry in respect to XY, YZ and XZ planes.

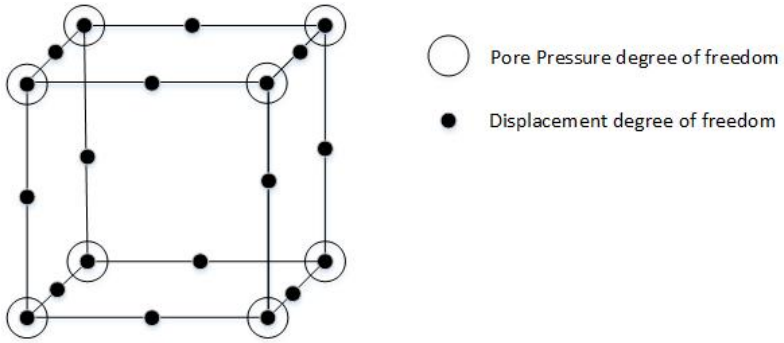

Figure 4-16. Degrees of freedom for 20-node hexahedron used in this model

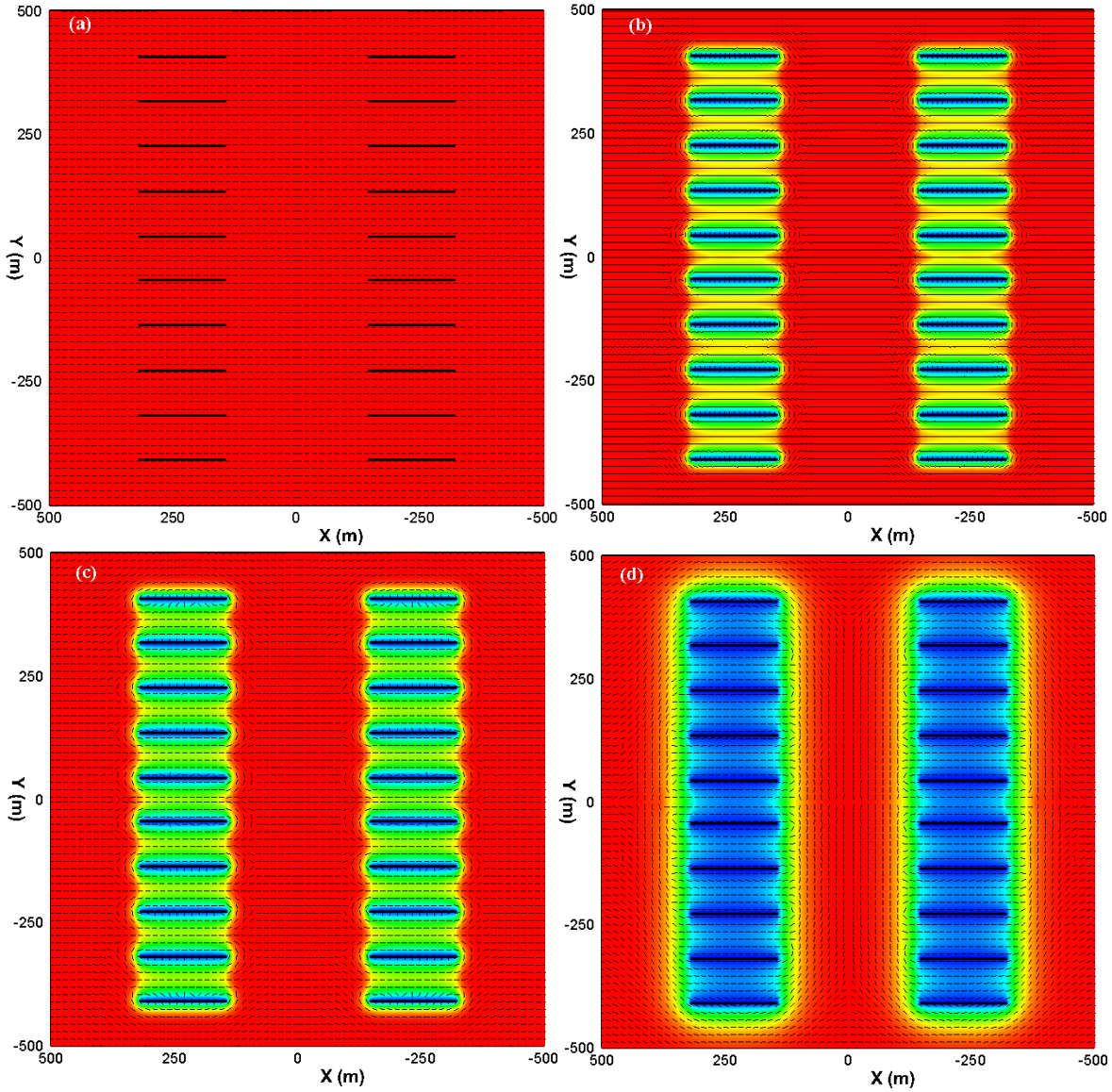

Figure 4-17. Evolution of pore pressure and maximum principal stress (maximum compressive stress) directions from fluid production after a) 0; b) 6 months; c) 9 months; d) 7.5 years of production

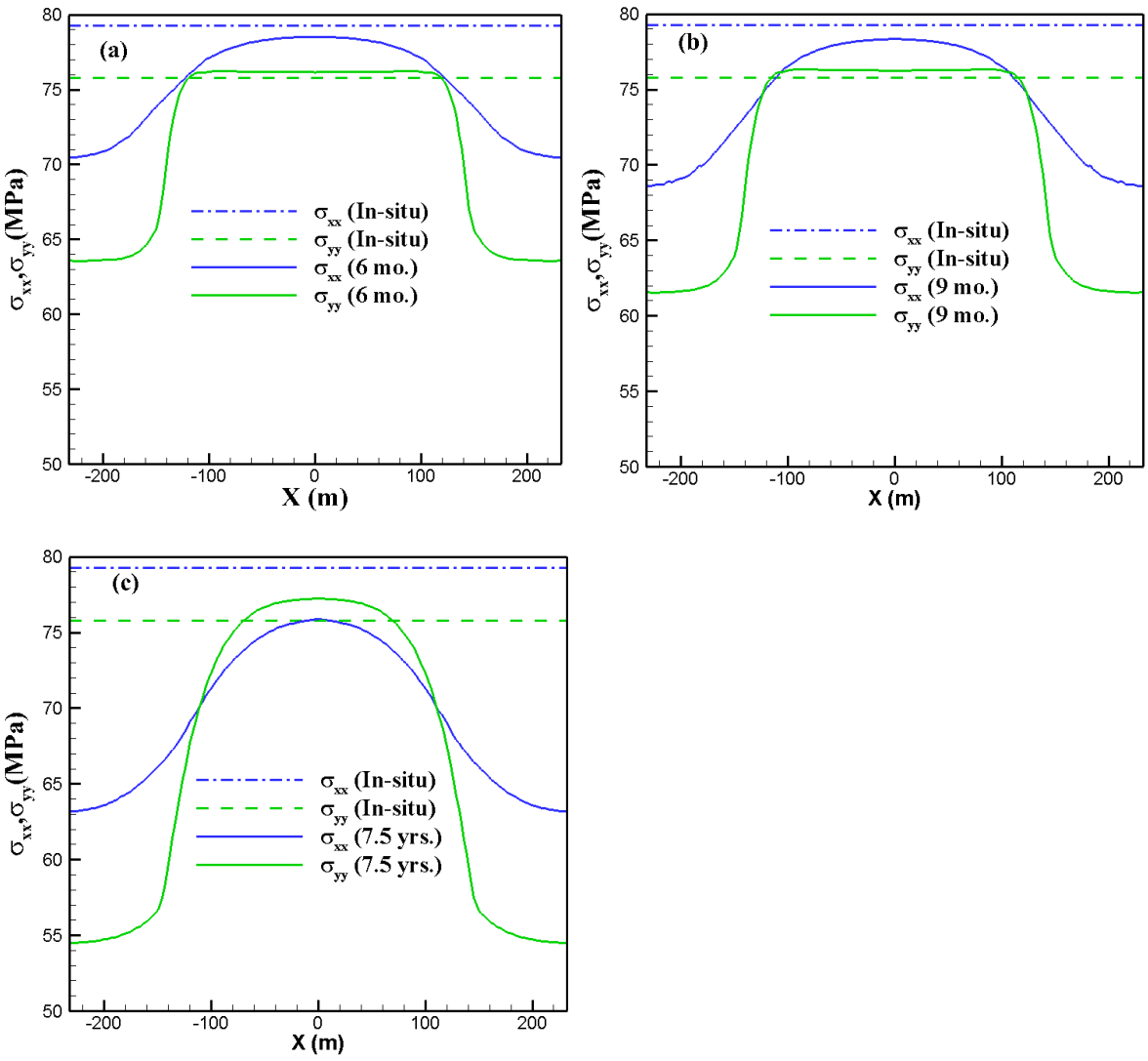

Figure 4-18. Total stress in X and Y directions in the infill region between two horizontal wells a) at t=0; b) after 6 months; c) after 9 months; d) after 7.5 years of production.

Over time the pore pressure gradient penetrates a larger area of the reservoir, consequently the ellipse expands and from Figure 4-17b to Figure 4-17c we can observe the principal directions have changed in a larger area around the fractures. After considerable time has passed, as in Figure 4-17d which shows the depletion pattern after 7.5 years of production, the pore pressures in the SRV zone equilibrate and the gradient of pore pressure will be very small in this region. Now we can assume all ten fractures along each horizontal well as one

fracture with its length equal to horizontal well length in y direction. The orthoradial pattern of maximum principal stress now will form around this huge fracture and causes the infill area to have principal stresses parallel to Y direction.

The maximum principal stress pattern in Figure 4-17 can also be used to figure out the directions along which fractures might propagate at different times and predict potential orientations of hydraulic fractures in infill wells. This is a useful tool to plan the optimum infill well drilling locations and time.

In Figure 4-18 the total horizontal stresses in X and Y direction are shown in the infill region at different times. The horizontal stress, σ_{xx}, is shown to be decreasing over time. Due to pore pressure reduction around the fractures, the total stress σ_{xx} decreases while the effective stress increases. The region next to faces of fracture experiences tension as fracture causes the reservoir rock to pull inward.

In Figure 4-18, it's also observed that σ_{yy} is increased slightly from its original in-situ value in the infill region. The stresses in Y direction in SRV region are decreasing due to the production from fractures. The decrease in the stresses could cause the infill region stresses in Y direction to increase so that total in situ stresses are carried by the reservoir. Over time, these stresses equilibrate and everywhere in the reservoir, σ_{yy} will be smaller compared to its original in situ magnitude.

Figure 4- 19 shows the evolution of stresses at a point halfway between two horizontal wells. The induced stress contrast is also shown in this figure. As discussed above, stresses in X direction decrease while in Y direction, stresses initially increase and then decrease after about 6 years of production. After about 4 years from start of production, the principal stress direction changes from X to Y direction due to the sharp decrease of stresses in X direction

compared to the Y direction. When the induced stress exceeds 500 psi, the reorientation of principal stresses takes place and after that time, YY will be the principal direction.

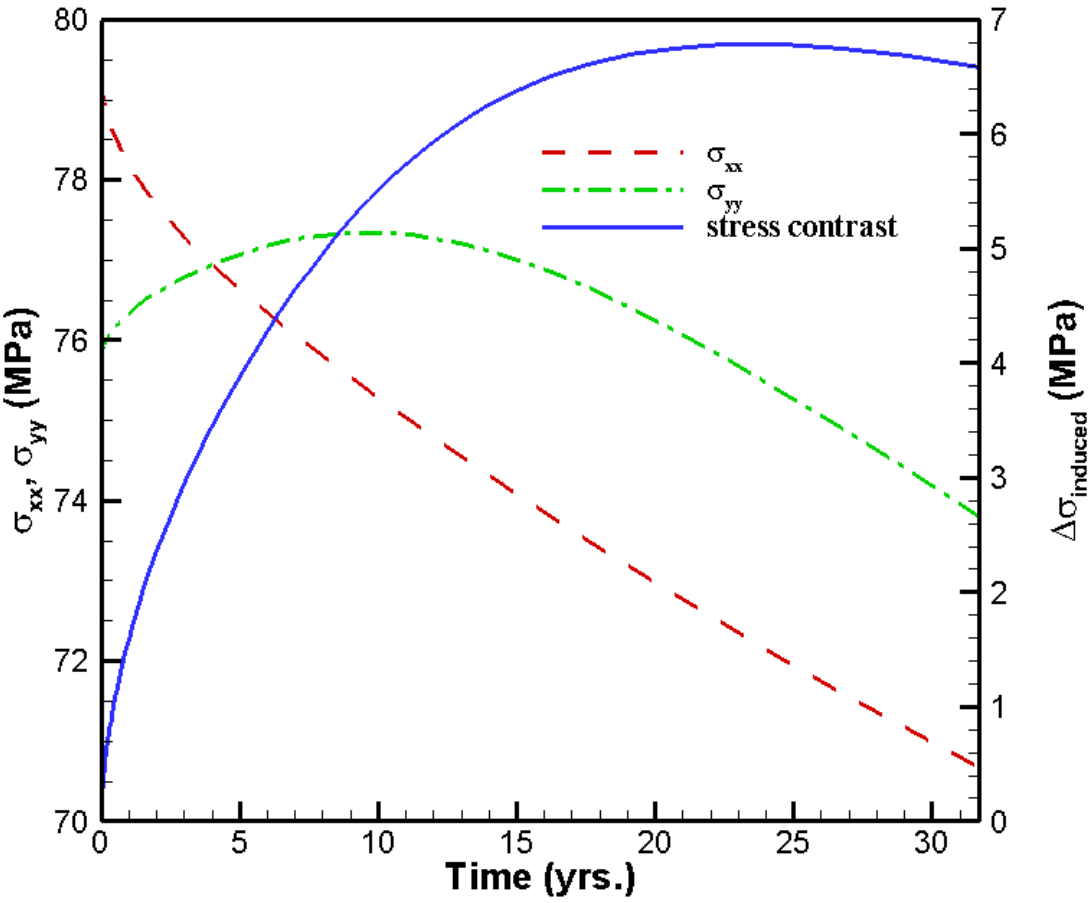

Figure 4-19. Horizontal stresses at a point in the infill region over time. Induced stress contrast is also plotted in this figure.

Results from current work and previous studies on a single fracture, confirm that total stress component parallel to a fracture (in X direction) reduces faster than the orthogonal direction (Y direction) as a function of time (Siebrits et al., 1998).

4.6 Case 4: Production from multiple fractures in a layered reservoir

4.6.1 Introduction

Well-to-well interference or communication between a primary production well (or "Parent" well) and the in-fill well (or "child" well) is one of the main concerns in horizontal wells refracturing, because it results in productivity reduction of both the wells. This section presents a geomechanical modeling and analysis to better understand the problem of "frac-hits" during infill fracturing.

4.6.2 Model description

For the numerical example in this section, we study production from a shale formation having five layers as shown in Figure 4-20. The poroelastic properties of the layered reservoir are summarized in Table 4-4 (Kumar et al., 2018). The reservoir rocks in each layer is assumed to be a homogenous, isotropic medium with uniform permeability. A 3D schematic of the parent well and the proposed location of the child well is shown in Figure 4-21a. Reservoir domain is 1220×1220×99.85 m. A horizontal cross-section of the parent well fractures and proposed location of the child well in the central XY-plane are shown in Figure 4-21b. The child well is located at a distance of 200 m from production well. The dash-dotted "blue line" shows a location in between the parent and child well (i.e., at Y =140 m) where depletion induced pore pressure and stress change orthogonal to the production fractures are evaluated; whereas, the dotted "green line" shows the location of a potential child well hydraulic fracture. The in-situ stress state of the reservoir is in the normal faulting regime. The minimum horizontal (σ_h) and maximum horizontal (σ_H) in-situ stresses are acting along the X- and Y-axes, respectively, and the vertical in-situ stress (σ_V) is acting along the Z-axis. Both, the parent and child wells are drilled parallel to the minimum horizontal stress (σ_h)

direction (i.e., along the X-axis in this case) and the production fractures are assumed planar and orthogonal to the wellbore axis (i.e., parallel to the YZ-plane). A single fracturing stage with six clusters spaced 25 m apart is considered. In each cluster, one fracture is propagated. The production fractures are fully propped with initial uniform fracture aperture equal to 2.0 mm. Each production fracture has half-length equal to 90 m and fracture height equal to 60 m. The in-situ stresses and fluid properties are listed in Table 4-5. Each fracture is explicitly modeled with an unstructured fine grid. Grid refinement is particularly important in areas with large pressure gradients such as in the vicinity of fractures. A horizontal well with a diameter of 0.152 m (6 inches) intersects each fracture and a bottomhole pressure of 10.5 MPa is applied at each intersection node as a boundary condition. Fluid phase is assumed to be isothermal, single phase and slightly compressible. Permeability is assumed to be isotropic. Due to symmetry in the YZ- and XZ-planes, only $\frac{1}{4}^{th}$ of the geometry is modeled and the plane of symmetry boundary conditions are applied on the XZ- and YZ-planes. The outer boundaries of the model are considered as "no flow" boundaries. Zero normal displacements are assigned to all outer boundaries except for the top boundary. The linear 8-node hexahedral elements are used for domain discretization. A stimulated reservoir volume (SRV) is modeled with the dimensions of 175 m x 230 m x 60 m as shown by "colored" region in Figure 4-21b and a permeability of 15 times higher than the reservoir layer permeabilities is assigned to the SRV region to capture the enhanced permeability in the region next to propped fractures. In this simulation example, an optimum configuration for the SRV region is considered where the entire region between hydraulic fractures is activated as fracture network. Hydraulic fracture properties are presented in Table 4-6.

The finite element mesh consists of 787,636 nodes and 749,700 elements. The initial time step is 62,700 s and it is increased by a factor of 1.1 at subsequent steps.

Production from the parent well fractures is carried-out at a constant bottomhole pressure (BHP) of 10.5 MPa for 2 years. In the figures presented in this section, the positive sign of stresses represents compression and negative sign represents tension. The depletion-induced reservoir pore pressure will affect both the total and effective reservoir stresses and are studied next.

4.6.3 Impact of Reservoir Depletion on the Total Stresses

The reservoir pore pressure and the total stresses distribution after 2 years of production are shown in Figures 4-22a, b, c and d, respectively. The reservoir pore pressure and the total stress are presented for a section of the reservoir volume in the vicinity of the parent well fractures. The reservoir pore pressure distribution is shown in Figure 4-22a, which demonstrates an ellipsoidal depletion zone formed around the production fractures. In this elliptical zone, pore pressure changes from minimum of 10.5 MPa at wellbore location to 50.38 MPa original pore pressure. The impact of reservoir depletion on the total horizontal stress component σ_{xx} is shown in Figure 4-22b indicating a decrease of 9.2 MPa (i.e., from in-situ value of 54.2 to 45.0 MPa). The impact of reservoir depletion on the total horizontal stress component σ_{yy} is shown in Figure 4-22c, which shows that its value has decreased to 46.0 MPa in the depletion zone from its original value of 57.5 MPa. Figure 4-22d shows that the vertical stress σ_V is decreased to 67.0 MPa from 72.83 MPa. Depending on the reservoir initial stress state, the depletion induced stress change might alter the stress regime. An assessment is carried out for the status of stress regime after 2 years of production time. The

difference between the vertical stress and minimum horizontal stress ($\sigma_V - \sigma_h$) and the maximum horizontal stress ($\sigma_V - \sigma_H$) are shown in Figure 4-23a and 4-23b, respectively. Positive values of the difference between the vertical and total horizontal stresses show that the reservoir stress state is still in the normal faulting regime (i.e., $\sigma_V > \sigma_H > \sigma_h$).

Another perspective of the reservoir pore pressure and the total stresses change is presented using a horizontal cross-section in the central XY-plane as shown in Figure 4-24. The reservoir pore pressure distribution and the local maximum principal stress trajectories after 2 years of production time are shown in Figure 4-24a. The pore pressure distribution plot shows an elliptical depletion zone around the production fractures. A significant reorientation of the stress state in the vicinity of production fractures has occurred. The total horizontal stress components σ_{xx} and σ_{yy} have decreased from their in-situ values around the production fractures (Figure 4-24b and Figure 4-24c). The plot of ($\sigma_{yy} - \sigma_{xx}$) in Figure 4-24d is shown to evaluate the stress reversal. If the stress contrast is negative, the magnitude of the maximum horizontal stress becomes less than the minimum horizontal stress and stress reversal takes place. As we can see from this figure, no negative values of stress contrast are observed. So, stress reversal doesn't happen.

4.6.4 Impact of Reservoir Depletion on the Effective Stresses and displacements

The impact of reservoir depletion on the effective stresses are presented in this section. A 3D visualization of the effective horizontal stress components σ'_{xx} and σ'_{yy}, and the effective vertical stress σ'_{zz} are shown in Figures 4-25a, b, and c, respectively. Due to reservoir depletion both the pore pressure and the total stress components are decreasing; However, the rate of pore pressure decrease is higher than the total stresses reduction. Hence, the resultant effective stress components ($\sigma'_{ij} = \sigma_{ij} - \delta_{ij}\alpha p$) are increasing. For example, in this case

after 2 years of production, at wellbore level, the maximum value of the effective horizontal stress component σ'_{xx} has increased to 36.0 MPa from its in-situ value of 21.4 MPa, the maximum value of effective horizontal stress component σ'_{yy} has increased to 39.1 MPa from its in-situ value equal to 24.8 MPa, and maximum value of effective vertical stress σ'_{zz} has increased to 59.3 MPa from its in-situ value equal to 40.2 MPa. The increase of the effective stresses results in increase of the reservoir rocks displacements around the parent well fractures. The reservoir rock displacements along X and Y axes are shown in Figures 4-26a and 426b, respectively. Figure 4-26c, depicts the magnitude of displacements and the "black" arrows show the resultant displacement directions. From Figure 4-26c, it can be observed that the reservoir rock is compressed in both the X and Y directions. A temporal variation of the resultant displacement along the parent well axis is shown in Figure 4-26d, which shows that reservoir compression is increasing with production time.

4.6.5 Impact of Production Time on Reservoir Pore pressure and Total Stresses

Figure 4-27 shows the temporal variation of the reservoir pore pressure, total horizontal stress components σ_{xx} and σ_{yy}, and the horizontal stress contrast $\Delta\sigma = (\sigma_{yy} - \sigma_{xx})$ along a line orthogonal to the parent well fractures in the central XY-plane (i.e., along the dash-dotted "blue line" in Figure 4-21b). With the increase in the production time, the reservoir pore pressure decreases (i.e., Figure 4-27a) resulting in the decrease of both the horizontal stress components σ_{xx} (Figure 4-27b) and σ_{yy} (Figure 4-27c). However, the stress component parallel to the production fractures (σ_{yy}) decreases at a higher rate as compared to the horizontal stress component perpendicular to the production fractures (σ_{xx}). For example, in this case after 2 years of production, the horizontal stress component σ_{yy} has decreased to 47.89 MPa from its in-situ value equal to 57.72 MPa (i.e., 17% reduction from

the in-situ value); whereas, the stress component σ_{xx} has decreased to 46.15 MPa from its in-situ value equal to 54.3 MPa (i.e., 15% reduction from the in-situ value). The contrast in the reduction of horizontal stresses may result in rotation of the principal stresses and lead to development of stress reversal zones as indicated by negative values in Figure 4-27d. It should be noted that in this case, the reservoir pore pressure and stress changes are occurring due to the combined effect of the mechanical closure of the production fractures and the depletion-induced poroelastic effect. From Figure 4-27b, it can be observed that in the early production time (i.e., 17 hrs. or 3.5 days) the stress component perpendicular to the parent well fractures, σ_{xx}, has increased from its in-situ value near the production fracture tips. When a fracture is producing the faces of fracture experience tension and fracture tips experience compression. The production induced stresses are opposite in sign to those when a fracture is propagated. In the latter case, the tips of fracture experience tension while its faces experience compressive stress. As a result of production, the horizontal stress component σ_{xx} has increased near the production fractures tips.

To investigate the impact of depletion-induced stress on subsequent child well fracture propagation paths, consider Figure 4-28 where the time variations of the reservoir pore pressure, the total horizontal stress components σ_{xx} and σ_{yy}, and the horizontal stress contrast in the central XY plane and parallel to the parent well fractures are presented (i.e., along the dashed "green line" in Figure 4-21b). It can be observed that with production time, an anisotropic reduction in the reservoir pore pressure is occurring (Figure 4-28a), which causes a heterogeneous reduction of the total horizontal stresses (Figures 4.28b and 4.28c). However, except for the region close to fracture tips, the stress component parallel to the production fractures (σ_{yy}) decreases at a higher rate as compared to the stress component perpendicular to the

production fractures (σ_{xx}). If a child well is drilled at a time and location where Δσ is negative, its fractures will turn away from the parent well fracture tips. As a result of stress reorientation, the child well fractures will turn away from the parent well fractures tips. It is observed that in areas very close to the production fracture tips (horizontal dashed line in Fig. 4-28d), the horizontal stress contrast values have increased and in fact their values are greater than the in-situ stress contrast value (i.e., 3.4 MPa in this case), which is the result of fracture closure.

4.6.6 Comparison of pore pressure from two modelling approaches

In this section, the results of simulation of two modelling approaches for hydraulic fracture have been compared. In the first approach which is used throughout this thesis, hydraulic fracture is modelled explicitly using elements with higher permeability (150 md) and smaller Young modulus (80% of reservoir rock *E*). In the second approach, hydraulic fracture is simulated as a joint or closed fracture with normal and shear stiffnesses using a boundary element method-based model, which can implicitly account for the stress shadowing effect among the production fractures. A description of the latter modeling approach is given in Masouleh et al. (2020). Pore pressure and stresses along a line parallel to production well (the blue line in Figure 4-21b) is compared for the two models in Figure 4-29. The maximum difference in pore pressure is about 8.6%, stresses in X direction 2.6%, stresses in Y direction 1.7% and stresses in Z direction 1.9% which implies that using explicit fracture model is an acceptable alternative with a significant reduction in computational effort. In fact, the effect of the stress shadowing on the pore pressure change is very localized in between the production fractures and we can barely notice an impact in the infill well zone.

4.7 Conclusions

A poroelastic 3D numerical model was developed to understand production induced stress reorientation in several cases including a single vertical well, a single fracture and a producing shale oil reservoir with multiple wells and fractures. The induced poroelastic stresses interact with initial in situ stresses to reorient the stresses away from their original principal directions. The change of principal directions is time and space dependent.

The present model is a valuable tool in determining the stress trajectories from which possible fracture orientations for infill drilling can be determined.

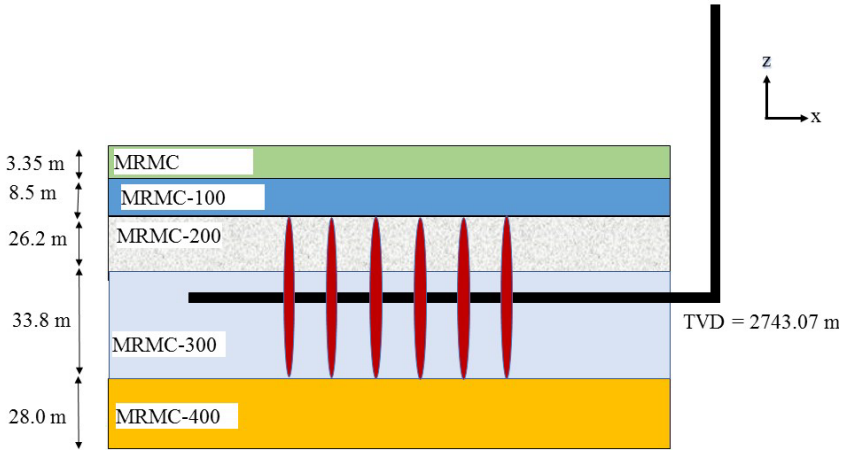

Figure 4-20. A vertical cross-section of the reservoir rock layers. Parent well fractures are assumed to be fully contained in the MRMC-200 and MRMC-300 layers.

Table 4-4. Physical properties of the reservoir rocks in different layers.

Parameter	MRMC	MRMC-100	MRMC-200	MRMC-300	MRMC-400
Layer thickness, d (m)	3.35	8.5	26.2	33.8	28.0
TVD of layer top, h (m)	2396.22	2699.57	2708.07	2734.27	2773.07
Young's modulus, E (GPa)	57.28	56.88	53.57	53.64	60.1
Poisson's ratio (ν)	0.29	0.29	0.29	0.29	0.29
Permeability, k (μd)	0.07	1.84	3.04	2.96	1.84
Matrix porosity, ϕ (%)	2.1	3.6	4.5	4.0	3.3
Biot's coefficient, α	0.65	0.65	0.65	0.65	0.65

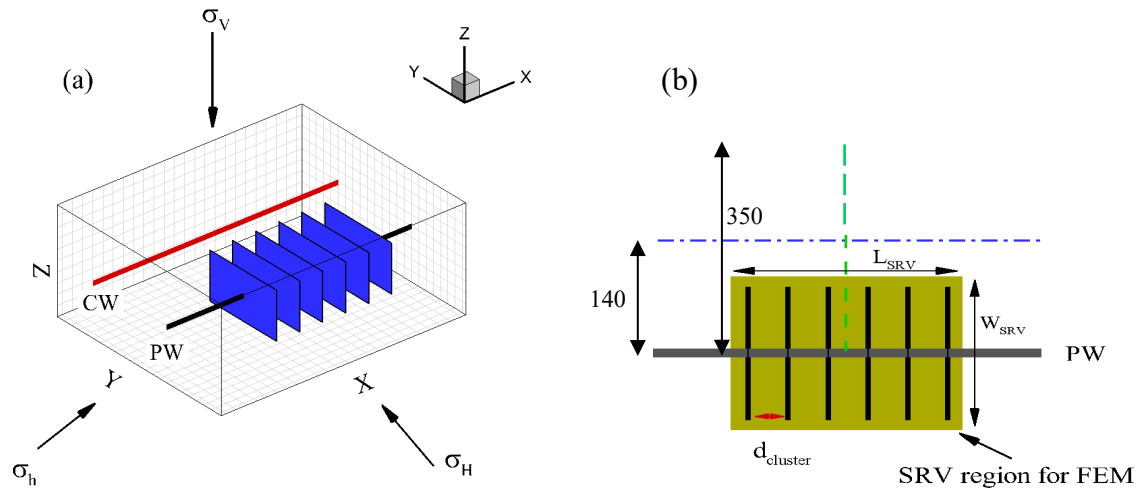

Figure 4-21. (a) A 3D schematic and (b) plan-view of reservoir showing "Parent" and "Child" well system (PW: Parent well; CW: Child well). Each production fracture has half-length = 90 m, height = 60 m and cluster spacing $d_{cluster}$= 25 m. The colored region around the "Parent" well fractures represents the stimulated reservoir volume (SRV) region for the finite element modeling. L_{SRV}=175 m, W_{SRV} = 230 m, H_{SRV} = 60 m

Table 4-5. Fluid properties and in-situ stresses.

Parameter	**Value**
Fluid viscosity, μ (Pa.s)	2.5×10^{-4}
Fluid bulk modulus, K_f (MPa)	2.0×10^{9}
Vertical stress (σ_V) gradient, (MPa/m)	0.0266
Max. horizontal stress (σ_H) gradient, (MPa/m)	0.0210
Min. horizontal stress (σ_h) gradient, (MPa/m)	0.0198
Reservoir pore pressure (p) gradient, (MPa/m)	0.0184
Bottomhole pressure, (MPa)	10.5

Table 4-6. Hydraulic fracture properties

Parameter	**Value**
Fracture stages	6
Fracture spacing, (m)	25
Fracture conductivity, (md.ft)	100
Fracture half-length, (m)	90
Fracture height, (m)	60
Fracture aperture, (m)	2×10^{-3}
SRV dimensions, (m×m×m)	175 × 230 × 60

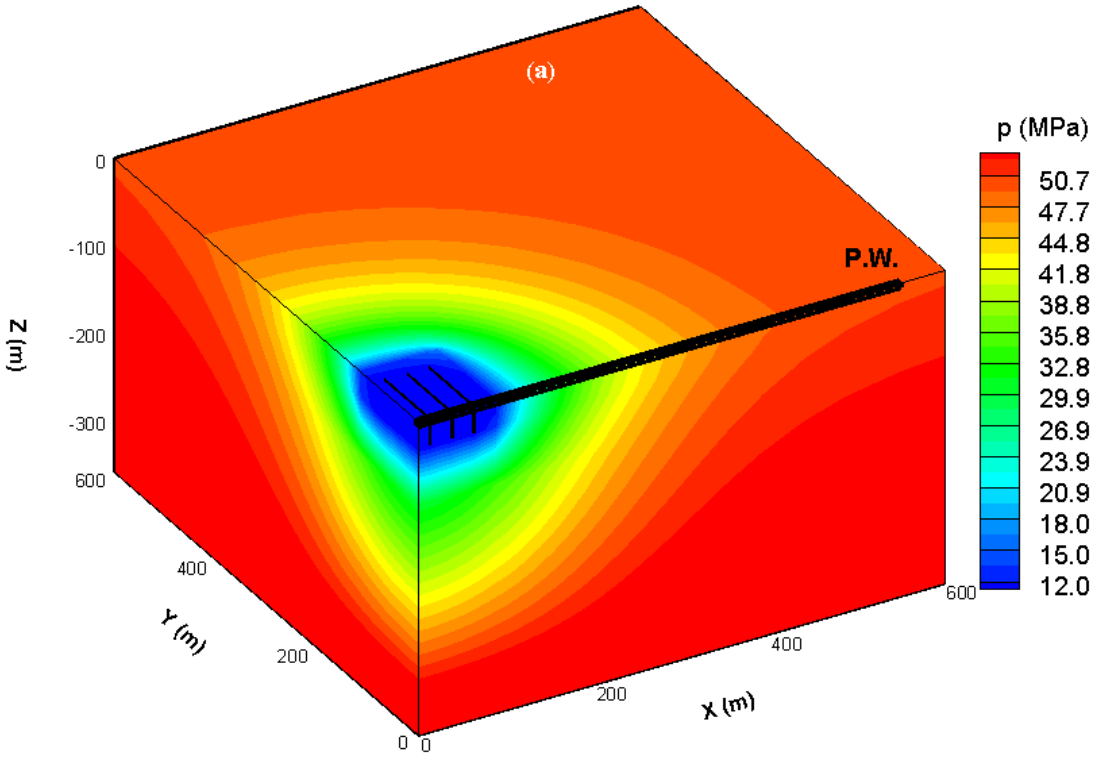
(a)
p (MPa)
50.7
47.7
44.8
41.8
38.8
35.8
32.8
29.9
26.9
23.9
20.9
18.0
15.0
12.0
P.W.
Z (m)
0
-100
-200
-300
600
400
200
0
Y (m)
X (m)

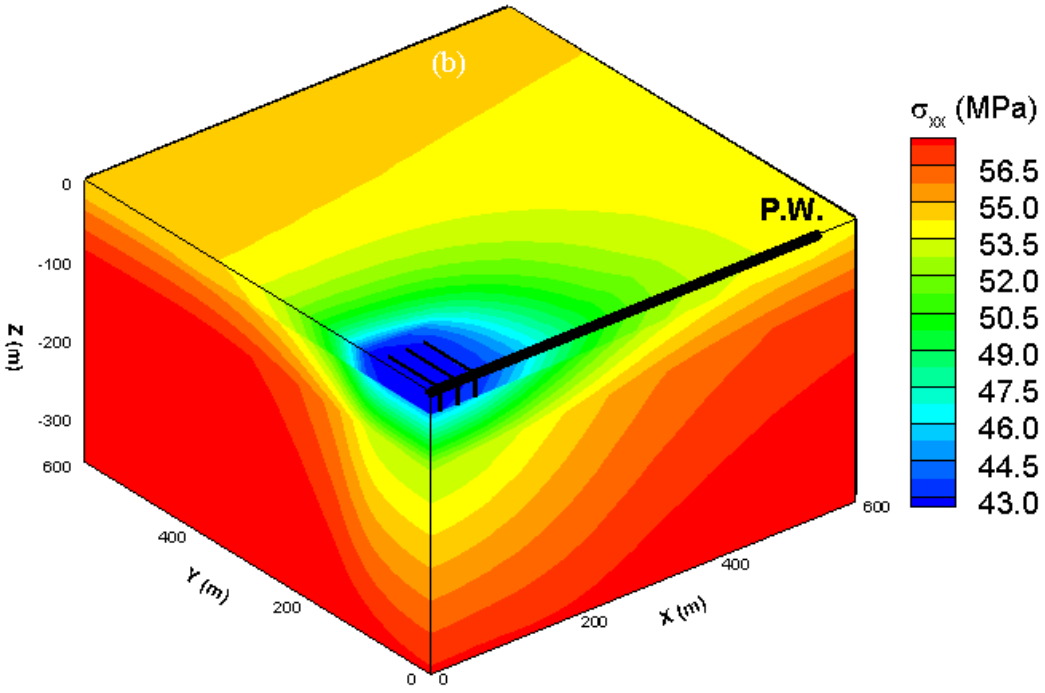
(b)
σxx (MPa)
56.5
55.0
53.5
52.0
50.5
49.0
47.5
46.0
44.5
43.0
P.W.
Z (m)
0
-100
-200
-300
600
400
200
0
Y (m)
X (m)

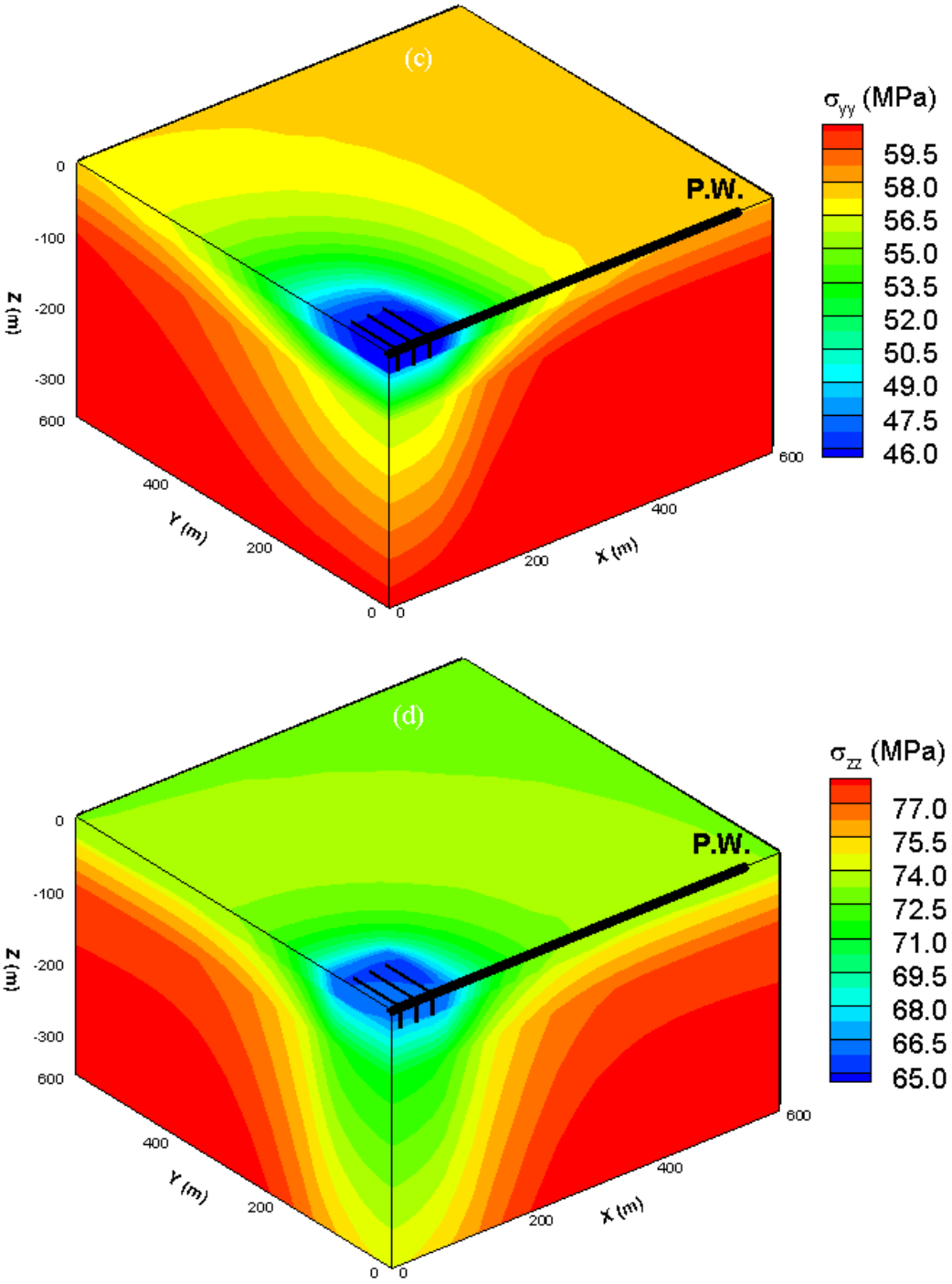

Figure 4-22. A 3D visualization of the reservoir pore pressure and total stress changes around "Parent" and "Child" wells after 2 years of production, (a) pore pressure, (b) horizontal stress component σ_{xx}, (c) horizontal stress component σ_{yy}, (d) the vertical stress σ_{zz}. Reservoir pore pressure is decreasing in an expanding ellipsoidal shape around the production fracture resulting in a decrease of all three total stress components. In-situ reservoir pore pressure and stresses at the wellbore level: p_0 = 50.38 MPa, $\sigma_V = 72.83$ MPa, $\sigma_H = 57.50$ MPa, $\sigma_h = 54.21$ MPa. It should be noted that pore pressure and stress gradients with formation depth are considered in the model.

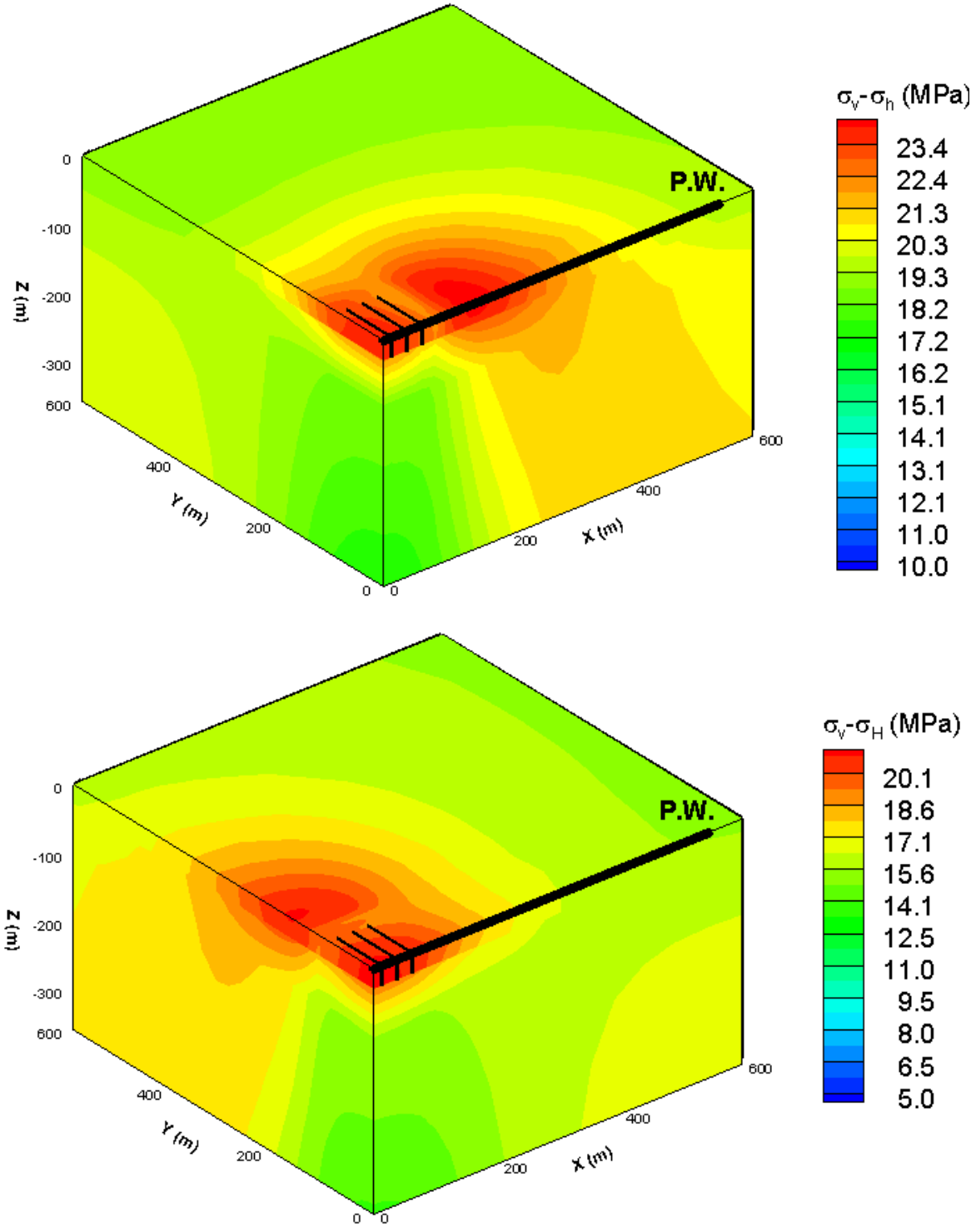

Figure 4-23. (a) Difference of the vertical stress and minimum horizontal stress ($\sigma_V - \sigma_h$), (b) difference of the vertical stress and maximum horizontal stress ($\sigma_V - \sigma_H$) . Positive values of difference between the vertical and horizontal stresses show that after 2 years of the production, the reservoir stress state is still in the normal faulting regime (i.e., $\sigma_V > \sigma_H > \sigma_h$).

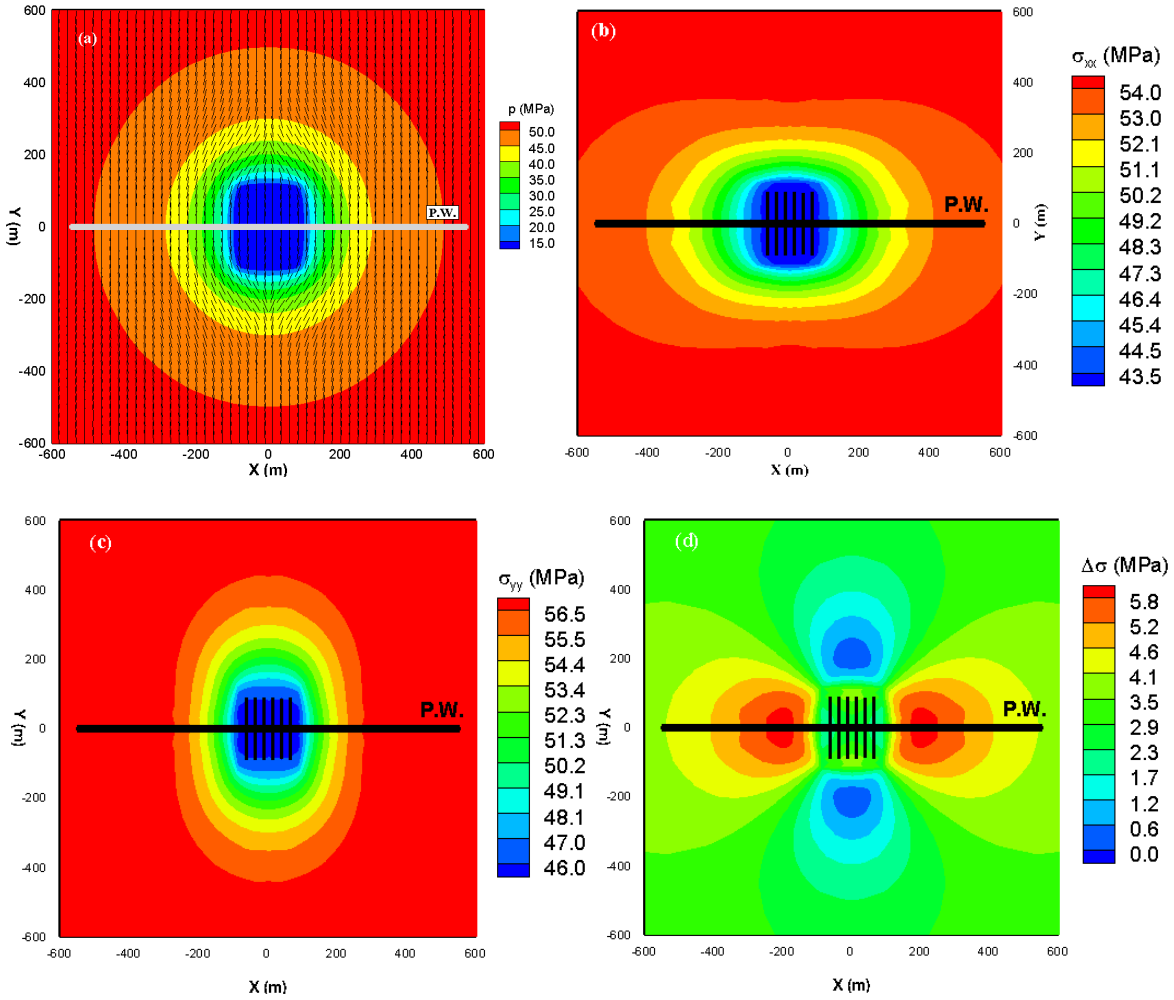

Figure 4-24. Reservoir pore pressure and total stresses distribution in a horizontal cross-section in the central XY-plane after 2 years of production: (a) reservoir pore pressure distribution (black lines are trajectories of the local maximum principal stress), (b) horizontal stress component σ_{xx}, (c) horizontal stress component σ_{yy}, (d) horizontal stress contrast, $(\sigma_{yy} - \sigma_{xx})$ distribution.

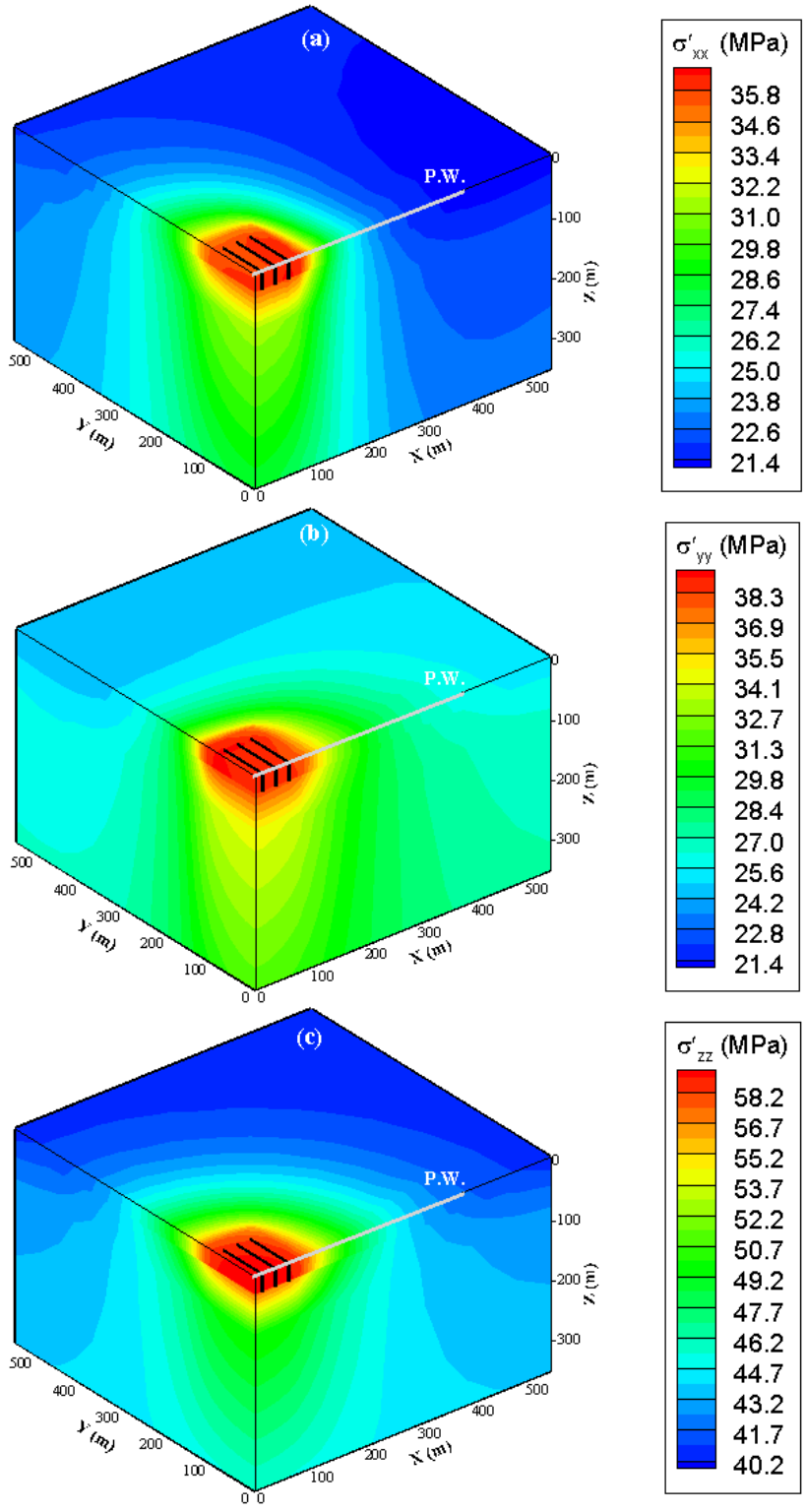

Figure 4-25. A 3D visualization of effective stress change around the production well after 2 years of production: (a) effective horizontal stress component σ'_{xx}, (b) effective horizontal stress component σ'_{yy}, (c) effective vertical stress σ'_{zz}. In-situ effective stresses at the wellbore level: $\sigma'_V = 40.2$ Mpa, $\sigma'_H = 24.8$ MPa, $\sigma'_h = 21.4$ Mpa.

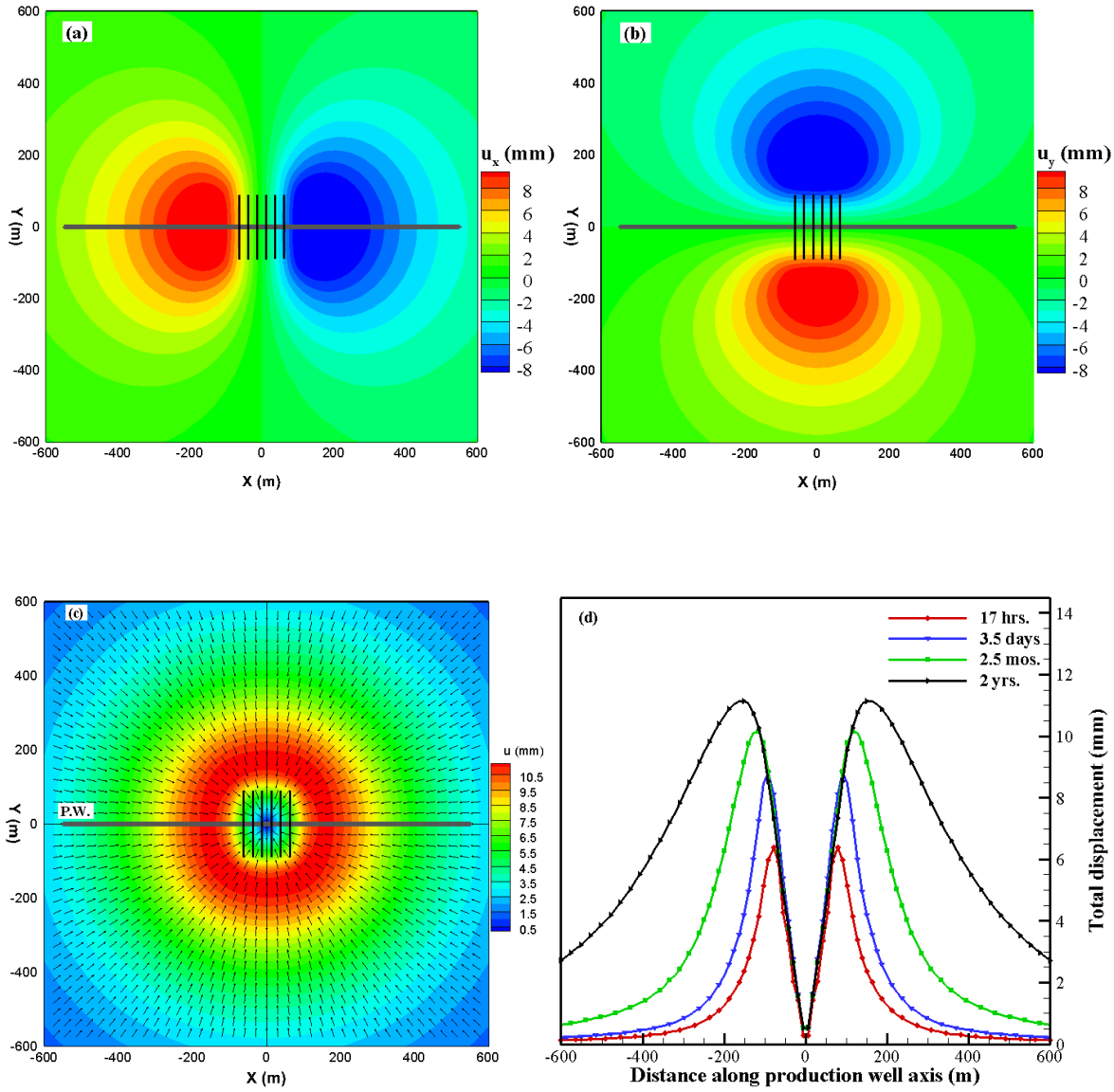

Figure 4-26. Depletion-induced reservoir displacements after 2 years of production: (a) displacement along wellbore axis (along X-axis), and (b) displacement perpendicular to the wellbore axis (along Y-axis), (c) resultant displacement; vectors show resultant displacement directions, and (d) time variation of the resultant displacement along the production well axis.

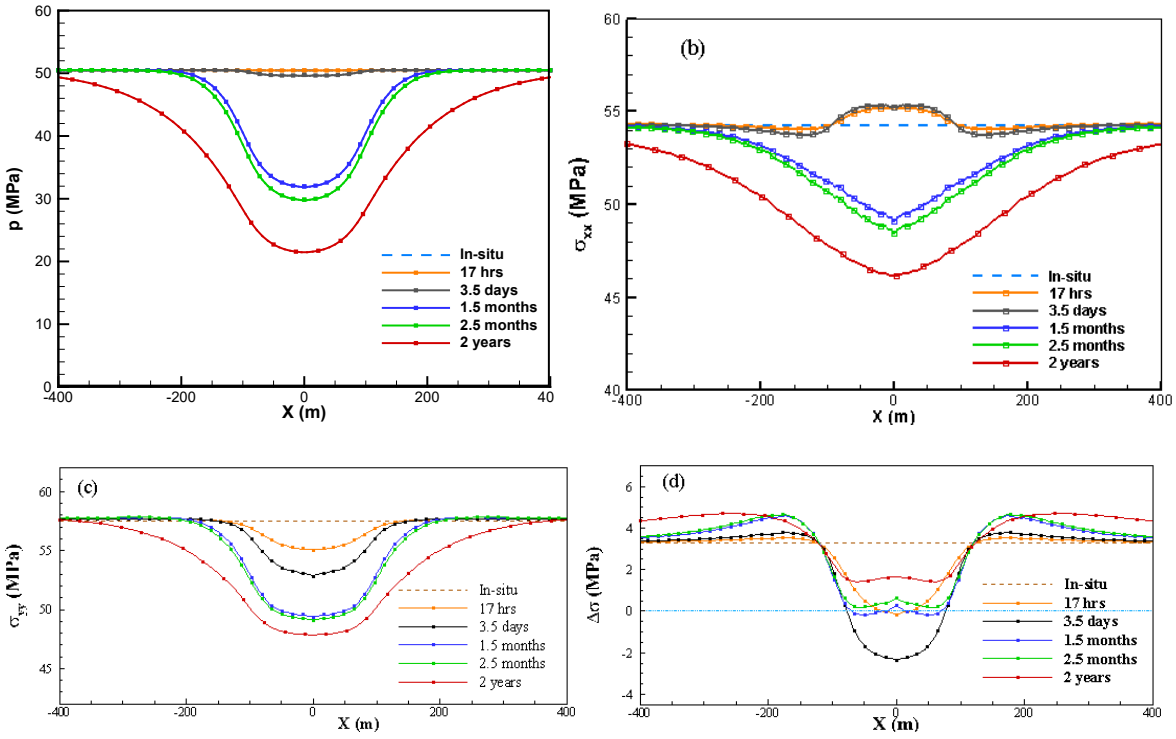

Figure 4-27. A time variation of: (a) reservoir pore pressure, (b) horizontal stress component σ_{xx}, (c) horizontal stress component σ_{yy} , and (d) horizontal stress anisotropy (σ_{yy}-σ_{xx}) along a line parallel to production well (dash-dotted "blue line" in Figure 4-21b). Negative values of the stress anisotropy show stress reversal zones. The extent of the stress reversal zone is increasing with production time.

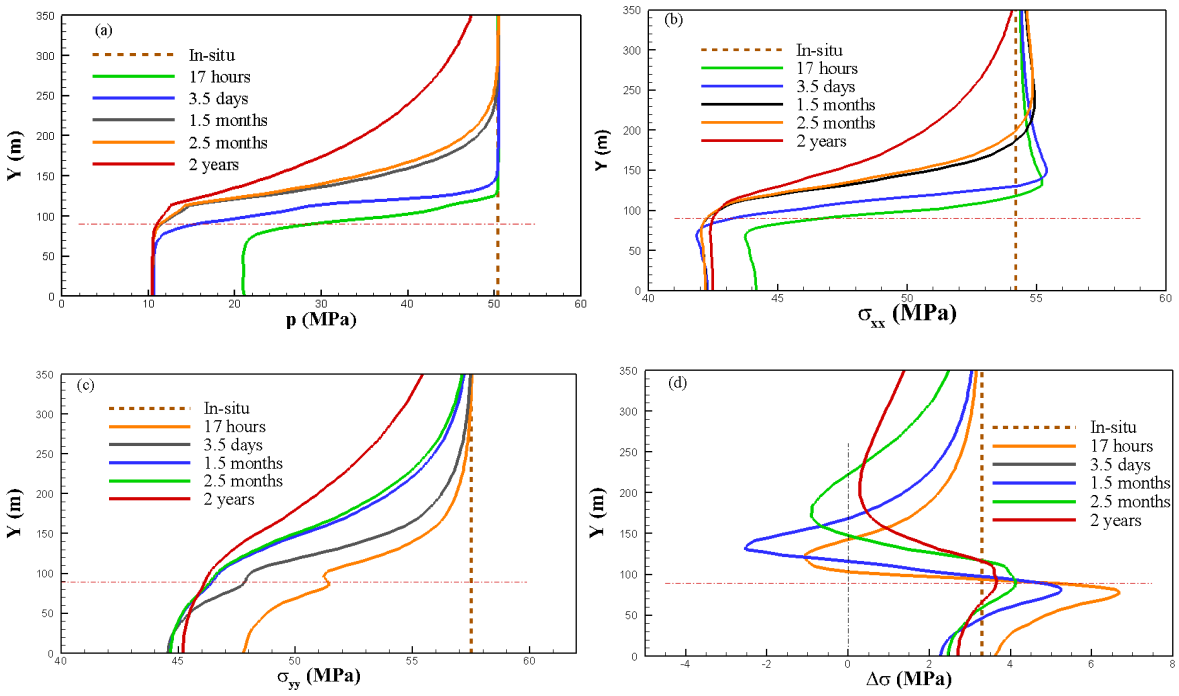

Figure 4-28. A time variation of: (a) reservoir pore pressure, (b) horizontal stress component σ_{xx}, (c) horizontal stress component σ_{yy} , and (d) horizontal stress anisotropy (σ_{yy}-σ_{xx}) along the potential propagation path of the child well fractures (along dotted "green line" in Figure 4-21b) in the central XY-plane. The dash-dot "red line" shows location of the parent well fracture tips.

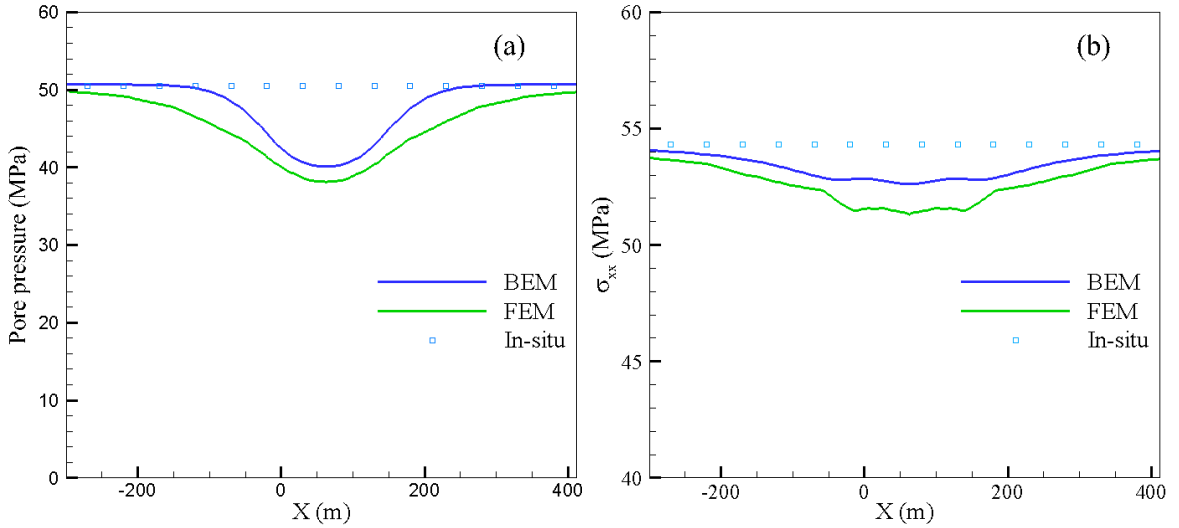

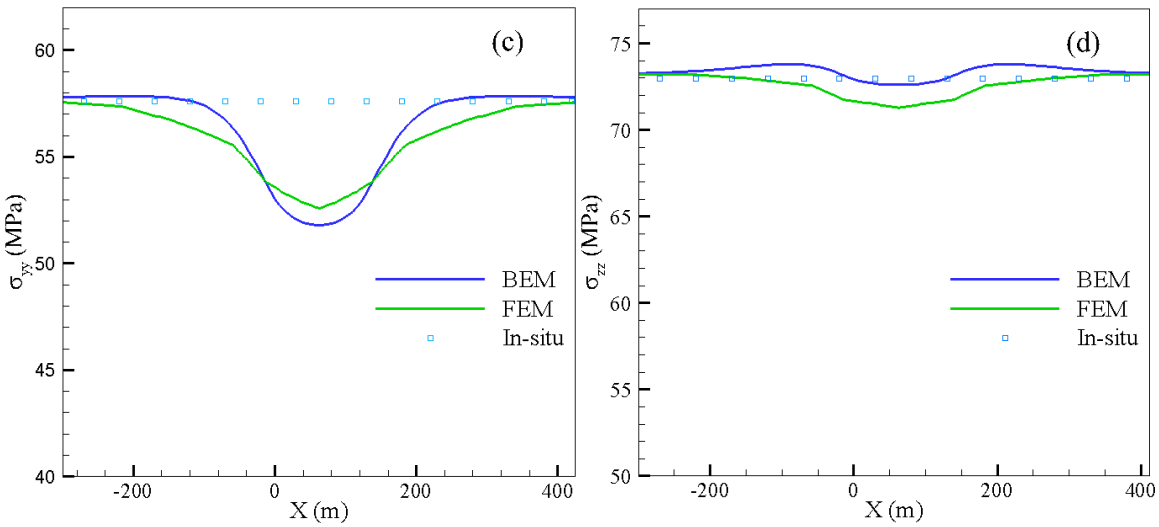

Figure 4-29. Pore pressure and stress difference between explicit fracture model and joint model considering stress shadow.

5. Isothermal Two-phase flow in the reservoir

5.1 Introduction

Numerical simulation of multiphase flow in deforming porous media is of significant interest in diverse range of engineering fields including nuclear waste disposal (Fall et al. 2014), geologic sequestration of CO_2 (Rutqvist et al. 2007), groundwater contamination in subsurface systems (Rahman et. al 1999), consolidation analysis of partially saturated soil (Khoei et al. 2011), wellbore stability and sand production (Wang and Lu 2001), reservoir compaction and surface subsidence due to production (Schrefler 2001, Lewis et al. 1993), waterflooding (Hwang et al. 2015) and hydraulic fracturing (Ji et al. 2009). Due to recent interest in hydraulic fracturing in oil and gas reservoirs, coupled multiphase flow is even of more significance today.

In traditional reservoir simulators, geomechanical effects are represented by pore compressibility. It is assumed that porosity changes with reservoir pressure in a linear manner. The slope of this line is called pore compressibility which is the only geomechanical parameter in traditional reservoir simulators and is assumed constant during the simulation (Minkoff et al. 2003, Mainguy et al. 2002). However, this parameter is not an intrinsic property of rock and can change due to loading history and boundary conditions.

Modeling poroelastic multiphase flow can be done in three ways (Kim et al. 2013, Jha and Juanes 2014, Mikelic et al. 2013, Wan 2002); fully implicit (fully coupled or monolithic), sequentially implicit (iterative coupling) and loosely coupled (explicit coupling). In the fully implicit method, coupled system of equations are solved simultaneously, commonly using Newton-Raphson or Picard method. In sequentially implicit coupling, separate modules are used for flow and geomechanics. Each module solves its own governing equations and at

each iteration the coupling variables are exchanged. In explicit coupling method, flow calculations are performed every time step and displacements are calculated only during selected time steps (Dean et al. 2006, Minkoff et al. 1999). This method is less accurate and needs a good estimate for when to update the displacements. In reservoir engineering, iterative coupling of finite difference or finite volume flow model with finite element stress model is very common (Jeannin et al. 2007, Kim 2010). Iterative coupling results in less computational effort compared to fully coupled approaches. Many commercial simulators use sequentially implicit method; examples include TOUGH+FLAC (Rutqvist and Tsang 2002), STOMP+ABAQUS (Nguyen et al. 2016) and OpenGeoSys (Kolditz et al. 2012). However, they may be limited in numerical stability and convergence. In some cases, a relaxation term was added to improve the stability and convergence rate of sequential method (Jeannin et al. 2007). There are four types of iterative coupling for coupling geomechanics and flow: undrained split, the fixed stress split, the drained split and the fixed strain split (Mikelic et al. 2013, Kim 2010). Fixed stress split scheme was shown to be the most stable of the four schemes. This method solves the flow problem first while freezing the rate of total mean stress. Then solves the mechanical problem by prescribing the pressure from flow step. The advantage of iterative coupling is that flow and geomechanics problem can be solved with separate software modules. However, the simulated examples are often homogenous, and it is not shown whether the method is stable in heterogenous conditions. The accuracy of these methods is still debatable and the parameter range that can be used in such simulators in not known (Garipov et al. 2018). Hence the practical performance of this method is still under investigation. One challenge is finding good preconditioners for each

module (flow and geomechanics) that can work well in large contrast materials (White et al. 2016).

Coupling the flow and deformation processes by fully implicit method has unconditional stability and internal consistency since the full system of equations are solved simultaneously. One other advantage of fully coupled approach is that it has second order convergence of nonlinear iterations. The Galerkin finite element method is a powerful tool for spatial discretization of flow and deformation equations. Reservoir geometries are complex, and FEM is very flexible in dealing with such geometries by employing unstructured mesh.

Coupling a flow simulator with geomechanics simulator has been investigated by many researchers and various coupling schemes have been implemented (Settari and Mourtis 1994, Dean et al. 2006, Kim 2010, Jha and Juanes 2014, Rutqvist 2007). Settari and Mourtis (1994, 1998) used a modular approach to sequentially and iteratively couple flow and geomechanics simulators. Porosity was used as coupling parameter between module for stress analysis and reservoir simulator. Flow problem was solved first and then pressure corrections from reservoir simulator were applied as equivalent nodal loads for geomechanical simulator. Geomechanical module predicted the porosity change and then corrected porosity was used by reservoir simulator. At each time step, an iterative process ensured that convergence has been achieved.

Gutierrez et al. (2001) identified a possible drawback in iteratively coupled approaches. For the cases with negative compressibility where pore pressure decreases with volume increase due to shear dilation, there is no proof that the solution is unique given that in such a case the pore compressibility would be negative and numerical instability may arise.

Some researchers (Lewis and Sukirman, 1993, Li and Zienkiewicz 1992, Yin et el. 2009, Meng 1998) developed a fully coupled multiphase flow model using finite element discretization. However, they used Bishop's average pressure in their formulations which isn't completely consistent with thermodynamic constraints.

Khoei and Mohammadnejad (2011) simulated the seismic behavior of partially saturated dams considering water and air as immiscible compressible fluids and used fully coupled Biot's formulation with finite element method. They used Bishop's average pressure concept for pore pressure. Full Newton approach was adopted to deal with nonlinearity of equations.

Georke et al. (2011) used a sequentially coupled multiphase model for the simulation of CO_2 gas injection into saline aquifers. However, they neglected the compressibility of phases and solid matrix.

To satisfy the local mass conservation in coupled poroelasticity, some researchers have proposed using mixed finite element method for flow equations and coupling it to a standard Galerkin finite element discretization for geomechanics (Daegil 2013). This method can deal with complex geometries and heterogeneities. In mixed formulation, velocity field is a primary unknown rather than being derived from pressure solution. But introducing a new unknown increases the number of equations to be solved and consequently computational cost.

Hwang et. al. (2015) used finite volume method and an explicitly coupled approach to model waterflooding and studied the stress magnitude and orientation changes in the reservoir.

Some authors have neglected the capillary pressure and defined a global pressure which is same as wetting and non-wetting pressure (Wang and Lu 2001, Jeannin 2007). Simplifying assumptions such as uniaxial strain (e.g. Eker et al. 2017) or incompressible phases (e.g.

Goerke et al. 2011) are also common in reservoir engineering literature considering poroelasticity. It's worth noting that in reservoir engineering, a simple relation for porosity change is assumed through pore compressibility, the validity of which cannot be verified (Pao et al. 2001):

$$\frac{\partial n}{\partial t} = n c_p \frac{\partial p}{\partial t} \tag{5.24}$$

In this chapter, a fully coupled finite element model for deforming porous media containing two immiscible pore fluids is introduced. The coupled governing equations of flow and geomechanics are solved simultaneously at every time step. A converged solution is obtained through iteration, using Newton-Raphson method. The fully coupled approach is unconditionally stable. The non-linear formulation can properly model systems with high compressibility or strong capillary pressure such as CO2 sequestration or shale gas production.

In order to avoid the complicated case of transition from two-phase flow formulation to one-phase flow, relative permeability of phases is kept above a very small but finite value (e.g. 1×10^{-4}) in the model to avoid change of formulation and maintain a two-phase system (Gawin and Schrefler, 1996). Primary unknowns include displacement, nonwetting phase and wetting phase pressures. In hydrocarbon reservoir when oil and water are present, oil is usually the nonwetting phase while water is the wetting phase.

Throughout this chapter following simplifying assumptions are made:

- The fluids are immiscible
- Temperature is constant and chemical reactions are neglected
- There is no spatial variation of density
- Capillary hysteresis (different paths between imbibition and drainage in saturation-capillary pressure curve) is not considered

- Porous medium is assumed to be elastic and isotropic
- Acceleration of fluid and solid phases is not considered

5.2 Mathematical formulation

In the model, we consider a porous medium which is filled by two fluids, one being the wetting phase, *w*, and the other the non-wetting phase, *n*. It is not possible to linearize the equation of poroelasticity due to its nonlinear nature. Thus, we use the incremental form of the equations.

5.2.1 Constitutive equations

The constitutive equation for the solid skeleton in incremental form may be written as:

$$\dot{\boldsymbol{\sigma}}' = \mathbf{D}_e \dot{\boldsymbol{\varepsilon}} \tag{5.1}$$

where $\boldsymbol{D_e}$ is elasticity matrix. Under assumptions of infinitesimal displacements, strain-displacement relation is given by:

$$\dot{\boldsymbol{\varepsilon}} = \mathbf{B}\dot{\mathbf{u}} \tag{5.2}$$

where $\boldsymbol{u}$ is solid phase displacement vector. Bishop (1955) introduced an effective stress parameter, χ, to define changes of effective stress in partially saturated soil due to changes in water content. His expression for effective stress was:

$$\boldsymbol{\acute{\sigma}} = \boldsymbol{\sigma} + \boldsymbol{m}\{p_{\boldsymbol{a}} - \chi(p_a - p_w)\} \tag{5.3}$$

where $\mathbf{m} = \begin{bmatrix} 1 & 1 & 1 & 0 & 0 & 0 \end{bmatrix}^T$ and χ was related to saturation and was equal to 1 for saturated soil rendering the above equation equivalent to Terzaghi effective stress. Later, same expression for effective stress was obtained by other researchers (Lewis and Schrefler 1998, Hassanizadeh and Gray 1979) using averaging techniques but with Bishop's parameter equal to saturation $\chi = S_w$. Substituting $\chi = S_w$ in Eq. (5.3) and considering solid grains compressibility, effective stress can be written as:

$$\boldsymbol{\acute{\sigma}} = \boldsymbol{\sigma} + \alpha \boldsymbol{m}\{S_w p_w + S_n p_n)\} \tag{5.4}$$

where p_n is non-wetting phase pressure, p_w is wetting phase pressure, S_n is non-wetting phase saturation and S_w is wetting phase saturation. The pressures p_n and p_w are relative pressures, usually measured with respect to atmospheric pressure. The validity of effective stress formulation using average pressure has been a subject of debate and different expressions have been used by authors (Li et al. 1990, Lewis et al. 1993, Kim et al. 2013). Defining pore pressure as $S_j p_j$ in Eq. (5.4) ignores the tensile surface stresses acting along the interfaces and their subsequent effects on the deformation of solid matrix (Coussy 2004). Alternatively, effective stress can be expressed as:

$$\boldsymbol{\acute{\sigma}} = \boldsymbol{\sigma} + \alpha \boldsymbol{m}(p_n - S_w p_c - U) \tag{5.5}$$

where U is the interfacial energy per unit of porous volume computed from capillary pressure:

$$U(S_w) = \int_{S_w}^{1} p_c(S_w) dS_w \tag{5.6}$$

Capillary pressure, p_c, is the pressure difference between wetting and non-wetting phases:

$$p_c = p_n - p_w \tag{5.7}$$

In hydrocarbon reservoirs, oil is usually the non-wetting phase and water is the wetting phase. Considering incremental form of Eqs. (5.1), (5.5), (5.6) and (5.7), total stress can be written as:

$$\dot{\sigma_{ij}} = 2G\dot{\epsilon}_{ij} + \frac{2G\nu}{1-2\nu}\dot{\varepsilon_{kk}}\delta_{ij} - \alpha\delta_{ij}(S_w\dot{p_w} + S_n\dot{p_n}) \tag{5.7b}$$

Therefore, an equivalent pressure can be defined as:

$$dp_E = S_w dp_w + S_n dp_n \tag{5.8}$$

It is assumed that the pore volume is filled entirely with both fluids such that:

$$S_w + S_n = 1 \tag{5.9}$$

At constant temperature, there is a unique relation between the liquid saturation and the capillary pressure. In general, capillary pressure is a nonlinear function of fluid saturation and is derived from lab experiments:

$$p_c = f(S_w) \tag{5.10}$$

Irreducible wetting phase saturation, S_{wr}, refers to the fraction of pore volume occupied by the wetting phase at maximum nonwetting phase saturation.

Following Biot's notation, for each fluid phase η, we introduce $d\zeta_\eta$ as the variation of fluid volume per unit of bulk volume due to diffusive mass transport. The rate of fluid accumulation for each fluid phase depends on the following factors (Rahman and Lewis, 1999):

1- Rate at which the volumetric strain changes

2- Rate of change of solid grains volume

3- Compression rate of fluid phase

4- Rate of fluid saturation change

5- Rate of solid grains compression due to effective stresses

Considering the above contributing factors, for each fluid phase η we can write:

$$\dot{\zeta}_\eta = \alpha S_\eta \dot{\varepsilon}_{ii} + S_\eta \left[\frac{(\alpha - n)}{K_s} \dot{p} + \frac{n}{K_\eta} \dot{p}_\eta \right] + n\dot{S}_\eta \tag{5.11}$$

where K_η is fluid bulk modulus.

5.2.3 Transport of pore fluids

The generalized Darcy's law for multiphase flow can be written as (Muskat 1981):

$$\boldsymbol{u}_\eta = \boldsymbol{k}_\eta(-\nabla p_\eta + \rho_\eta \boldsymbol{g}) \tag{5.14}$$

where $\boldsymbol{g}$ is the gravity vector, ρ_η is phase density, and $\boldsymbol{k_\eta}$ is given by:

$$\boldsymbol{k}_\eta = \boldsymbol{k}\frac{k_{r\eta}}{\mu_\eta} \tag{5.25}$$

$\boldsymbol{k}$ is the intrinsic permeability of the matrix and μ_η is the η-th phase dynamic viscosity. $k_{r\eta}$ is the relative permeability of the η-th phase which depends on the saturation of that phase:

$$k_{r\eta} = f(S_\eta) \tag{5.36}$$

The product of $kk_{r\eta}$ is referred to as effective permeability to phase η and $\frac{k_{r\eta}}{\mu_\eta}$ is defined as mobility of phase η.

5.2.4 Equations of state

The equations of state are needed to express the fluid densities as a function of pressure. For isothermal conditions and compressible phases, the following relations are assumed for each phase.

Non-wetting phase:

$$\frac{1}{K_n}\frac{dp_n}{dt} = \frac{1}{\rho_n}\frac{d\rho_n}{dt} \tag{5.47}$$

Wetting phase:

$$\frac{1}{K_w}\frac{dp_w}{dt} = \frac{1}{\rho_w}\frac{d\rho_w}{dt} \tag{5.58}$$

where K_w is the bulk modulus of wetting phase and K_n is the bulk modulus of non-wetting phase.

5.2.5 Equilibrium equations

Under quasi-static conditions ($\ddot{u} = 0$), the linear momentum balance equation of a continuum in terms of its averaged Cauchy stress is given by:

$$\nabla.\boldsymbol{\sigma} + \rho\mathbf{g} = 0 \tag{5.19}$$

Or its time derivation:

$$\nabla.\dot{\boldsymbol{\sigma}} + \dot{\rho}\boldsymbol{g} = 0 \tag{5.20}$$

where ρ is the average density of the medium and is defined as:

$$\rho = nS_w\rho_w + n(1 - S_w)\rho_n + (1 - n)\rho_s \tag{5.21}$$

5.2.6 Wetting phase continuity

Similar to Eq. 2.22 for single phase flow, we can write the continuity equation for wetting phase as:

$$\dot{\zeta}_w + \nabla.\boldsymbol{u}_w = q^{ws} \tag{5.22}$$

where q^{ws} *is* the rate of injected wetting phase volume per unit bulk volume of the porous solid (represents sources/sinks. If it's positive, it represents injection).

Variation of wetting phase content from the relation (5.11) for wetting phase may be written as:

$$\dot{\zeta}_w = \alpha S_w\dot{\varepsilon}_{ii} + S_w\left[\frac{(\alpha - n)}{K_s}\dot{p} + \frac{n}{K_w}\dot{p}_w\right] + n\dot{S_w} \tag{5.23}$$

Substituting Eq. (5.14) in Eq. (5.23) gives:

$$\dot{\zeta}_w = S_w\alpha\frac{\partial\varepsilon_v}{\partial t} + n\frac{\partial S_w}{\partial t} + \frac{nS_w}{K_w}\frac{\partial p_w}{\partial t} + S_w\frac{\alpha - n}{K_s}\frac{\partial p}{\partial t} \tag{5.25}$$

Since saturation is a function of capillary pressure, the chain rule can be applied for time derivative of saturation resulting in:

$$\frac{\partial S_w}{\partial t} = \frac{\partial S_w}{\partial p_c}\frac{\partial p_c}{\partial t} = S'_w(\frac{\partial p_n}{\partial t} - \frac{\partial p_w}{\partial t}) \tag{5.26}$$

Combination of Eqs. (5.8) and (5.26) with Eq. (5.25) leads to the following relation:

$$\dot{\zeta}_w = S_w\alpha\frac{\partial\varepsilon_v}{\partial t} + nS'_w(\frac{\partial p_n}{\partial t} - \frac{\partial p_w}{\partial t}) + \frac{nS_w}{K_w}\frac{\partial p_w}{\partial t} + S_w\frac{\alpha - n}{K_s}\left\{S_w\frac{\partial p_w}{\partial t} + S_n\frac{\partial p_n}{\partial t}\right\} \tag{5.27}$$

Using Eq. (5.9), Eq. (5.27) can be rewritten as:

$$\dot{\zeta}_w = S_w\alpha\frac{\partial\varepsilon_v}{\partial t} + \left\{S_w^{\,2}\frac{(\alpha - n)}{K_s} + \frac{nS_w}{K_w} - nS'_w\right\}\frac{\partial p_w}{\partial t} + \left\{S_w(1 - S_w)\frac{(\alpha - n)}{K_s} + nS'_w\right\}\frac{\partial p_n}{\partial t} \tag{5.28}$$

Finally, from Eqs. (5.14), (5.22) and (5.28), the continuity equation of wetting phase can be derived as:

$$S_w\alpha\frac{\partial\varepsilon_v}{\partial t}+\left\{S_w{}^2\frac{(\alpha-n)}{K_s}+\frac{nS_w}{K_w}-nS'_w\right\}\frac{\partial p_w}{\partial t}+\left\{S_w(1-S_w)\frac{(\alpha-n)}{K_s}+nS'_w\right\}\frac{\partial p_n}{\partial t}+$$
$$\nabla.\{\mathbf{k}_w(-\nabla p_w+\rho_w\mathbf{g})\}=q^{ws} \tag{5.28}$$

5.2.7 Non-wetting phase continuity

Mass conservation equation for non-wetting phase is as follows:

$$\dot{\zeta}_n+\nabla.\boldsymbol{u_n}=q^{ns} \tag{5.29}$$

where q^{ns} is the rate of injected non-wetting fluid volume per unit bulk volume of the porous solid (represents sources and sinks. If it's positive, it represents injection).

Variation of non-wetting phase content from relation (5.11) may be written as:

$$\dot{\zeta}_n=\alpha S_n\dot{\varepsilon}_{ii}+S_n\left[\frac{(\alpha-n)}{K_s}\dot{p}+\frac{n}{K_n}\dot{p}_n\right]+n\dot{S_n} \tag{5.30}$$

From Eq. (5.9) it follows:

$$\frac{\partial S_n}{\partial t}=-\frac{\partial S_w}{\partial t} \tag{5.32}$$

Substituting Eqs. (5.32), (5.26) and (5.8) and (5.9) in Eq. (5.30) gives:

$$\dot{\zeta}_n=\alpha S_n\frac{\partial\varepsilon_v}{\partial t}-n\left\{S'_w(\frac{\partial p_n}{\partial t}-\frac{\partial p_w}{\partial t})\right\}+\frac{nS_n}{K_n}\frac{\partial p_n}{\partial t}$$
$$+S_n\frac{\alpha-n}{K_s}\left\{S_w\frac{\partial p_w}{\partial t}+(1-S_w)\frac{\partial p_n}{\partial t}\right\} \tag{5.33}$$

Or:

$$\dot{\zeta}_n=\alpha(1-S_w)\dot{\varepsilon}_v+\left\{nS'_w+S_w(1-S_w)\frac{(\alpha-n)}{K_s}\right\}\frac{\partial p_w}{\partial t}$$
$$+\left\{-nS'_w+(1-S_w)^2\frac{(\alpha-n)}{K_s}+\frac{n(1-S_w)}{K_n}\right\}\frac{dp_n}{dt} \tag{5.34}$$

Finally, from Eqs. (5.14), (5.29) and (5.34), the continuity equation of non-wetting phase can be derived as:

$$\alpha(1-S_w)\dot{\varepsilon}_v + \left\{ nS_w' + S_w(1-S_w)\frac{(\alpha-n)}{K_s} \right\}\frac{\partial p_w}{\partial t}$$
$$+\left\{ -nS_w' + (1-S_w)^2\frac{(\alpha-n)}{K_s} + \frac{n(1-S_w)}{K_n} \right\}\frac{dp_n}{dt} + \nabla.\{\mathbf{k}_n(-\nabla p_n + \rho_n \mathbf{g})\} = q^{ns} \tag{5.34a}$$

5.2.8. Casting 2-phase constitutive relations in the poroelasticity framework

The constitutive poroelastic Eq. (5.28) can also be written in the following form:

$$\dot{\zeta}_w = \alpha_w \dot{\varepsilon}_v + \frac{1}{M_{11}}\dot{p}_w + \frac{1}{M_{12}}\dot{p}_n \tag{5.28b}$$

where:

$$\alpha_w = S_w \alpha$$
$$\frac{1}{M_{11}} = {S_w}^2\frac{(\alpha-n)}{K_s} + \frac{nS_w}{K_w} - n\acute{S_w} \tag{5.29c}$$
$$\frac{1}{M_{12}} = S_w(1-S_w)\frac{(\alpha-n)}{K_s} + n\acute{S_w}$$

Also, Eq. (5.34) can also be written as:

$$\dot{\zeta}_n = \alpha_n \dot{\varepsilon}_v + \frac{1}{M_{21}}\dot{p}_w + \frac{1}{M_{22}}\dot{p}_n \tag{5.34d}$$

where:

$$\alpha_n = (1-S_w)\alpha$$
$$\frac{1}{M_{21}} = S_w(1-S_w)\frac{(\alpha-n)}{K_s} + n\acute{S_w} \tag{5.34e}$$
$$\frac{1}{M_{22}} = (1-S_w)^2\frac{(\alpha-n)}{K_s} + \frac{n(1-S_w)}{K_n} - n\acute{S_w}$$

M_{11}, M_{12}, M_{21} and M_{22} can be considered as elements of Biot modulus matrix M. In generalized form, we can write two-phase constitutive relations as:

$$\dot{\sigma_{ij}} = 2G\dot{\epsilon}_{ij} + \frac{2G\nu}{1-2\nu}\dot{\varepsilon_{kk}}\delta_{ij} + \alpha\delta_{ij}S_k\dot{p_k}$$
$$\dot{\zeta_j} = \alpha_j\dot{\varepsilon_v} + \frac{1}{M_{jk}}\dot{p_k} \tag{5.34f}$$

where:

$$\alpha_j = S_j \alpha$$

$$\frac{1}{M_{12}} = \frac{1}{M_{21}} = S_w(1 - S_w)\frac{(\alpha - n)}{K_s} + n\acute{S_w} \qquad (5.29a)$$

$$\frac{1}{M_{\eta\eta}} = {S_\eta}^2 \frac{(\alpha - n)}{K_s} + \frac{nS_\eta}{K_\eta} - n\acute{S_w}$$

5.2.8 Initial and boundary conditions

It is further necessary to define the initial and boundary conditions. The initial conditions specify the full fields of displacement, wetting and non-wetting pore pressure at $t = t_0$:

$$u = u_0 \,; p_w = p_{w0} \,; p_n = p_{n0} \qquad at \quad t = t_0 \qquad (5.35)$$

The boundary conditions can be of the first kind or Dirichlet boundary condition, Γ_i^1 or of the second type or Neumann boundary condition, Γ_i^2.

Boundary condition of the first kind, where displacement, wetting pore pressure and non-wetting pore pressure are prescribed on the boundary are as follows:

$$u = \hat{u} \qquad on \quad \Gamma_u^1 \qquad (5.36)$$

$$p_w = \hat{p}_w \qquad on \quad \Gamma_w^1 \qquad (5.37)$$

$$p_n = \hat{p}_n \qquad on \quad \Gamma_n^1 \qquad (5.38)$$

Boundary condition of the second kind, where tractions or fluxes on the boundary are prescribed can be written in the form:

$$\mathbf{l}^{\mathbf{T}}\boldsymbol{\sigma} = \mathbf{t} \qquad on \qquad \Gamma_u^2 \qquad (5.39)$$

$$\left(-\boldsymbol{k_w}(\nabla p_w - \rho_w \boldsymbol{g})\right).\boldsymbol{n} = q^w \qquad on \quad \Gamma_w^2 \qquad (5.40)$$

$$\left(-\boldsymbol{k}_n(\nabla p_n - \rho_n \boldsymbol{g})\right).\boldsymbol{n} = q^n \qquad on \quad \Gamma_n^2 \qquad (5.41)$$

where $\boldsymbol{n}$ is the unit normal vector, $\mathbf{t}$ is the applied traction, and q^w and q^n are the prescribed wetting and non-wetting phase fluid flux. $\mathbf{l}$ is given by:

$$\mathbf{l} = \begin{bmatrix} n_x & 0 & 0 \\ 0 & n_y & 0 \\ 0 & 0 & n_z \\ n_y & n_x & 0 \\ 0 & n_z & n_y \\ n_z & 0 & n_x \end{bmatrix} \tag{5.42}$$

5.3 Numerical scheme

The numerical treatment of the coupled two-phase problem in deformable porous media is based on governing field equations together with discretization in space and time. The weighted residual method is applied to previously mentioned governing equations to derive the weak formulations. In two-phase flow problems, selection of primary unknowns is very important for modeling efficiency and stability of the solution due the highly nonlinear nature of multiphase coupled problems. Here, we have chosen displacements and wetting and non-wetting phase pressures as primary unknowns. The choice of saturation as a primary unknown can introduce infinity or near infinity terms to the Jacobian matrix (Khoei et al. 2011).

The displacements and pore pressures for any point in the element domain are approximated in terms of shape functions and nodal unknowns as:

$$u = N_i^u \bar{u}_i \tag{5.43}$$

$$p_w = N_i^p \bar{p}_{wi} \tag{5.44}$$

$$p_n = N_i^p \bar{p}_{ni} \tag{5.45}$$

where N_i^u and N_i^p are shape functions for displacement and pressures and $\bar{u}_i$ are nodal displacements, $\bar{p}_{wi}$ and $\bar{p}_{ni}$ are the wetting phase and non-wetting phase pressures at node *i* respectively. In this study, 8-node isoparametric brick elements are used.

Using weighted residual method for continuity equation of wetting phase Eq. (5.28) and boundary condition Eq. (5.40):

$$\begin{aligned}
&\int_{\Omega} N_k^p \left\{ {S_w}^2 \frac{\alpha - n}{K_s} + \frac{nS_w}{K_w} - nS'_w \right\} \frac{\partial p_w}{\partial t} d\Omega + \\
&\int_{\Omega} N_k^p \left\{ S_w \frac{\alpha - n}{K_s} (1 - S_w) + nS'_w \right\} \frac{\partial p_n}{\partial t} d\Omega + \\
&\int_{\Omega} N_k^p S_w \alpha \dot{\varepsilon}_v d\Omega + \int_{\Omega} N_k^p (\nabla . \{ \mathbf{k_w} (-\nabla p_w + \rho_w \mathbf{g}) \}) d\Omega - \\
&\int_{\Omega} N_k^p q^{ws} d\Omega - \int_{\Gamma_w^2} N_k^p [(-\mathbf{k}_w (\nabla p_w - \rho_w \mathbf{g})) . \mathbf{n} - q^w] d\Gamma = 0
\end{aligned} \tag{5.46}$$

Using Green's theorem:

$$\begin{aligned}
&\int_{\Omega} N_k^p \left\{ S_w \frac{\alpha - n}{K_s} (1 - S_w) + nS'_w \right\} \frac{\partial p_n}{\partial t} d\Omega + \\
&\int_{\Omega} N_k^p \left\{ {S_w}^2 \frac{\alpha - n}{K_s} + \frac{nS_w}{K_w} - nS'_w \right\} \frac{\partial p_w}{\partial t} d\Omega + \\
&\int_{\Omega} N_k^p S_w \alpha \dot{\varepsilon}_v d\Omega + \int_{\Gamma} N_k^p \{ \mathbf{k_w} (-\nabla p_w + \rho_w \mathbf{g}) \} . \mathbf{n} d\Gamma - \\
&\int_{\Omega} \nabla N_k^p . \mathbf{k_w} (-\nabla p_w + \rho_w \mathbf{g}) d\Omega - \int_{\Omega} N_k^p q^{ws} d\Omega - \\
&\int_{\Gamma_w^2} N_k^p [(-\mathbf{k}_w (\nabla p_w - \rho_w \mathbf{g})) . \mathbf{n} - q^w] d\Gamma = 0
\end{aligned} \tag{5.47}$$

Since $\Gamma = \Gamma_w^1 + \Gamma_w^2$ and $N_i^p = 0$ on Γ_w^1 :

$$\begin{aligned}
&\int_{\Omega} N_k^p \left\{ S_w \frac{\alpha - n}{K_s} (1 - S_w) + nS'_w \right\} \frac{\partial p_n}{\partial t} d\Omega + \\
&\int_{\Omega} N_k^p \left\{ {S_w}^2 \frac{\alpha - n}{K_s} + \frac{nS_w}{K_w} - nS'_w \right\} \frac{\partial p_w}{\partial t} d\Omega + \\
&\int_{\Omega} N_k^p S_w \alpha \dot{\varepsilon}_v d\Omega - \int_{\Omega} \nabla N_k^p . \mathbf{k_w} (-\nabla p_w + \rho_w \mathbf{g}) d\Omega - \int_{\Omega} N_k^p q^{ws} d\Omega + \int_{\Gamma_w^2} N_k^p q^w d\Gamma = 0
\end{aligned} \tag{5.48}$$

Using the approximation stated in Eqs. (5.43), (5.44) and (5.45) and strain-displacement Eq. (5.2):

$$\int_{\Omega}\left[N^{p}\right]^{T}\left\{S_{w}\frac{\alpha-n}{K_{s}}(1-S_{w})+nS'_{w}\right\}\left[N^{p}\right]\left[\dot{\bar{p}}_{n}\right]d\Omega+$$
$$\int_{\Omega}\left[N^{p}\right]^{T}\left\{{S_{w}}^{2}\frac{\alpha-n}{K_{s}}+\frac{nS_{w}}{K_{w}}-nS'_{w}\right\}\left[N^{p}\right]\left[\dot{\bar{p}}_{w}\right]d\Omega+$$
$$\int_{\Omega}\left[N^{p}\right]^{T}S_{w}\alpha\left[m\right]^{T}\left[B\right]\left[\dot{\bar{u}}\right]d\Omega+ \tag{5.49}$$
$$+\int_{\Omega}\left[\nabla N^{p}\right]^{T}\left[\mathbf{k_w}\right]\left[\nabla N^{p}\right]\left[\overline{p}_{w}\right]d\Omega-\int_{\Omega}\left[\nabla N^{p}\right]^{T}\left[\mathbf{k_w}\right]\rho_{w}\mathbf{g}d\Omega-\int_{\Omega}\left[N^{p}\right]^{T}q^{ws}d\Omega+$$
$$\int_{\Gamma_{w}^{2}}\left[N^{p}\right]^{T}q^{w}d\Gamma=0$$

In matrix form the wetting phase continuity equation can be written as:

$$\left[L_{w}\right]^{T}\left[\dot{\bar{u}}\right]+\left[S_{ww}\right]\left[\dot{\bar{p}}_{w}\right]+\left[L_{nw}\right]\left[\dot{\bar{p}}_{n}\right]+\left[K_{cw}\right]\left[\overline{p}_{w}\right]=\left[f^{w}\right] \tag{5.50}$$

Using weighted residual method for non-wetting phase continuity Eq. (5.34) and boundary condition (5.41), it follows:

$$\int_{\Omega}N_{i}^{p}(\left\{nS'_{w}+S_{w}(1-S_{w})\frac{\alpha-n}{K_{s}}\right\}\frac{\partial p_{w}}{\partial t}d\Omega+$$
$$\int_{\Omega}N_{i}^{p}\left\{-nS'_{w}+(1-S_{w})^{2}\frac{\alpha-n}{K_{s}}+\frac{n(1-S_{w})}{K_{n}}\right\}\frac{dp_{n}}{dt}d\Omega+\int_{\Omega}N_{i}^{p}\alpha(1-S_{w})\dot{\varepsilon}_{v}d\Omega+ \tag{5.51}$$
$$\int_{\Omega}N_{i}^{p}(\frac{\partial}{\partial x_{i}}\left\{\mathbf{k}_{n}(-\frac{\partial p_{n}}{\partial x_{i}}+\rho_{n}g_{i})\right\}-q^{ns})d\Omega-$$
$$\int_{\Gamma_{n}^{2}}N_{i}^{p}(-\mathbf{k}_{n}(\nabla p_{n}-\rho_{n}\mathbf{g}).\mathbf{n}-q^{n})d\Gamma=0$$

It can be reorganized to give:

$$\int_{\Omega}N_{i}^{p}(\left\{nS'_{w}+S_{w}(1-S_{w})\frac{\alpha-n}{K_{s}}\right\}\frac{\partial p_{w}}{\partial t}d\Omega+$$
$$\int_{\Omega}N_{i}^{p}\left\{-nS'_{w}+(1-S_{w})^{2}\frac{\alpha-n}{K_{s}}+\frac{n(1-S_{w})}{K_{n}}\right\}\frac{dp_{n}}{dt}d\Omega+ \tag{5.52}$$
$$\int_{\Omega}N_{i}^{p}\alpha(1-S_{w})\dot{\varepsilon}_{v}d\Omega+\int_{\Omega}N_{i}^{p}\nabla.\left\{\mathbf{k}_{n}(-\nabla p_{n}+\rho_{n}\mathbf{g}\ )\right\}d\Omega-$$
$$\int_{\Omega}N_{i}^{p}q^{ns}d\Omega+\int_{\Gamma_{n}^{2}}N_{i}^{p}\mathbf{k}_{n}(\nabla p_{n}-\rho_{n}\mathbf{g}).\mathbf{n}d\Gamma+\int_{\Gamma_{n}^{2}}N_{i}^{p}q^{n}d\Gamma=0$$

Using Green's theorem gives:

$$\begin{aligned}
&\int_{\Omega} N_i^p \left(\left\{ nS_w' + S_w(1-S_w)\frac{\alpha-n}{K_s} \right\}\frac{\partial p_w}{\partial t} d\Omega + \right. \\
&\int_{\Omega} N_i^p \left\{ -nS_w' + (1-S_w)^2 \frac{(\alpha-n)}{K_s} + \frac{n(1-S_w)}{K_n} \right\}\frac{dp_n}{dt} d\Omega + \int_{\Omega} N_i^p \alpha(1-S_w)\dot{\varepsilon}_v d\Omega + \\
&\int_{\Gamma} N_i^p \mathbf{k}_n(-\nabla p_n + \rho_n \mathbf{g}\ ).\mathbf{n} d\Gamma - \int_{\Omega} \nabla N_i^p \mathbf{k}_n(-\nabla p_n + \rho_n \mathbf{g}) d\Omega - \int_{\Omega} N_i^p q^{ns} d\Omega - \\
&\int_{\Gamma_n^2} N_i^p(-\mathbf{k}_n(\nabla p_n - \rho_n \mathbf{g}).\mathbf{n}) d\Gamma + \int_{\Gamma_n^2} N_i^p q^n d\Gamma = 0
\end{aligned} \tag{5.53}$$

Since $\Gamma = \Gamma_n^1 + \Gamma_n^2$ and $N_i^p = 0$ on Γ_n^1 we have:

$$\begin{aligned}
&\int_{\Omega} N_i^p \left(\left\{ nS_w' + S_w(1-S_w)\frac{(\alpha-n)}{K_s} \right\}\frac{\partial p_w}{\partial t} d\Omega + \right. \\
&\int_{\Omega} N_i^p \left\{ -nS_w' + (1-S_w)^2 \frac{(\alpha-n)}{K_s} + \frac{n(1-S_w)}{K_n} \right\}\frac{dp_n}{dt} d\Omega + \int_{\Omega} N_i^p \alpha(1-S_w)\dot{\varepsilon}_v d\Omega - \\
&\int_{\Omega} \nabla N_i^p \mathbf{k}_n(-\nabla p_n + \rho_n \mathbf{g}) d\Omega - \int_{\Omega} N_i^p q^{ns} d\Omega + \int_{\Gamma_n^2} N_i^p q^n d\Gamma = 0
\end{aligned} \tag{5.54}$$

Using the approximation stated in Eqs. (5.43) through (5.45) and strain-displacement relation (5.2) we obtain:

$$\begin{aligned}
&\int_{\Omega} \left[N^p\right]^T \left(\left\{ nS_w' + S_w(1-S_w)\frac{(\alpha-n)}{K_s} \right\}\left[N^p\right]\left[\dot{\bar{p}}_w\right] d\Omega + \right. \\
&\int_{\Omega} \left[N^p\right]^T \left\{ -nS_w' + (1-S_w)^2 \frac{(\alpha-n)}{K_s} + \frac{n(1-S_w)}{K_n} \right\}\left[N^p\right]\left[\dot{\bar{p}}_n\right] d\Omega + \\
&\int_{\Omega} \left[N^p\right]^T \alpha(1-S_w)[m]^T[B]\left[\dot{\bar{u}}\right] d\Omega + \int_{\Omega} \left[\nabla N^p\right]^T [k_n]\left[\nabla N^p\right]\left[\bar{p}_n\right] d\Omega - \\
&\int_{\Omega} \left[\nabla N^p\right]^T [k_n]\rho_n[g] d\Omega - \int_{\Omega} \left[N^p\right]^T q^{ns} d\Omega + \int_{\Gamma_n^2} \left[N^p\right]^T q^n d\Gamma = 0
\end{aligned} \tag{5.55}$$

In matrix form the non-wetting phase continuity equation can be written as:

$$[L_n]^T\left[\dot{\bar{u}}\right] + [L_{nw}]\left[\dot{\bar{p}}_w\right] + [S_{nn}]\left[\dot{\bar{p}}_n\right] + [K_{cn}][\bar{p}_n] = \left[f^n\right] \tag{5.56}$$

Eq. (5.20) can be written as:

$$\boldsymbol{L^T \dot{\sigma}} + \dot{\rho}\mathbf{g} = \mathbf{0} \tag{5.57}$$

where L is written as:

$$\mathbf{L} = \begin{bmatrix} \frac{\partial}{\partial x} & 0 & 0 \\ 0 & \frac{\partial}{\partial y} & 0 \\ 0 & 0 & \frac{\partial}{\partial z} \\ \frac{\partial}{\partial y} & \frac{\partial}{\partial x} & 0 \\ 0 & \frac{\partial}{\partial z} & \frac{\partial}{\partial y} \\ \frac{\partial}{\partial z} & 0 & \frac{\partial}{\partial x} \end{bmatrix} \tag{5.58}$$

Applying weighted residual method to equilibrium Eq. (5.57) and using boundary condition (5.39) we obtain:

$$\int_{\Omega} \boldsymbol{N_u}^T \boldsymbol{L^T} \dot{\boldsymbol{\sigma}}\, d\Omega + \int_{\Omega} \boldsymbol{N_u}^T \dot{\rho} \boldsymbol{g} d\Omega - \int_{\Gamma_u^2} \boldsymbol{N_u}^T (\mathbf{l}^T \dot{\boldsymbol{\sigma}} - \dot{\boldsymbol{t}}) d\Gamma = 0 \tag{5.59}$$

Using Green's theorem gives:

$$\int_{\Gamma} \boldsymbol{N}_u{}^T \mathbf{l}^T \dot{\boldsymbol{\sigma}} d\Gamma - \int_{\Omega} (\boldsymbol{L N_u})^T \dot{\boldsymbol{\sigma}} d\Omega + \int_{\Omega} \boldsymbol{N_u}^T \dot{\rho} \boldsymbol{g} d\Omega - \int_{\Gamma_u^2} \boldsymbol{N_u}^T (\mathbf{l}^T \dot{\boldsymbol{\sigma}} - \dot{\boldsymbol{t}}) d\Gamma = 0 \tag{5.60}$$

Since $\Gamma = \Gamma_u^1 + \Gamma_u^2$ and $\boldsymbol{N}_u = 0$ on Γ_u^1 it follows:

$$\int_{\Omega} (\boldsymbol{L N_u})^T \dot{\boldsymbol{\sigma}} d\Omega - \int_{\Omega} \boldsymbol{N_u}^T \dot{\rho} \boldsymbol{g} d\Omega - \int_{\Gamma_u^2} \boldsymbol{N_u}^T \dot{\boldsymbol{t}} d\Gamma = 0 \tag{5.60}$$

Substituting effective stress relation in Eq. (5.5) and considering Eq. (5.6) gives:

$$\int_{\Omega} (\boldsymbol{L N_u})^T \dot{\boldsymbol{\sigma}} d\Omega - \int_{\Omega} (\boldsymbol{L N_u})^T \alpha \boldsymbol{m} (\dot{p}_w S_w + \dot{p}_n S_n) d\Omega - \int_{\Omega} \boldsymbol{N_u}^T \dot{\rho} \boldsymbol{g} d\Omega - \int_{\Gamma_u^2} \boldsymbol{N_u}^T \dot{\boldsymbol{t}} d\Gamma = 0 \tag{5.61}$$

Using approximations (5.44) and (5.45):

$$\int_{\Omega} (\boldsymbol{LN_u})^T \dot{\boldsymbol{\sigma}} d\Omega - \int_{\Omega} (\boldsymbol{LN_u})^T \alpha \boldsymbol{m} (\boldsymbol{N_p} \dot{\vec{\boldsymbol{p}}}_{\boldsymbol{w}} S_w + \boldsymbol{N_p} \dot{\vec{\boldsymbol{p}}}_{\boldsymbol{n}} S_n) d\Omega - \int_{\Omega} \boldsymbol{N_u}^T \dot{\rho} \boldsymbol{g} d\Omega - \int_{\Gamma_u^2} \boldsymbol{N_u}^T \dot{\boldsymbol{t}} d\Gamma = 0 \tag{5.62}$$

In this work, rock is assumed to be elastic and isotropic. From Eqs. (5.1) and (5.2) it follows:

$$\dot{\boldsymbol{\sigma}} = \boldsymbol{D\varepsilon} = \boldsymbol{DB}\dot{\bar{\boldsymbol{u}}} \tag{5.63}$$

Eq. (5.33) can be written as:

$$\int_{\Omega} \boldsymbol{B}^T \boldsymbol{DB} \dot{\bar{\boldsymbol{u}}} d\Omega - \int_{\Omega} \boldsymbol{B}^T \alpha S_w \boldsymbol{m} \boldsymbol{N_p} \dot{\bar{\boldsymbol{p}}}_{\boldsymbol{w}} d\Omega - \int_{\boldsymbol{\Omega}} \boldsymbol{B}^T \alpha (1 - S_w) \boldsymbol{m}\, \boldsymbol{N_p} \dot{\vec{\boldsymbol{p}}}_{\boldsymbol{n}} d\Omega - \int_{\Omega} \boldsymbol{N_u}^T \dot{\rho} \boldsymbol{g} d\Omega - \int_{\Gamma_u^N} \boldsymbol{N_u}^T \dot{\boldsymbol{t}} d\Gamma = 0 \tag{5.64}$$

In matrix form the equilibrium equation can be written as:

$$[K]\left[\dot{\bar{u}}\right] - [L_w]\left[\dot{\bar{p}}_w\right] - [L_n]\left[\dot{\bar{p}}_n\right] = \left[\dot{f}_u\right] \tag{5.65}$$

Eqs. (5.50), (5.56) and (5.65) can be combined into the following system of nonlinear algebraic equations:

$$\begin{bmatrix} -K & L_w & L_n \\ {L_w}^T & S_{ww} & L_{nw} \\ {L_n}^T & L_{nw} & S_{nn} \end{bmatrix} \begin{bmatrix} \dot{\bar{u}} \\ \dot{\bar{p}}_w \\ \dot{\bar{p}}_n \end{bmatrix} + \begin{bmatrix} 0 & 0 & 0 \\ 0 & K_{cw} & 0 \\ 0 & 0 & K_{cn} \end{bmatrix} \begin{bmatrix} \bar{u} \\ \bar{p}_w \\ \bar{p}_n \end{bmatrix} = \begin{bmatrix} -\dot{f}^u \\ f^w \\ f^n \end{bmatrix} \tag{5.66}$$

The coefficients in the above matrix are given in appendix A. We can also write the above in terms of capillary pressure instead of non-wetting phase pressure resulting in:

$$\begin{bmatrix} K & -L_w - L_n & -L_n \\ {L_w}^T & S_{ww} + L_{nw} & L_{nw} \\ {L_n}^T & L_{nw} + S_{nn} & S_{nn} \end{bmatrix} \begin{bmatrix} \dot{\bar{u}} \\ \dot{\bar{p}}_w \\ \dot{\bar{p}}_c \end{bmatrix} + \begin{bmatrix} 0 & 0 & 0 \\ 0 & K_{cw} & 0 \\ 0 & K_{cn} & K_{cn} \end{bmatrix} \begin{bmatrix} \bar{u} \\ \bar{p}_w \\ \bar{p}_c \end{bmatrix} = \begin{bmatrix} \dot{f}^u \\ f^w \\ f^n \end{bmatrix} \tag{5.67}$$

To make the coefficient matrix symmetric, we can rewrite the above equation as:

$$\begin{bmatrix} -K & L_w + L_n & L_n \\ L_w{}^T + L_n{}^T & S_{ww} + L_{nw} + L_{nw} + S_{nn} & L_{nw} + S_{nn} \\ L_n{}^T & L_{nw} + S_{nn} & S_{nn} \end{bmatrix} \begin{bmatrix} \dot{\bar{u}} \\ \dot{\bar{p}}_w \\ \dot{\bar{p}}_c \end{bmatrix} + \begin{bmatrix} 0 & 0 & 0 \\ 0 & K_{cw} + K_{cn} & K_{cn} \\ 0 & K_{cn} & K_{cn} \end{bmatrix} \begin{bmatrix} \bar{u} \\ \bar{p}_w \\ \bar{p}_c \end{bmatrix} = \begin{bmatrix} -\dot{f}^u \\ f^w + f^n \\ f^n \end{bmatrix} \tag{5.68}$$

5.4 Solution of FEM equations

For a compact representation of the system of equations in (5.68), they can be written symbolically as:

$$\left[A(x)\right]\left[\dot{x}\right] + \left[B(x)\right]\left[x\right] = \left[C(x)\right] \tag{5.69}$$

We use fully implicit method to discretize the Eq. (5.69) in time. So, it follows:

$$\boldsymbol{\Psi}(\boldsymbol{x}_{n+1}) = \boldsymbol{A}(\boldsymbol{x}_{n+1}) \frac{\boldsymbol{x}_{n+1} - \boldsymbol{x}_n}{\Delta t} + \boldsymbol{B}(\boldsymbol{x}_{n+1})\boldsymbol{x}_{n+1} - \boldsymbol{C}(\boldsymbol{x}_{n+1}) = 0 \tag{5.70}$$

In the above equation, the subscripts denote the time step number. The coupled system of equations in (5.66) or (5.68) is highly nonlinear and requires linearizing by an iterative method. In this work, Newton-Raphson method is used to solve the system of equations:

$$\begin{aligned} &\left[\frac{1}{\Delta t}\left(\left[\frac{\partial \mathbf{A}(\mathbf{x}_{n+1}^l)}{\partial \mathbf{x}}(\mathbf{x}_{n+1}^l - \mathbf{x}_n)\right] + \mathbf{A}(\mathbf{x}_{n+1}^l)\right) + \left[\frac{\partial \mathbf{B}(\mathbf{x}_{n+1}^l)}{\partial \mathbf{x}}\right]\mathbf{x}_{n+1}^l + \mathbf{B}(\mathbf{x}_{n+1}^l) - \frac{\partial \mathbf{C}(\mathbf{x}_{n+1}^l)}{\partial \mathbf{x}}\right] \\ &\Delta \mathbf{x}_{n+1}^l = -\left[\mathbf{A}(\mathbf{x}_{n+1}^l)\frac{\mathbf{x}_{n+1}^l - \mathbf{x}_n}{\Delta t} + \mathbf{B}(\mathbf{x}_{n+1}^l)\mathbf{x}_{n+1}^l - \mathbf{C}(\mathbf{x}_{n+1}^l)\right] \end{aligned} \tag{5.71}$$

where l is iteration number. After solving the above equation, set:

$$\boldsymbol{x}_{n+1}^{l+1} = \boldsymbol{x}_{n+1}^l + \Delta \boldsymbol{x}_{n+1}^l \tag{5.72}$$

The iterations are continued until the residuals are below a convergence tolerance.

The iterative solution sequence is as follows:

1. From the solution of previous time step, obtain the initial guess for the unknowns.
2. Calculate the coefficient matrix and right-hand side vector and solve for unknowns.

3. Using the new unknown values calculate coefficient matrix and right-hand side vector and solve.
4. Repeat until acceptable convergence is achieved. Then go to next time step.

5.4.1 Time step size

The time step size is adaptively adjusted according to the convergence behavior of the previous nonlinear iteration to optimize convergence and CPU efficiency. At each time step of the simulation, the current time step size is increased by a factor of 1.14, if the convergence at the previous iteration is achieved in fewer than 5 iterations. If the theme is not convergent after 5 iterations, the time step is decreased by a factor of 0.5. The main advantage of dynamic time marching is that it avoids undesirable abrupt changes in time step.

5.5 Verification examples

In order to show the validity of the multiphase numerical model, some examples are solved and compared with already available solutions. The first example is drainage from a saturated vertical column and the second example is consolidation of partially saturated soil column.

5.5.1 Gravity drainage of a saturated soil column

The water drainage of a vertical saturated soil column is a typical problem for the validation of coupled two-phase models. This problem has been solved by many researchers (Gawin et al. 1997, Ehlers et al. 2004, Nagel and Meschke 2010). If a saturated sample of soil with zero initial water pressure is let to drain and it's open to air on top and bottom, water will flow out of the bottom due to gravity forces and air will gradually flow in from top to replace water. This will result in negative gauge pressures for both water and air inside the sample. As the flow progresses, the length of unsaturated section on top of sample will increase. This

process was studied by Liakopoulos (1965). In his PhD thesis he conducted experiments on the drainage of water from a fully saturated vertical sand column of Del Monte sand under the effect of gravity. The test was conducted on a 1 m column of sand with 0.1 m diameter which was instrumented to measure moisture tension at several points along its height. Before the beginning of the test, the water was continuously added from the top and allowed to drain freely at the bottom through a filter until steady state water flow was established. The fully saturated steady state flow is associated with zero water pressure over the entire height of the column. After this initial stage, the water supply was ceased, and the specimen was allowed to drain from bottom. At this stage, the ends of the column were exposed to atmosphere. A tensiometer recorded the capillary pressure at several points along the column. The water outflow at the draining end was periodically measured.

Capillary pressure and water relative permeability are dependent on water saturation by the following relationships (Liakopoulos, 1965):

$$S_w = 1.0 - 1.9722 \times 10^{-11} {p_c}^{2.4279} \tag{5.73}$$

$$k_{rw} = 1.0 - 2.207(1 - S_w)^{1.0121} \tag{5.74}$$

The above relation between saturation and capillary pressure is valid for $S_w \geq 0.91$. p_c is in Pascals. The relationship between relative permeability of pore air and water saturation follows Brooks and Corey (Brooks et al. 1964) model:

$$k_{rg} = (1 - S_e)^2 (1 - S_e^{\frac{(2+\lambda)}{\lambda}}) \tag{5.75}$$

$$S_e = \frac{S_w - S_{rw}}{1 - S_{rw}} \tag{5.76}$$

where λ is the pore size distribution index, $\lambda = 3$.

5.5.1.1 Initial condition

Initially, steady state water flow is established throughout the column while both ends are exposed to atmosphere. Since the specimen is fully saturated at the initial stage of the test, water and air pressure are atmospheric for the whole domain. The column is at a state of mechanical equilibrium at t=0.

Table 5-1. Material properties of the sand column model for Liakopoulos (1965) test verification

Property	Value
Young's modulus (E), MPa	1.3
Poisson's ratio (ν)	0.4
Porosity (n)	0.2975
Water density (ρ_w), kg/m^3	1000
Solid phase density (ρ_s), kg/m^3	2000
Air density (ρ_g) at P_{atm}, kg/m^3	1.2
Solid phase bulk modulus (K_s), Pa	1×10^{12}
Water bulk modulus (K_w), Pa	2×10^{9}
Intrinsic permeability (k), m^2	4.5×10^{-13}
Water viscosity (μ_w), Pa.s	1.0×10^{-3}
Air viscosity (μ_a), Pa.s	1.8×10^{-5}
Irreducible water saturation (S_{rw})	0.2
Gravitational acceleration (g), m/s^2	9.806
Atmospheric pressure (P_{atm}), Pa	1.01325×10^{5}

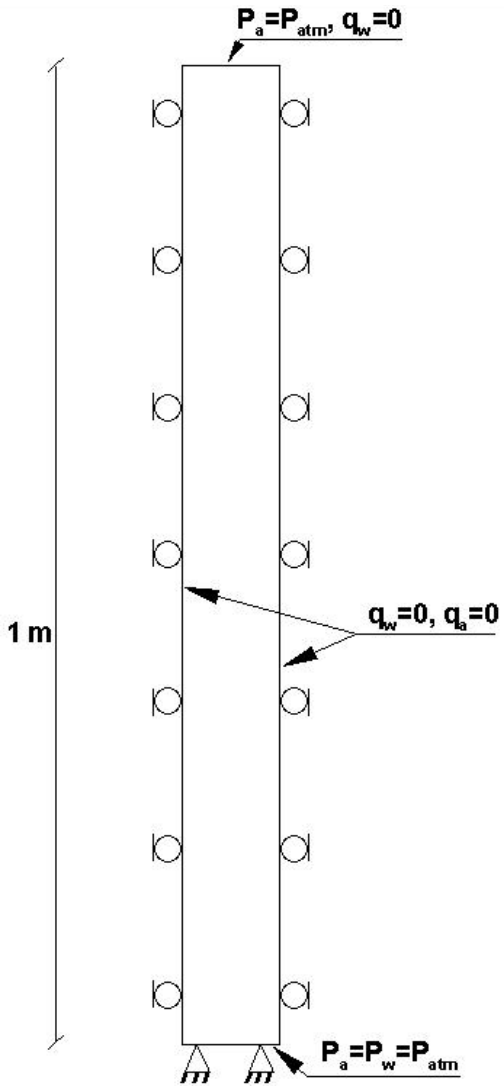

Figure 5-1. Schematic of soil column and boundary conditions for the Liakopoulos test

5.5.1.2 Boundary condition

The air pressure at both upper and lower ends of the column and the water pressure at the bottom are equal to the atmospheric pressure as shown in Figure 5-1. Water can only flow through the bottom end of the column. Sides are impermeable to both water and air. The lower boundary is prescribed with fully constrained displacements while the side boundaries are constrained in normal direction.

5.5.1.3. Simulation model and Results

Simulations were made with finite element method. Eight-node isoparametric brick elements were used to discretize the domain and the resulting mesh consists of 6929 nodes and 5760 elements. A constant time step of 2 seconds was used in the simulations.

The constitutive model was assumed to be elastic. The material properties of the Del Monte sand are given in Table 5-1.

The results of simulations including the water pressure, air pressure, water saturation, vertical displacement and flow rate is shown in Figure 5-2 through 5-6 and compared with existing numerical and experimental results.

An important check of the obtained results is performed with comparing the outflow rate at the bottom of the column with results from other researchers. The outflow is the result of the desaturation of the column as well as squeezing effect related to soil deformation. The time history of the simulated water outflow rate through the bottom of the column is shown in Figure 5-2 and compared with other numerical results and experimental results of Liakopoulos (1964). It is observed that the outflow gradually decreases over time and if the test were long enough, water outflow rate could approach zero. The flow rates show similar trend having a better match at later stages of the test. Simulated results deviate from experimental results as seen in the figure but keep the same trend. In Figure 5-4, it can be observed that the air pressure is negative. The reason could be that as water is draining, the air moves inside the column from top boundary to fill in the empty pore space, but it cannot totally fill the pore volume left by water and this results in a pressure less than atmospheric pressure. In Figure 5-5, we can observe that the column vertical displacements increase over time.

This could be because as water is draining, the column effective stress increases, and consolidation takes place resulting in continuous settlement of the column over time. A good match is observed between results from this work and the results obtained by Samimi and Pak (2016).

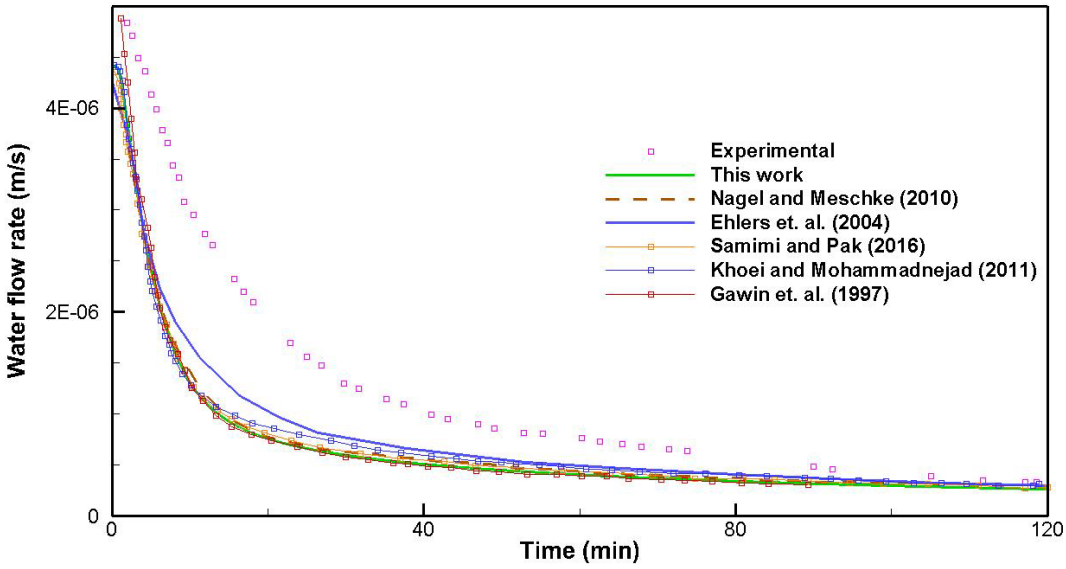

Figure 5-2. Evolution of water outflow rate through the bottom surface of the column (comparison of experimental and numerical results)

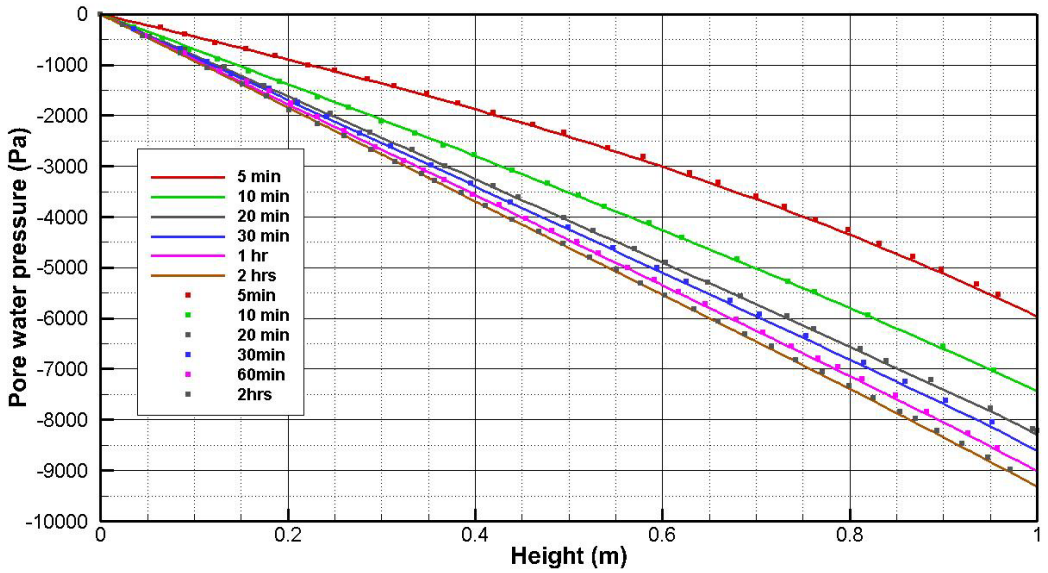

Figure 5-3. Comparison of water pressure profiles. Lines show results from this work and symbols are the results from Samimi and Pak (2016)

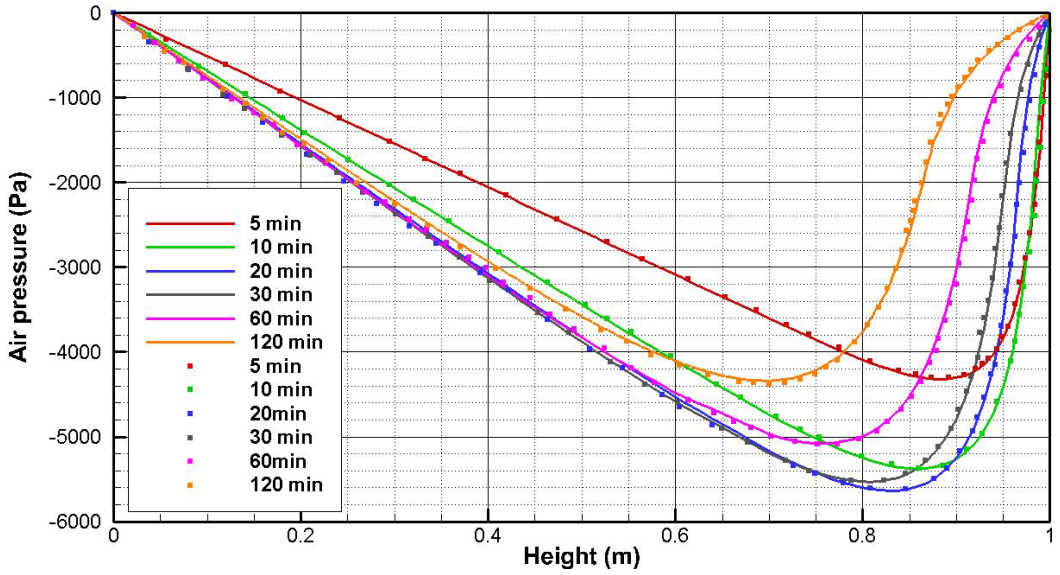

Figure 5-4. Comparison of air pressure profiles. Lines show results from this work and symbols are the results from Samimi and Pak (2016).

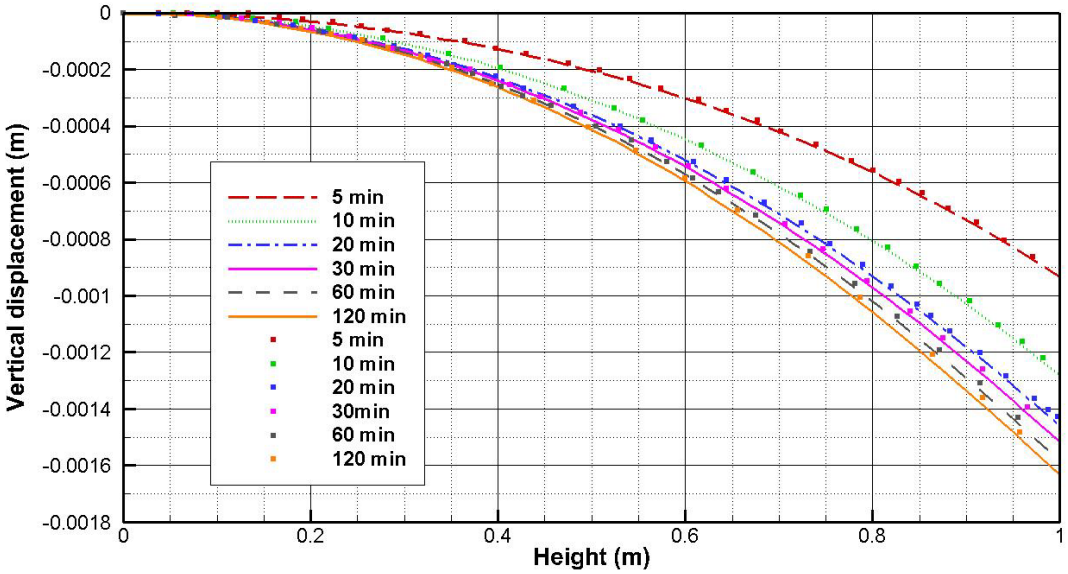

Figure 5-5. Comparison of vertical displacement profiles. Lines show results from this work and symbols are the results from Samimi and Pak (2016).

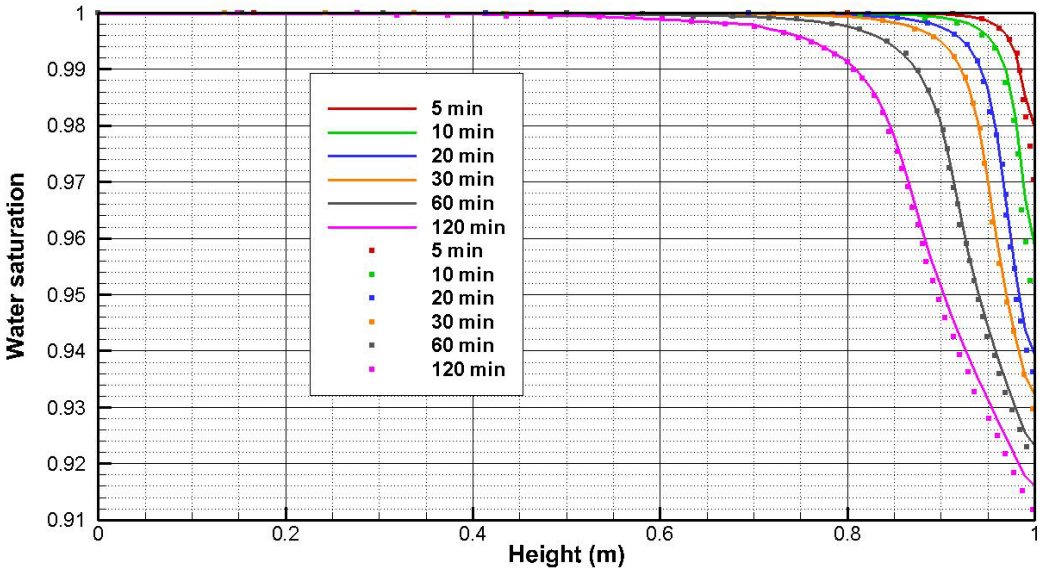

Figure 5-6. Comparison of water saturation profiles. Lines show results from this work and symbols are the results from Samimi and Pak (2016)

5.5.2 Coupled two-phase consolidation

Two-phase (air and water) consolidation of a column of soil under vertical loading is considered in this example. This problem was solved numerically by Rahman and Lewis (1999), Khoei and Mohammadnejad (2011) and Asadi et. al. (2015). A partially saturated soil column with linear elastic material is subject to an external surface load of 1000 Pa. The column is 1 m in height and has a rectangular cross section of 0.1 m × 0.1 m. It is initially unsaturated with an initial pore water pressure of -280 kPa and initial water saturation of 0.52. An initial state of equilibrium is assumed. This column is subject to an instantaneous pore water pressure change from -280 kPa to -420 kPa at its top surface. In practice, similar changes can arise from environmental changes affecting surface soil systems, such as evaporation from soil surface which builds up a negative pore pressure. Because of surface pressure change, the soil layer experiences a decrease in volume or consolidation. Material properties used in the simulation are given in Table 5-2. For the air phase, the ideal gas equation is used to compute air bulk modulus. The boundary conditions are as follows:

-lateral surfaces: $q_w = 0$; $q_a = 0$; $u_h = 0$

-top surface: $p_a = P_{atm}$; $p_w = -420\ kPa$; F= $-1\ kPa$

-Bottom surface: $u_v = 0$; $q_a = 0$; $q_w = 0$

Brooks and Corey (1964) relationship for the dependence of capillary pressure on saturation was used in this model:

$$p_c = p_e(S_e)^{-\frac{1}{\lambda}} \qquad (p_c > p_e) \tag{5.77}$$

$$S_e = \frac{S_w - S_{rw}}{1 - S_{rw}} \tag{5.78}$$

where p_e is entry pressure (or displacement pressure) and λ is pore size distribution index. These parameters are given in Table 5-2. Brook and Corey (1964) relation is used for the relative permeability which is given by Eq. (5.75) for gas phase and by the following relation for water phase:

$$k_{rw} = S_e^{\frac{2+3\lambda}{\lambda}} \tag{5.79}$$

To achieve a non-oscillating solution for fluid pressures, a lower limit of relative gas permeability equal to 1×10^{-4} is used in the simulations.

Figure 5-7 depicts the evolution of saturation over time at different heights within the column. Pore water pressure distribution throughout the soil column at different time intervals is shown in Figure 5-8. The figure shows how the applied pore pressure on top boundary is gradually transferred to the bottom over time and finally entire soil column will have the same pore water pressure. The results are in good agreement with results shown in Asadi et. al. (2015). Figure 5-9 shows the time evolution of vertical displacements for different points during the consolidation process. The points are located at 0.1, 0.5, 0.7 and 0.95 m from the column base. Good agreement is observed with the results reported in Asadi et. al. (2015).

Table 5-2. Material properties for partially satuated consolidation problem

Properties	Values
Young's modulus (E), MPa	6.0
Poisson's ratio (ν)	0.4
Porosity (n)	0.3
Intrinsic permeability (k), m^2	0.46×10^{-11}
Water viscosity (μ_w), Pa.s	1×10^{-3}
Gas viscosity (μ_a), Pa.s	1×10^{-3}
Water bulk modulus (K_w), Pa	0.43×10^{13}
Solid phase bulk modulus (K_s), Pa	0.14×10^{13}
Displacement pressure (p_e), Pa	225×10^{6}
Pore size distribution index, λ	3.0
Residual water saturation (S_{rw})	0.3966
Initial gas density (ρ_g), kg/m^3	1.22
Water density (ρ_w), kg/m^3	1000
Solid phase density (ρ_s), kg/m^3	2000

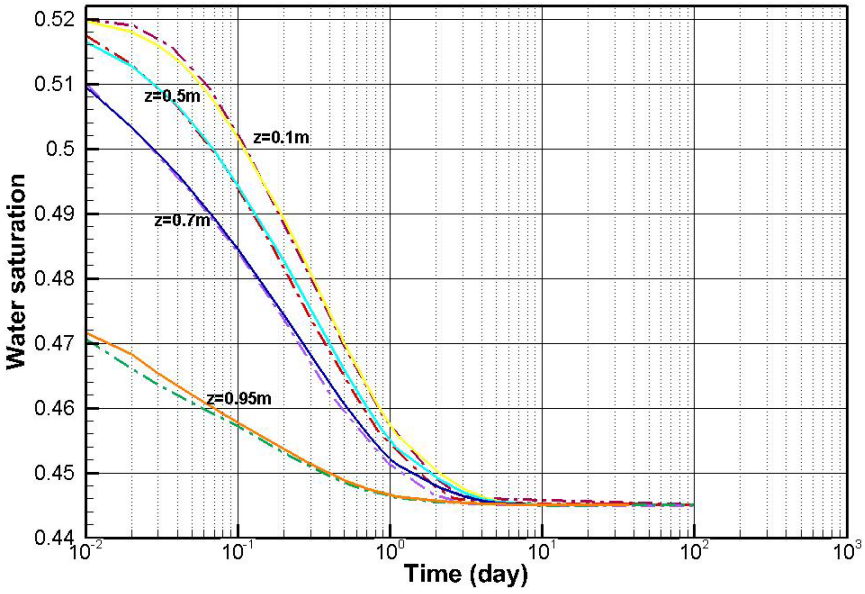

Figure 5-7. Time history of saturation at different heights. solid lines: this study; dashed lines: Asadi et al. (2015).

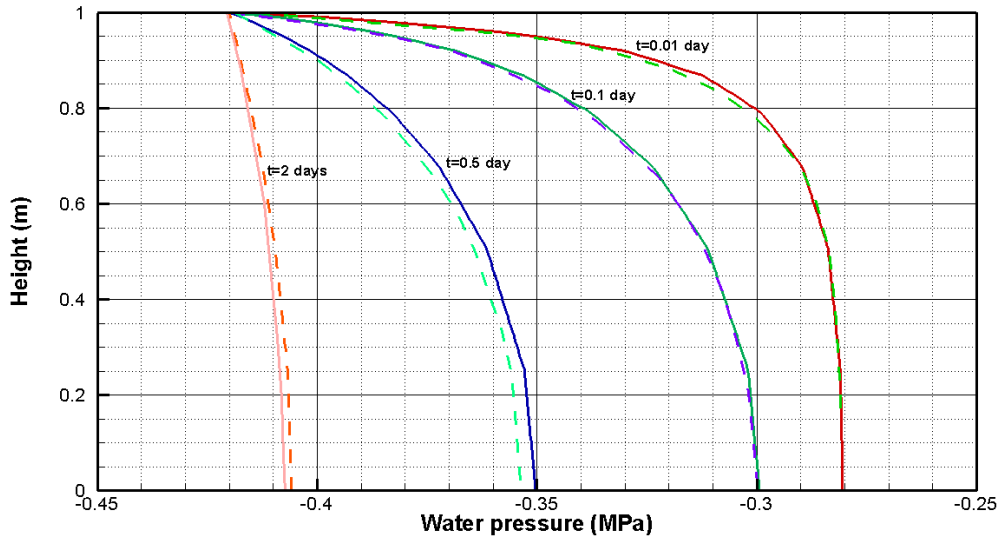

Figure 5-8. Water pressure profile at different times. solid lines: this study; dashed lines: Asadi et al. (2015).

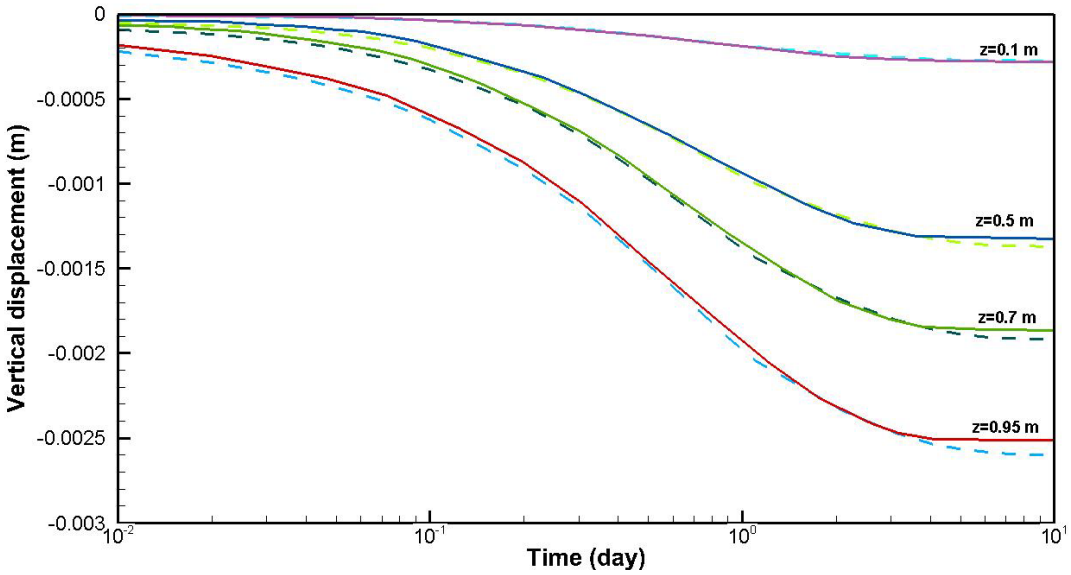

Figure 5-9. Time history of vertical displacement at different heights. Solid lines: Asadi et al. (2015); dashed lines: this study.

5.6 Case studies

In the following sections, two case studies will be considered. First, water injection/production in a water oil system is simulated. In the second case, production from a single fracture in a two-phase reservoir with oil and water will be considered. The results of the simulation

will be compared with a similar reservoir which contains oil only and conclusions will be made.

5.6.1 Waterflooding problem

A waterflooding problem in a homogenous oil reservoir under plane strain conditions is considered. Similar problems were solved by Kim et al. (2013), Sangnimnuan (2020) and Daegil (2013). Kim et al. (2013) investigated whether Bishop's average pressure or equivalent pressure is appropriate for multiphase flow in porous media and tested the stability of these two definitions for different values of capillarity. They found that average pressure formulation can become unstable for low porosity formations but using equivalent formulation results in stable and accurate solutions. In this work, same definition of pressure is adopted.

A schematic of the problem and initial and boundary conditions are shown in Figure 5-10. Water (wetting phase) is injected at a constant rate of 250 kg/m/day at the lower right corner and a mixture of oil and water is produced at the upper left zone. The initial oil saturation is 0.58 and water is injected at a constant rate and fluids are produced at the same rate of injection.

The domain considered for reservoir model is rectangular with a width of 20 m (in Y direction) and a length of 100 m (in the X direction). Fluids cannot flow through boundaries. The horizontal displacements of the left boundary as well as the vertical displacements of lower boundary are constrained. For simplicity, the rock is considered elastic and isotropic. Rate of water injection and total liquid production are identical $q_{inj}=q_{prod}=250$ kg/day/m and were kept constant over the duration of simulation time. Water and oil in the system are assumed to be immiscible. Gravity effects are neglected. The basic reservoir and fluid properties used in this problem are shown in Table 5-3. The simulations are performed for 40 days. The

discretization of the domain is accomplished using hexahedral elements as shown in Figure 5-12. The mesh is comprised of 69,856 elements and 141,134 nodes. A monitoring point is considered which has coordinates of X=25m, Y=12.5m and its location is shown in Figure 5-10.

The relative permeability of oil and water phases are based on the modified Brooks-Corey relative permeability relation (Charoenwongsa et. al. 2010):

$$k_{rw} = k_{rw}^{*}\left[\frac{S_w - S_{rw}}{1 - S_{ro} - S_{rw}}\right]^{n_w} \tag{5.80}$$

$$k_{ro} = k_{ro}^{*}\left[\frac{1 - S_w - S_{ro}}{1 - S_{ro} - S_{rw}}\right]^{n_o} \tag{5.81}$$

The relative permeability parameters used are shown in Table 5-4 and the corresponding curves are shown in Figure 5-13.

The capillary pressure model used for this simulation model is from van Genuchten (1980):

$$p_c - p_e = M\left(S_e^{-\frac{1}{m}} - 1\right)^{1-m} \quad 0<m<1 \quad S_e = \frac{S_w - S_{rw}}{1 - S_{ro} - S_{rw}} \tag{5.82}$$

where M is capillary modulus, p_e is entry pressure and S_{rw} and S_{ro} are residual water and oil saturation respectively. m is a parameter that characterizes the shape of capillary pressure curve and is between 0 and 1. The capillary pressure plot as a function of water saturation for M=0.2 MPa and different values of parameter m is shown in Figure 5-12. The parameters used for van Genuchten model in this example problem are given in Table 5-5. Since the value of m is close to 1, the capillary pressure is nearly constant (Figure 5-12). The finite element mesh consists of 69,856 elements and 141,134 nodes. Initial time step size is 1,800 s and is increased by a factor of 1.14 using considerations of section 5.4.1.

The distribution of saturation after 35 days of waterflooding is shown in Figure 5-14. Due to water injection, the water saturation increases in a radial pattern around the injection point.

The displacement vectors after 35 days are shown in Figures 5-15. The displacement in the left half are to the left and downwards due to the production and consolidation under over-burden. For the right half, the displacements are upward and to the left due to the expansion resulting from injection of water into the reservoir.

Figure 5-16 shows the distribution of pore pressure after 35 days of injection. It is observed that pore pressure in the vicinity of the injection point has increased and in the vicinity of production point decreased as we expect.

Figures 5-17 and 5-18 show the oil and water velocity direction and magnitude near the production zone and injection zone respectively. The oil and water velocity are highest in magnitude closer to production and injection zone and as we get farther, the magnitude is decreased. Also next to boundaries the velocity is parallel to boundary due to its impermeability. Also, it's observed that water velocity is greater in magnitude and larger in extension compared to oil velocity.

In Figure 5-19, the time evolution of oil pressure at the monitoring point is depicted. It is observed that in the initial phase of waterflooding the pressure decreases at the monitoring point as it is closer to the production point. However, over time the water injection causes the pressure at the monitoring point to reach a steady state condition where it stays constant over time.

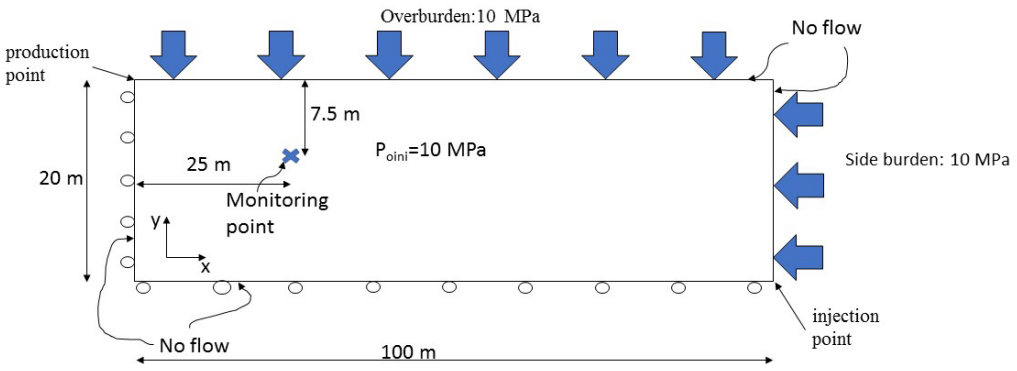

Figure 5-10. Sketch of the domain used for modeling. Initial and boundary conditions for coupled 2-phase flow problem of waterflooding are shown in this figure.

Table 5-3. Material properties for the analysis of waterflooding problem

Properties	Values
Oil density (ρ_o), kg/m^3	1000
Water density (ρ_w), kg/m^3	1000
Oil viscosity (μ_o), cp	1.0
Water viscosity (μ_w), cp	1.0
Porosity (n)	0.3
Intrinsic permeability (k), md	500
Young modulus (E), MPa	24.0
Poisson's ratio(ν)	0.3
Biot coefficient (α)	1.0
Initial oil saturation (S_{wi})	0.58
Water bulk modulus (K_w), Pa	2.5×10^9
Oil bulk modulus (K_o), Pa	2.5×10^8
Residual oil saturation (S_{ro})	0.0
Residual water saturation (S_{rw})	0.0
Initial pressure (P_i), MPa	9.95
Initial oil pressure (Po_i), MPa	10.145

Table 5-4. Parameters for modified Brooks-Corey relative permeability relation

Parameter	Value
k_{rw}^{*}	1
k_{ro}^{*}	1
n_w	2
n_o	2

Table 5-5. Parameters for van Genuchten (1980) capillary curve used in the analysis

Parameter	Value
Entry pressure, p_e	0.0 MPa
m	0.98
Capillary modulus, M	0.2 MPa

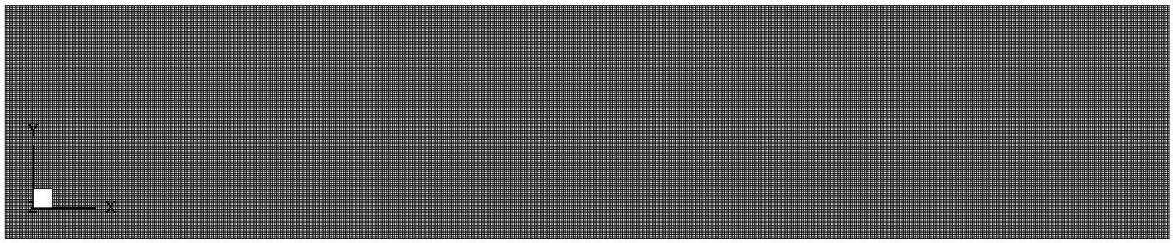

Figure 5-11. Discretization of the domain used for simulation of waterflooding problem. The mesh consists of 69,856 hexahedral elements and 141,134 nodes

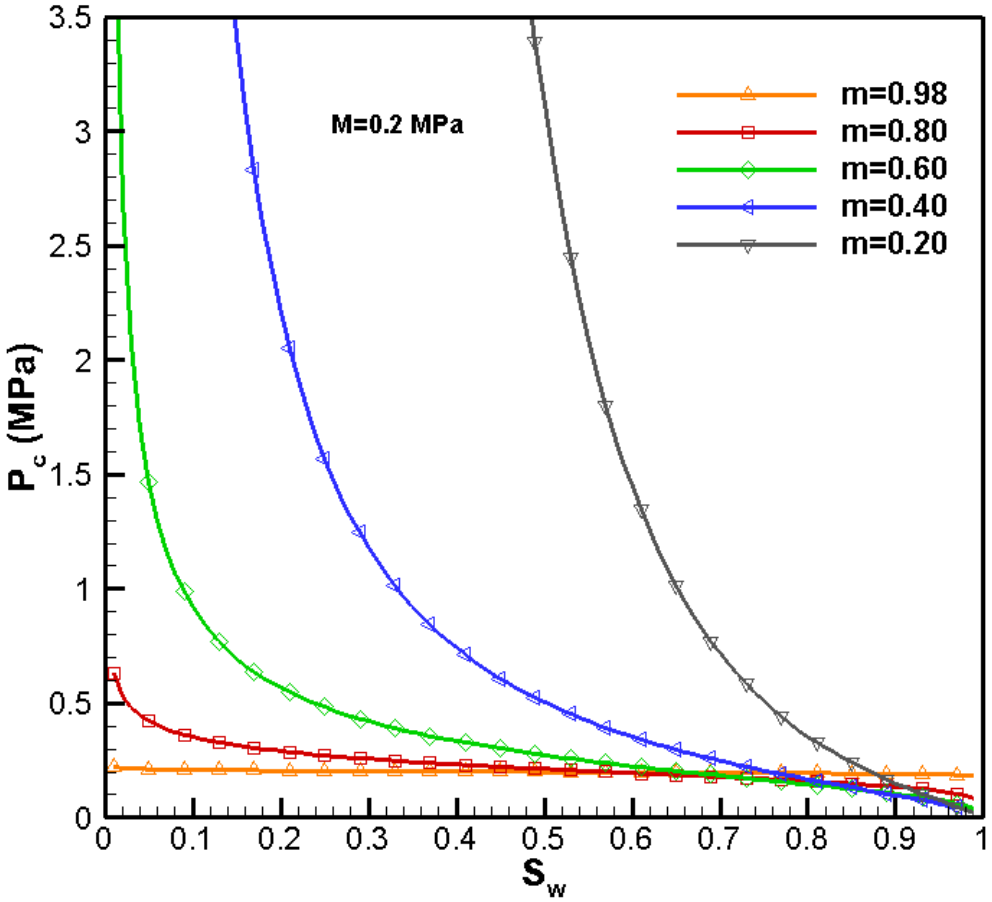

Figure 5-12. The shape of van Genuchten (1980) capillary pressure (Eq. 5.82) for M=0.2, S_{rw}=0, S_{ro}=0 and different values of parameter *m*

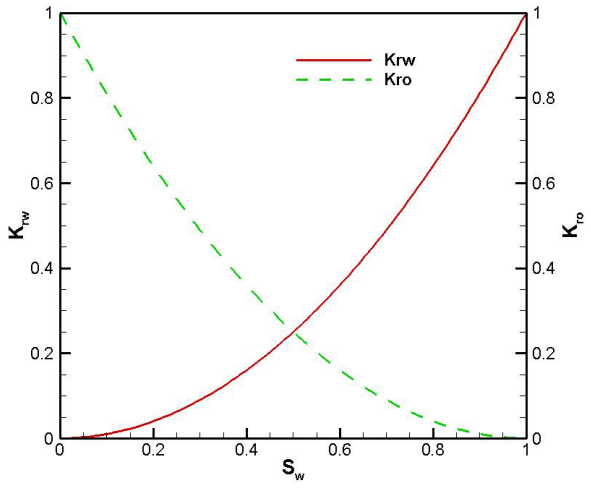

Figure 5-13. Relative permeability as a function of water saturation based on modified Brooks and Corey model used in the waterflooding simulation (parameters given in Table 5-4)

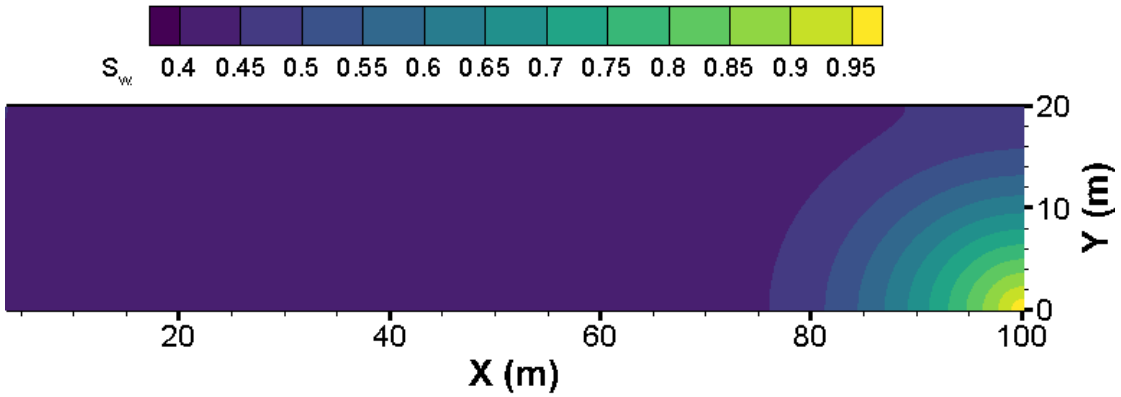

Figure 5-14 Water saturation distribution after 35 days of injection

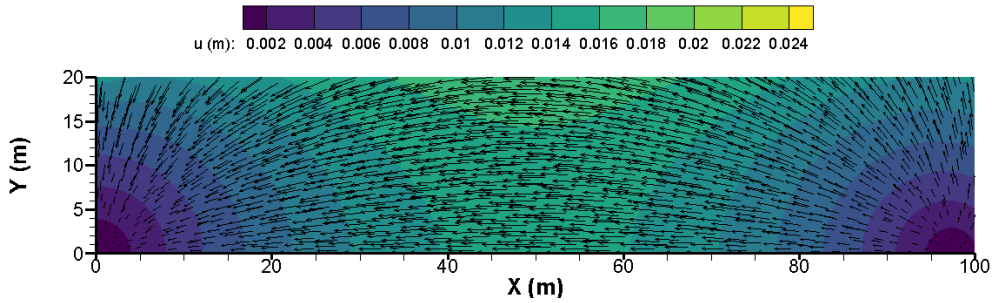

Figure 5-15. Rock displacement magnitude and direction after 35 days of waterflooding

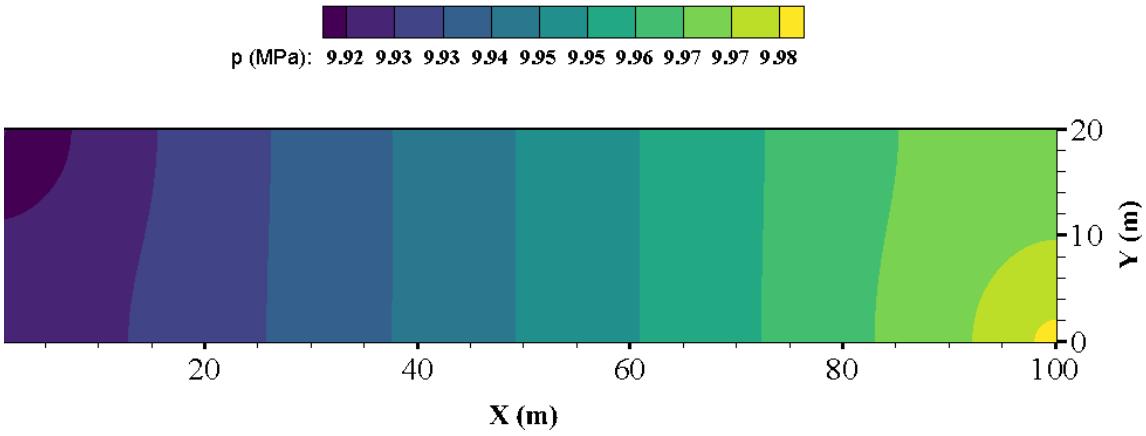

Figure 5-16. Pore pressure distribution after 35 days of waterflooding

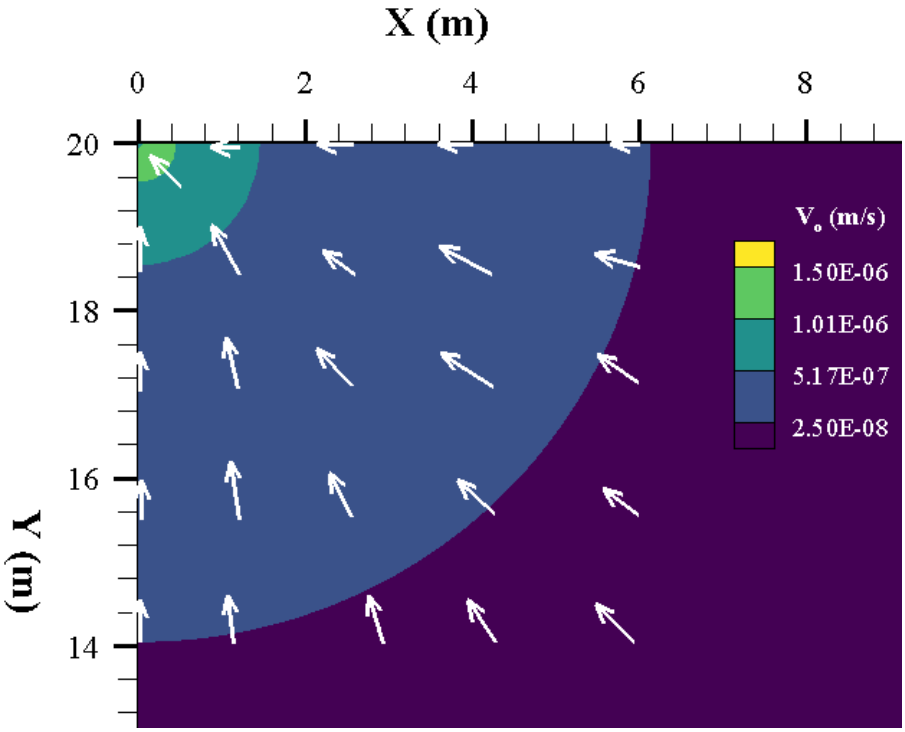

Figure 5-17. Oil velocity direction (vectors) and magnitude (contours) near the production point

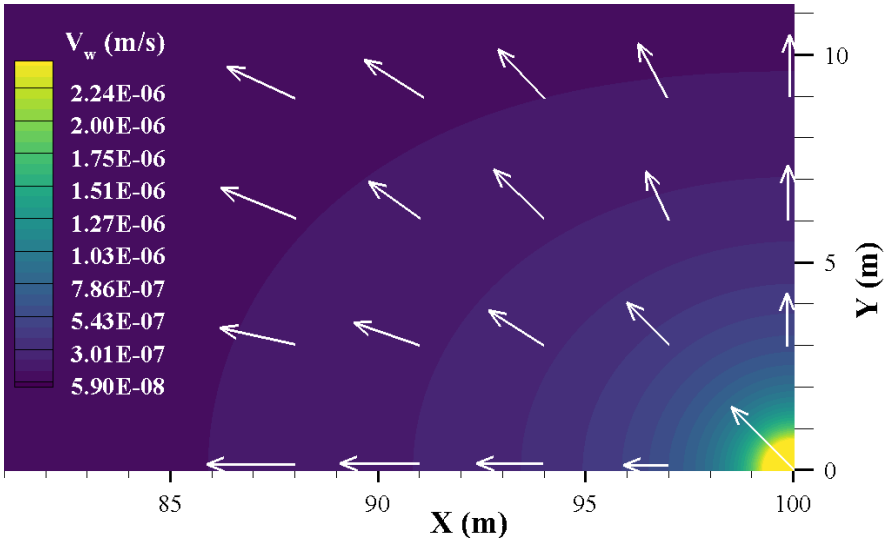

Figure 5-18. Water velocity direction (vectors) and magnitude (contours) near the injection point

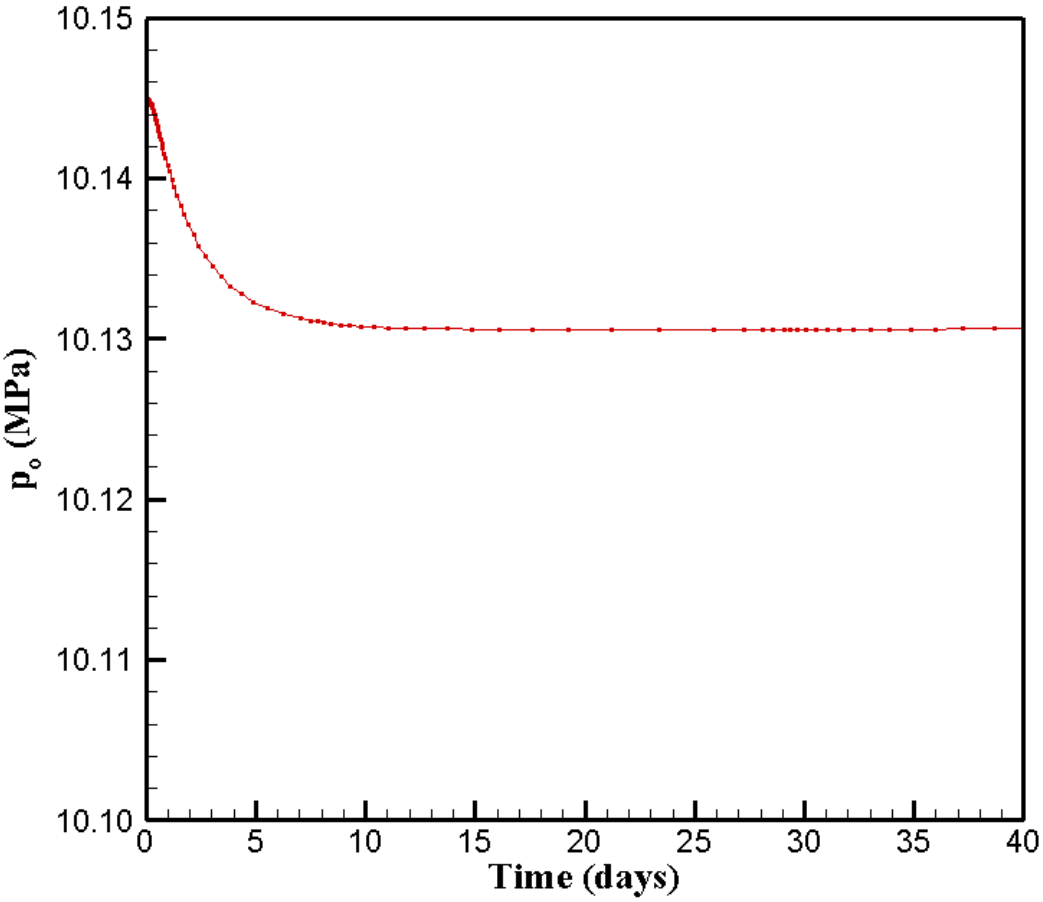

Figure 5-19. Evolution of oil pressure at the monitoring point

In the following section, 3D simulation of production from a hydraulic fracture in a two-phase reservoir is performed.

5.6.2 Production from a single fracture

In conventional reservoirs, capillary pressure is relatively small (Siripatrachai et al. 2017) and is sometimes ignored. However, in tight formations such as shales, the capillary pressure can be high and in the order of thousands of psi (Holditch 1979). Neglecting the inherent high capillary pressure can lead to inaccurate prediction of production performance. This study evaluates the geomechanical effects of producing oil above bubble point pressure in a low permeability unconventional oil formation with two phases.

A single planar hydraulic fracture intersected by a horizontal well in a rectangular reservoir is simulated in this example problem. Fracture is perpendicular to the horizontal well penetrating total reservoir thickness and is assumed to be planar. The pay zone is 60 m thick bounded by a 400 m layer of overburden on the top and 400 m of underburden on the bottom. The permeability of the bounding layers is negligible, so flow occurs mainly within the reservoir. The reservoir domain is 1200 m× 1200 m× 860 m in X, Y and Z directions respectively. Fracture dimensions are given in Table 5-6. A normal faulting stress regime (i.e., $\sigma_V > \sigma_H > \sigma_h$) with an in-situ horizontal stress contrast equal to 0.69 (MPa) is assumed. The minimum horizontal (σ_h) and maximum horizontal (σ_H) in situ stresses are acting along the x- and y-axes, respectively, and the vertical in situ stress (σ_V) is acting along the z-axis. The production well is drilled parallel to the minimum horizontal stress (σ_h) direction (i.e., along the x-axis in this case). The production fracture is assumed to be fully propped, with the initial uniform fracture aperture equal to 1.0 cm. Figure 5-20 shows a section of the model domain passing through the fracture. Due to symmetry in the XY, YZ and XZ planes, only 1/8th of the geometry is modeled, and the plane of symmetry boundary conditions are applied on the XY, XZ and YZ planes, respectively. No flow conditions are imposed at all outer boundaries and planes of symmetry. The zero normal displacements are applied to the outer and bottom boundary. The production from the fracture is carried out at a constant bottomhole pressure (BHP) of 9.3 MPa for 4 years. The fracture is modeled explicitly with a structured fine grid representation. The refined grid can capture large pressure gradients near matrix-fracture interface. In total, the mesh consists of 141,192 nodes and 132,860 hexahedral elements. The initial time step is 0.05 s and it is increased by a factor of 1.25 in the subsequent time steps. The entire reservoir is initialized to 18.1 MPa in-situ pore pressure.

The relative permeability to oil and water in the matrix and fracture is assigned according to the relations shown in Figure 5-21a and 5-21b. The capillary pressure curve for shale matrix is based on the empirical relation given by Nojabaei et al. (2014) for Bakken rock and shown in Figure 5-21c. The in-situ stresses and poroelastic properties of the reservoir rocks are listed in Table 5-7.

Two cases are considered and compared to see the difference between production from an oil saturated reservoir (single phase) and a two-phase reservoir consisting of oil and water. For the oil saturated reservoir, properties of oil are identical to the oil properties for two-phase reservoir and the initial pressure is the same for two cases. The simulation results are presented in a horizontal cross-section in the central XY-plane passing through the production well. Comparisons of the reservoir pore pressure distribution from single phase and multiphase FEM models after 18 days and 4 years of production are shown in Figure 5-22a–d. It can be observed that at the early stage of production, the difference between single phase and multiphase flow is small, but after 4 years, the fluid diffusion front advances faster in the case of single-phase flow compared to multiphase flow. The relative permeability causes the fluid to have more resistance to flow compared to the oil saturated case. This is because the sum of effective permeability to oil and water phases is less than the absolute permeability of the matrix. The impact of reservoir depletion on the total horizontal stress components σ_{xx} and σ_{yy} after 18 days and 4 years is shown in Figures 5-23 and 5-24, which show that their magnitude have decreased from their in-situ values in the depletion zone for both flow cases. However, a larger extent of reservoir experienced stress decrease in the single flow case. Also, over time, as diffusion front advances, more areal extent of the res-

ervoir experiences decreased stresses in both X and Y direction. Figure 5-25 shows the cumulative production from the fractured well for single and multi-phase flow cases. In the case of single-phase flow, the resistance to flow is lower; Consequently, the cumulative oil recovery is 42 percent higher than two-phase flow scenario. The water production rate is small in the two-phase flow case since the initial water saturation is 0.32 and from Figure 5-21a we can observe that at this saturation, the water relative permeability is very small which makes the water phase nearly immobile. Noting the negligible water production, the total fluids production is 58% higher in case of single-phase flow compared to two-phase flow.

Figure 5-26 depicts the rotation of principal stresses after 18 days and 4 years of production for single phase and multiphase flow cases (counterclockwise is positive). A stress reversal zone (red regions) is formed in the vicinity of the fracture where the maximum horizontal stress rotates 90 degrees. It is observed that the extent of stress reversal region has increased over time. Also, since single phase flow diffuses farther into reservoir, the reorientation region is larger compared to multiphase flow case and the rotation evolves as a function of time for both scenarios. Figure 5-27 shows a closer view of pore pressure and trajectories of the local maximum principal stress in the vicinity of fracture. The pore pressure distribution shows an elliptical depletion zone around the production fracture. A significant reorientation of the stress state in the vicinity of the production fracture has occurred with more pronounced rotation in case of single flow. The isotropic point (definition is given in section 4.4) distance from the well after 4 years of production has decreased from 18.12 m for single-phase case to 15.03 m for two-phase case. This represents a 17% decrease in the extent of

reorientation zone. After 18 days of production the isotropic point is 5.05m away from production well in single-phase scenario and 2.85 m in two-phase scenario showing a reduction of 43.5%.

Figure 5-28 shows the distribution of water saturation and maximum principal stress trajectories for two-phase flow after 18 days and 4 years of production. It can be observed that water saturation increases as a result of depletion. Since initial water saturation is relatively small (0.32), the relative permeability to water is much less than relative permeability to oil (Figure 5-19a). Therefore, compared to water, oil can flow much easier in the reservoir which leads to an increase in the water saturation in the reservoir as oil flows into the well and is produced. As diffusion front advances, more regions of the reservoir experience the increase in the saturation. As expected, the saturation front is also elliptical, similar to the pressure front.

In Figure 5-29, the principal stress reorientation angle along a potential infill well with a distance of 135 m from production well (with the same elevation) is shown at different times for single-phase and two- phase flow cases. It can be observed that before 5 months of production the difference between single-phase and two-phase cases are minimal but after 5 months of production the reorientation angle is noticeably larger for single-phase model. After five months of production, the maximum difference is 28% or 2.14 degrees. After 4 years of production, the maximum difference is 15.2 degrees or 23%. The difference between the reorientation angles is significant and can introduce meaningful difference in the propagation path of new fractures stimulated from infill well. It can be concluded that con-

sidering two-phase model can greatly improve our predictions of infill fracture paths. Considering that the case studied in this example pertains to 50% depletion, a higher depletion case may lead to greater differences and it's an important case to be studied in future work.

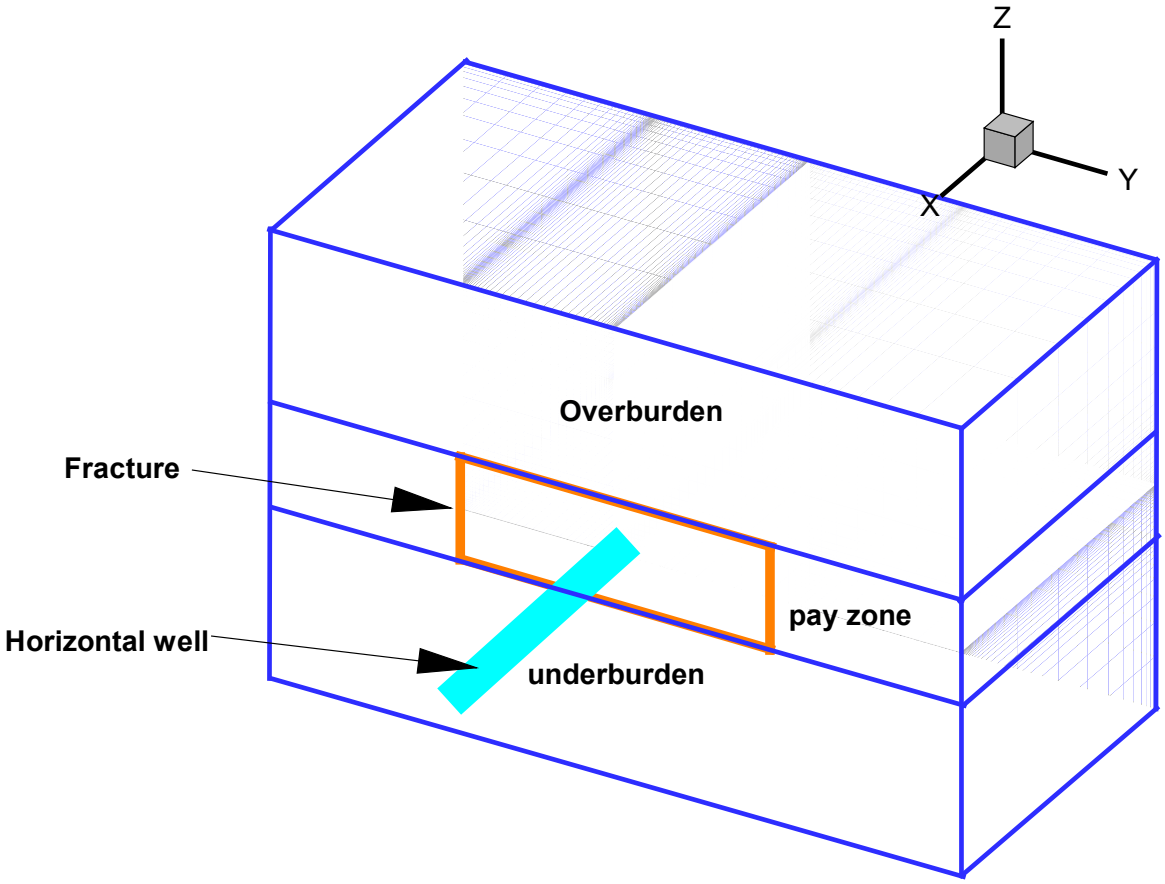

Figure 5-20. Schematic 3D view of a section of reservoir model crossing fracture plane

Table 5-6. Hydraulic fracture properties

Parameter	**Units**	**Value**
Fracture half-length, X_f	m (ft)	90.0 (295.3)
Fracture height, h_f	m (ft)	60.0 (196.8)
Fracture aperture, w	cm (ft)	1.0 (0.03)

Table 5-7. Reservoir properties for the single fracture analysis

Parameter	Value
Water viscosity, μ_w (Pa.s)	5.0×10^{-4}
Oil viscosity, μ_o (Pa.s)	3.6×10^{-4}
Water bulk modulus, K_w (Mpa)	2.5×10^{9}
Oil bulk modulus, K_o (MPa)	3.33×10^{8}
Vertical stress , σ_V (Mpa)	55.16
Max. horizontal stress, σ_H (Mpa)	42.06
Min. horizontal stress, σ_h (Mpa)	41.37
Initial pressure, p (Mpa)	18.10
Bottomhole oil pressure, p_{well} (MPa)	9.3
Pay zone thickness, d (m)	60.0
Young's modulus, E (Gpa)	20.0
Poisson's ratio, ν	0.22
Matrix permeability, k (μd)	0.3
Matrix porosity, n	0.09
Biot's coefficient, α	1.0
Initial water saturation, S_{wi}	0.32
Irreducible water saturation, S_{rw}	0.20

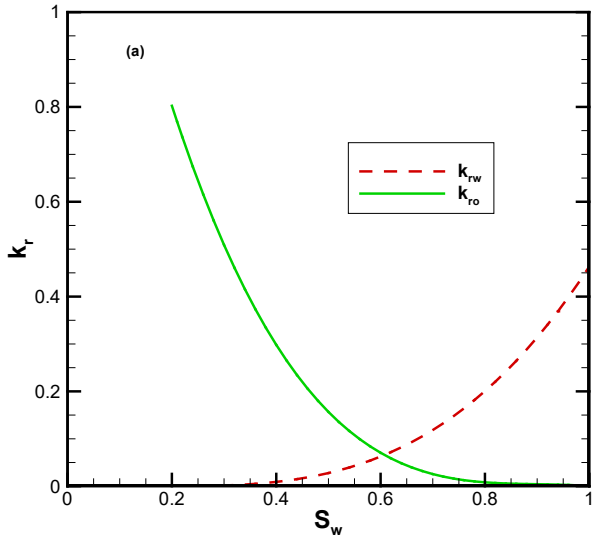

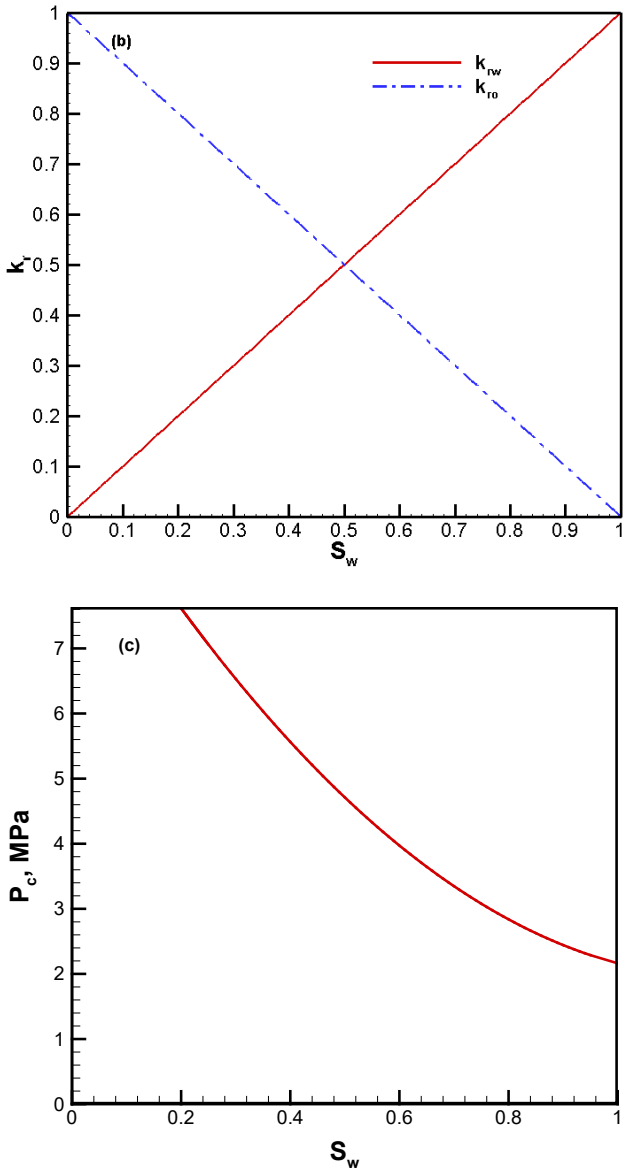

Figure 5-21. Relative permeability and capillary pressure relations used in the model (a) matrix relative permeability (Wang and Leung 2015) (b) fracture relative permeability (Wang and Leung 2015) (c) capillary pressure (Nojabaei et al. 2014).

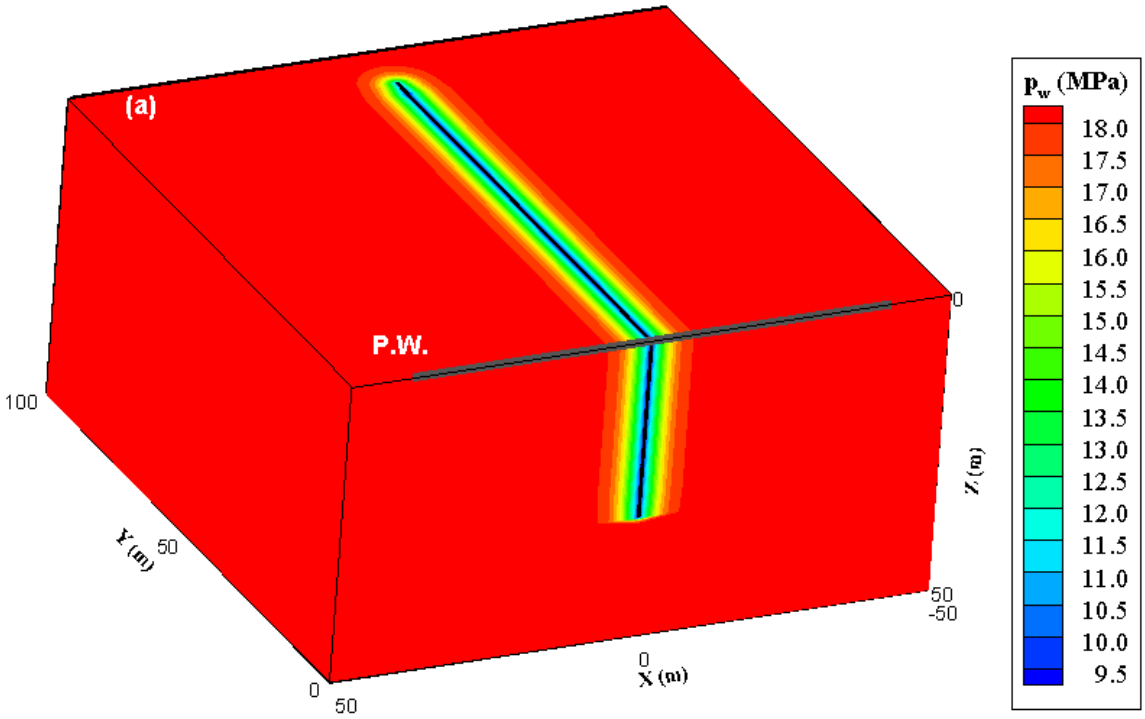
(a)
P.W.
100
Y (m)
50
0
0
50
X (m)
0
50
-50
Z (m)
p_w (MPa)
18.0
17.5
17.0
16.5
16.0
15.5
15.0
14.5
14.0
13.5
13.0
12.5
12.0
11.5
11.0
10.5
10.0
9.5

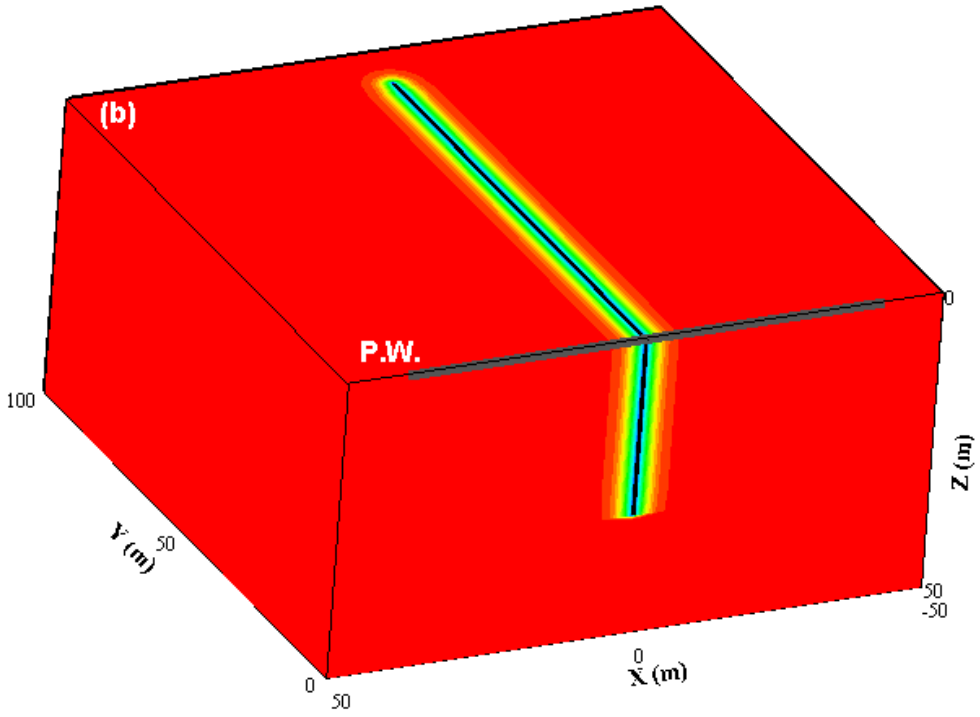
(b)
P.W.
100
Y (m)
50
0
0
50
X (m)
0
50
-50
Z (m)

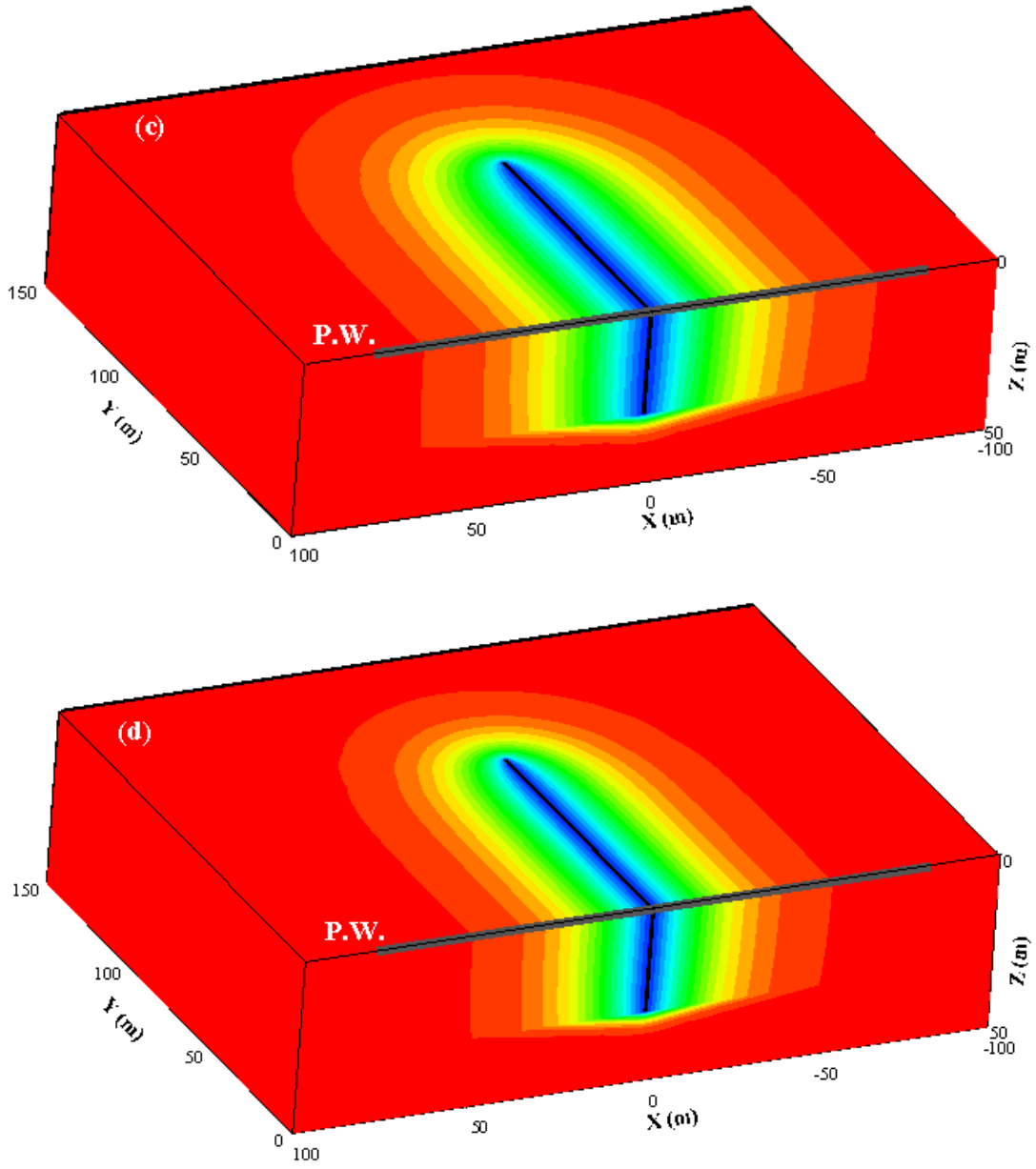

Figure 5-22. Pore pressure distribution in the vicinity of fracture after 18 days (a, b) and 4 years of production (c, d). One-phase analysis: (a, c); two-phase analysis: (b, d). It is observed that the diffusion front advances slower in the case of two-phase model. The coefficient of diffusion is decreased due to the effect of relative permeability in a two-phase flow, resulting in less diffusion.

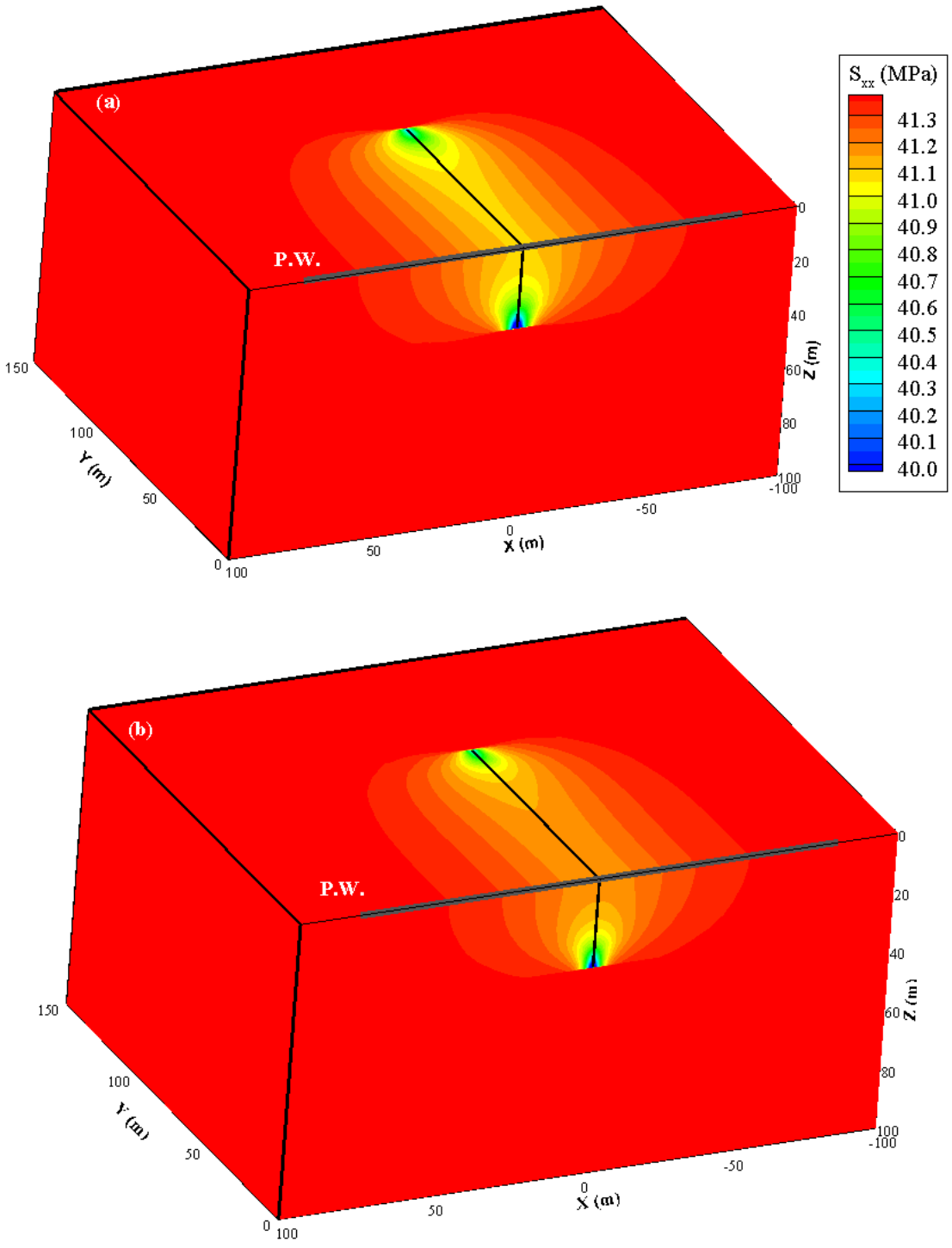
(a)
P.W.
S_{xx} (MPa)
41.3
41.2
41.1
41.0
40.9
40.8
40.7
40.6
40.5
40.4
40.3
40.2
40.1
40.0
150
100
50
0
Y (m)
100
50
0
-50
-100
X (m)
0
20
40
60
80
100
Z (m)
(b)
P.W.
150
100
50
0
Y (m)
100
50
0
-50
-100
X (m)
0
20
40
60
80
100
Z (m)

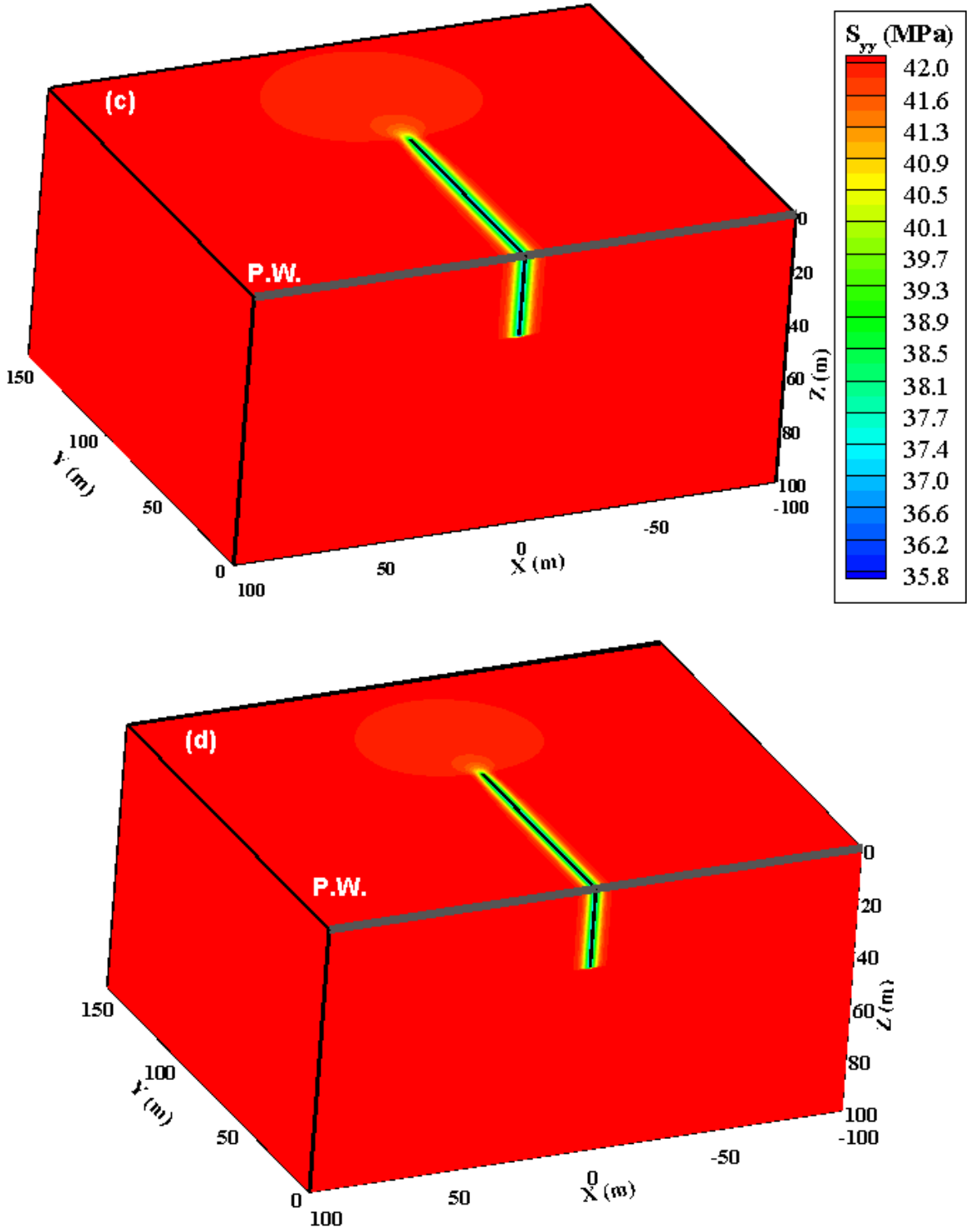

Figure 5-23. Total stress distribution after 18 days of production (a) horizontal stress in X direction for one phase model, (b) horizontal stress in X direction for two-phase model, (c) horizontal stress in Y direction for one phase model, (d) horizontal stress in Y direction for two-phase model

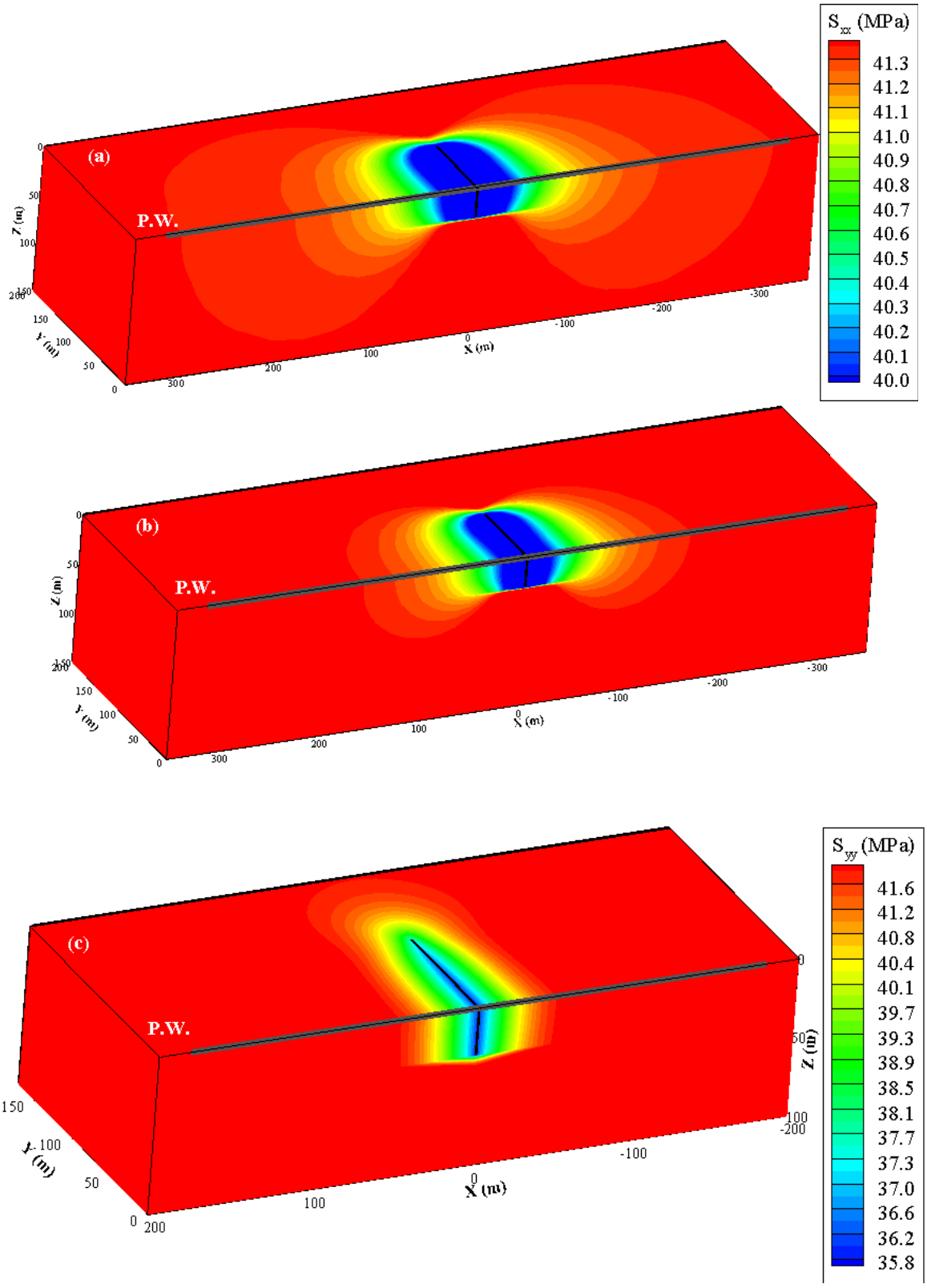
(a)
P.W.
Z (m)
Y (m)
X (m)
S_{xx} (MPa)
41.3
41.2
41.1
41.0
40.9
40.8
40.7
40.6
40.5
40.4
40.3
40.2
40.1
40.0
(b)
P.W.
Z (m)
Y (m)
X (m)
(c)
P.W.
Z (m)
Y (m)
X (m)
S_{yy} (MPa)
41.6
41.2
40.8
40.4
40.1
39.7
39.3
38.9
38.5
38.1
37.7
37.3
37.0
36.6
36.2
35.8

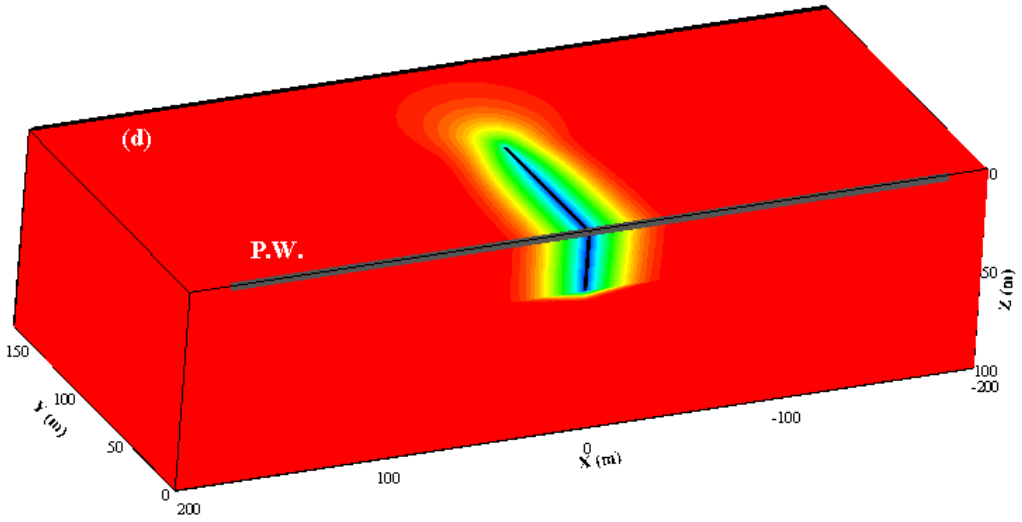

Figure 5-24. Total stress distribution after 4 years of production (a) horizontal stress in X direction for one phase model, (b) horizontal stress in X direction for two-phase model, (c) horizontal stress in Y direction for one phase model, (d) horizontal stress in Y direction for two-phase model

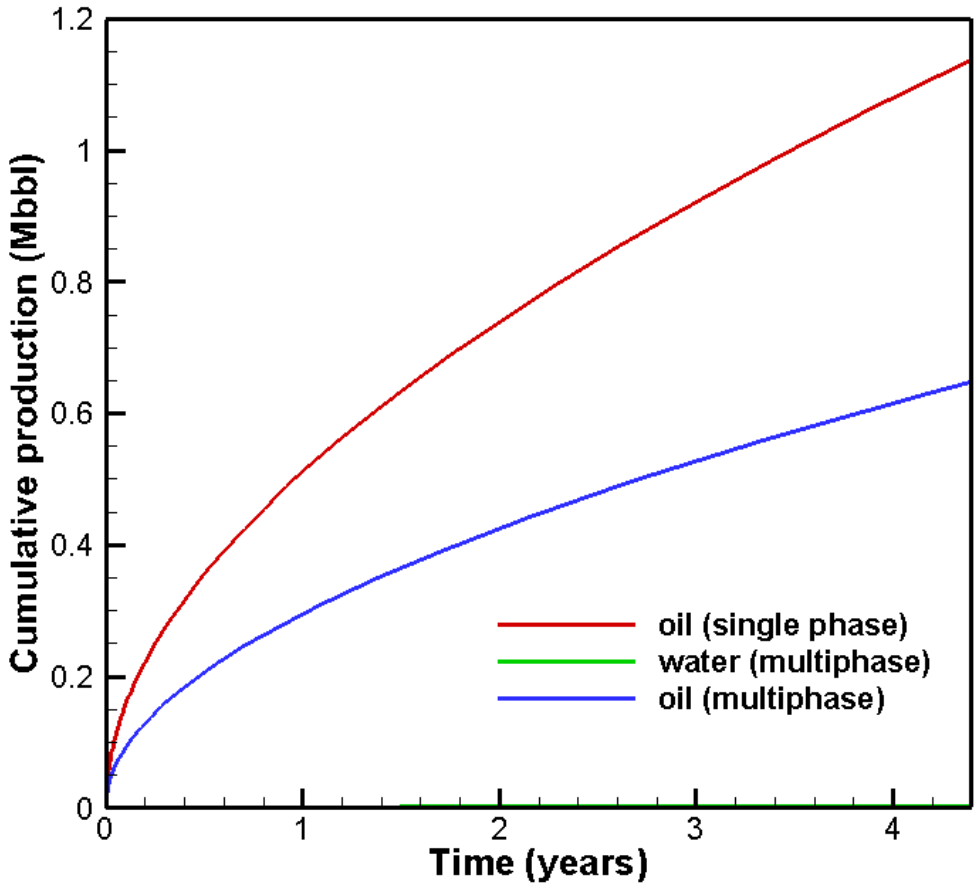

Figure 5-25. Comparison of cumulative production for single and 2-phase flow cases

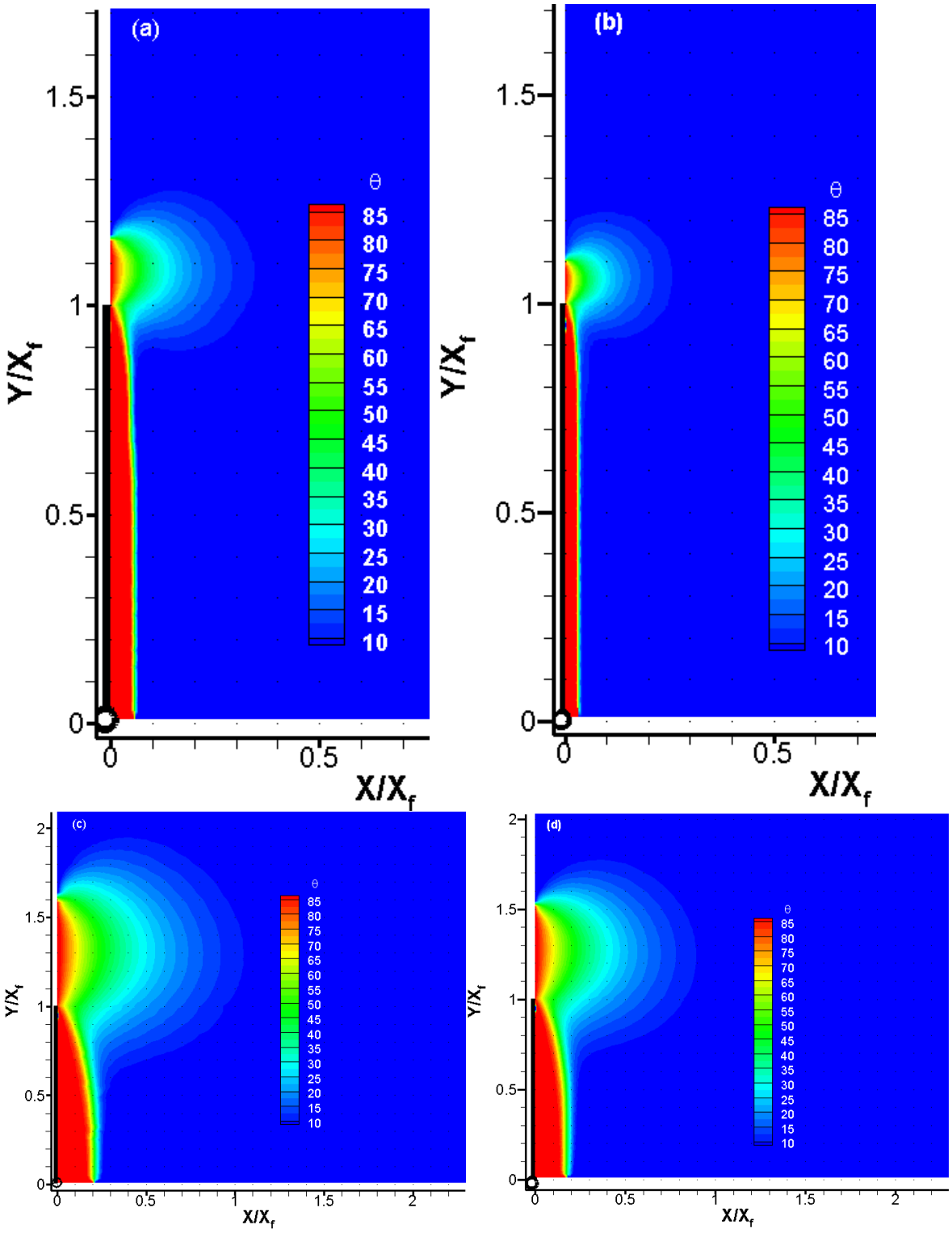

Figure 5-26. Rotation of maximum principal stress after 18 days (a and b), and 4 years (c and d) of production for single phase flow (a and c), and multiphase flow (b and d).

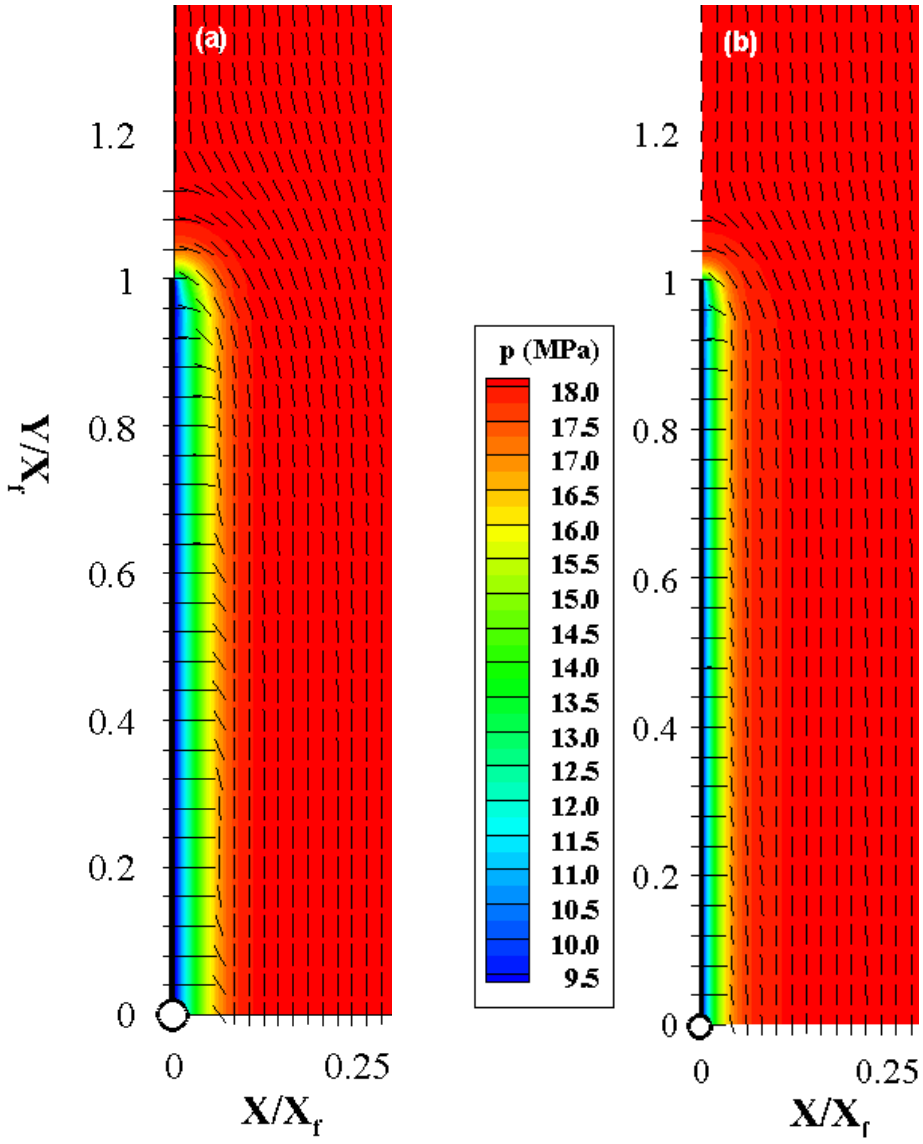
(a)
(b)
1.2
1
0.8
0.6
0.4
0.2
0
0
0.25
Y/X_f
X/X_f
p (MPa)
18.0
17.5
17.0
16.5
16.0
15.5
15.0
14.5
14.0
13.5
13.0
12.5
12.0
11.5
11.0
10.5
10.0
9.5

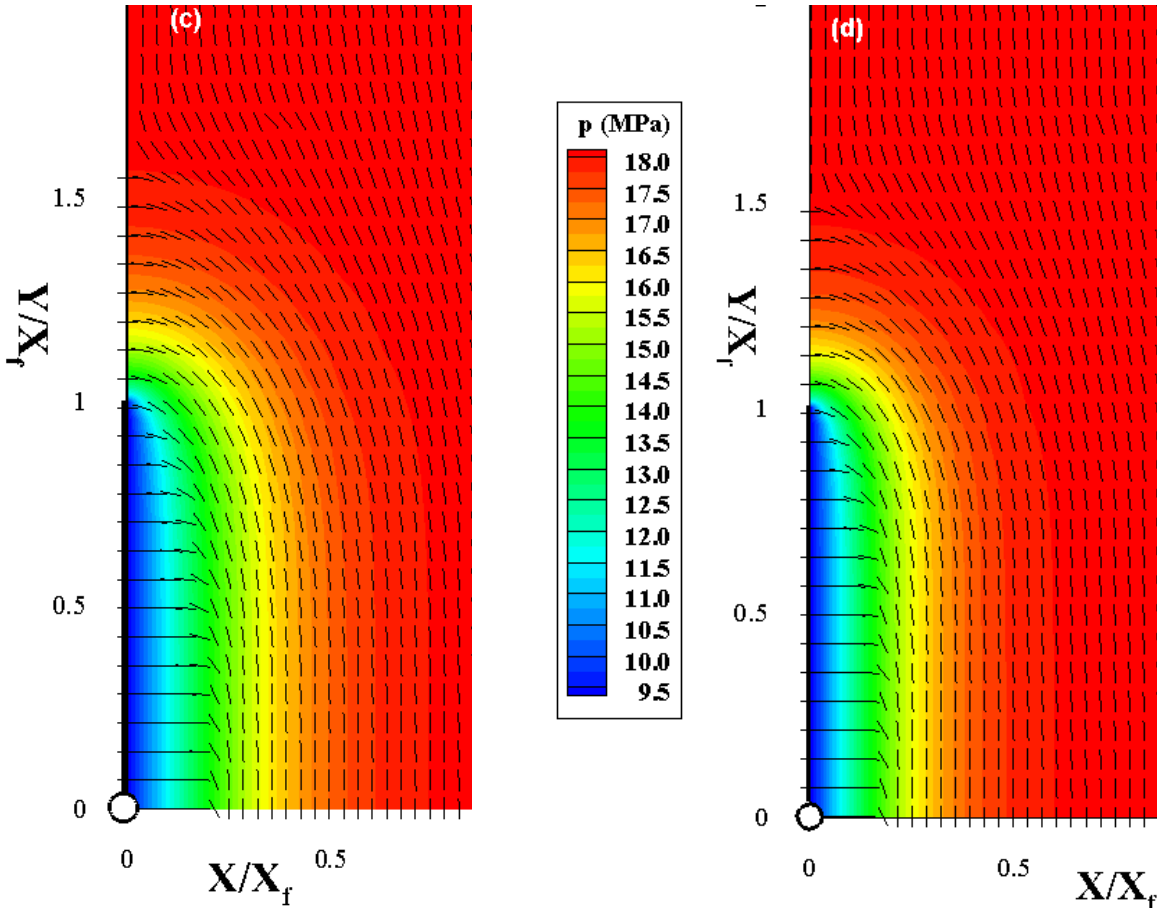

Figure 5-27. Direction of maximum principal stress and pressure distribution in the vicinity of fracture after 18 days (a, b) and 4 years of production (c, d) for one-phase analysis (a, c), two-phase analysis (b, d). For all cases, the stress reversal zone is more extensive in case of one phase flow since pore pressure diffuses more in this case compared to multi-phase flow

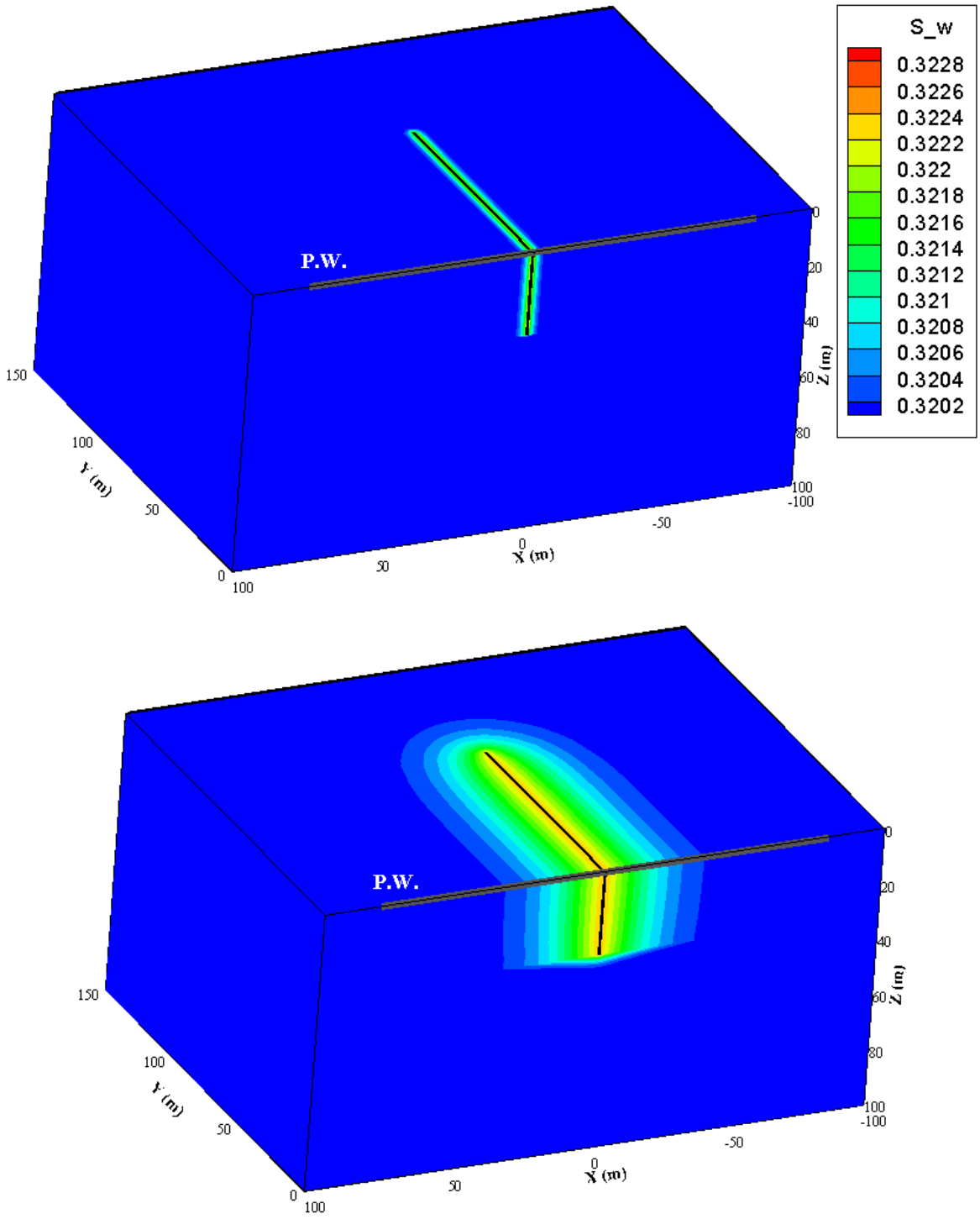

Figure 5-28. Distribution of saturation and direction of max. principal stress after 18 days (top) and 4 years of production (bottom)

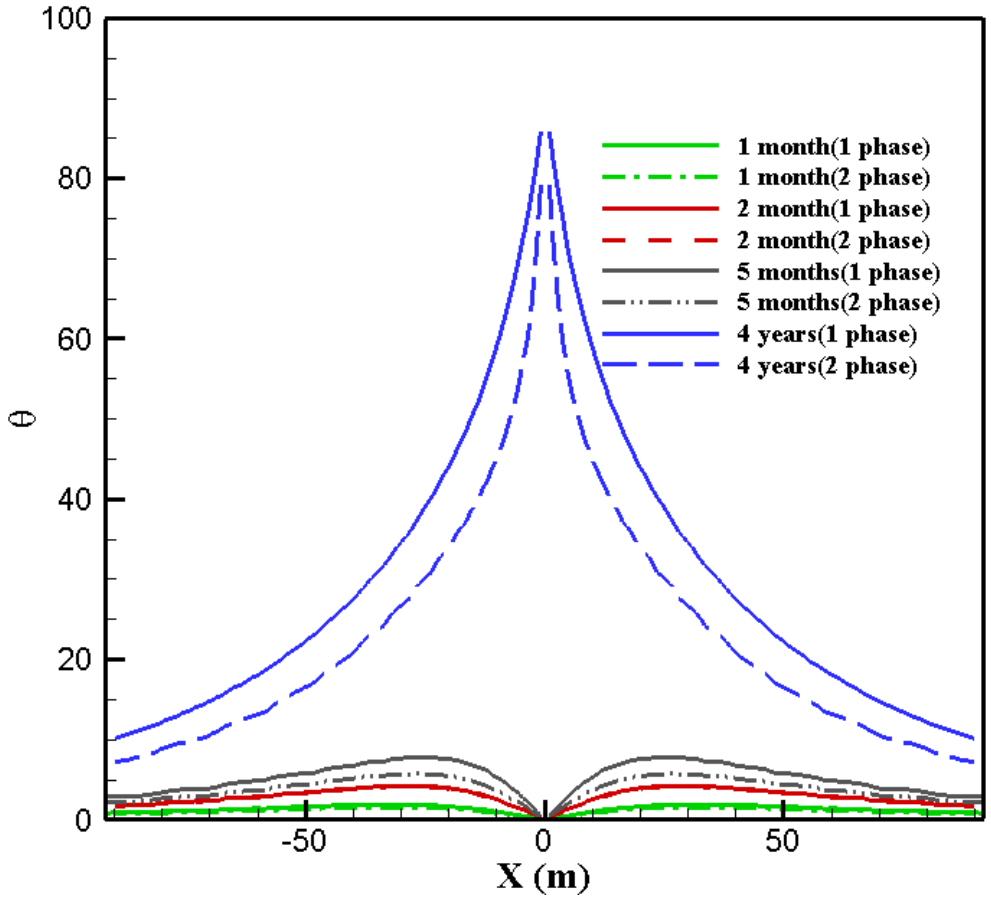

Figure 5- 29. Comparison of angle of principal stress reorientation in case of singe-phase and two-phase flow at different production times

5.7 Conclusion

A two-phase finite element-based geomechanical model is presented using fully coupled 3D poroelastic simulation. The poroelastic model used in this study is a computationally efficient numerical technique for porous rock deformation and matrix fluid flow simulations when two fluids are present. The model was verified for two cases involving gravity drainage of a saturated soil column and the consolidation analysis of an unsaturated soil. Two case studies were simulated involving waterflooding an oil reservoir and production from a frac-

ture in a two-phase reservoir. Capillary effect is included in the formulations, verified examples and case studies unlike previous studies in this field which neglected it for most of their solved examples. The modeling results show that production from production w
ell fracture leads to a nonuniform reduction of the reservoir pore pressure around the production well, leading to an anisotropic decrease of the total stress, resulting in stress reorientation and/or reversal.

Production induced stress reorientation can be more realistically evaluated using this model compared to single-flow models and stimulation efficiency can be increased when designing infill horizontal wells.

6. Conclusions and future work

In this study, a fully coupled poroelastic model was developed to study various phenomena in unconventional reservoir development. The model has been applied to a variety of benchmark and example problems with different characteristics including plain strain, axisymmetric, 3D poro-thermoelastic, 3D single phase poroelastic and 3D multiphase poroelastic cases. All the field equations are solved using finite element method and verified with appropriate analytical solutions. The simulator is based on finite element method and capable of modeling field scale reservoir in three dimensions. The present model can handle both structured as well as unstructured meshes. Reservoir rock heterogeneity can be accounted for in this model.

The axisymmetric model was used to model a wellbore in a poroelastic medium which is injected at a constant rate. The distribution of induced pore pressure in the reservoir was compared with available solutions. Drilling a vertical wellbore in porous rock formation in a non-hydrostatic stress field was addressed by decomposing the problem to three problems (modes) and each mode solution was compared with the corresponding analytical solution. Mandel's problem as a popular benchmark problem for validating numerical codes of poroelasticity was used to validate the model. Coupled thermo-hydro-mechanical behavior of saturated media is very important in many applications including enhanced geothermal systems, wellbore stability and coalbed methane exploitations. Our model was successfully applied to model a buried cylindrical heat source in porous rock and was able to replicate the induced pore pressure and temperature distribution in the medium.

The 3D geomechanical study of frac-hits is discussed in Chapter 4. The current method has been applied to different cases to better understand the mechanisms associated with this

problem including production from a single vertical well, a single vertical fracture, two horizontal wells each having 10 stages with one cluster per stage, and finally a one horizontal well with 6 stages in a layered reservoir. It was observed that production time has a significant impact in stress reorientations. At early stages of production, stress reorientation might not be observed but over time reorientation happens. Also, the in-situ stress contrast is very important in predicting the stress reorientation. When in-situ stress contrast was very high, principal stresses didn't rotate compared with case where in-situ stress contrast was small. It's important to note that coupled poroelastic phenomena can be complex and the exact behavior of porous rock is sometimes hard to predict unless a simulation model is built. For example, in early stages of production from two parallel horizontal wells, the component of stress perpendicular to fractures slightly increased in the infill region. Same behavior was observed in poroelastic displacement discontinuity models for similar problems (Masouleh et. al. 2020). By optimizing well and fracture spacing, fracturing fluid viscosity, and the timing of refracturing job, frac-hit problems can be minimized.

In chapter 5, the poroelastic model was expanded to include 2-phase problems. In the formulation of the model, capillary pressure was accounted for and in all the solved problems its effect is included. The model was verified against known solutions including gravity drainage of a saturated soil, consolidation analysis of unsaturated soil, and waterflooding of an oil reservoir. The model was then used to simulate production from a single fracture intersected by a horizontal well. The available reservoir simulation models incorporate the geomechanical effects by iteratively coupling approach. This method will reduce the accuracy of the solution. Another restriction is that to maintain stability, time step sizes have

limitations (Horgue et al., 2014). In contrast, fully coupling the flow and deformation processes results in unconditional stability and internal consistency since the full system of equations are solved simultaneously.

By comparing the performance of production from a fracture in one phase reservoir vs. a two-phase reservoir, it was observed that due to relative permeability effects, the diffusion front expanded more into the reservoir in case of single-phase flow. Consequently, less principal stress reorientation was observed in the 2-phase flow problem. Furthermore, the cumulative production of oil in the single-phase case is much greater than the total fluid produced in the 2-phase flow case. This model can be further applied to more complex cases including multiple horizontal wells and fractures and study the frac-hit risk in those conditions.

References

Aboustit, B.L., Advani, S.H. and Lee, J.K., 1985. Variational principles and finite element simulations for thermo-elastic consolidation. International journal for numerical and analytical methods in geomechanics, 9(1), pp.49-69.

Abousleiman, Y.N. and Kanj, M.Y., 2004. The generalized Lamé problem—part II: applications in poromechanics. J. Appl. Mech., 71(2), pp.180-189.

Agharazi, A., and Kashikar, S. 2016. A geomechnical study of refracturing based on microseismic observations-case study of Haynesville and Eagle Ford wells. Unconventional Resources Technology Conference, San Antonio, TX, USA: 1-19.

Asadi, R. and Ataie-Ashtiani, B., 2015. A comparison of finite volume formulations and coupling strategies for two-phase flow in deforming porous media. Computers and Geotechnics, 67, pp.17-32.

Berchenko, I. and Detournay, E., 1997. Deviation of Hydraulic Fractures through Poroelastic Stress Changes Induced by Fluid Injection and Pumping. Int. J. Rock Mech. Min. Sci., Vol. 34, No. 6: 1009-1019.

Biot, M.A., 1941. General theory of three-dimensional consolidation. Journal of applied physics, 12(2), pp.155-164.

Biot, M.A. and Willis, D.G., 1957. The elastic coefficients of the theory of consolidation. J Appl Mech, 15, pp.594-601.

Bishop, A.W., 1959. The principle of effective stress. Teknisk ukeblad, 39, pp.859-863.

Booker, J.R. and Savvidou, C., 1985. Consolidation around a point heat source. International Journal for Numerical and Analytical Methods in Geomechanics, 9(2), pp.173-184.

Brooks, R. and Corey, T., 1964. Hydraulic properties of porous media. Hydrology Papers, Colorado State University, 24, p.37.

Brownell Jr, D.H., Garg, S.K. and Pritchett, J.W., 1977. Governing equations for geothermal reservoirs. Water Resources Research, 13(6), pp.929-934.

Charoenwongsa, S., Kazemi, H., Miskimins, J. and Fakcharoenphol, P., 2010, January. A fully coupled geomechanics and flow model for hydraulic fracturing and reservoir engineering applications. In Canadian Unconventional Resources and International Petroleum Conference. Society of Petroleum Engineers.

Chen, G. and Ewy, R.T., 2005. Thermoporoelastic effect on wellbore stability. SPE Journal, 10(02), pp.121-129.

Cheng, A.H.D. and Detournay, E., 1988. A direct boundary element method for plane strain poroelasticity. International Journal for Numerical and Analytical Methods in Geomechanics, 12(5), pp.551-572.

Chun, K.H., 2013. Thermo-poroelastic fracture propagation modeling with displacement discontinuity boundary element method (Doctoral dissertation).

Coussy, O., 2004. Poromechanics. John Wiley & Sons.

Cryer, C.W.A., 1963. A comparison of the three-dimensional consolidation theories of Biot and Terzaghi. The Quarterly Journal of Mechanics and Applied Mathematics, 16(4), pp.401-412.

Dakshanamurthy, V. and Fredlund, D.G., 1981. A mathematical model for predicting moisture flow in an unsaturated soil under hydraulic and temperature gradients. Water Resources Research, 17(3), pp.714-722.

Dean, R.H., Gai, X., Stone, C.M. and Minkoff, S.E., 2006. A comparison of techniques for coupling porous flow and geomechanics. Spe Journal, 11(01), pp.132-140.

Detournay, E. and Cheng, A.H.D., 1993. Fundamentals of poroelasticity. In Analysis and design methods (pp. 113-171). Pergamon.

Diersch, H.J.G., 2013. FEFLOW: finite element modeling of flow, mass and heat transport in porous and fractured media. Springer Science & Business Media.

Duveau, G., Jia, Y. and Shao, J.F., 2008, January. A simplified hydro-mechanical approach taking into account gas effect in underground waste disposal. In The 42nd US Rock Mechanics Symposium (USRMS). American Rock Mechanics Association.

Economides, M.J., Hill, A.D., Ehlig-Economides, C. and Zhu, D., 2013. Petroleum production systems. Pearson Education.

Ehlers, W., Graf, T. and Ammann, M., 2004. Deformation and localization analysis of partially saturated soil. Computer methods in applied mechanics and engineering, 193(27-29), pp.2885-2910.

Eker, E., Uzun, I. and Kazemi, H., 2017, February. Numerical simulation of dual-porosity multiphase flow using poroelasticity theory. In SPE Reservoir Simulation Conference. Society of Petroleum Engineers.

Elbel, J.L. and Mack, M.G.1993. Refracturing: Observations and Theories. SPE 25464, the Production Operations Symposium, Oklahoma City, OK, USA: 21-23.

Fall, M., Nasir, O. and Nguyen, T.S., 2014. A coupled hydro-mechanical model for simulation of gas migration in host sedimentary rocks for nuclear waste repositories. Engineering Geology, 176, pp.24-44.

Gai, X., 2004. A coupled geomechanics and reservoir flow model on parallel computers (Doctoral dissertation).

Gao, C. and Gray, K.E., 2017, October. The development of a coupled geomechanics and reservoir simulator using a staggered grid finite difference approach. In SPE Annual Technical Conference and Exhibition. Society of Petroleum Engineers

Garipov, T.T., Tomin, P., Rin, R., Voskov, D.V. and Tchelepi, H.A., 2018. Unified thermo-compositional-mechanical framework for reservoir simulation. Computational Geosciences, 22(4), pp.1039-1057

Gawin, D., Schrefler, B.A. and Galindo, M., 1996. Thermo-hydro-mechanical analysis of partially saturated porous materials. Engineering Computations: Int J for Computer-Aided Engineering, 13(7), pp.113-143.

Gawin, D., Simoni, L. and Schrefler, B.A., 1997. Numerical model for hydro-mechanical behavior in deformable porous media: A benchmark problem.

Gdanski, R.D., Fulton, D.D. and Shen, C., 2009. Fracture-Face-Skin Evolution During Cleanup. SPE Prod & Oper 24 (1): 22–34. SPE-101083-PA.

Geuzaine, C. and Remacle, J.F., 2009. Gmsh: A 3-D finite element mesh generator with built-in pre-and post-processing facilities. International journal for numerical methods in engineering, 79(11), pp.1309-1331.

Ghassemi, A. and Diek, A., 2003. Linear chemo-poroelasticity for swelling shales: theory and application. Journal of Petroleum Science and Engineering, 38(3-4), pp.199-212.

Ghassemi, A. and Zhang, Q., 2006. Porothermoelastic analysis of the response of a stationary crack using the displacement discontinuity method. Journal of engineering mechanics, 132(1), pp.26-33.

Ghassemi, A., Nygren, A. and Cheng, A., 2008. Effects of heat extraction on fracture aperture: A poro–thermoelastic analysis. Geothermics, 37(5), pp.525-539.

Ghassemi, A., X., Zhou, and C., Rawal. 2013. A three-dimensional poroelastic analysis of rock failure around a hydraulic fracture. J. of Petro. Sci. and Eng., 108:118-127.

Goerke, U.J., Park, C.H., Wang, W., Singh, A.K. and Kolditz, O., 2011. Numerical simulation of multiphase hydromechanical processes induced by CO2 injection into deep saline aquifers. Oil & Gas Science and Technology–Revue d'IFP Energies nouvelles, 66(1), pp.105-118.

Gutierrez, M., Lewis, R.W. and Masters, I., 2001. Petroleum reservoir simulation coupling fluid flow and geomechanics. SPE Reservoir Evaluation & Engineering, 4(03), pp.164-172

Hassanizadeh, M. and Gray, W.G., 1979. General conservation equations for multi-phase systems: 1. Averaging procedure. Advances in water resources, 2, pp.131-144.

Heidug, W.K. and Wong, S.W., 1996. Hydration swelling of water-absorbing rocks: a constitutive model. International journal for numerical and analytical methods in geomechanics, 20(6), pp.403-430.

Hwang, J., Bryant, E.C. and Sharma, M.M., 2015, February. Stress reorientation in waterflooded reservoirs. In SPE Reservoir Simulation Symposium. Society of Petroleum Engineers.

Islam, M., Hye, A. and Mamun, A., 2017. Nonlinear Effects on the Convergence of Picard and Newton Iteration Methods in the Numerical Solution of One-Dimensional Variably Saturated–Unsaturated Flow Problems. Hydrology, 4(4), p.50.

Jaeger, J.C., Cook, N.G. and Zimmerman, R., 2009. Fundamentals of rock mechanics. John Wiley & Sons.

Jeannin, L., Mainguy, M., Masson, R. and Vidal-Gilbert, S., 2007. Accelerating the convergence of coupled geomechanical-reservoir simulations. International journal for numerical and analytical methods in geomechanics, 31(10), pp.1163-1181.

Ji, L., Settari, A. and Sullivan, R.B., 2009. A novel hydraulic fracturing model fully coupled with geomechanics and reservoir simulation. Spe Journal, 14(03), pp.423-430.

Kaewjuea, W., Senjuntichai, T. and Rajapakse, R.K.N.D., 2011. Poromechanical response of a finite elastic cylinder under axisymmetric loading. International Journal of Solids and Structures, 48(2), pp.346-356.

Khoei, A.R. and Mohammadnejad, T., 2011. Numerical modeling of multiphase fluid flow in deforming porous media: a comparison between two-and three-phase models for seismic analysis of earth and rockfill dams. Computers and Geotechnics, 38(2), pp.142-166.

Kim, J., 2010. Sequential methods for coupled geomechanics and multiphase flow (Vol. 71, No. 04).

Kim, J., Tchelepi, H.A. and Juanes, R., 2013. Rigorous coupling of geomechanics and multiphase flow with strong capillarity. SPE journal, 18(06), pp.1-123.

Kim, N.H., 2014. Introduction to nonlinear finite element analysis. Springer Science & Business Media.

Kirsch, C., 1898. Die theorie der elastizitat und die bedurfnisse der festigkeitslehre. Zeitschrift des Vereines Deutscher Ingenieure, 42, pp.797-807.

Kolditz, O., Bauer, S., Bilke, L., Böttcher, N., Delfs, J.O., Fischer, T., Görke, U.J., Kalbacher, T., Kosakowski, G., McDermott, C.I. and Park, C.H., 2012. OpenGeoSys: an

open-source initiative for numerical simulation of thermo-hydro-mechanical/chemical (THM/C) processes in porous media. Environmental Earth Sciences, 67(2), pp.589-599.

Kumar, D., Masouleh, S.F., Ghassemi, A., Riley, S. and Elliott, B., 2018, August. A 3D Geomechanical Analysis of Horizontal Well Refracturing and "Frac-Hits". In 52nd US Rock Mechanics/Geomechanics Symposium. American Rock Mechanics Association.

Lee, I.S., 2008. Computational techniques for efficient solution of discretized Biot's theory for fluid flow in deformable porous media (Doctoral dissertation, Virginia Tech).

Lewis, R.W., Majorana, C.E. and Schrefler, B.A., 1986. A coupled finite element model for the consolidation of nonisothermal elastoplastic porous media. Transport in porous media, 1(2), pp.155-178.

Lewis, R.W. and Schrefler, B.A., 1982. A finite element simulation of the subsidence of gas reservoirs undergoing a water drive. Finite element in fluids, 4, pp.179-199.

Lewis, R.W. and Schrefler, B.A., 1998. The finite element method in the static and dynamic deformation and consolidation of porous media. John Wiley.

Lewis, R.W. and Sukirman, Y., 1993. Finite element modelling for simulating the surface subsidence above a compacting hydrocarbon reservoir. International journal for numerical and analytical methods in geomechanics, 18(9), pp.619-639.

Li, W. and Wei, C., 2015. An efficient finite element procedure for analyzing three-phase porous media based on the relaxed Picard method. International Journal for Numerical Methods in Engineering, 101(11), pp.825-846.

Li, X., Zienkiewicz, O.C. and Xie, Y.M., 1990. A numerical model for immiscible two-phase fluid flow in a porous medium and its time domain solution. International Journal for Numerical Methods in Engineering, 30(6), pp.1195-1212.

Liakopoulos, A.C., 1965. Transient flow through unsaturated porous media [Ph. D. thesis]. University of California, Berkeley, Calif, USA.

Liu, G.R. and Quek, S.S., 2013. The finite element method: a practical course. Butterworth-Heinemann.

Madenci, E. and Guven, I., 2015. The finite element method and applications in engineering using ANSYS®. Springer.

Mainguy, M. and Longuemare, P., 2002. Coupling fluid flow and rock mechanics: formulations of the partial coupling between reservoir and geomechanical simulators. Oil & Gas Science and Technology, 57(4), pp.355-367.

Mandel, J., Consolidation des sols (étude mathématique), Géotechnique 30 (1953) 287 – 289.

Mansi, M., Mehana, M., Fahes, M. and Viswanathan, H., 2020. Thermodynamic modeling of the temperature impact on low salinity waterflooding performance in sandstones. Colloids and Surfaces A: Physicochemical and Engineering Aspects, 586, p.124207.

Martinez, R., Rosinski, J., and Dreher, D. 2012. Horizontal pressure sink mitigation completion design: a case study in the Haynesville Shale. SPE Annual Technical Conference and Exhibition, San Antonio, TX, USA, 8-10 October.

Masouleh, S.F.; Kumar, D.; Ghassemi, A. Three-Dimensional Geomechanical Modeling and Analysis of Refracturing and "Frac-Hits" in Unconventional Reservoirs. Energies 2020, 13, 5352.

McTigue, D.F., 1986. Thermoelastic response of fluid-saturated porous rock. Journal of Geophysical Research: Solid Earth, 91(B9), pp.9533-9542.

Meng, F., 1998. Three-dimensional finite element modeling of two-phase fluid flow in deformable naturally fractured reservoirs (Doctoral dissertation).

Mikelić, A. and Wheeler, M.F., 2013. Convergence of iterative coupling for coupled flow and geomechanics. Computational Geosciences, 17(3), pp.455-461.

Miller. G., Linsay, G., Baihly, J., and Xu, T. 2016. Parent well refracturing: economic safety nets in an uneconomic market. SPE Low Perm Symposium, Denver, CO, USA: 1-15.

Minkoff, S.E., Stone, C.M., Arguello, J.G., Bryant, S., Eaton, J., Peszynska, M. and Wheeler, M., 1999, January. Staggered in time coupling of reservoir flow simulation and geomechanical deformation: Step 1-one-way coupling. In SPE Reservoir Simulation Symposium. Society of Petroleum Engineers.

Minkoff, S.E., Stone, C.M., Bryant, S., Peszynska, M. and Wheeler, M.F., 2003. Coupled fluid flow and geomechanical deformation modeling. Journal of Petroleum Science and Engineering, 38(1-2), pp.37-56.

Morales, A., Zhang, K., Gakhar, K., Porcu, M.M., Lee, D., Shan, D., Malpani, R., Sobernheim, D., and Acock, A. 2016. Advanced modeling of interwell fracturing interference: An Eagle Ford Shale oil study-refracturing. SPE Hydraulic Fracturing Technology Conference, Woodlands, TX, USA: 1-19.

Muskat, M., 1981. Physical principles of oil production.

Nagel, F. and Meschke, G., 2010. An elasto-plastic three phase model for partially saturated soil for the finite element simulation of compressed air support in tunnelling. International Journal for Numerical and Analytical Methods in Geomechanics, 34(6), pp.605-625.

Neaupane, K.M., Yamabe, T. and Yoshinaka, R., 1999. Simulation of a fully coupled thermo–hydro–mechanical system in freezing and thawing rock. International Journal of Rock Mechanics and Mining Sciences, 36(5), pp.563-580.

Nguyen, T.S., 1995. Computational modelling of thermal-hydrological-mechanical processes in geological media (Doctoral dissertation, McGill University Libraries).

Nur, A. and Byerlee, J., 1971. An exact effective stress law for elastic deformation of rock with fluids. Journal of geophysical research, 76(26), pp.6414-6419.

Palmar, I.D. 1993. Induced stresses due to propped hydraulic fracture coalbed methane wells. SPE 25861: 221-232.

Pao, W.K., Lewis, R.W. and Masters, I., 2001. A fully coupled hydro-thermo-poro-mechanical model for black oil reservoir simulation. International journal for numerical and analytical methods in geomechanics, 25(12), pp.1229-1256.

Pepper, D.W. and Heinrich, J.C., 2017. The Finite Element Method: Basic Concepts and Applications with MATLAB, MAPLE, and COMSOL. CRC Press.

Perkins, T.K. and Gonzalez, J.A., 1985. The effect of thermoelastic stresses on injection well fracturing. Society of Petroleum Engineers Journal, 25(01), pp.78-88

Rahman, N.A. and Lewis, R.W., 1999. Finite element modelling of multiphase immiscible flow in deforming porous media for subsurface systems. Computers and Geotechnics, 24(1), pp.41-63.

Rajapakse, R.K.N.D., 1993. Stress analysis of borehole in poroelastic medium. Journal of engineering mechanics, 119(6), pp.1205-1227.

Rezaei, A., Rafiee, M., Bornia, G., Soliman, M., and Morse, S. 2017. Protection Refrac: Analysis of pore pressure and stress change due to refracturing of Legacy Wells. Unconventional Resources Technology Conference, held in Austin, Texas, USA, pp.1-16.

Rice, J.R. and Cleary, M.P., 1976. Some basic stress diffusion solutions for fluid-saturated elastic porous media with compressible constituents. Reviews of Geophysics, 14(2), pp.227-241.

Roussel, N.P., Florez, H. and Rodriguez, A.A., 2013, September. Hydraulic fracture propagation from infill horizontal wells. In SPE Annual Technical Conference and Exhibition. Society of Petroleum Engineers.

Rutqvist, J., Wu, Y.S., Tsang, C.F. and Bodvarsson, G., 2002. A modeling approach for analysis of coupled multiphase fluid flow, heat transfer, and deformation in fractured porous rock. International Journal of Rock Mechanics and Mining Sciences, 39(4), pp.429-442.

Rutqvist, J., Birkholzer, J., Cappa, F. and Tsang, C.F., 2007. Estimating maximum sustainable injection pressure during geological sequestration of CO2 using coupled fluid flow and geomechanical fault-slip analysis. Energy Conversion and Management, 48(6), pp.1798-1807.

Rutqvist, J., 2011. Status of the TOUGH-FLAC simulator and recent applications related to coupled fluid flow and crustal deformations. Computers & Geosciences, 37(6), pp.739-750

Rutqvist, J., Rinaldi, A.P., Cappa, F. and Moridis, G.J., 2013. Modeling of fault reactivation and induced seismicity during hydraulic fracturing of shale-gas reservoirs. Journal of Petroleum Science and Engineering, 107, pp.31-44.

Safari, R., and A., Ghassemi. 2015. 3D thermos-poroelastic analysis of the fracture network deformation and induced micro-seismicity in enhanced geothermal systems. Geothermics, Vol.58: 1-14.

Safari, R., Ma, X., Mutlu, O., Ghassemi, A. 2016. Infill well fracturing optimization in tightly spaced horizontal wells. SPE Journal. SPE-178513-PA.

Samimi, S. and Pak, A., 2016. A fully coupled element-free Galerkin model for hydro-mechanical analysis of advancement of fluid-driven fractures in porous media. International Journal for Numerical and Analytical Methods in Geomechanics, 40(16), pp.2178-2206.

Sangnimnuan, A., Li, J., Wu, K., Development of Coupled Two phase Flow and Geomechanics Model to Predict Stress Evolution in Unconventional Reservoirs with Complex Fracture Geometry, Journal of Petroleum Science and Engineering, https://doi.org/10.1016/j.petrol.2020.108072

Schrefler, B.A. and Gawin, D., 1996. The effective stress principle: incremental or finite form? International journal for numerical and analytical methods in geomechanics, 20(11), pp.785-814.

Schrefler, B.A., 2001. Modelling of subsidence due to water or hydrocarbon withdrawal from the subsoil. In Environmental Geomechanics (pp. 235-301). Springer, Vienna.

Schrefler, B.A., Zhan, X. and Simoni, L., 1995. A coupled model for water flow, airflow and heat flow in deformable porous media. International Journal of Numerical Methods for Heat & Fluid Flow, 5(6), pp.531-547.

Schümann, B., 2010. Modeling of soils as multiphase materials with Abaqus. In 2010 SIMULIA Customer Conference (pp. 1-15).

Settari, A. and Mourits, F.M. (1994) Coupling of Geomechanics and Reservoir Simulation Models. Computer Methods and Advances in Geomechanics, 2151-2158.

Settari, A. and Mourits, F.M., 1998. A coupled reservoir and geomechanical simulation system. Spe Journal, 3(03), pp.219-226.

Siebrits, E., Elbel, J.L., Detournay, E., Detournay-Piette, C., Christianson, M., Robinson, B.M. and Diyashev, I.R., 1998, January. Parameters affecting azimuth and length of a secondary fracture during a refracture treatment. In SPE Annual Technical Conference and Exhibition. Society of Petroleum Engineers.

Siripatrachai, N., Ertekin, T. and Johns, R.T., 2017. Compositional simulation of hydraulically fractured tight formation considering the effect of capillary pressure on phase behavior. SPE Journal, 22(04), pp.1-046.

Smith, I.M. and Griffiths D.V. ,2004. Programming the finite element method, 4th edn. Wiley, Hoboken

Terzaghi, K., Peck, R.B. and Mesri, G., 1996. Soil mechanics in engineering practice. John Wiley & Sons.

Van Genuchten, M.T., 1980. A closed-form equation for predicting the hydraulic conductivity of unsaturated soils 1. Soil science society of America journal, 44(5), pp.892-898.

Verruijt, A., 2013. Theory and problems of poroelasticity. Delft University of Technology, p.71.

Wan, J., 2003. Stabilized finite element methods for coupled geomechanics and multiphase flow (Doctoral dissertation, stanford university).

Wang, M. and Leung, J.Y., 2015, July. Numerical Investigation of Coupling Multiphase Flow and Geomechanical Effects on Water Loss During Hydraulic Fracturing Flow Back Operation. In Unconventional Resources Technology Conference, San Antonio, Texas, 20-22 July 2015 (pp. 1224-1243).

Wang, Y. and Lu, B., 2001, January. A coupled reservoir-geomechanics model and applications to wellbore stability and sand prediction. In SPE International Thermal Operations and Heavy Oil Symposium. Society of Petroleum Engineers.

Warpinski, N.R. and Branagan, P.T. 1989. Altered Stress Fracturing. JPT (Sept. 1989): 990-997.

White, J.A., Castelletto, N. and Tchelepi, H.A., 2016. Block-partitioned solvers for coupled poromechanics: A unified framework. Computer Methods in Applied Mechanics and Engineering, 303, pp.55-74.

Wright, C.A., and R.A., Conant. 1995. Hydraulic fracture reorientation in primary and secondary recovery from low-permeability reservoirs. SPE Annual Technical Conference and Exhibition, Dallas, Oct. 22-25.

Yang, D., 2013. A Simulator with numerical upscaling for the analysis of coupled multiphase flow and geomechanics in heterogeneous and deformable porous and fractured media (Doctoral dissertation).

Zhang, 2004. A boundary element method for thermos-poroelasticity with applications in rock mechanics. MS Thesis, University of North Dakota. 144 p.

Zhou, X. and Ghassemi, A., 2009. Finite element analysis of coupled chemo-poro-thermo-mechanical effects around a wellbore in swelling shale. International Journal of Rock Mechanics and Mining Sciences, 46(4), pp.769-778.

7. Appendix A: Finite element discretization and Galerkin method

A.1 Boundary value problem

Suppose we seek a solution to the following differential equation:

$$\mathcal{L}u = -\bar{f} \quad in\ \Omega \tag{A.1}$$

$\mathcal{L}$ is a differential operator; u is the unknown field variable and $\bar{f}$ is the force term.

The boundary enclosing Ω, here denoted as Γ is divided into a Dirichlet, Γ_1 and a Neumann boundary, Γ_2 where:

$$\Gamma = \Gamma_1 \cup \Gamma_2 \tag{A.2}$$

Boundary conditions are as follows:

$$u = \bar{u} \ \ on\ \Gamma_1 \tag{A.3}$$

$$Bu = \bar{t} \ \ on\ \Gamma_2 \tag{A.4}$$

where B is an operator.

A.2 Method of weighted residuals

In general, it is difficult to obtain the exact solution u that satisfies the boundary value problem in section A.2.1. Therefore, we seek an approximate trial function $\tilde{u}$ that satisfies those conditions. $\tilde{u}$ may be expressed as:

$$u \approx \tilde{u}(x) = \sum_{i=1}^{n} N_i(x)\hat{u}_i \tag{A.5}$$

where N_i are linearly independent functions called shape functions and $\hat{u}_i$ are unknowns that need to be determined. After substitution of $\tilde{u}$ for u in Eqs. (A.1), (A.3) and (A.4), non-zero residuals are obtained:

$$R_D(x) = \mathcal{L}\tilde{u} + \bar{f} \neq 0 \quad in\ \Omega \tag{A.6}$$

$$R_S(x) = \tilde{u} - \bar{u} \neq 0 \quad on\ \Gamma_1 \tag{A.7}$$

$$R_N(x) = B\tilde{u} - \bar{t} \neq 0 \quad on\ \Gamma_2 \tag{A.8}$$

To find a good approximation $\tilde{u}$ for *u*, the residuals are forced to zero in an average sense. That is, the integral of weighted residuals in each element should be zero:

$$\int_\Omega w_{\Omega \mathrm{i}}(x) R_D(x) d\Omega + \int_{\Gamma_1} w_{Di}(x) R_S(x) d\Gamma + \int_{\Gamma_2} w_{Ni}(x) R_N(x) d\Gamma = 0 \tag{A.9}$$

We assume that the solution satisfies the boundary condition Eq. (A.3) as shape functions are required to be zero at all locations where Dirichlet boundary condition is specified. Consequently, the residuals on Γ_1 disappear in Eq. (A.9). Weighting functions $w_{\Omega \mathrm{i}}(x)$ and $w_{Ni}(x)$ are chosen in such a way that:

$$w_{\Omega \mathrm{i}}(x) = w_i(x) \quad in\ \Omega \tag{A.10a}$$

$$w_{Ni}(x) = -w_i(x) \quad in\ \Gamma_2 \tag{A.10b}$$

where $w_i(x)$ is a weighting function. *n* independent equations are required to solve Eq. (A.9) for $\hat{u}_i$. Therefore, *n* independent weighting functions are required. In standard Galerkin method, which is the one of the most widely used weighted residual methods, weighting functions are selected to be the same as shape functions (Liu and Quek, 2013), i.e.:

$$w_i(x) = N_i(x) \quad i=1,..,\ n \quad \text{in } \Omega \tag{A.21}$$

Thus Eq. (A.9) can be written as:

$$\int_\Omega N_{\mathrm{i}}(x)(\mathcal{L}\tilde{u} + \bar{f}) d\Omega - \int_{\Gamma_2} N_i(x)(B\tilde{u} - \bar{t}) d\Gamma = 0 \tag{A.32}$$

A set of simultaneous algebraic equations is generated from evaluation of Eq. (A.12) for each value of *i*. The system of equations can be written as:

$$\sum_{j=1}^{n} K_{ij}\hat{u}_j = f_i \quad i=1,2,..,n \tag{A.43}$$

Since the governing differential Eq. (A.1) is valid for the entire domain, Ω, it is valid in each subdivision of the domain or element, Ω^e as $\Omega = \bigcup_{e=1}^{nel} \Omega_e$. This subdivision describes what we refer to as a finite element mesh. Applying Galerkin method with weighting functions $w_i(x) = N_i^{(e)}(x)$ over each element domain results in:

$$\sum_{e=1}^{nel}\left(\int_{\Omega^e} N_j^{(e)}(x)R_D^{(e)}(x)d\Omega - \int_{\Gamma_2^{(e)}} N_j^{(e)}(x)R_N^{(e)}(x)d\Gamma\right) = 0 \tag{A.54}$$

In each element, the approximation of the variable is expressed as:

$$\tilde{u}^{(e)}(x) = \sum_{j=1}^{n} N_j^{(e)}(x)\hat{u}_j^{(e)} \tag{A.65}$$

n represents the number of nodes associated with element *e*. The nodal unknowns are denoted by $\hat{u}_j^{(e)}$ (Madenci and Guven 2015).

A.3 Finite element formulation of thermo-poroelasticity for axisymmetric case

In this section we will apply standard finite element discretization to the governing equations derived in chapter 2. As discussed in the previous section, the displacements, pore pressures and temperatures for any point in the element domain are approximated in terms of shape functions and nodal unknowns as:

$$u = N_i^u \hat{u}_i \tag{A.16}$$

$$v = N_i^u \hat{w}_i \tag{A.17}$$

$$p = N_i^p \hat{p}_i \tag{A.18}$$

$$T = N_i^T \hat{T}_i \tag{A.19}$$

where N_i^u, N_i^p and N_i^T are shape functions for displacement, pressure and temperature and $\hat{u}_i$ and $\hat{w}_i$ are nodal displacement components in r and z directions respectively. $\hat{p}_i$ and $\hat{T}_i$ are the temperature and pressure at node *i* respectively. In this study, 4-node quadrilateral elements are used. The total stress, strain, effective stress and displacement components can be written in vector form as:

$$\boldsymbol{\sigma} = \begin{bmatrix} \sigma_{rr} & \sigma_{zz} & \sigma_{rz} & \sigma_{\theta\theta} \end{bmatrix}^T \tag{A.20}$$

$$\boldsymbol{\varepsilon} = \begin{bmatrix} \varepsilon_{rr} & \varepsilon_{zz} & \gamma_{rz} & \varepsilon_{\theta\theta} \end{bmatrix}^T \tag{A.21}$$

$$\boldsymbol{\sigma}' = \begin{bmatrix} \sigma'_{rr} & \sigma'_{zz} & \sigma_{rz} & \sigma'_{\theta\theta} \end{bmatrix}^T \tag{A.22}$$

$$\hat{\boldsymbol{u}} = [u_i \quad w_i]^T \tag{A.23}$$

where:

$$\gamma_{rz} = 2\varepsilon_{rz} \tag{A.24}$$

Using the approximation stated in Eqs. (A.16) and (A.17) and strain-displacement Eqs. (2.12) through (2.15), a matrix form of strain-displacement relations can be found as follows:

$$\boldsymbol{\varepsilon} = \boldsymbol{B}\hat{\boldsymbol{u}} \tag{A.25}$$

where:

$$B = \begin{bmatrix} \frac{\partial N_1}{\partial r} & 0 & \frac{\partial N_2}{\partial r} & 0 & \frac{\partial N_3}{\partial r} & 0 & \frac{\partial N_4}{\partial r} & 0 \\ 0 & \frac{\partial N_1}{\partial z} & 0 & \frac{\partial N_2}{\partial z} & 0 & \frac{\partial N_3}{\partial z} & 0 & \frac{\partial N_4}{\partial z} \\ \frac{\partial N_1}{\partial z} & \frac{\partial N_1}{\partial r} & \frac{\partial N_2}{\partial z} & \frac{\partial N_2}{\partial r} & \frac{\partial N_3}{\partial z} & \frac{\partial N_3}{\partial r} & \frac{\partial N_4}{\partial z} & \frac{\partial N_4}{\partial r} \\ \frac{N_1}{r} & 0 & \frac{N_2}{r} & 0 & \frac{N_3}{r} & 0 & \frac{N_4}{r} & 0 \end{bmatrix} \cdots \tag{A.26}$$

Constitutive equation in matrix form can be written as:

$$\boldsymbol{\sigma}' = \boldsymbol{\sigma} + \alpha \boldsymbol{m} p = \boldsymbol{D}(\boldsymbol{\varepsilon} - \boldsymbol{\varepsilon}_0) \tag{A.27}$$

where $\mathbf{m} = \begin{bmatrix} 1 & 1 & 0 & 1 \end{bmatrix}^T$ and:

$$\mathbf{D} = \frac{E(1-\nu)}{(1+\nu)(1-2\nu)} \begin{bmatrix} 1 & \frac{\nu}{1-\nu} & 0 & \frac{\nu}{1-\nu} \\ \frac{\nu}{1-\nu} & 1 & 0 & \frac{\nu}{1-\nu} \\ 0 & 0 & \frac{1-2\nu}{2(1-\nu)} & 0 \\ \frac{\nu}{1-\nu} & \frac{\nu}{1-\nu} & 0 & 1 \end{bmatrix} \tag{A.28}$$

$\boldsymbol{\varepsilon}_0$ is the thermal strain caused by temperature change and is given by:

$$\boldsymbol{\varepsilon_0} = \frac{\alpha_m T}{3}\boldsymbol{m} \tag{A.29}$$

A.3.1 Numerical implementation

By applying Galerkin method to equilibrium Eq. (2.18) and traction boundary condition (2.31) we have:

$$\iiint_{\Omega^e} N_i^u \left(\frac{\partial \sigma_{rr}}{\partial r} + \frac{\partial \sigma_{rz}}{\partial z} + \frac{1}{r}(\sigma_{rr} - \sigma_{\theta\theta})\right) d\Omega^e - \int_{\Gamma_u^2} N_i^u (\sigma_{rr} n_r + \sigma_{rz} n_z - t_r) d\Gamma = 0 \tag{A.30}$$

For an element in cylindrical coordinates, the infinitesimal volume and area are:

$$d\Omega^e = r d\theta dA \tag{A.31}$$

$$d\Gamma^e = r d\theta ds \tag{A.32}$$

where s is the arc length on which the traction t_r is applied and dA is the differential area in r-z plane. When integrating over volume, θ can come out of the area integral and be integrated from 0 to 2π yielding:

$$d\Omega^e = 2\pi r dA \tag{A.33}$$

$$d\Gamma^e = 2\pi r ds \tag{A.34}$$

So, Eq. (A.30) can be written as:

$$\iint_A 2\pi N_i^u \left(r\frac{\partial \sigma_{rr}}{\partial r} + r\frac{\sigma_{rz}}{\partial z} + (\sigma_{rr} - \sigma_{\theta\theta})\right) dA - \int_{\Gamma_u^2} 2\pi r N_i^u (\sigma_{rr} n_r + \sigma_{rz} n_z - t_r) ds = 0 \tag{A.35}$$

By cancelling 2π out from the above equation:

$$\iint_A N_i^u \left(\frac{\partial(\sigma_{rr} r)}{\partial r} + \frac{\partial(\sigma_{rz} r)}{\partial z} - \sigma_{\theta\theta}\right) dA - \int_{\Gamma_u^2} r N_i^u (\sigma_{rr} n_r + \sigma_{rz} n_z - t_r) ds = 0 \tag{A.36}$$

If we apply Green's identity to the above equation, it results in:

$$\begin{aligned} &\int_{\Gamma_u} N_i^u \sigma_{rr} r n_r ds - \iint_A N_{i,r}^u \sigma_{rr} r dA + \int_{\Gamma_u} N_i^u \sigma_{rz} r n_z ds - \iint_A N_{i,z}^u \sigma_{rz} r dA - \iint_A N_i^u \sigma_{\theta\theta} dA - \\ &\int_{\Gamma_u^2} N_i^u \sigma_{rr} r n_r ds - \int_{\Gamma_u^2} N_i^u \sigma_{rz} r n_z ds + \int_{\Gamma_u^2} N_i^u r t_r ds = 0 \end{aligned} \tag{A.37}$$

We restrict the choice of N_i^u to functions which satisfy $N_i^u = 0$ on Γ_u^1. Using Eq. (A.2) and by rearranging Eq. (A.37) we get:

$$-\iint_A (N_{i,r}^u \sigma_{rr} r + N_{i,z}^u \sigma_{rz} r + N_i^u \sigma_{\theta\theta}) dA + \int_{\Gamma_u^2} r N_i^u t_r ds = 0 \tag{A.38}$$

where t_r is the traction component in r direction normal to the boundary. By substituting stresses from constitutive Eqs. (A.20), (A.21), (A.27), (A.28) and (A.29) yields:

$$\begin{aligned} &\int_{\Gamma_u^2} r N_i^u t_r ds = \iint_A ((r D_{11} \varepsilon_{rr} + r D_{12} \varepsilon_{zz} + r D_{14} \varepsilon_{\theta\theta}) N_{i,r}^u - \alpha p r N_{i,r}^u - \beta T r N_{i,r}^u)) dA \\ &+ \iint_A r N_{i,z}^u D_{33} \gamma_{rz} dA + \iint_A N_i^u (D_{41} \varepsilon_{rr} + D_{42} \varepsilon_{zz} + D_{44} \varepsilon_{\theta\theta}) dA \\ &+ \iint_A N_i^u (-\alpha p) dA + \iint_A N_i^u (-\beta T) dA \end{aligned} \tag{A.39}$$

where $\beta = K\alpha_m$. Using Eqs. (A.16) through (A.19) and (A.21) through (A.26) yields:

$$\int_{\Gamma_u^2} N_i^u r t_r ds = \iint_A r D_{11} N_{i,r}^u N_{k,r}^u dA\,[\hat{u}_k] + \iint_A r D_{12} N_{i,r}^u N_{k,z}^u dA[\hat{w}_k] + \iint_A D_{14} N_k^u N_{i,r}^u dA\,[\hat{u}_k] - \iint_A \alpha r N_{i,r}^u N_k^p dA[\hat{p}_k] - \iint_A \beta N_k^T r N_{i,r}^u dA[\hat{T}_k] + \iint_A r N_{i,z}^u D_{33} N_{k,z}^u dA\,[\hat{u}_k] + \iint_A r N_{i,z}^u D_{33} N_{k,r}^u dA[\hat{w}_k] + \iint_A (N_i^u D_{41} N_{k,r}^u dA[\hat{u}_k] + \iint_A N_i^u D_{42} N_{k,z}^u dA[\hat{w}_k] + \iint_A N_i^u D_{44} \frac{N_k^u}{r} dA[\hat{u}_k] - \iint_A \alpha N_i^u N_j^p dA[\hat{p}_j] - \iint_A \beta N_i^u N_j^T dA\,[\hat{T}_j] \tag{A.40}$$

In matrix form:

$$K_{uu}\hat{u} + K_{uw}\hat{w} - L_u\hat{p} - R_u\hat{T} = F_u \tag{A.41}$$

Eq. (2.19) states that:

$$\frac{\partial \sigma_{rz}}{\partial r} + \frac{\partial \sigma_{zz}}{\partial z} + \frac{1}{r}\sigma_{rz} + \rho g = 0 \tag{A.42}$$

Applying Galerkin method to the above equation and using Eq. (2.32) we have:

$$\iiint_{\Omega_e} N_i^u \left(\frac{\partial \sigma_{rz}}{\partial r} + \frac{\partial \sigma_{zz}}{\partial z} + \frac{1}{r}\sigma_{rz} + \rho g\right) d\Omega - \int_{\Gamma_w^2} N_i^u (\sigma_{rz} n_r + \sigma_{zz} n_z - t_z) d\Gamma = 0 \tag{A.43}$$

Using Eqs. (A.33) and (A.34) we have:

$$\iint_A N_i^u \left(r\frac{\partial \sigma_{rz}}{\partial r} + r\frac{\partial \sigma_{zz}}{\partial z} + \sigma_{rz} + r\rho g\right) dA - \int_{\Gamma_w^2} N_i^u r(\sigma_{rz} n_r + \sigma_{zz} n_z - t_z) ds = 0 \tag{A.44}$$

The above equation can be reorganized as:

$$\iint_A N_i^u \left(\frac{\partial (r\sigma_{rz})}{\partial r} + \frac{\partial (r\sigma_{zz})}{\partial z} + r\rho g\right) dA - \int_{\Gamma_u^2} N_i^u r(\sigma_{rz} n_r + \sigma_{zz} n_z - t_z) ds = 0 \tag{A.45}$$

Using Green's theorem, we get:

$$\int_{\Gamma} N_i^u \sigma_{rz} n_r r ds - \iint_A \sigma_{rz} N_{i,r}^u r dA + \int_{\Gamma} N_i^u \sigma_{zz} n_z r ds - \int_A \sigma_{zz} N_{i,z}^u r dA + \iint_A N_i^u \rho g r dA - \int_{\Gamma_w^2} N_i^u (\sigma_{rz} n_r + \sigma_{zz} n_z - t_z) r ds = 0 \tag{A.46}$$

We restrict the choice of N_i^u to functions which satisfy $N_i^u = 0$ on Γ_u^1. Considering Eq. (A.2), the above equation can be written as:

$$-\iint_A \sigma_{rz} N_{i,r}^u r dA - \iint_A \sigma_{zz} N_{i,z}^u r dA + \iint_A N_i^u \rho g r dA + \int_{\Gamma_u^2} N_i^u t_z r ds = 0 \tag{A.47}$$

where t_z is the traction component in z direction. By substituting stresses from Eqs. (A.27) through (A.28) in Eq. (A.47) we have:

$$\int_{\Gamma_w^2} N_i^u t_z r ds + \iint_A N_i^u \rho g r dA = \iint_A N_{i,r}^u (D_{33}\gamma_{rz}) r dA + \iint_A N_{i,z}^u (D_{21}\varepsilon_{rr} + D_{22}\varepsilon_{zz} + D_{24}\varepsilon_{\theta\theta}) r dA - \iint_A N_{i,z}^u \alpha p r dA - \iint_A N_{i,z}^u \beta T r dA \tag{A.48}$$

Using Eqs. (2.12) through (2-15), (A.16) through (A.19) and (A.21) through (A.26), we will have:

$$\begin{aligned} \int_{\Gamma_u^2} N_i^u t_z r ds + \iint_A N_i^u \rho g r dA &= \iint_A N_{i,r}^u D_{33} (N_{j,r}^u [\hat{w}_j] + N_{k,z}^u [\hat{u}_k]) r dA \\ &+ \iint_A N_{i,z}^u D_{21} N_{j,r}^u r dA [\hat{u}_j] + \iint_A N_{i,z}^u D_{22} N_{j,z}^u r dA [\hat{w}_j] \\ &+ \iint_A N_{i,z}^u D_{24} \frac{N_j^u}{r} [\hat{u}_j] r dA - \iint_A N_{i,z}^u \alpha N_j^p r dA [\hat{p}_j] \\ &- \iint_A N_{i,z}^u \beta N_k^T r dA [\hat{T}_k] \end{aligned} \tag{A.49}$$

or:

$$\int_{\Gamma_2^u} N_i^u t_z r ds + \iint_A N_i^u \rho g r dA$$

$$= \iint_A N_{i,r}^u D_{33} N_{j,r}^u r dA \left[\hat{w}_j\right] + \iint_A N_{i,r}^u D_{33} N_{k,z}^u r dA \left[\hat{u}_k\right]$$

$$+ \iint_A N_{i,z}^u D_{21} N_{j,r}^u r dA \left[\hat{u}_j\right] + \iint_A N_{i,z}^u D_{22} N_{j,z}^u r dA \left[\hat{w}_j\right] \quad \text{(A.50)}$$

$$+ \iint_A N_{i,z}^u D_{24} N_j^u dA \left[\hat{u}_j\right]$$

$$- \iint_A N_{i,z}^u \alpha N_j^p r dA \left[\hat{p}_j\right] - \iint_A N_{i,z}^u \beta N_k^T r dA \left[\hat{T}_k\right]$$

Eq. (A.50) can be written in matrix format by the following equation:

$$K_{wu}\hat{u} + K_{ww}\hat{w} - L_w\hat{p} - R_w\hat{T} = F_w + F_b \quad \text{(A.51)}$$

Using Eq. (2.23) and flow boundary condition (2.33) and applying Galerkin's method we have:

$$\iint_A N_i^p \left[\alpha\dot{\varepsilon}_{ii} + \frac{1}{M}\dot{p} - \gamma_2\dot{T} - \frac{\kappa}{r}\frac{\partial}{\partial r}\left(r\frac{\partial p}{\partial r}\right) - \kappa\frac{\partial}{\partial z}\left(\frac{\partial p}{\partial z} - \rho_w g\right) - q^f\right] r dA$$
$$- \int_{\Gamma_p^2} N_i^p(-\kappa\frac{\partial p}{\partial r}n_r - \kappa\frac{\partial p}{\partial z}n_z + \kappa\rho_w g - q^w) r ds = 0 \quad \text{(A.52)}$$

Using Eqs. (2.12) through (2.15) we have:

$$\iint_A N_i^p \frac{1}{M}\frac{\partial p}{\partial t} r dA + \iint_A N_i^p \alpha \frac{\partial}{\partial t}\left[\frac{\partial u}{\partial r} + \frac{u}{r} + \frac{\partial w}{\partial z}\right] r dA - \iint_A \gamma_2 N_i^p \frac{\partial T}{\partial t} r dA - \iint_A N_i^p q^f r dA$$
$$- \iint_A N_i^p \kappa \frac{\partial}{\partial r}(r\frac{\partial p}{\partial r}) dA - \iint_A N_i^p \kappa \frac{\partial}{\partial z}(\frac{\partial p}{\partial z}) r dA + \iint_A N_i^p \kappa \frac{\partial(\rho_w g)}{\partial z} r dA + \quad \text{(A.53)}$$
$$\int_{\Gamma_p^2} N_i^p(\kappa\frac{\partial p}{\partial r}n_r + \kappa\frac{\partial p}{\partial z}n_z - \kappa\rho_w g + q^w) r ds = 0$$

Using Eqs. (A.16) through (A.19) and applying Green's theorem we will have:

$$\frac{1}{M}\iint_A N_i^p N_j^p r dA[\dot{\hat{p}}_j] + \alpha \iint_A N_i^p N_{j,r}^u r dA\,[\dot{\hat{u}}_j] + \alpha \iint_A N_i^p N_j^u dA\,[\dot{\hat{u}}_j]$$
$$+\alpha \iint_A N_i^p N_{j,z}^u r dA\,[\dot{\hat{q}}_j] - \gamma_2 \iint_A N_i^p N_j^T r dA\left[\dot{\hat{T}}_j\right]$$
$$-\left[\int_\Gamma N_i^p \kappa N_{j,r}^p n_r r\, ds[\hat{p}_j] - \iint_A \kappa N_{j,r}^p N_{i,r}^p r dA\,[\hat{p}_j]\right]$$
$$-\left[\int_\Gamma N_i^p \kappa N_{j,z}^p n_z r ds[\hat{p}_j] - \iint_A \kappa N_{j,z}^p N_{i,z}^p r dA\,[\hat{p}_j]\right] - \iint_A N_{i,z}^p \kappa \rho_w g r dA \qquad (A.54)$$
$$+\int_{\Gamma_p^2} N_i^p \kappa N_{j,r}^p n_r r ds\,[\hat{p}_j] + \int_{\Gamma_p^2} N_i^p \kappa N_{j,z}^p n_z r ds\,[\hat{p}_j]$$
$$+\int_{\Gamma_p^2} N_i^p q^w r ds - \iint_A N_i^p q^f r dA = 0$$

We restrict the choice of N_i^p to functions which satisfy $N_i^p = 0$ on Γ_p^1. Using Eq. (A.2), the above equation can be written as:

$$\frac{1}{M}\iint_A N_i^p N_j^p r dA[\dot{\hat{p}}_j] + \alpha \iint_A N_i^p N_{j,r}^u r dA\,[\dot{\hat{u}}_j] + \alpha \iint_A N_i^p N_j^u dA\,[\dot{\hat{u}}_j]$$
$$+\alpha \iint_A N_i^p N_{j,z}^u r dA[\dot{\hat{w}}_j] - \gamma_2 \iint_A N_i^p N_j^T r dA\left[\dot{\hat{T}}_j\right] + \iint_A \kappa N_{i,r}^p N_{j,r}^p r dA\,[\hat{p}_j]$$
$$+\iint_A \kappa N_{j,z}^p N_{i,z}^p r dA\,[\hat{p}_j] + \int_{\Gamma_p^2} N_i^p q^w r ds - \iint_A N_i^p q^f r dA \qquad (A.55)$$
$$-\iint_A N_{i,z}^p \kappa \rho_w g r dA = 0$$

In matrix form:

$$K_{pu}\dot{\hat{u}} + K_{pw}\dot{\hat{w}} + K_{pp}\dot{\hat{p}} + H_{pp}\hat{p} - K_{pT}\dot{\hat{T}} = -Q^w + Q^f + Q^b \qquad (A.56)$$

Applying Galerkin method to heat diffusivity Eq. (2.24) considering the boundary condition (2.34) we get:

$$\iint_A \rho c N_i^T \left[\frac{\partial T}{\partial t}\right] r dA - \iint_A k^T N_i^T \frac{1}{r}\frac{\partial}{\partial r}(r\frac{\partial T}{\partial r}) r dA - \iint_A k^T N_i^T \frac{\partial}{\partial z}(\frac{\partial T}{\partial z}) r dA$$
$$-\int_{\Gamma_T^2} N_i^T(-\mathbf{k}^T \nabla T - \mathbf{q}^T).\mathbf{n} r ds = \iint_A N_i^T q^{th} r dA \qquad (A.57)$$

By using Eq. (A.19) and using Green's theorem we get:

$$\iint_A \rho c N_i^T N_j^T r dA \left[\dot{\hat{T}}_j\right] - \left[\int_\Gamma N_i^T k^T N_{j,r}^T n_r r ds \left[\hat{T}_j\right] - \iint_A r k^T N_{i,r}^T N_{j,r}^T dA \left[\hat{T}_j\right]\right]$$
$$- \left[\int_\Gamma N_i^T r k^T N_{j,z}^T n_z ds \left[\hat{T}_j\right] - \iint_A r k^T N_{i,z}^T N_{j,z}^T dA \left[\hat{T}_j\right]\right]$$
$$+ \int_{\Gamma_T^2} N_i^T \boldsymbol{k}^T \nabla T . \boldsymbol{n} r ds \tag{A.58}$$
$$+ \int_{\Gamma_T^2} N_i^T \boldsymbol{q}^T . \boldsymbol{n} r ds = \iint_A N_i^T q^{th} r dA$$

Or:

$$\iint_A \rho c N_i^T N_j^T r dA \left[\dot{\hat{T}}_j\right] - \int_\Gamma N_i^T k^T N_{j,r}^T n_r r ds \left[\hat{T}_j\right] + \iint_A k^T N_{i,r}^T N_{j,r}^T r dA \left[\hat{T}_j\right]$$
$$- \int_\Gamma N_i^T k^T N_{j,z}^T n_z r ds \left[\hat{T}_j\right] + \iint_A k^T N_{i,z}^T N_{j,z}^T r dA \left[\hat{T}_j\right]$$
$$+ \int_{\Gamma_T^2} N_i^T k^T N_{j,r}^T n_r r ds \left[\hat{T}_j\right] \tag{A.59}$$
$$+ \int_{\Gamma_T^2} N_i^T k^T N_{j,z}^T n_z r ds \left[\hat{T}_j\right] + \int_{\Gamma_T^2} N_i^T \boldsymbol{q}^T . \boldsymbol{n} r ds = \iint_A N_i^T q^{th} r dA$$

We restrict the choice of N_i^T to functions which satisfy $N_i^T = 0$ on Γ_T^1. By using Eq. (A.2), above equation can be written as:

$$\iint_A \rho c N_i^T N_j^T r dA \left[\dot{\hat{T}}_j\right] + \iint_A r k^T N_{i,r}^T N_{j,r}^T dA \left[\hat{T}_j\right] + \iint_A r k^T N_{i,z}^T N_{j,z}^T dA \left[\hat{T}_j\right]$$
$$+ \int_{\Gamma_T^2} N_i^T \boldsymbol{q}^T . \boldsymbol{n} r ds \tag{A.60}$$
$$- \iint_A N_i^T q^{th} r dA = 0$$

or:

$$K_{TT} \dot{\hat{T}} + H_{TT} \hat{T} = -Q^T + Q^{th} \tag{A.61}$$

Eqs. (A.41), (A.51), (A.56) and (A.61) can be written in the matrix form as below:

$$\begin{bmatrix} K_{uu} & K_{uw} & -L_u & -R_u \\ K_{wu} & K_{ww} & -L_w & -R_w \\ K_{pu} & K_{pw} & K_{pp} & -K_{pT} \\ 0 & 0 & 0 & K_{TT} \end{bmatrix} \frac{d}{dt} \begin{bmatrix} \hat{u} \\ \hat{w} \\ \hat{p} \\ \hat{T} \end{bmatrix} + \begin{bmatrix} 0 & 0 & 0 & 0 \\ 0 & 0 & 0 & 0 \\ 0 & 0 & H_{pp} & 0 \\ 0 & 0 & 0 & H_{TT} \end{bmatrix} \begin{bmatrix} \hat{u} \\ \hat{w} \\ \hat{p} \\ \hat{T} \end{bmatrix}$$
$$= \begin{bmatrix} \frac{dF_u}{dt} \\ \frac{dF_w}{dt} + \frac{dF_b}{dt} \\ -Q^w + Q^f + Q^b \\ -Q^T + Q^{th} \end{bmatrix} \tag{A.62}$$

The above matrix coefficients are given in detail in next section.

A.3.2 Discretization in time

Finite differences in time are used for temporal discretization ($[0,T] = \cup_1^{n_T}[t_n, t_{n+1}]$). For any variable '$r$', if we assume linear interpolation over a time slab]t_0, t_1[, we can write:

$$r_1 = r_0 + \Delta t[(1-\theta)\dot{r}_0 + \theta\dot{r}_1] \qquad 0 \le \theta \le 1 \tag{A.63}$$

where r_0 and r_1 are the values of r at times "0" and "1" and θ is the time stepping factor in the range $0 \le \theta \le 1$. If $\theta = 1$ the algorithm is fully implicit and is referred to as backward Euler scheme. Taking constant values of $\theta = 0$ and $\theta = 0.5$, the method is called forward Euler scheme and Crank-Nicholson scheme respectively. The time stepping process is un-conditionally stable if $\theta \ge 0.5$.

By rewriting Eq. (A.62) at two different time levels t_0 and t_1 and using Eq. (A.63) and some rearranging, we can get the following matrix form:

$$\begin{bmatrix} K_{uu} & K_{uw} & -L_u & -R_u \\ K_{wu} & K_{ww} & -L_w & -R_w \\ K_{pu} & K_{pw} & (K_{pp} + \theta\Delta t H_{pp}) & -K_{pT} \\ 0 & 0 & 0 & -(K_{TT} + \theta\Delta t H_{TT}) \end{bmatrix} \begin{bmatrix} \Delta u \\ \Delta w \\ \Delta p \\ \Delta T \end{bmatrix} = \begin{bmatrix} \Delta F_u \\ \Delta F_w + \Delta F_b \\ -\Delta t Q^w + \Delta t Q^f + \Delta t Q^b - \Delta t H_{pp} p_0 \\ \Delta t Q^T - \Delta t Q^{th} + \Delta t H_{TT} T_0 \end{bmatrix} \tag{A.64}$$

where:

$$[K_{uu}]_{ij} = \sum_{elem} \iint_A D_{11} N_{i,r}^u N_{j,r}^u r dA + \sum_{elem} \iint_A D_{14} N_j^u N_{i,r}^u dA$$

$$+ \sum_{elem} \iint_A D_{33} N_{i,z}^u N_{j,z}^u r dA$$

$$+ \sum_{elem} \iint_A D_{41} N_i^u N_{j,r}^u dA + \sum_{elem} \iint_A D_{44} N_i^u N_j^u r^{-1} dA$$

$$[K_{uw}]_{ij} = \sum_{elem} \iint_A D_{12} N_{i,r}^u N_{j,z}^u r dA$$

$$+ \sum_{elem} \iint_A N_{i,z}^u D_{33} N_{j,r}^u r dA + \sum_{elem} \iint_A N_i^u D_{42} N_{j,z}^u dA$$

$$[L_u]_{ij} = \sum_{elem} \iint_A \alpha N_{i,r}^u N_j^p r dA + \sum_{elem} \iint_A \alpha N_i^u N_j^p dA$$

$$[R_u]_{ij} = \sum_{elem} \iint_A \beta N_j^T N_{i,r}^u r dA + \sum_{elem} \iint_A \beta N_i^u N_j^T dA$$

$$[K_{wu}]_{ij} = \sum_{elem} \iint_A N_{i,r}^u D_{33} N_{j,z}^u r dA$$

$$+ \sum_{elem} \iint_A N_{i,z}^u D_{21} N_{j,r}^u r dA + \sum_{elem} \iint_A N_{i,z}^u D_{24} N_j^u dA$$

$$[K_{ww}]_{ij} = \sum_{elem} \iint_A N_{i,r}^u D_{33} N_{j,r}^u r dA + \sum_{elem} \iint_A N_{i,z}^u D_{22} N_{j,z}^u r dA$$

$$[L_w]_{ij} = \sum_{elem} \iint_A N_{i,z}^u \alpha N_j^p r dA$$

$$[R_w]_{ij} = \sum_{elem} \iint_A N_{i,z}^u \beta N_j^T r dA$$

$$[K_{pu}]_{ij} = \sum_{elem} \iint_A \alpha N_i^p N_{j,r}^u r dA + \sum_{elem} \iint_A \alpha N_i^p N_j^u dA$$

$$[K_{pw}]_{ij} = \sum_{elem} \iint_A \alpha N_i^p N_{j,z}^u r dA$$

$$[K_{pp}]_{ij} = \sum_{elem} \iint_A \frac{1}{M} N_i^p N_j^p r dA$$

$$[H_{pp}]_{ij} = \sum_{elem} \iint_A \kappa N_{i,r}^p N_{j,r}^p r dA + \sum_{elem} \iint_A \kappa N_{i,z}^p N_{j,z}^p r dA$$

$$[K_{pT}]_{ij} = -\sum_{elem} \iint_A \gamma_2 N_i^p N_j^T r dA$$

$$[K_{TT}]_{ij} = \sum_{elem} \iint_A \rho c N_i^T N_j^T r dA$$

$$[H_{TT}]_{ij} = \sum_{elem} \iint_A k^T N_{i,r}^T N_{j,r}^T r dA + \sum_{elem} \iint_A k^T N_{i,z}^T N_{j,z}^T r dA$$

$$[F_u]_i = \sum_{elem} \int_{\Gamma_u^2} N_i^u t_r r dS$$

$$[F_w]_i = \sum_{elem} \int_{\Gamma_u^2} N_i^u t_z r dS$$

$$[F_b]_i = \sum_{elem} \iint_A N_i^u \rho g r dA$$

$$[Q^w]_i = \sum_{elem} \int_{\Gamma_p^2} N_i^p q^w r dS$$

$$[Q^T]_i = \sum_{elem} \int_{\Gamma_T^N} N_i^T \boldsymbol{q}^T . \boldsymbol{n} r dS$$

$$[Q^f]_i = \sum_{elem} \iint_A N_i^p q^f r dA$$

$$[Q^{th}]_i = \sum_{elem} \iint_A N_i^T q^{th} r dA$$

$$[Q^b]_i = \sum_{elem} \iint_A N_{i,z}^p \kappa_z \rho_w g_z r dA$$

A.4 Finite element formulation of poroelasticity for plane strain case

Following a similar approach to above, after temporal discretization, we obtain the following system of equations for FEM modelling of plane strain poroelasticity:

$$\begin{bmatrix} \boldsymbol{K} & -\boldsymbol{C} \\ \boldsymbol{C}^T & (\boldsymbol{K_{pp}} + \theta \Delta t \boldsymbol{K_c}) \end{bmatrix} \begin{bmatrix} \Delta \boldsymbol{u} \\ \Delta \boldsymbol{p} \end{bmatrix} = \begin{bmatrix} \Delta \boldsymbol{f} \\ -\Delta t \boldsymbol{K_c p_0} + \Delta \boldsymbol{Q} \end{bmatrix} \quad \text{(A.65)}$$

where:

$$\boldsymbol{K} = \sum_{elem} \int_{A} [\boldsymbol{B}]^T [\boldsymbol{D}][\boldsymbol{B}]\, dA$$

$$\boldsymbol{C} = \sum_{elem} \int_{A} \boldsymbol{B}^T \alpha \boldsymbol{m} \boldsymbol{N_p} dA$$

$$\boldsymbol{K}_c = \sum_{elem} \int_{A} \left(\nabla \boldsymbol{N_p}\right)^T \left(\frac{\boldsymbol{k}}{\mu}\right) (\nabla \boldsymbol{N_p}) dA$$

$$\boldsymbol{K_{pp}} = \sum_{elem} \int_{\boldsymbol{A}} \boldsymbol{N_p}^{\boldsymbol{T}} \left(\frac{\boldsymbol{1}}{\boldsymbol{M}}\right) \boldsymbol{N_p} dA$$

$$\boldsymbol{f} = \sum_{elem} \int_{\boldsymbol{\Gamma_u^2}} \boldsymbol{N_u}^{\boldsymbol{T}} \boldsymbol{t} dS$$

$$\boldsymbol{\Delta Q} = -\Delta t \sum_{elem} \left(\int_{\Gamma_p^2} \boldsymbol{N_p}^T q^w \, dS - \int_{A} \boldsymbol{N_p}^T q^f dA - \int_{A} (\nabla \boldsymbol{N_p}) \frac{k}{\mu} \rho_w \boldsymbol{g} dA \right)$$

$$\boldsymbol{D} = \frac{E(1-\upsilon)}{(1+\upsilon)(1-2\upsilon)} \begin{bmatrix} 1 & \frac{\upsilon}{1-\upsilon} & 0 \\ \frac{\upsilon}{1-\upsilon} & 1 & 0 \\ 0 & 0 & \frac{1-2\nu}{2(1-\nu)} \end{bmatrix}$$

$$\boldsymbol{B} = \begin{bmatrix} \frac{\partial N_1^u}{\partial x} & 0 & \frac{\partial N_2^u}{\partial x} & 0 \\ 0 & \frac{\partial N_1^u}{\partial y} & 0 & \frac{\partial N_2^u}{\partial y} \dots \\ \frac{\partial N_1^u}{\partial y} & \frac{\partial N_1^u}{\partial x} & \frac{\partial N_2^u}{\partial y} & \frac{\partial N_2^u}{\partial x} \end{bmatrix}$$

$$\boldsymbol{u} = [u_1 \quad v_1 \dots]^T$$

$$\boldsymbol{m} = [1 \quad 1 \quad 0]^T$$

Evaluation of the above-mentioned integrals is achieved using 4-point Gaussian integration.

8. Appendix B: Terms in finite element matrices in two-phase model

For the case of two phase poroelastic model, the matrices appearing in Eq. (5.68) are given below:

$$\boldsymbol{K} = \int_{\Omega} [\boldsymbol{B}^T][\boldsymbol{D}][\boldsymbol{B}] d\Omega$$

$$\boldsymbol{L}_w = \int_{\Omega} [\boldsymbol{B}^T][\boldsymbol{m}][\boldsymbol{N}_p] \alpha S_w d\Omega$$

$$\boldsymbol{L}_n = \int_{\Omega} [\boldsymbol{B}^T] \alpha (1 - S_w)[\boldsymbol{m}][\boldsymbol{N}_p] d\Omega$$

$$\boldsymbol{S}_{ww} = \int_{\Omega} [\boldsymbol{N}_p^T] \left[\frac{nS_w}{K_w} - n\acute{S}_w + {S_w}^2 \frac{(\alpha - n)}{K_s} \right] [\boldsymbol{N}_p] d\Omega$$

$$\boldsymbol{K}_{cw} = \int_{\Omega} [\nabla {\boldsymbol{N}_p}^T][\boldsymbol{k}_w] [\nabla \boldsymbol{N}_p] d\Omega$$

$$\boldsymbol{L}_{nw} = \int_{\Omega} [\boldsymbol{N}_p]^T \left\{ n\acute{S}_w + S_w(1 - S_w) \frac{(\alpha - n)}{K_s} \right\} [\boldsymbol{N}_p] d\Omega$$

$$\boldsymbol{K}_{cn} = \int_{\Omega} [\nabla \boldsymbol{N}_p]^T [\boldsymbol{k}_n] [\nabla \boldsymbol{N}_p] d\Omega$$

$$\boldsymbol{S}_{nn} = \iint_{\Omega} [\boldsymbol{N}_p]^T \left[\frac{n(1 - S_w)}{K_n} - n\acute{S}_w + (1 - S_w)^2 \frac{(\alpha - n)}{K_s} \right] [\boldsymbol{N}_p] d\Omega$$

$$\mathbf{f}^{\mathbf{u}} = \int_{\Omega} \left[\mathbf{N}^{\mathbf{u}} \right]^T \rho [\mathbf{g}] d\Omega + \int_{\Gamma_u^N} \left[\mathbf{N}^{\mathbf{u}} \right]^T [\mathbf{t}] d\Gamma$$

$$\mathbf{f}^w = \int_{\Omega} \left[\nabla \mathbf{N}^p \right]^T [\mathbf{k}_w] \rho_w [\mathbf{g}] d\Omega + \int_{\Omega} \left[\mathbf{N}^p \right]^T q^{ws} d\Omega - \int_{\Gamma_w^N} \left[\mathbf{N}^p \right]^T q^w d\Gamma$$

$$\mathbf{f}^n = \int_{\Omega} \left[\nabla \mathbf{N}^p \right]^T [\mathbf{k}_n] \rho_n [\mathbf{g}] d\Omega + \int_{\Omega} \left[\mathbf{N}^p \right]^T q^{ns} d\Omega - \int_{\Gamma_n^N} \left[\mathbf{N}^p \right]^T q^n d\Gamma$$

where $\mathbf{m} = \begin{bmatrix} 1 & 1 & 1 & 0 & 0 & 0 \end{bmatrix}^T$